STUDY OF WAVE-CURRENT-ICE INTERACTIONS
OVER THE NORTHWEST ATLANTIC

by

Shangfei Lin

Submitted in partial fulfilment of the requirements
for the degree of Doctor of Philosophy

at

Dalhousie University
Halifax, Nova Scotia
April 2021

i

TABLE OF CONTENTS

LIST OF TABLES

LIST OF FIGURES

ABSTRACT

This thesis investigates the effects of important physical processes of the wave-current-ice interactions on the surface waves and three-dimensional (3D) circulations in the northwest Atlantic (NWA). These physical processes include the wind input, wave dissipation, depth-induced wave breaking, and wave dissipation and scattering in ice for wave evolution and wave-current interactions (WCIs). The approaches include analyses of observational data and the use of numerical models with different levels of complexity for surface waves and 3D circulations. A one-way coupled wave-circulation-ice model for the NWA is developed to evaluate four different packages (known as ST2/3/4/6) for the wind input and wave dissipation. The model results demonstrate that ST6 has the best performance but underestimates significant wave heights (SWHs) under the swell-dominated sea states partially due to low drag coefficient. The model is also used to investigate wave propagations in ice. Wave scattering significantly modifies wave parameters in ice over the NWA during winter storms due to the nonlinear effect on the wind input. To improve the performance of the commonly-used drag coefficient, a new parameterization of the drag coefficient is proposed based on observations. The new parameterization has different dependences of sea surface roughness on the wave age under different sea states and thus reduces deficiencies of three existing parameterizations. A new parameterization for depth-induced wave breaking over shallow waters is also proposed, in which the breaker index has a nonlinear dependence on the bottom slope. The new parameterizations of drag coefficient and depth-induced wave breaking are used in a two-way coupled wave-circulation model for the study of WCIs during Hurricanes Earl and Igor in 2010. The inclusion of WCIs in the coupled model significantly improves the model performance. Wave propagations are strongly affected by hurricane-driven currents, tides, and large-scale circulations. Surface waves modulate tides mainly due to the wave-induce bottom stress and enhance the storm surge mainly due to additional wave forces. Surface waves also affect the current patterns, water temperature and salinity from the surface to depths of more than ~100 m during hurricanes.

LIST OF ABBREVIATIONS AND
SYMBOLS USED

Abbreviation	Definition
1D	One-dimensional
2D	Two-dimensional
3D	Three-dimensional
AMSR2	Advanced Microwave Scanning Radiometer 2
ASCAT	Advanced Scatterometer
ASIS	Air-Sea Interaction Spar
ASSP	Arctic Sea State Program
BBL	Bottom-boundary layer
BoF	Bay of Fundy
CCI	Climate Change Initiative
CFSR	Climate Forecast System Reanalysis
CFSv2	Climate Forecast System reanalysis version 2
CICE	Los Alamos Community Ice Code
CIS	Canadian Ice Service
CISDA	Canadian Ice Service digital archive
COAWST	Coupled Ocean-Atmosphere-Wave-Sediment Transport
DELILAH	The Duck Experiment on Low frequency and Incident-band Longshore and Across-shore Hydrodynamics
DIA	Discrete Interaction Approximation
ECCC	Environment and Climate Change Canada
ECS	Eastern Canadian Shelf
ERA5	Fifth generation of the European Center for Medium-Range Weather Forecasts reanalysis
ESA	European Space Agency
FETCH	Flux, sea state, and remote sensing in conditions of variable fetch experiment

Abbreviation	Definition
FC	Fully-coupled run
GeB	Georges Bank
GEBCO	General Bathymetric Chart of the Oceans
GLORYS	Global ocean reanalysis and simulation dataset
GLS	Generic Length Scale
GoM	Gulf of Maine
GOTEX	Gulf of Tehuantepec Experiment
GrB	Grand Banks
GS	Gulf Stream
GSL	Gulf of St. Lawrence
HEXMAX	Humidity Exchange over the Sea Main Experiment
HWIND	Hurricane Wind Analysis System
HYCOM	Hybrid Coordinate Ocean Model reanalysis dataset
IFREMER	The French Research Institute for Exploitation of the Sea
JONSWAP	Joint North Sea Wave Project
LCh	Laurentian Channel
LHS	Left-Hand Side
MAB	Mid-Atlantic Bight
MABL	Marine Atmospheric Boundary Layer
MCT	Model Coupling Toolkit
MIZ	Marginal Ice Zone
MIZFP	Marginal Ice Zone Field Program
MLD	Mixed Layer Depth
MOST	Monin-Obukhov Similarity Theory
MSL	Mean Sea Level
MWP	Mean Wave Period
NBS	Coupled model no wave effects on bottom stress
NCEP	National Centers for Environmental Prediction
NDBC	National Buoy Data Center

Abbreviation	Definition
NERACOOS	Northeastern Regional Association of Coastal Ocean Observing Systems
NF	Newfoundland
NHC	National Hurricane Center
NLS	Newfoundland and Labrador Shelves
NVM	Coupled model no wave effects on vertical mixing
NWA	Northwest Atlantic
NWF	Coupled model no wave forces on currents
NWS	Coupled model no wave effects on wind stress
OISST	Optimally Interpolated sea surface temperature
OTIS	Oregon State University Tidal Inversion Software
PEI	Prince Edward Island
PWPs	Peak Wave Period
RAD	Relative Amplitude Difference
RANS	Reynolds-averaged Navier-Stokes
RASEX	Risø Air-Sea Exchange experiment
RB	Relative Bias
RHS	Right-Hand Side
RMSE	Root Mean Square Error
ROMS	Regional Ocean Modeling System
RS	Radiational Stress
RSS	Remote Sensing Systems
SAA	SmartAtlantic Alliance
ScS	Scotian Shelf
SI	Scatter Index
SIO	Scripps Institution of Oceanography
SIPEE	Sea Ice Physics and Ecosystem Experiment
SLRE	St. Lawrence River Estuary

Abbreviation	Definition
SSMI	Special Sensor Microwave Imager
SSS	Sea Surface Salinity
SST	Sea Surface Temperature
SWADE	Surface Wave Dynamics Experiment
SWAN	Simulating Waves Nearshore
SWH	Significant Wave Height
SAR	Synthetic Aperture Radar
TKE	Turbulent Kinetic Energy
US	United States
USGS	United States Geological Survey
WAVES	Water-Air Vertical Exchange Study
WCIIs	Wave-Current-Ice Interactions
WCIs	Wave-Current Interactions
WO	Wave-only model
WW3	WAVEWATCH III
WW3DG	WW3 Development Group

Symbol	Description	Unit
a	Coefficient for the relative wind	
a_1, a_2, a_3	Coefficients for the breaker index	
b_0, b_1, b_2	Coefficients for the breaker index	
B	Coefficient for the wave breaking intensity breaking	
B_1	Hurricane shape parameter	
B_n	Wave spectral saturation	
c	Tracer concentration	
c_i	Ice concentration	
$\boldsymbol{c_g}$	Group velocity of surface waves	$m\ s^{-1}$
c_p	Peak phase speed of surface waves	$m\ s^{-1}$
$c_k(c_\sigma)$, c_θ	Wave propagation speed in the frequency and directional spaces	$m\ s^{-1}$
C	Strength of nonlinear wave interaction	
C_{source}	Tracer source or sink	
C_d, C_{dz}, C_{dN}	Sea surface drag coefficient	
$C_{d,max}$	Maximum sea surface drag coefficient	
d	Total water depth	m
D_{tot}	Mean rate of total wave energy dissipation	$m^2\ s^{-1}$
D_{max}	Maximum ice floe size	m
E	Wave variance spectrum	m^2
E_s	Swell energy	m^2
E_w	Wind wave energy	m^2
E_{tot}	Total wave energy	m^2
f	Wave frequency	s^{-1}
Δf	Wave frequency increment	s^{-1}
$\bar{f}$, f_p	Mean and peak wave frequency	s^{-1}
f_c	Coriolis parameter	s^{-1}
f_s	Splitting frequency of wave spectra	s^{-1}
$\boldsymbol{F}$	Non-wave forces in the momentum equation	$m\ s^{-2}$
$\boldsymbol{F_w}$	Wave forces due to con-conservative wave dissipation	$m\ s^{-2}$
F_x	Wave-induced force per unit surface area	Pa
F_{ww}	Wind to wave energy flux	$W\ m^{-2}$
F_{wo}	Wave to ocean energy flux	$W\ m^{-2}$
F_{wi}	Wave to ice energy flux	$W\ m^{-2}$

Symbol	Description	Unit
g	Gravitational acceleration of the Earth	$m\ s^{-2}$
G	Ice elasticity	Pa
h_i	Ice thickness	m
H_s	Significant wave height	m
H_b	Breaking wave height	m
H_s^{max}	Maximum significant wave height	m
H_{max}	Maximum individual wave height	m
H_{rms}	Root-mean-square wave height	m
(J, K)	Horizontal and vertical components of the vortex force	$m\ s^{-2}$
$k,\ \boldsymbol{k}$	Wavenumber and wavenumber vector	m^{-1}
$k_r,\ k_i$	Real and imaginary parts of the complex wavenumber	m^{-1}
k_p	Peak wavenumber	m^{-1}
L	Local wavelength	m
L_0	Deep-water wavelength	m
L_1	Obukhov length	m
L_p	Wavelength of the spectral peak	m
m	Local bottom slope	
$m_1, m_2, n_1, n_2, A_1, A_2$	Coefficients for sea surface roughness parameterizations	
M	Simulated variables	
N	Wave action density	$m^2\ s$
n	Number of observations	
O	Observed variables	
p	Hydrostatic pressure	Pa
p_c	Central pressure	Pa
p_n	Ambient pressure	Pa
$p(H)$	Rayleigh wave height probability density function	
Q	Coefficient accounting for the modification of wave dispersion	
Q_b	Fraction of breaking waves	
r	Radius	m
R_m	Radius of the maximum wind	m
(s, q)	Coordinates in the wave direction and perpendicular to s	
(S_{xx}, S_{xy}, S_{yy})	Horizontal radiation stress components	Pa
S_{in}	Atmospheric wind input	$m^2\ s^{-1}$

Symbol	Description	Unit
S_{ds}	Wave energy dissipation	$m^2\,s^{-1}$
S_{nl4}	Nonlinear quadruplet wave interactions	$m^2\,s^{-1}$
S_{nl3}	Nonlinear triad wave interactions	$m^2\,s^{-1}$
S_{bot}	Bottom friction	$m^2\,s^{-1}$
S_{db}	Depth-induced wave breaking	$m^2\,s^{-1}$
S_{ice}	Non-conservative wave dissipation in ice	$m^2\,s^{-1}$
S_{is}	Conservative wave scattering in ice	$m^2\,s^{-1}$
t	Time	s
T_{air}	Air temperature	$°C$
T_{m01}	First order mean wave period	s
T_{m02}	Second order mean wave period	s
T_p	Peak wave period	s
$\boldsymbol{u}, w$	Horizontal and vertical quasi-Eulerian mean velocity	$m\,s^{-1}$
$\boldsymbol{u}_s, w_s$	Horizontal and vertical Stokes drift	$m\,s^{-1}$
u_*	Friction velocity	$m\,s^{-1}$
$\boldsymbol{U}$	Depth-weighted mean ocean current	$m\,s^{-1}$
$\boldsymbol{U_z},\ U_z$	Wind vector and speed at z m	$m\,s^{-1}$
$\boldsymbol{U_{10}},\ U_{10}$	Wind vector and speed at 10 m	$m\,s^{-1}$
$U_{zN},\ U_{10N}$	Corresponding wind speeds under neutral atmospheric conditions	$m\,s^{-1}$
V_g	Gradient wind speed	$m\,s^{-1}$
$W(H)$	Weighting function	
(x, y, z)	spatial coordinates	m
X	Wind fetch	km
$\dot{X}$	Wave propagation velocity in space	$m\,s^{-1}$
$\hat{\boldsymbol{z}}$	unit vector in the vertical direction	m
z_0	Sea surface roughness	m
$z_0^s,\ z_0^r$	Smooth and rough flow components of sea surface roughness	m
z_α	Tuning parameter for the wind input in ST3/4	
α	Wave dissipation rate in ice	m^{-1}
α_1	Apparent wave dissipation rate in ice	m^{-1}
α_c	Charnock parameter	
α_{BJ}	Parameter for the depth-induced wave breaking	
β	Non-dimensional wind-wave interaction parameter in ST2	

Symbol	Description	Unit
$\beta_{\max}$	Wind wave growth parameter in ST3/4	
γ, γ_{TG}	Breaker index	
γ_0, γ_1, γ_2	Parameters for the breaker index	
γ^2	Relative variance	
ϵ	Wave-induced tracer diffusivity	
θ	Wave direction	°
$\Delta\theta$	Wave direction increment	°
θ_w	Wind direction	°
ρ	Water density	$kg\ m^{-3}$
ρ_0	Reference water density	$kg\ m^{-3}$
ρ_a	Air density	$kg\ m^{-3}$
σ	Relative radian wave frequency	s^{-1}
σ_θ	Wave directional spread	°
v	Kinematic viscosity	$m^2\ s^{-1}$
τ	Wind stress	$kg\ m^{-1}\ s^{-2}$
η	Surface elevation	m
κ	von Karman's constant	
ψ_m	Dimensionless function of the Obukhov length	
λ_0	Deep-water wave steepness	
∇_h	Horizontal Laplace operator	
φ	Dynamic pressure	$m^2\ s^{-2}$
$\mathcal{R}$	Bernoulli-head	$m^2\ s^{-2}$

ACKNOWLEDGEMENTS

Firstly, I would like to express my deep and sincere gratitude to my supervisor Dr. Jinyu Sheng for giving me the opportunity to work on my doctoral research. Throughout my doctoral research, he has provided invaluable guidance for carrying out the research, presenting the research work, and writing the thesis. Without his continuous support and encouragement, this thesis research would hardly have been completed. His patience, motivation, enthusiasm, and immense knowledge have deeply inspired me. It was a great privilege and honor to work and study under his guidance.

Secondly, I would like to thank the rest of my thesis committee: Drs. William Perrie, David Barclay, Haibo Niu and Anya Waite, for their encouragement, insightful comments, and contributions to my thesis work. I would also like to thank my external examiner Dr. Meng Xia for taking the time to read my thesis and providing constructive comments.

Thirdly, I would like to thank Drs. Jinhai Zheng, Keith Thompson, Clark Richards, Jiuxing Xing, Qingtao Song and Bash Toulany for their suggestions and help during my doctoral study. I also appreciate the help from Drs. John Warner, Kyoko Ohashi and Lanli Guo for sharing some of the source codes used in this study. I am grateful to Dr. Rod Johnson for providing a research cruise opportunity at Bermuda to fulfill one of my PhD program requirements. Thanks also go to the faculty, staff and fellow graduate students in the department for stimulating discussions and for all the fun we have had in the last six years.

Finally, I would like to express my deepest appreciation to my parents and family members for their love and support throughout my life. Thank you for giving me the strength to chase my dreams. A very special word of thanks goes to my girlfriend for her accompany, support and encouragement, and all the treasured memories we have created.

CHAPTER 1

INTRODUCTION

1.1 Background

The northwest Atlantic (NWA) to be considered in my doctoral research comprises the Newfoundland and Labrador Shelves (NLS), Gulf of St. Lawrence (GSL), Scotian Shelf (ScS), Gulf of Maine (GoM), Mid-Atlantic Bight (MAB) and their adjacent deep waters. The NWA is socially and economically important since it supports commercial and recreational fisheries, offshore oil and gas exploration and production, marine recreation and tourism, transportation, and many other economic activities. Three-dimensional (3D) circulations over this region are influenced by two large-scale gyre systems: the north Atlantic subpolar gyre and the North Atlantic subtropical gyre (*Urrego-Blanco and Sheng,* 2012). The NWA is thus strongly affected by two large-scale ocean currents known as the Labrador Current and the Gulf Stream. The NWA also has several subregions with strong tidal currents, such as the GoM (*Chen et al.,* 2011). In addition, the NWA is subjected to extreme weather events such as hurricanes and winter storms. In the winter, ocean surface waves and currents are strongly affected by the formation and dispersal of the sea ice over the eastern Canadian shelf (ECS). With strong tidal flows, complex circulation patterns, hurricane-driven waves and the presence of sea ice, the interactions between ocean surface waves, 3D circulations and sea ice are very important physical mechanisms affecting the physical environments in this region.

1.1.1 Ocean Surface Wave

Wind-generated surface waves are the most prominent feature at the ocean surface and provide an essential part of marine environments that are used for coastal engineering

design, ship navigation, offshore operation, the management of costal hazards and recreational activities (*Stopa et al.,* 2016b). On the other hand, surface waves are of interest scientifically for many research purposes, such as the air-sea interactions, wave-current interactions, and beach morphology. Ocean surface waves receive energy from the atmosphere through the wind stress acting on the ocean surface. Surface waves, in turn, affect the air-sea fluxes through the modulation of sea surface roughness (*Drennan et al.,* 2003). Wave energy is then transferred among different frequencies through nonlinear wave interactions and dissipated through whitecapping and swell dissipation (Fig. 1.1). The process of wave dissipation then feeds the turbulent and large scale motions of the oceans (*Janssen,* 2004). In the nearshore area, depth-induced wave breaking becomes the primary process for wave dissipation (*Salmon et al.,* 2015) and is one of the primary mechanisms affecting surf zone hydrodynamics, sediment transport, beach transformation and wave-current interactions in coastal regions (*Guérin et al.,* 2018). It is therefore important to model surface waves sufficiently accurately and to enhance our understandings on the physical processes for wave evolution.

Over the past several decades, significant progress has been made for the numerical modelling of ocean surface waves (e.g., *Cavaleri et al.,* 2007; *Babanin,* 2011; *Babanin,* 2012). Forecasting and hindcasting of ocean surface waves are now commonly conducted by numerical simulation of the evolution of wave energy spectrum using the third-generation spectral wave models, such as the Simulating Waves Nearshore (SWAN) and WAVEWATCH III (WW3) models. In the third-generation spectral wave models, waves are adequately described by the wave spectrum E, but the evolution of the wave spectrum is in terms of the wave action density N, which is more suitable for the use of numerical models to accommodate wave-current interactions (*Komen et al.,* 1996).

In the open ocean, the source term used in these models generally consists of three main physical processes: the atmospheric wind input, wave dissipation and nonlinear wave interactions. The atmospheric wind input (S_{in}) depends on the estimation of wind stress, which is typically converted from the wind speed using bulk formulations in terms of a drag coefficient. The drag coefficient is traditionally expressed a function of the wind speed (e.g., *Smith,* 1980; *Large and Pond,* 1981). However, many studies have pointed out that

drag coefficient depends on not only the wind speed but also the wave state (e.g., *Smith et al.,* 1992; *Johnson et al.,* 1998; *Taylor and Yelland,* 2001; *Drennan et al.,* 2003; *Edson et al.,* 2013). Thus, the inclusion of both the wind speed and wave state dependences of wind stress is important for the accurate estimation of atmospheric wind input contributing to the growth of surface waves.

Wave dissipation mainly due to whitecapping is one of the least well understood parts among all the physical processes for wave growth and decay (*Babanin et al.,* 2017). Several analytical and semi-empirical parameterizations for wave dissipation now have been implemented into the third-generation spectral wave models (SWAN and WW3), together with the wind input parameterizations integrating into several source term packages (known as ST1/2/3/4/6). The uncertainty in the source terms is one of the major problems affecting the accuracy of wave model results (*Babanin,* 2011). It is therefore necessary to assess the performances of these source term packages in representing wave parameters especially in the dynamically complex region with the presence of currents and sea ice (*Stopa et al.,* 2016b).

As waves move into increasingly shallow waters, depth-induced wave breaking becomes the primary dissipation mechanism and thus is additional considered together with the bottom friction. The most widely-used parameterization for depth-induced wave breaking was suggested by *Battjes and Janssen* (1978, BJ78). BJ78 combined the wave breaking probability within a random wave field and an individual breaking wave height calculated from a constant breaker index. Since BJ78, various parameterizations have been proposed for the breaker index or wave breaking probability (e.g. *Thornton and Guza,* 1983; *Nelson,* 1987; *Battjes and Stive,* 1985; *Ruessink et al.,* 2003; *Goda,* 2010; *Salmon et al.,* 2015). However, these parameterizations were shown to have their own limitations (*Salmon et al.,* 2015). Thus, part of my PhD thesis work is to assess the performances of six existing parameterizations for depth-induced wave breaking in spectral wave models and to introduce a new parameterization to improve the performance of spectral wave models in simulating wave variables in coastal waters.

1.1.2   Wave-Ice Interactions

As mentioned above, the ECS is seasonally covered by sea ice over coastal regions. It is necessary and scientifically interesting to investigate wave propagations in ice and their interactions in this region. Intense wave-ice interactions occur in the region between the open water and interior pack ice, which is referred to as the marginal ice zone (MIZ). The ice cover in the MIZ is inhomogeneous and highly dynamic, consisting of different types of ice, such as grease ice, pancake ice and continuous ice sheet. Wave energy is dissipated and wave dispersion is modified over the MIZ (*Collins et al.,* 2017). Surface gravity waves, in turn, are responsible for the breakup of ice floes and determine the extent of the MIZ and floe size distribution (*Kohout et al.,* 2016).

Wave energy dissipation in the MIZ includes two major physical mechanisms, namely the non-conservative dissipative process and the conservative scattering process. The former includes a number of physical processes, such as wave breaking, turbulence, ice floe collisions, ice breakup and drifting. The latter redistributes wave energy in all directions. A wave dissipation rate α is commonly used to represent the complexity of modelling all the non-conservative wave dissipation processes in the ice (*Mosig et al.,* 2015). The wave dissipation rate can be parameterized as empirical functions of wave and ice characteristics based on field measurements (e.g., *Wadhams et al.,* 1988; *Doble et al.,* 2015). Alternatively, the wave dissipation rate α represents the exponential decay of wave energy, and it can be calculated from the imaginary part of wavenumber given as $\alpha = 2k_i$. The wavenumber can be obtained by solving the dispersion relations of different theories for wave propagation in the MIZ. However, the wave characteristics and dispersion relations through an ice cover differ significantly between different theories (*Zhao et al.,* 2015).

Several observational studies revealed some basic physics on waves in ice. *Wadhams et al.* (1988) reported the measurement of wave attenuation in the Arctic MIZ, showing directional spread of wave energy and frequency-dependent wave attenuation. They found that surface waves with long periods attenuate at slower rates and propagate greater distances into the ice field than the short period wave components. Based on the measurements of surface waves in the Antarctic MIZ, *Kohout et al.* (2014) found that the

attenuation rate is proportional to the SWH at small wave heights and remains as a constant at large wave heights. However, the analysis made by *Kohout et al.* (2014) did not consider the dependence of the attenuation rate on the wave period. Using the same dataset, *Meylan et al.* (2014) found smaller attenuation rates for longer wave periods, which is consistent with the findings of *Wadhams et al.* (1988). Based on the wave observations derived from the synthetic aperture radar (SAR), *Shen et al.* (2018) found the increased dominant wavelengths and shifted mean wave directions as waves penetrate into the MIZ. Due to the limited and sparse observations of surface gravity waves in ice and different ice types, the magnitude of the dissipation rate varies in a wide range (*Collins and Rogers,* 2017). The applicability of different theories and empirical formulas for wave propagations in ice in different ice types remain to be studied. Moreover, the treatment of wave propagations in ice over the ECS in previous studies (e.g., *Ruest et al.,* 2016; *Guo and Sheng,* 2015; *Guo and Sheng,* 2017; *Wang et al.,* 2018) is coarse and the effects of wave dissipation and scattering in ice require further investigations.
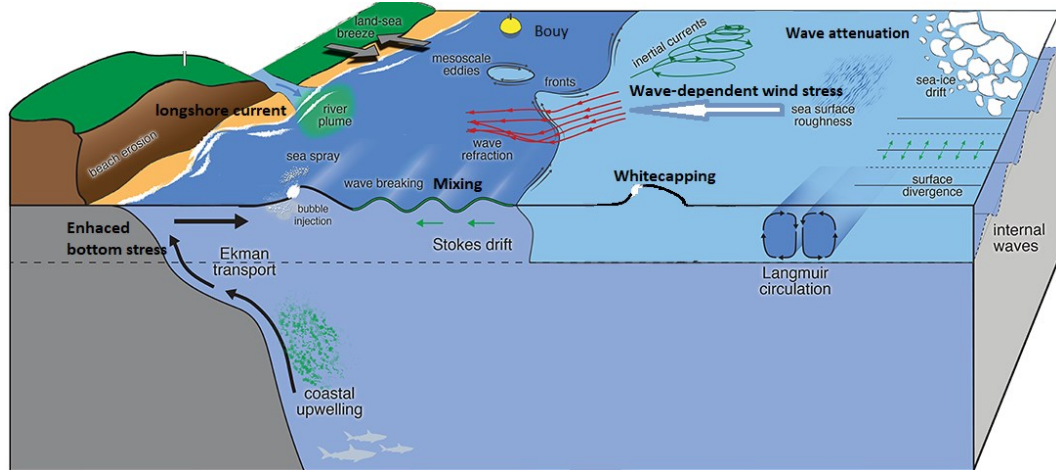
Figure 1.1: Schematic showing important processes for wave evolution and wave-current-ice interactions (Modified from *Villas Boas et al.,* 2019).

1.1.3   Wave-Current Interactions

When ocean surface waves encounter ocean currents, wave-current interactions (WCIs) can induce changes in the wave energy distribution, wave height, period and direction (*Babanin et al.,* 2017). Physically, ocean currents can modify the relative speeds of the air above the sea surface and affect the air-sea fluxes, which is known as the relative wind

effect (*Ardhuin et al.,* 2012). Ocean currents also affect the horizontal advection of surface waves and change the absolute frequencies of surface waves as a result of the Doppler shift. Spatially varying currents can induce wavenumber shift and cause wave refraction (*Wang and Sheng,* 2018). In addition to ocean currents, the variation of the sea level modifies the total water depth experienced by surface waves and thus can greatly affect wave propagations over coastal waters (*Dietrich et al.,* 2011).

Current-induced effects on waves have been widely investigated from coastal regions to deep waters (e.g., *Dietrich et al.,* 2011; *Olabarrieta et al.,* 2011; *Ardhuin et al.,* 2017; *Zou and Xie,* 2016; *Mao and Xia,* 2018; *Wang and Sheng,* 2018). It was suggested that, for example, coastal currents can modulate significantly the wave characteristics at tidal frequencies and have a significant impact on wave energy redistribution over frequency and directional domains (*Ardhuin et al.,* 2012; *Wang and Sheng,* 2018; *Zou and Xie,* 2016). In the open ocean, large-scale ocean circulations such as the Gulf Stream (*Ardhuin et al.,* 2017) can have significant effects on surface waves mainly due to wave refraction. The current-induced wave refraction is potentially responsible for the energy convergence and the enhanced probability of freak wave occurrence (*Rapizo et al.,* 2016).

Ocean surface gravity waves, in turn, can influence ocean currents by various processes, including the wave-dependent wind stress, wave-induced bottom stress, wave-enhanced mixing, and additional wave forces on currents (Fig. 1.1). Surface waves affect the wind stress through the modulation of sea surface roughness (*Drennan et al.,* 2003) and modify the air-sea momentum flux through wave growth and dissipation (*Perrie et al.,* 2003). Ocean currents and wave heights were found to be sensitive to the sea surface roughness parameterizations (e.g., *Sheng et al.,* 2010; *Olabarrieta et al.,* 2012; *Shi and Bourassa,* 2019). Therefore, significant efforts have been made to quantify the wave effects on the wind stress (e.g., *Smith et al.,* 1992; *Taylor and Yelland,* 2001; *Oost et al.,* 2002; *Drennan et al.,* 2003). At the ocean bottom, the interactions of surface waves with the sea bed can enhance the bottom shear stress experienced by currents (e.g., *Wolf and Prandle,* 1999; *Olabarrieta et al.,* 2011; *Dalyander et al.* 2013). *Wolf and Prandle* (1999) demonstrated that ocean surface waves can cause a decrease in tidal-current amplitudes with increasing wave heights through enhancement of the wave-averaged bottom stress. *Wu et al.* (2015)

investigated the effects of surface gravity waves on the vertical mixing in the ocean upper layer through mainly four processes: wave breaking, Stokes drift interaction with the Coriolis force, Langmuir circulation, and stirring by nonbreaking waves.

Previous studies also showed that the wave-induced forces can escalate surge elevations (*Huang et al.,* 2010) and cause alongshore and rip currents (*Kumar et al.,* 2011). The additional wave forces on currents are introduced in the 3D Reynolds-averaged Navier-Stokes equations (RANS) through the radiational stress (RS) formulation (e.g., *Mellor,* 2008 and 2015) or the vortex force (VF) formulation (e.g., *McWilliams et al.,* 2004; *Ardhuin et al.,* 2008; *Bennis et al.,* 2011). The RS formulation suggested by *Mellor* (2003 and 2008) has been widely implemented in various coastal ocean models and found to be able to improve the model performance (e.g., *Benetazzo et al.,* 2013; *Moghimi et al.,* 2013). However, recent studies found that (e.g., *Bennis et al.,* 2011; *Kumar et al.,* 2011; *Wang et al.,* 2017; *Xia et al.,* 2020) the RS formulation can create unrealistic flows in the wave shoaling regions and the VF formulation is superior to the RS formulation in simulating the wave-induced 3D currents from the surf zone to the open shelf waters.

These previous studies have broadened our understandings on the WCIs and laid the foundations for the numerical modelling of WCIs. However, some of the important physical processes in the WCIs were not included or not well represented, such as the effect of waves on the wind stress. Considering the complicated dynamics in the NWA, the interactions between surface waves and tides, river runoff, storms and large-scale circulations can significantly change the physical conditions in this region. It is necessary to investigate and quantify the effects of WCIs in different scales and different environmental conditions.

1.2 Objectives of the Thesis

The overall objective of my doctoral research is to advance our quantitative and predictive understandings of important mechanisms in the wave-current-ice interactions (WCIIs) and examine their effects on the ocean surface gravity waves and 3D circulations over the NWA. Previous studies have revealed some basic physics for WCIIs, which lay the foundations for the development of numerical models with different levels of complexity for the study

of WCIIs. However, there are many important scientific issues that remain to be addressed as mentioned in the above literature review. To make further progress, my doctoral research has five specific objectives, which include: (i) assessing the performances of various source term packages for the wind input and wave dissipation in the present of currents and sea ice, (ii) investigating wave dissipation and scattering in the ice-covered regions of the ECS, (iii) investigating the effect of waves on the wind stress and developing a more suitable parameterization representing the wave-dependent wind stress, (iv) assessing the performances of existing parametrizations for depth-induced wave breaking and developing a more suitable parameterization representing wave evolution at shallow waters, and (v) developing an effective coupled wave-circulation model for the NWA with appropriate representations of WCIs and then using this model to quantify the main physical processes affecting waves and circulations in this region. Addressing these issues would transform our understandings on the role of surface waves in the air-sea interactions, wave energy dissipation in deep and shallow waters, wave propagations in ice and WCIs.

The approaches used in my doctoral research include analyses of comprehensive observational data and the use of numerical models with different levels of complexity for simulating ocean surface gravity waves and 3D ocean circulations. To investigate the wave-dependent drag coefficient, observational data for the wind stress and wave parameters from eight literature-cited field experiments were collected. To assess the performances of various parametrizations for depth-induced wave breaking, 882 cases of laboratory and field observations from 14 literature-cited data sources were collected. To assess the performance of various source terms for the wind input and wave dissipation, a one-way coupled wave-ice-current modelling system was developed for the NWA based on the third-generation wave model WW3, an ocean reanalysis dataset known as HYCOM (*Cummings and Smedstad,* 2013), and a sea ice observational dataset from the Canadian Ice Service (CIS). This one-way coupled wave-ice-current modelling system was also used to investigate wave propagations in ice over the ECS. Moreover, a two-way coupled wave-circulation modelling system was developed to investigate the main physical mechanisms affecting WCIs over the NWA based on the Coupled Ocean-Atmosphere-Wave-Sediment Transport (COAWST) modeling system (*Warner et al.,* 2010). In the COAWST modelling system, the Simulating Waves Nearshore model (SWAN) and Regional Ocean Modeling

System (ROMS) are two-way coupled using the Model Coupling Toolkit (MCT). ROMS provides the current vector and the sea surface elevation to SWAN. SWAN, in turn, transfers wave dissipation source terms, surface and bottom wave parameters (including wave height, period, direction, wavelength, orbital velocity, Stokes drift and Bernoulli-head) to ROMS.

1.3 Outline of the Thesis

The structure of this thesis is as follows.

In Chapter 2, the one-way coupled wave-circulation-ice model for the NWA is used to evaluate four different source term packages for the wind input and wave dissipation during two periods: (i) winter storms in February and (ii) Hurricane Ophelia in 2011. The effects of ocean currents and sea ice on the wind input and wave dissipation are also investigated.

In Chapter 3, the one-way coupled wave-circulation-ice model for the NWA is used to investigate wave propagations in the ice-covered regions of the ECS during a winter storm in March 2014. This is in light of the results in Chapter 2 that there are large uncertainties for the numerical modelling of wave propagations in ice. Two viscoelastic models (known as IC3 and IC5) for wave dissipation in ice are applied in the modelling system by calibrating two essential ice rheological parameters (kinetic viscosity v and elasticity G) in these two viscoelastic models. The effect of wave scattering on wave propagations in ice is also investigated.

In Chapter 4, a new parameterization for the sea surface roughness is proposed to better represent the wind stress at the sea surface. This is inspired by the finding in Chapter 2 that one of the drawbacks for the source term packages is the low drag coefficient at low winds. The new parameterization proposed in Chapter 4 has different dependences of sea surface roughness on the wave age under different sea states based on observations. The performances of the new parameterization and three other existing parameterizations are further assessed using the one-way coupled wave-circulation-ice model for the NWA.

In Chapter 5, limitations of six commonly-used parameterizations for depth-induced wave breaking at shallow waters are identified based on laboratory and field observations. A new

parameterization with a nonlinear dependence on the local bottom slope is proposed and its performance is assessed.

In Chapter 6, the important processes discussed in previous chapters are incorporated into a two-way coupled wave-circulation model for the study of WCIs over the NWA. The package for the wind input and wave dissipation with the best performance (Chapter 2), and new schemes for the wave-dependent wind stress (Chapter 4) and depth-induced wave breaking (Chapter 5) are used in the two-way coupled wave-circulation model to investigate the WCIs during Hurricanes Earl and Igor in 2010. The effects of tides, wind-driven and large-scale circulations on ocean surface waves and the effects of waves on the sea level, current, temperature and salinity are investigated.

An overall summary is given in Chapter 7.

Chapters 2-6 are based on five separate papers. Therefore, some similar background material can be found in these Chapters. In particular, text describing the models are similar in several chapters. Chapter 2 was published in Atmosphere-Ocean under the title of "Performance evaluation of parameterizations for wind input and wave dissipation in the spectral wave model for the northwest Atlantic Ocean" (*Lin et al.,* 2020). Chapter 3 was in press in Continental Shelf Research under the title of "A comparative study of viscoelastic models for ocean wave dissipation in ice-covered regions of the eastern Canadian shelf". Chapter 4 was published in Continental Shelf Research under the title of "Revisiting Dependences of the Drag Coefficient at the Sea Surface on Wind Speed and Sea State" (*Lin and Sheng,* 2020). Chapter 5 was published in Ocean Modelling under the title of "Assessing the Performance of Wave Breaking Parameterizations in Shallow Waters in Spectral Wave Models" (*Lin and Sheng,* 2017). Chapter 6 will be submitted to the Journal of Geophysical Research-Oceans under the title of "Wave-current interactions during Hurricanes Earl and Igor in the northwest Atlantic".

CHAPTER 2

PERFORMANCES OF PARAMETERIZATIONS FOR WIND INPUT AND WAVE DISSIPATION IN THE SPECTRAL WAVE MODEL[1]

2.1 Introduction

Ocean surface gravity waves are of significant importance for ship navigation, ocean engineering, and many other scientific research and applications. Surface waves modulate the exchange of momentum, heat, and mass between the atmosphere and ocean (*Babanin,* 2011). Wave breaking drives currents (*Pizzo et al.,* 2016) and mixing in the upper layer of the ocean (*Wang and Sheng,* 2016) and enhances gas exchange across the air-sea interface (*Emerson and Bushinsky,* 2016). Particularly, accurate and timely predictions of severe sea states under extreme weather conditions, such as winter storms and hurricanes, are essential for engineering applications, studies of air-sea interactions and wave-current interactions, and accurate estimations of important air-sea fluxes under climate change (*Babanin,* 2011).

Ocean surface gravity waves are generated by energy input from winds. Wave energy is then transferred to different frequencies through nonlinear wave interactions and dissipated through wave dissipation. The primary mode of wave dissipation is whitecapping due to wave breaking, which is an intermittent, rapid, and highly nonlinear process. Wave dissipation is one of the least well known parts of all the physical processes for wave evolution and is often considered a tuning parameter to balance the residual energy of the

wind input in numerical wave models (*Cavaleri et al.,* 2007). Numerical modelling of ocean surface gravity waves is commonly accomplished by solving the wave action balance equation for the evolution of wave energy spectra. Several analytical expressions (e.g., *Phillips,* 1985) and physical features for wave dissipation (e.g., *Babanin et al.,* 2001) have been implemented in third-generation spectral wave models, such as the WAVEWATCH III (WW3). Five source term packages known as ST1, ST2, ST3, ST4, and ST6 were implemented in WW3 for the wind input and wave dissipation. These five packages have different parameterizations for the drag coefficient, wind input, whitecapping, and swell dissipation. Significant efforts have been made in assessing the performance of these source term packages in representing the evolution of ocean surface waves (e.g., *Kalantzi et al.,* 2009; *Liu et al.,* 2017). The uncertainties of these source term packages for wind input and wave dissipation remain one of the major issues affecting the accuracy of wave model results (*Babanin,* 2011).

Kalantzi et al. (2009) and *Seemanth et al.* (2016) found that insufficient swell dissipation in ST1 and ST2 can cause overestimations of significant wave heights (SWHs) during the monsoon transition season in the north Indian Ocean. *Fan et al.* (2009) showed that the use of WW3 with the ST2 package overestimates SWHs due to unrealistically high drag coefficients at high winds. *Rascle and Ardhuin* (2013) and *Stopa et al.* (2016b) demonstrated that ST4 generates more accurate predictions for mean wave parameters than ST2 or ST3 based on global hindcasts of ocean waves using WW3 (version 4.18). *Zieger et al.* (2015) calibrated the observational-based source term package ST6 under Hurricane Katrina in 2005 in the Gulf of Mexico and found that the accuracy of ST6 is comparable to ST2 and ST4. They showed that ST6 yields stronger input around the peak frequency, resulting in fast wave growth for young seas compared with ST2 and ST4. *Xu et al.* (2017) examined model results from WW3 (version 4.18) using three different source term packages (ST2, ST4, and ST6) with buoy observations during three typhoons in the South China Sea. *Liu et al.* (2017) assessed the performances of four different source term packages (ST2, ST3, ST4, and ST6) in WW3 (version 4.18) during Hurricane Ivan (2004), but they were unable to determine the most accurate package because of the large uncertainty in the wind forcing. *Perrie et al.* (2018) investigated the performances of ST1

and ST4 in three third-generation wave models during three storm events in the northwest Atlantic and found that wave models using ST4 perform better than those using ST1.

The presence of ocean currents and sea ice significantly affects surface gravity waves (e.g., *Ardhuin et al.,* 2012; *Meylan et al.,* 2014; *Ardhuin et al.,* 2017), which has generally not been considered in previous studies. Because most source term packages are highly empirical and were usually tested for simple wave conditions, it is important to assess their performance in dynamically complex regions with strong currents and sea ice, such as the northwest Atlantic (NWA). The NWA is frequently subject to extreme weather events, such as hurricanes and winter storms. This region is also affected by strong large-scale circulations, such as the Labrador Current and the Gulf Stream. It is also a seasonally ice-covered region with the presence of ice in winter over the eastern Canadian shelf (ECS). In addition, it is necessary to examine the performances of these packages across the wave spectrum to reveal the inherent physical characteristics of different packages (*Kalantza et al.,* 2009; *Xu et al.,* 2017). This study aims to examine the applicability of four source term packages (ST2, ST3, ST4, and ST6) for the wind input and wave dissipation for surface waves in the presence of strong currents and sea ice over the NWA using WW3. Two periods are considered in this study: a period with several winter storms in February 2011 and Hurricane Ophelia that occurred from late September into early October 2011.

This chapter is structured as follows. Section 2.2 describes the observational and reanalysis data used in this chapter. Section 2.3 introduces the spectral wave model, source term packages for the wind input and wave dissipation, and model setup. Section 2.4 presents the comparisons of model results with observations. Section 2.5 investigates the model performances under different sea states, the variations of the drag coefficient, and the effects of currents and sea ice on waves. Conclusions are presented in Section 2.6.

2.2 Observational and Reanalysis Data

2.2.1 Observational Data

The observational data used here include in-situ observations from buoys, as well as remote sensing measurements from satellite altimeters and scatterometers. These observational

data are used here to assess the accuracy of wind forcing and wave model results. The in-situ wind and wave observations at 38 buoy stations within the model domain (Fig. 2.1) were obtained from the National Data Buoy Center (NDBC), the Northeastern Regional Association of Coastal Ocean Observing Systems (NERACOOS), Scripps Institution of Oceanography (SIO), Environment and Climate Change Canada (ECCC), and the SmartAtlantic Alliance (SAA). The SWHs (H_s) were measured at all buoys. The frequency wave spectra were available only at 26 buoy stations indicated by the red labels in Fig. 2.1. The mean and peak wave periods, wave direction, wind speed at 10 m above mean sea level (U_{10}), and wind direction were measured at most of these buoys. The calculations of integral wave variables are shown in Appendix A.
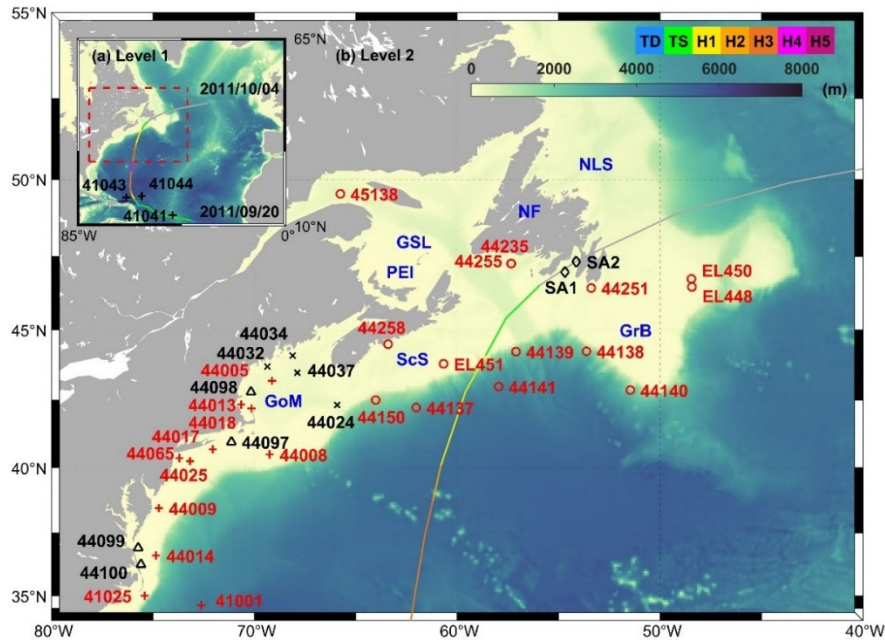
Figure 2.1: Domains and major topographic features of (a) the outer model for the north Atlantic and (b) the inner model for the northwest Atlantic. Black markers denote buoy stations with wind and wave observations. Red markers denote buoy stations with additional frequency wave spectra. The storm track of Hurricane Ophelia is shown by the solid line, together with hurricane strength indicated by the colors. Abbreviations are used for the Newfoundland and Labrador Shelves (NLS), Gulf of St. Lawrence (GSL), Newfoundland (NF), Prince Edward Island (PEI), Grand Banks (GrB), Scotian Shelf (ScS), and Gulf of Maine (GoM).

The altimeter data were taken from the database constructed by the GlobWave project that involved nine satellite altimeter missions from 1985 to the present. The GlobWave data (U_{10} and H_s) were calibrated to in-situ buoy measurements, with three different quality

levels (good, acceptable, and bad measurements) (*GlobWave Product User Guide*, 2013). Similar to the criteria used by *Young et al.* (2017), the following three quality control criteria were applied to the calibrated U_{10} and H_s used in this chapter: (i) only data with good quality are used to exclude the effects of rain and ice, (ii) the ratio of the standard deviation to the mean value should be less than 20%, and (iii) data should be more than 50 km offshore. The wind vectors inferred by the Advanced Scatterometer (ASCAT) obtained from Remote Sensing Systems (RSS; www. remss.com) are also used to examine the accuracy of the wind fields. Previous calibrations of these satellite measurements showed that the inferred U_{10} is of high quality with an average root mean square error less than 1.5 m/s (e.g., *Zieger et al.,* 2009; *Young et al.,* 2017).

2.2.2 Atmospheric Forcing

The spectral wave model for the NWA is forced by hourly wind fields ($\boldsymbol{U_{10}}$) extracted from the Climate Forecast System version 2 (CFSv2) reanalysis (*Saha et al.,* 2014) with a horizontal resolution of ~38 km. It should be noted that the CFSv2 winds are not fine enough to represent the structure of the winds associated with Hurricane Ophelia. To improve the representation of the wind fields associated with Hurricane Ophelia, a parametric vortex based on *Hu et al.* (2012) is inserted into the CFSv2 wind fields. Details of the parametric vortex insertion are given in Appendix B.

Figure 2.2 shows the original CFSv2 winds at 0000 UTC (Universal Time Coordinated) 18 February 2011 and the modified CFSv2 winds at 0000 UTC 3 October 2011. In February 2011, several large-scale winter storms swept northeastward from the east coast of the United States (US) toward the Newfoundland and Labrador Shelves (NLS) and adjacent deep waters of the NWA (Fig. 2.2a). The ECS and adjacent deep waters were thus strongly affected by the winter storms with intense winds in this month. In late September and early October 2011 (Fig. 2.2b), Hurricane Ophelia swept through the NWA and reached peak intensity with maximum sustained winds of 61 m/s (Category 4) around 0000 UTC 2 October over northeastern Bermuda. Hurricane Ophelia then accelerated northeastward and weakened rapidly to a tropical storm by 0600 UTC 3 October before approaching the south coast of Newfoundland and finally dissipating near the Mid-Atlantic

Ridge around 1800 UTC 4 October. During this hurricane period, wind speeds were intense around the storm and generally weak over regions far from the storm center.

To examine the accuracy of the wind fields, the wind fields are compared with observations from buoy stations, altimeters, and scatterometers (Fig. 2.3) mentioned in Section 2.2.1. The accuracy of the winds is quantified using four statistical error metrics including the relative bias (RB), root mean square error (RMSE), scatter index (SI), and correlation coefficient (R). These four metrics are defined in Appendix A. During the winter storms between 16 and 24 February 2011 (termed the winter-storm period), the wind speeds from the original CFSv2 agree well with the observed values, with an average RMSE of ~1.60 m/s and an average SI of ~17.7% (Figs. 2.3a-2.3c). During Hurricane Ophelia between 25 September and 5 October 2011 (termed the hurricane period), by comparison, the original CFSv2 wind speeds agree less well with observations (Figs. 2.3d-2.3f). Figures 2.3g-2.3i demonstrate that the errors become smaller by inserting the parametric vortex to the CFSv2 winds, with better agreement between the modified CFSv2 winds and observations for winds greater than 15.0 m/s. The modified CFSv2 winds agree reasonably well with the buoy observations (Fig. 2.3g), but slightly weaker than the winds inferred from altimeters and scatterometers (Figs. 2.3h-2.3i) at high winds. It should be noted that the wind speeds inferred from altimeters and scatterometers were found to be higher than the observed winds at buoys at high values of U_{10} (*Young et al.,* 2017).
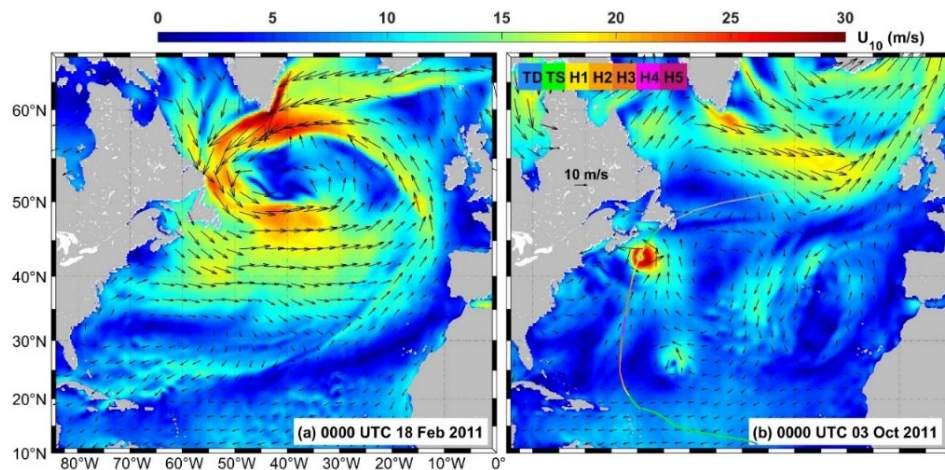
Figure 2.2: Snapshots of wind fields (U_{10}) based on (a) the original CFSv2 winds at 0000 UTC 18 February and (b) the modified CFSv2 winds at 0000 UTC 3 October in 2010. The solid line in (b) denotes the storm track of Hurricane Ophelia.
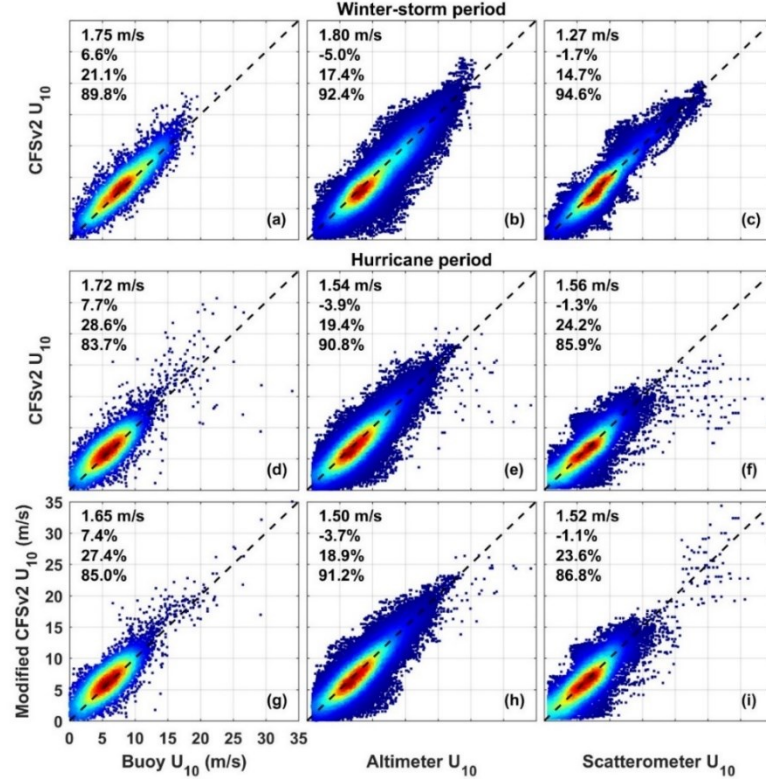
Figure 2.3: Scatter plots for U_{10} between the CFSv2 (a-f) and observed values from buoy stations (first column), altimeters (second column) and scatterometers (third column) during the winter-storm period (a-c) and hurricane period (d-f) in 2011. The modified CFSv2 winds with a parametric vortex are shown in the bottom panels (g-i). Black dashed lines are the perfect-fit lines. Colors represent the density of data points. Values for the RMSE, RB, SI and R are shown in sequence in each panel.

2.2.3   Ocean Surface Current

Ocean surface currents can modulate surface wave fields. The eddies and strong currents of the Gulf Stream (GS), for example, were found to significantly affect the spatial and temporal variations of wave fields in the NWA (*Ardhuin et al.,* 2017). By comparing the GS in 13 widely-used global ocean reanalysis products with different spatial resolutions, *Chi et al.* (2018) found that the ocean circulation reanalysis dataset based on the Hybrid Coordinate Ocean Model (HYCOM; *Cummings and Smedstad,* 2013) represents the GS reasonably well in terms of the Straits of Florida transport, the GS path, the separation of the GS near Cape Hatteras, and the GS north wall positions. Moreover, HYCOM has the advantage of an eddy-resolving resolution (1/12°). Therefore, the ocean surface currents and elevations extracted from the 3-hourly HYCOM global reanalysis are used in wave simulations to account for the current effects on waves.

2.2.4 Sea Ice Condition

The presence of sea ice during the winter season insulates the ocean from the atmosphere and modifies the air-sea momentum and heat fluxes over the ECS. In addition to the reduction of wind input for wave growth resulting from the presence of sea ice, ocean surface waves are dissipated and scattered in the ice field. Thus, the ice floes and ice properties significantly affect local wave dynamics. Waves in ice have been simulated in several previous studies using spectral wave models with ice fields from ice model results (*Rogers et al.,* 2016), reanalysis products (*Stopa et al.,* 2016a; *Li et al.,* 2015; *Boutin et al.,* 2018) or remote sensing observations (*Ardhuin et al.,* 2016). However, none of these provide information on the ice floe sizes. One of the difficulties in simulating waves in ice arises from the accuracy of ice data and the absence of ice floe sizes (*Boutin et al.,* 2018). In this study, daily ice data from the Canadian Ice Service (CIS) are used in wave simulations during the winter storms of February 2011, including the ice concentration, thickness, and floe size (Fig. 2.4). Daily ice data from the CIS are produced using observations from a variety of sources, such as satellite data, as well as ship and aircraft-based visual observations, and represent the best estimate of current ice conditions. More detailed information about the ice data and associated uncertainties can be found in *CIS* (2005) and *Tivy et al.* (2011). To our knowledge, the present study is the first to simulate waves in ice by considering wave scattering using realistic ice floe sizes.

Figure 2.4 shows the ice concentration, thickness, and floe size at 0000 UTC 21 February 2011. At this time, sea ice has mostly formed along the coasts of Labrador and the northern and western Gulf of St. Lawrence (GSL), with the maximum concentrations occurring around Prince Edward Island (PEI) and Labrador. There were some ice floes along the coasts of Newfoundland (NF) and Nova Scotia (NS) with ice concentrations less than 0.05. Correspondingly, ice thicknesses and floe sizes were large around PEI and Labrador. The sizes of ice floes were clearly not constant but varied from meters to kilometers. In February 2011, sea ice properties varied from time to time but with patterns similar to those mentioned above.
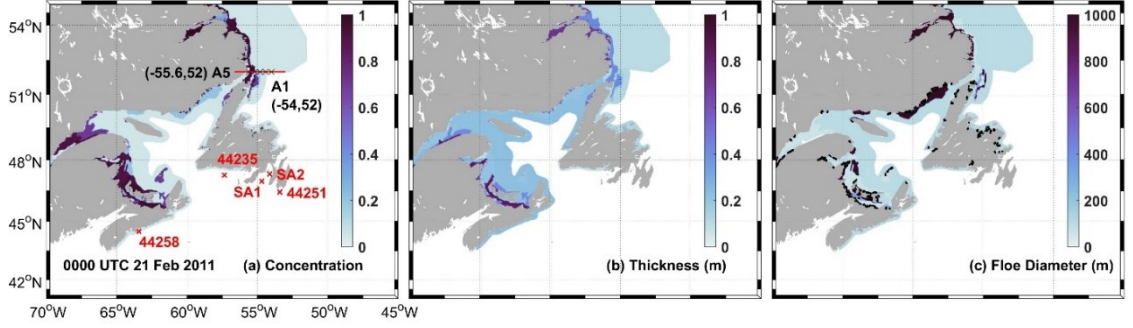
Figure 2.4: Snapshots of the (a) ice concentration, (b) thickness and (c) floe diameter at 0000 UTC 18 February 2011 extracted from the daily CIS ice data. Red crosses denote buoy stations and black crosses denote locations (A1-A5) along the transect at 52°N.

2.3 Numerical Wave Model and Setup

2.3.1   Spectral Wave Model

The wave model used in this study is the third-generation spectral wave model WW3 (version 5.16), which solves the wave action balance equation given as (*WW3 Development Group,* 2016):

$$\frac{\partial N}{\partial t} + \nabla \cdot (\boldsymbol{c_g} + \boldsymbol{U})N + \frac{\partial}{\partial k}(c_k N) + \frac{\partial}{\partial \theta}(c_\theta N) = \frac{S_{tot}}{\sigma} \tag{2.1}$$

with

$$S_{tot} = S_{in} + S_{ds} + S_{nl4} + S_{nl3} + S_{ice} + S_{is} + \cdots \tag{2.2}$$

where $N = E(k,\theta)/\sigma$ is defined as the ratio of wave energy E over the relative radian frequency σ, and wave energy E is defined as a function of the wavenumber k and wave direction θ. Here $\boldsymbol{c_g}$ is the group velocity of surface waves, $\boldsymbol{U}$ is the ocean surface current (based on HYCOM), and c_k and c_θ are the propagation speeds of waves in the frequency space and directional space, respectively. The left-hand side (LHS) of Eq. 2.1 represents, respectively, the local rate of change of the wave action density, the wave propagations in the geographic space, frequency space, and directional space. The right-hand side (RHS) of Eq. 2.1 represents the effects of the generation and dissipation of waves, generally including the physical processes (Eq. 2.2) of the atmospheric wind input (S_{in}), wave energy dissipation (S_{ds}), nonlinear quadruplet (S_{nl4}) and triad (S_{nl3}) wave interactions, non-conservative wave attenuation (S_{ice}), and conservative wave scattering (S_{is}) in ice.

19

The current effects on waves specified in WW3 include the horizontal current advection of surface waves ($\mathbf{c}_g + \boldsymbol{U}$), the change of wavenumber (c_k) as a result of the Doppler shift, and the current-induced refraction (c_θ). The relative wind effect is also included by using the relative wind vector ($\boldsymbol{U_r} = \boldsymbol{U_{10}} - a\boldsymbol{U}$), where a is a tuning coefficient. Surface currents can affect the atmospheric boundary layer and the wind profile. A proper account of the relative wind effect requires a fully coupled wave-ocean-atmosphere model. The use of the full effect of the current ($a = 1.0$) was found to exaggerate the relative wind effect (*Ardhuin et al.,* 2017). Different values of a have been suggested in previous studies (*Zieger et al.,* 2015; *Wang and Sheng,* 2016; *Ardhuin et al.,* 2017). In this study, $a = 0.7$, suggested by *Wang and Sheng* (2016), is used as a simple approximation. The simulated sea surface elevation field taken from HYCOM is used in the wave model for calculating total water depth although this effect is only large over shallow water regions.

In the ice-covered regions, S_{ice} is scaled by the ice concentration c_i, and S_{in} and S_{ds} are scaled by the open water fraction ($1 - c_i$). The source term for wave scattering (S_{is}) already contains an ice concentration dependency and thus is not scaled with c_i. The source term for the nonlinear wave interactions can be used in areas of open water and ice (*Polnikov and Lavrenov,* 2007) and thus is also not modified. This particular choice follows several previous studies (e.g., *Perrie and Hu,* 1996; *Cheng et al.,* 2017; *Rogers et al.,* 2016; *Boutin et al.,* 2018) and may underestimate possible wind-wave growth over ice. In the presence of ice, therefore, the total source term in Eq. 2.2 is modified as

$$S_{tot} = (1 - c_i)(S_{in} + S_{ds}) + c_i S_{ice} + S_{is} + S_{nl4} + S_{nl3} \qquad (2.3)$$

2.3.2 Source Term Packages for Wind Input and Wave Dissipation

Four different source term packages for the wind input and wave dissipation (ST2, ST3, ST4, and ST6) implemented in WW3 are considered in this study. These four packages have very different parameterizations for the drag coefficient, wave growth, swell dissipation, and whitecapping (Table 2.1). Brief summaries of these four packages can also be found in *Stopa et al.* (2016b) and *Liu et al.* (2017). The reader is referred to WW3 Development Group (*WW3DG,* 2016) for detailed formulations and descriptions of these four packages.

Package ST2 is based on parameterizations discussed in *Tolman and Chalikov* (1996), which consists of the input source term of *Chalikov and Belevich* (1993) and Chalikov (1995). The wave growth in ST2 is mainly controlled by the non-dimensional wind-wave interaction parameter β, which depends on the wave frequency, drag coefficient, wind speed, and wind direction. During the opposing wind, ST2 yields a negative wind input representing swell dissipation. The dissipation source term in ST2 consists of a dominant low-frequency dissipation due to turbulence and a diagnostic high-frequency dissipation. The drag coefficient in ST2 is based on the scheme suggested by *Chalikov* (1995) using a wave age dependent high-frequency energy level. Based on previous studies (e.g., *Powell et al.,* 2003; *Fan et al.,* 2009; *Holthuijsen et al.,* 2012) on the drag coefficient at high winds, the drag coefficient is normally capped with a maximum value.

Package ST3 is based on the wave growth theory suggested by *Miles* (1957) and modified by *Janssen* (1991, 2004). A linear negative wind input term was suggested by *Janssen* (2004) to represent swell dissipation. Package ST3 in WW3 uses the default settings suggested by *Bidlot et al.* (2007) without swell dissipation. Wave dissipation in ST3 is a combination of linear and nonlinear functions of the normalized wavenumber. The wave dissipation is sensitive to swells in that an increase in swell height typically reduces the wind-wave dissipation.

Package ST4 uses the positive part of the wind input from ST3 with a reduction in wind input for high frequencies and high winds (*Ardhuin et al.,* 2010). In both ST3 and ST4, $\beta_{\max}$ and z_α are two key tuning parameters for the wind input and have different values in the two packages. The former represents the strength of the wind-wave growth, and the latter represents the wave age shift of the long waves to account for gustiness. Swell dissipation in ST4 is implemented as a negative wind input using a combination of linear viscous decay and nonlinear turbulent decay (*Ardhuin et al.,* 2009). Different swell conditions are considered in ST4 with the opposing swells being more dissipated than the following swells. Whitecapping dissipation in ST4 is parameterized from the wave spectrum saturation, defined as the sum of a saturation-based term and a cumulative breaking term (*Ardhuin et al.,* 2010). The drag coefficients in both ST3 and ST4 are set to be implicit functions of the wind speed (U_{10}) and wave support stress (τ_w).

Package ST6 includes new physical features for the wind-wave exchange, which uses a nonlinear wind input to represent the dependence on wave steepness and includes a relative reduction of wind input for strong winds and steep waves to represent the air-flow separation (*Babanin,* 2011; *Rogers et al.,* 2012; *Zieger et al.,* 2015). The wave growth rate in ST6 is a function of spectral saturation B_n (*Phillips,* 1984), which is a power function of the wavenumber ($B_n \sim k^3$). Package ST6 also has a negative input term in order to attenuate waves in the presence of swells but with the same dissipation rate for different swell conditions. Similar to ST4, whitecapping dissipation in ST6 is parameterized by new physics of wave-breaking behaviors, such as the threshold behavior (*Babanin et al.,* 2001) and cumulative behavior at small scales (*Young and Babanin,* 2006). In addition, ST6 uses the wind-speed-dependent drag coefficient from *Hwang* (2011) to account for its saturation and decrease at high winds (*Powell et al.,* 2003).

Table 2.1: Summary of the source term packages for the wind input and wave dissipation. $C_{d,max}$ is the maximum value for the drag coefficient at high winds in ST2 package. The proportionality constant C used in the DIA approach are different for each package. β_{max} and z_α are tuning parameters for the wave growth in ST3 and ST4 packages.

Package	Reference	Features	Parameters
ST2	*Chalikov and Belevich* (1993); *Tolman and Chalikov* (1996); *Tolman* (2002)	Wind speed and wave age dependent drag coefficient with limits at high winds. A dominant low-frequency dissipation and a diagnostic high-frequency dissipation.	$C_{d,max} = 2.5 \times 10^{-3}$, $C = 1.0 \times 10^7$
ST3	*Janssen* (1991 and 2004); *Bidlot et al.* (2007)	A nonlinear function of the wind speed and wave support stress for the drag coefficient. A combination of linear and nonlinear functions of wavenumber normalized by the mean wavenumber.	$\beta_{max} = 1.2$, $z_\alpha = 0.011$, $C = 2.78 \times 10^7$,
ST4	*Ardhuin et al.* (2009); *Ardhuin et al.* (2010); *Rascle and Ardhuin* (2013)	A similar function of the drag coefficient as ST3 but with a limit for surface roughness. A similar function of the wind input as ST3 but with a reduction of input at high frequencies. A combination of linear viscous decay and nonlinear turbulent decay for the swell dissipation. Threshold behavior and cumulative behavior for the wave dissipation.	$\beta_{max} = 1.43$, $z_\alpha = 0.006$, $C = 2.5 \times 10^7$,
ST6	*Hwang* (2011); *Babanin* (2011); *Zieger et al.* (2015)	A parabolic function of the wind speed for the drag coefficient with decreasing values at high winds. A nonlinear wind input including the dependences on wave steepness and air-sea flow separation. Negative wind input for opposing winds and swell dissipation due to non-breaking effects. Threshold behavior and cumulative behavior for the wave dissipation.	$C = 3.0 \times 10^7$

2.3.3   Model Setup

A two-level nested-grid wave model based on WW3 (version 5.16) is used to simulate surface gravity waves over the NWA. The two-level nested-grid wave model is integrated separately for (i) February 2011 and (ii) September/October 2011. The inner model results during the period between 16 and 24 February 2011 (winter-storm period) and during Hurricane Ophelia between 25 September and 5 October 2011 (hurricane period) are used in the following analyses. As shown in Fig. 2.1, the outer model (Level 1) covers the North Atlantic (85°W-0°, 10°N-65°N) at a horizontal resolution of 1/4°. The inner model (Level 2) covers the northwest Atlantic (80°W-40°W, 34°N-55°N) at a horizontal resolution of 1/12°. The model bathymetry is based on the General Bathymetric Chart of the Oceans gridded bathymetric dataset (GEBCO, www.gebco.net), which is a global terrain model with a resolution of 1/120°. The model computations are carried out in a spherical coordinate system with a discrete spectrum consisting of 36 directions ($\Delta\theta = 10°$) and 31 frequencies ranging from 0.04 to 0.70 Hz at a logarithmic increment of 0.1.

The nonlinear quadruplet wave interactions (S_{nl4}) are computed in the model using the Discrete Interaction Approximation (DIA) of *Hasselmann et al.* (1985) for all four source term packages (ST2, ST3, ST4, and ST6). The DIA algorithm for S_{nl4} was known to have some shortcomings (*Cavaleri et al.,* 2007; *Perrie et al.,* 2013; *Liu et al.,* 2017). The reason for using the DIA here is that the source term packages for wind input and wave dissipation were calibrated with the DIA algorithm for S_{nl4}. In the calibrations, the proportionality constant C, representing the strength of nonlinear wave interactions, was set to different values in each package (Table 2.1). The nonlinear triad wave interactions (S_{nl3}) are computed using the Lumped Triad Approximation method of *Eldeberky* (1996). The wave model uses the bottom friction dissipation term derived from the Joint North Sea Wave Project (JONSWAP) results (*Hasselmann et al.,* 1973) and the depth-induced wave-breaking parametrization based on *Battjes and Janssen* (1978). The default values are used for all the physical tuning parameters in WW3 unless otherwise specified.

Different approaches for the wave dissipation and scattering in ice are examined and the following options with the best performance for wave propagations in ice during the

winter-storm period are used here. A wave attenuation rate α is commonly used to represent the complexity of modelling all the non-conservative wave dissipation processes in ice (*Rogers et al.,* 2016). Here, α is set to a step function of wave frequency based on the measurements of *Rogers et al.* (2016; known as IC4M6). Wave scattering in ice is floe-size dependent following the approach of *Meylan and Masson* (2006; known as IS2). Four different packages for the wind input and wave dissipation (ST2, ST3, ST4, and ST6) introduced in Section 2.3.2 are tested in the outer model. As the model results using ST6 have the best agreement with buoy observations in the deep waters (see Section 2.4), the results produced by the outer model using ST6 are used to specify the open boundary conditions for the inner model with the four different packages. Different values for the wind-wave growth parameter β_{max} and the wave age shift parameter z_α in ST4 are examined. The wave model using ST4 with β_{max} = 1.43 and z_α = 0.006 is found to have the best performance when forced by the CFSv2 winds for the NWA. These two values are thus used in this study. It should be noted that the value of β_{max} is larger than the default physics parameters (β_{max} = 1.33) based on global ocean applications, which is consistent with *Perrie et al.* (2018). *Perrie et al.* (2018) demonstrated that the model accuracy can be enhanced by increasing the wind-wave interaction parameter (β_{max}) in ST4 to represent the regional characteristics of the NWA.

2.4 Model Validations

2.4.1 Significant Wave Height

Figure 2.5 shows the observed SWHs (H_s) inferred from satellite altimeters during the winter-storm period and the hurricane period in 2011. Because of different wind patterns, the observed sea states were very different during these two study periods. During the winter-storm period in 2011, the observed sea states were generally dominated by large wind waves caused by large-scale strong winds. Over the deep waters of the NWA and NLS, for example, the observed SWHs were large and up to 12 m (Fig. 2.5a). During the hurricane period in 2011, the satellite altimeters mainly captured the large surface gravity waves on the right-hand side of the hurricane track over the south of Newfoundland with SWHs up to 10 m (Fig. 2.5b). Over regions away from the hurricane center, the observed

sea states were generally dominated by swells with the SWHs less than 4 m. The classification of the sea states based on the observed wave spectra will be discussed in Section 2.5.1.
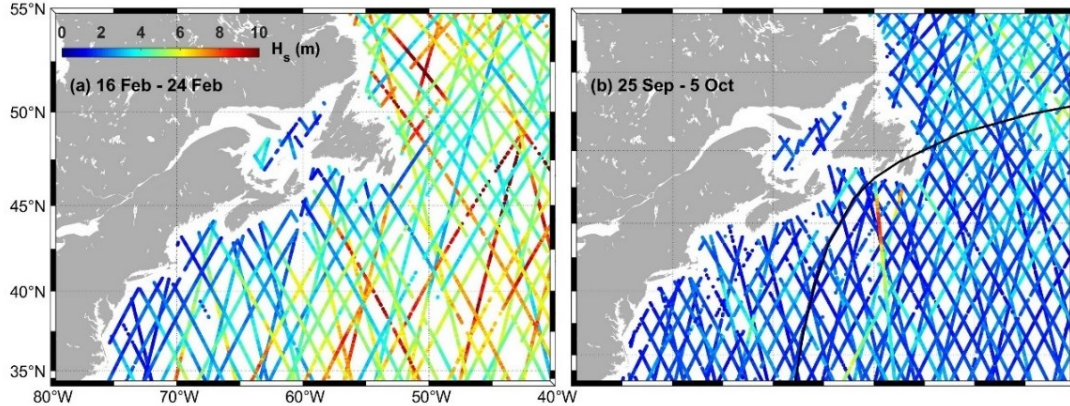
Figure 2.5: Observed SWHs inferred from satellite altimeters during (a) the winter-storm period (16-24 February) and (b) the hurricane period (25 September-5 October) in 2011. The black line in panel (b) denotes the storm track of Hurricane Ophelia.

We now assess the performance of the inner model by comparing simulated SWHs with observations inferred from the satellite altimeter data in terms of the scatter plots shown in Fig. 2.6. The corresponding error metrics (RMSE, RB, SI, and R) are also shown in the figure and Table 2.2. Of the four packages, ST2 performs least well with significant underestimates of the observed SWHs (Figs. 2.6a and 2.6e) with a RB value of ~-16.4% (-12.8%) during the winter-storm (hurricane) period. Package ST3 performs better than ST2, but still underestimates the observed SWHs, with a RB of ~-4.5% (-3.3%) and a RMSE of ~0.67 m (0.41 m) during the winter-storm (hurricane) period. By comparison, ST4 performs better than either ST2 or ST3, with a RMSE of ~0.62 m (0.37 m) and a SI of ~13.3% (16.7%) for the winter-storm (hurricane) period. Figures 2.6d and 2.6h show that ST6 performs equally well as ST4 in reproducing the observed SWHs with a RMSE of ~0.61 m (0.38 m) and a SI of ~13.1% (17.1%) for the winter-storm (hurricane) period. Of the four packages, both ST4 and ST6 have relatively small RB values (between -1.8% and 1.6%) , indicating that the systematic underestimation issue is less severe in ST4 and ST6 than in ST2 and ST3. It should be noted that the different performances of the four packages during the two study periods are attributed to different behaviors of the packages under the wind-wave-dominated and swell-dominated sea states (discussed further in Section 2.5.1).
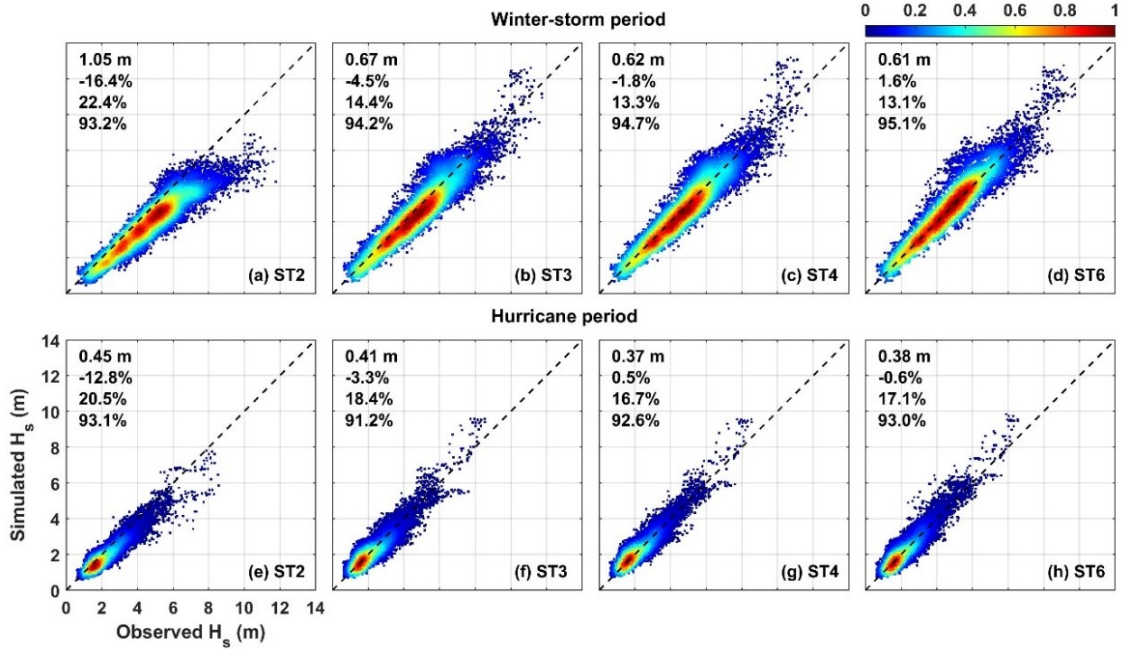
Figure 2.6: Scatter plots for SWHs between simulated values using different packages (ST2/3/4/6) and observed values from satellite altimeters during (a-d) the winter-storm period and (e-h) the hurricane period.

Figure 2.7 presents time series of observed SWHs at 12 buoy stations (Fig. 2.1) during the winter-storm period, along with the simulated SWHs from the four packages. The average error metrics for 35 buoy stations within the inner model domain are presented in Table 2.2. During the winter-storm period of 2011, the observed SWHs were less than 4 m near the east coast of the US resulting from limited wind fetches and relatively weak wind conditions (Figs. 2.7a-2.7c). Over the Scotian Shelf Break (Figs. 2.7d-2.7g) and Grand Banks (Fig. 2.7h), sea states were rough with observed SWHs up to 12 m. Near Halifax Harbour (Fig. 2.7i) and the south coast of Newfoundland (Figs. 2.7j-2.7l), where the growth of waves was limited by the wind fetch and water depth, the observed SWHs were generally less than 6 m during the same period.

The time series of SWHs shown in Fig. 2.7 demonstrate that, except for ST2, the inner wave model of the four packages reproduces the observed temporal and spatial variability of the SWHs well during the winter-storm period. Package ST2 significantly underestimates the observed large SWHs during this period, with an average RB of ~-30.2% (Table 2.2). In comparison with ST2, packages ST3 and ST4 perform significantly better but still noticeably underestimate the SWHs during the winter-storm period particularly the

peak values of observed SWHs, with an average RB of ~-9.0% and ~-7.6% and an average RMSE of ~0.42 m and ~0.40 m, respectively. Of the four packages, ST6 performs best with an average RB of ~2.2% and an average RMSE of ~0.39 m. It should be noted that ST6 overestimates the peak values of the observed SWHs, for example on 20 February at buoy 44008 (Fig. 2.7b), mainly because of the fast and strong wind input in ST6 under wind-wave-dominated conditions (further discussed in Section 2.5.1).
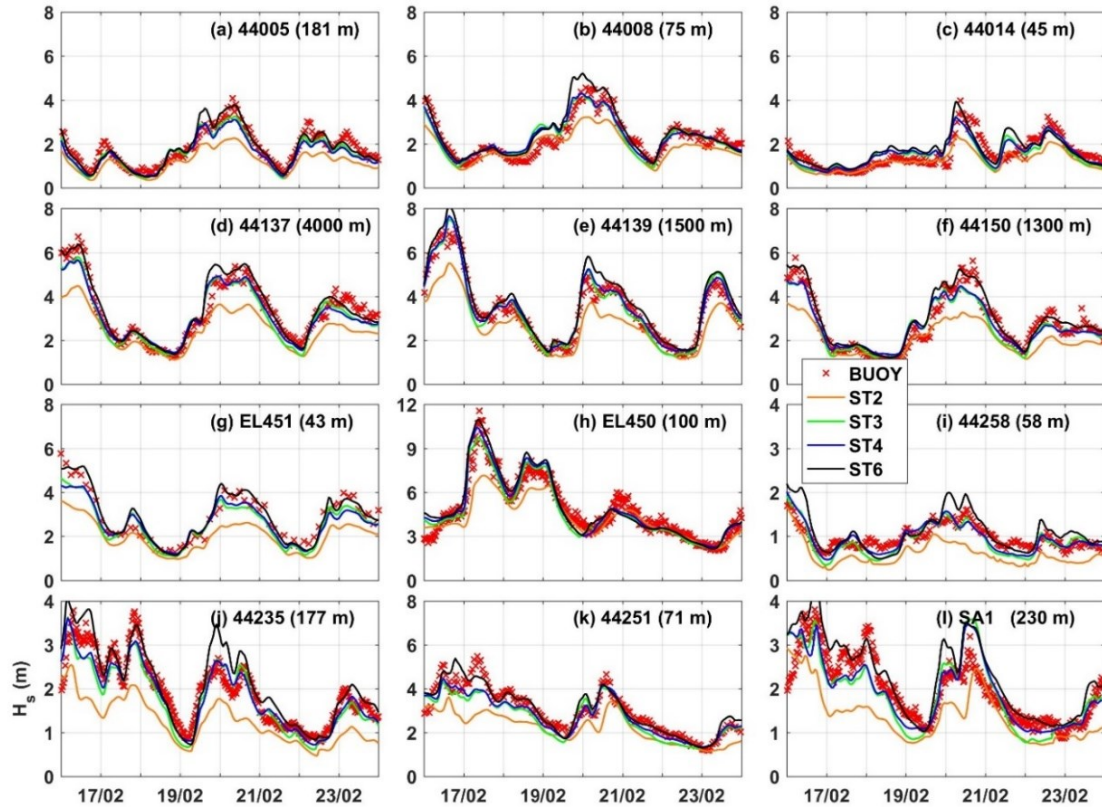
Figure 2.7: Time series of simulated SWHs using four different packages against the observed values at buoy stations during the winter-storm period. The name and water depth of each buoy station are shown in each panel.

Figure 2.8 presents time series of observed and simulated SWHs at 12 buoy stations during Hurricane Ophelia. At buoy stations near the east coast of the US (Figs. 2.8a-2.8c), the observed SWHs were less than 3 m because this hurricane was far from these buoy stations. At stations over the ECS (Figs. 2.8d-2.8k), by comparison, the observed sea states became highly energetic on 3 October during the passage of Hurricane Ophelia, with observed SWHs up to 13.7 m near the Scotia Shelf Break (Fig. 2.8g). The observed SWHs at buoy

45138 in the northwest GSL (Fig. 2.8l) were less than 2.2 m because of the limited wind fetch.

The inner wave model reproduces the observed SWHs well during the hurricane period using ST3, ST4, and ST6. Of the four packages, ST2 generally underestimates SWHs with an average RB of ~-11.8% and average RMSE of ~0.38 m (Table 2.2). Both ST3 and ST4 perform better than ST2 in simulating the SWHs during this period, with an average RB of ~1.2% and ~4.6% and average RMSE of ~0.32 m and ~0.31 m, respectively. By comparison, ST6 performs best, with an average RB of ~-1.1% and average RMSE of ~0.31 m (Table 2.2).
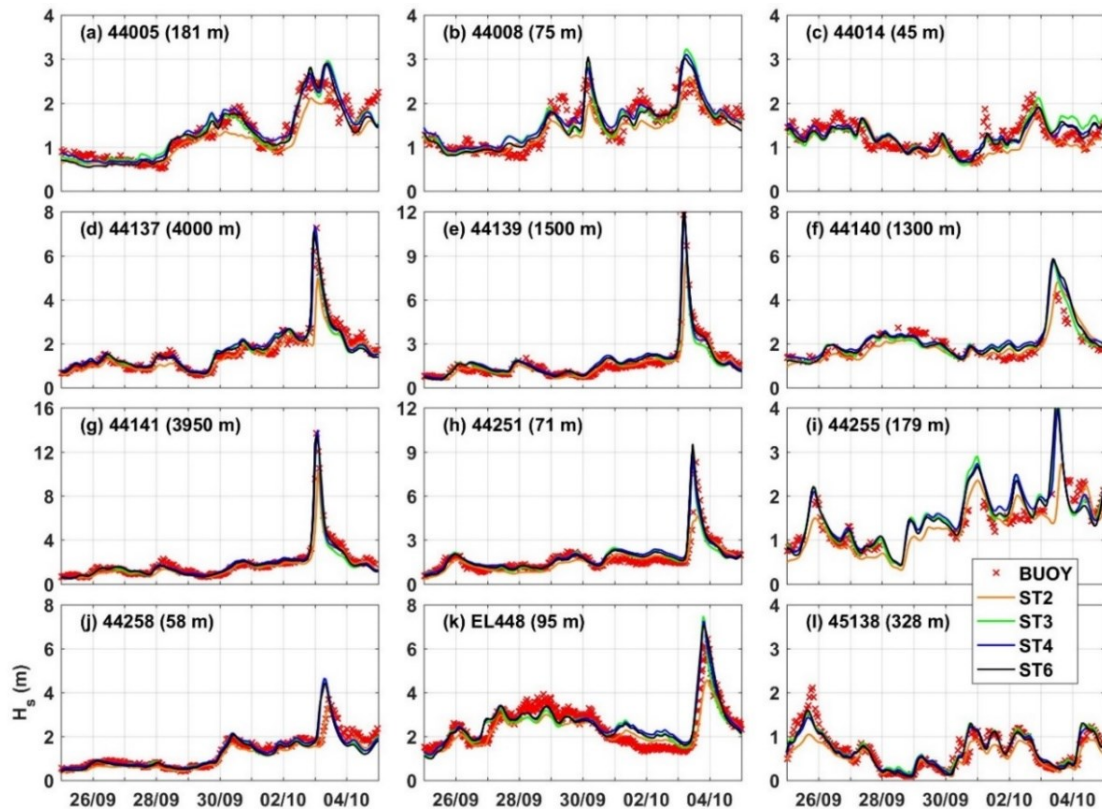
Figure 2.8: As in Fig. 2.7, but for the hurricane period.

Table 2.2: Summary of four error metrics for quantifying model performances in simulating SWHs using different source term packages (ST2/3/4/6) based on observations from altimeters and buoy stations during the winter-storm and hurricane periods. The error metrics includes root mean square error (RMSE), relative bias (RB), scatter index (SI), and correlation coefficients (R). The average values for all altimeter data or all buoy stations are reported. The best error metrics are shown in bold.

Package		Winter storms				Hurricane Ophelia			
		RMSE (cm)	RB (%)	SI (%)	R (%)	RMSE (cm)	RB (%)	SI (%)	R (%)
Altimeter	ST2	1.05	-16.4	22.4	93.2	0.45	-12.8	20.5	**93.1**
	ST3	0.67	-4.5	14.4	94.2	0.41	-3.3	18.4	91.2
	ST4	0.62	-1.8	13.3	94.7	**0.37**	**0.5**	**16.7**	92.6
	ST6	**0.61**	**1.6**	**13.1**	**95.1**	0.38	-0.6	17.1	93.0
Buoy	ST2	0.73	-30.2	37.6	88.0	0.38	-11.8	26.1	85.5
	ST3	0.42	-9.0	21.8	89.9	0.32	1.2	21.4	85.2
	ST4	0.40	-7.6	21.0	90.5	0.31	4.6	21.1	86.6
	ST6	**0.39**	**2.2**	**20.0**	**91.4**	**0.31**	**-1.1**	**20.7**	**86.7**
Average	ST2	0.89	-23.3	30.0	90.6	0.42	-12.3	23.3	89.3
	ST3	0.55	-6.8	18.1	92.1	0.37	-1.1	19.9	88.2
	ST4	0.51	-4.7	17.2	92.6	**0.34**	2.6	**18.9**	89.6
	ST6	**0.50**	**1.9**	**16.6**	**93.3**	0.35	**-0.9**	**18.9**	**89.9**

2.4.2 Mean Wave Period

In this section we examine the performance of the inner wave model in simulating the mean wave periods (MWPs). Figure 2.9 presents scatter plots of the simulated second-order MWPs (T_{m02}, see Appendix A) and the observed values from buoys with the average four error metrics for the four different packages (ST2, ST3, ST4, and ST6). It should be noted that the observed first-order MWPs (T_{m01}) reported by the SIO buoys are excluded in Fig. 2.9. Most of the data points shown in Fig. 2.9 spread below the perfect-fit line during both study periods, indicating the underestimates of T_{m02} by the model. Statistically, all the packages underestimate T_{m02} during both study periods, with a negative RB between -19.7% and -6.8%, and have lower correlation coefficients for T_{m02} (80.9-86.0%), than their counterparts for H_s (85.2-91.4%). This indicates that although the total wave energy can be well predicted, the energy distribution across the frequency in the model has large biases. The model underestimates of T_{m02} can be attributed to underestimates of peak wave energy and the shifting of wave energy to high frequencies (see Section 2.5.1).

Furthermore, the simulated T_{m02} is calculated over a frequency range of 0.04 to 0.70 Hz, which is different from the typical frequency range (0.0325-0.485 Hz) used in the wave analyses for the buoy observations. The second-order MWP (T_{m02}), which is sensitive to the high-frequency wave components, can be underestimated because of the extra high-frequency wave energy in the wave model.

Compared with ST3 and ST4, ST6 predicts a relatively larger T_{m02} during the winter-storm period but a relatively smaller T_{m02} during the hurricane period because of the stronger wind input under wind-wave-dominated sea states and stronger swell dissipation under swell-dominated sea states in ST6 than in ST3 or ST4 (Section 2.5.1). Overall, ST6 performs best in predicting T_{m02} with a SI of ~14.9%, followed by ST4 (~16.2%) and ST3 (~16.8%) during the winter-storm period. Package ST4 has the lowest SI (~14.2%) for T_{m02}, followed by ST6 (~15.0%) and ST3 (~15.6%) during the hurricane period.
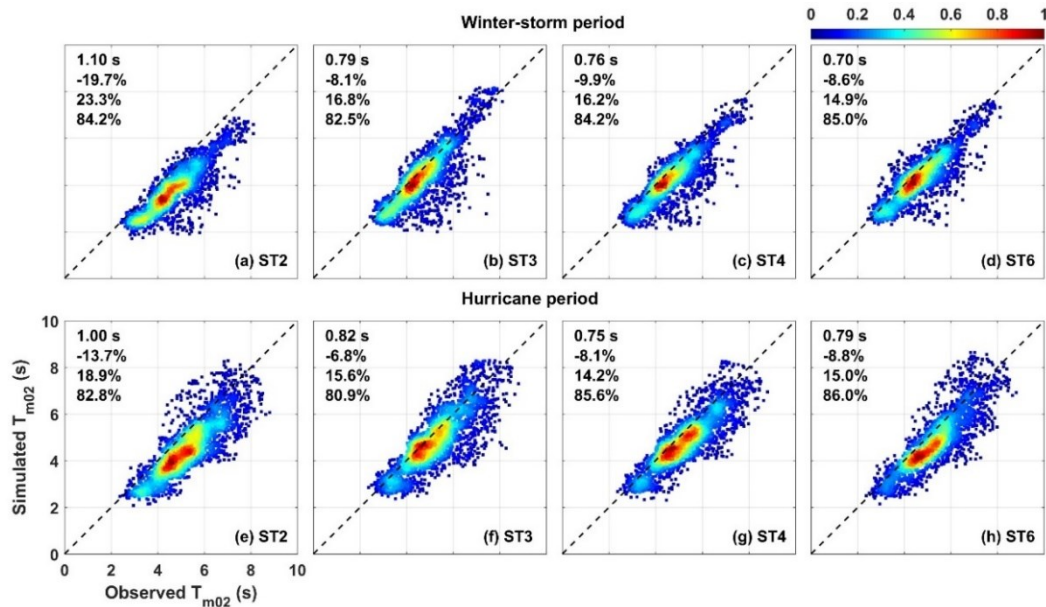
Figure 2.9: Scatter plots for the mean wave periods T_{m02} between simulated values using four different packages (ST2/3/4/6) and observed values at buoy stations during (a-d) the winter-storm period and (e-h) the hurricane period.

Overall, ST4 and ST6 have the best performance in predicting H_s and T_{m02}. It should be noted that third-generation spectral wave models have many tuning parameters to produce a best-fit to the measurements. The uncertainties in parameterizations for a single physical process may be well compensated for by deficiencies in other parameterizations or the

tuning of parameters (*Cavaleri et al.,* 2007). For example, the source and sink terms in spectral wave model can compensate for each other due to the inaccurate DIA for the nonlinear wave interactions (*Perrie et al.,* 2013). The features and limitations of these four packages (ST2, ST3, ST4, and ST6) are discussed in Section 2.5.

2.5 Results

2.5.1   Model Performances under Different Sea States

As mentioned in Section 2.4.1, sea states during the winter-storm and hurricane periods are quite different. Different sea states can be categorized using the wave spectra. We follow *Smedman et al.* (2003) and separate the observed one-dimensional (1D) wave spectra into the swell (E_s) and wind sea (E_w) components using a splitting frequency (f_s) given as:

$$f_s = g/(2.4\pi U_r \cos(\theta - \theta_w)) \tag{2.4}$$

$$E_s = \int_0^{f_s} E(f)\, df \tag{2.5}$$

$$E_w = \int_{f_s}^{\infty} E(f)\, df \tag{2.6}$$

where θ and θ_w are the mean wave and wind directions, and $E(f)$ is the observed 1D wave spectrum. For simplicity, the relative wind speed U_r is used in Eq. 2.4 for the presence of surface currents. The wind-wave ratio is defined as E_w/E_s, which is used to classify different types of sea states. Based on the values of the wind-wave ratio, sea states are classified into three groups (*Potter,* 2015): wind-wave-dominated conditions ($E_w/E_s >$ 2.0), mixed-sea conditions ($0.5 \le E_w/E_s \le 2.0$), and swell-dominated conditions ($E_w/E_s < 0.5$).

During the winter-storm period in February 2011, the wind-wave ratios (E_w/E_s) at six buoy locations shown in Fig. 2.10 were mostly larger than 2.0, indicating the observed sea states were generally dominated by wind waves during this period at these buoys. At buoy stations off the eastern coast of the US (Figs. 2.10a-2.10c), wave energy was less intense and mainly distributed at high frequencies ($f > 0.1$ Hz). By comparison, at buoy stations over the Scotian Shelf (Figs. 2.10d-2.10e), the observed sea states were energetic with large wind-wave energy spreading over low frequencies ($f < 0.1$ Hz). The observed sea states at buoy EL450 were dominated by large wind waves before 19 February and swells

dominated the sea states after the local wind speeds became weak. By comparison, the observed sea states were generally either under mixed or swell-dominated conditions at most of the buoy stations during the hurricane period (Fig. 2.11). At buoys 44141 and 44251 (Figs. 2.11e-2.11f), wind waves reached maximum values and dominated the sea states on 3 October during the passage of Hurricane Ophelia. The observed sea states were dominated by swells after the passage of Hurricane Ophelia.

We now discuss the performances of the four packages (ST2, ST3, ST4, and ST6) under different sea states. The bin-averaged values of RB for SWHs in terms of different sea states are shown in Fig. 2.12 based on observations from both altimeters and buoys. The data points for ST2 are excluded because ST2 has large negative biases (i.e., underestimates) for all sea states. Sea states during the winter-storm period were energetic with most observed SWHs (10-90%) between 0.9 m and 6.5 m (Fig. 2.12a). During Hurricane Ophelia, sea states away from the hurricane center were generally swell-dominated with most of the observed SWHs (10-90%) between 0.8 m and 3.2 m (Fig. 2.12b). During the winter-storm period (Fig. 2.12a), ST3 and ST4 generally have negative biases within 10% for the majority of wave conditions (0.9 m < H_s < 9.0 m) but may overestimate large waves (H_s > 9.0 m). In comparison, ST6 also overestimates large waves but has relatively small and positive biases with RB values less than 5% for the majority of wave conditions (0.9 m < H_s < 7.5 m). During the hurricane period (Fig. 2.12b), ST3 and ST4 have positive RB values and ST6 has negative RB values for swell-dominated sea states (H_s < 1.5 m). Packages ST3, ST4, and ST6 slightly overestimate extreme waves during both study periods. One interesting finding in Fig. 2.12 is that ST4 consistently predicts larger SWHs than ST3. Compared with ST4, ST6 generally has even larger SWHs under the wind-wave-dominated sea states but smaller SWHs under the most energetic and swell-dominated sea states. Overall, ST6 performs best in terms of RB distributions for both study periods but with the limitations of overestimates of SWHs under wind-wave-dominated conditions and underestimates of SWHs under swell-dominated conditions.
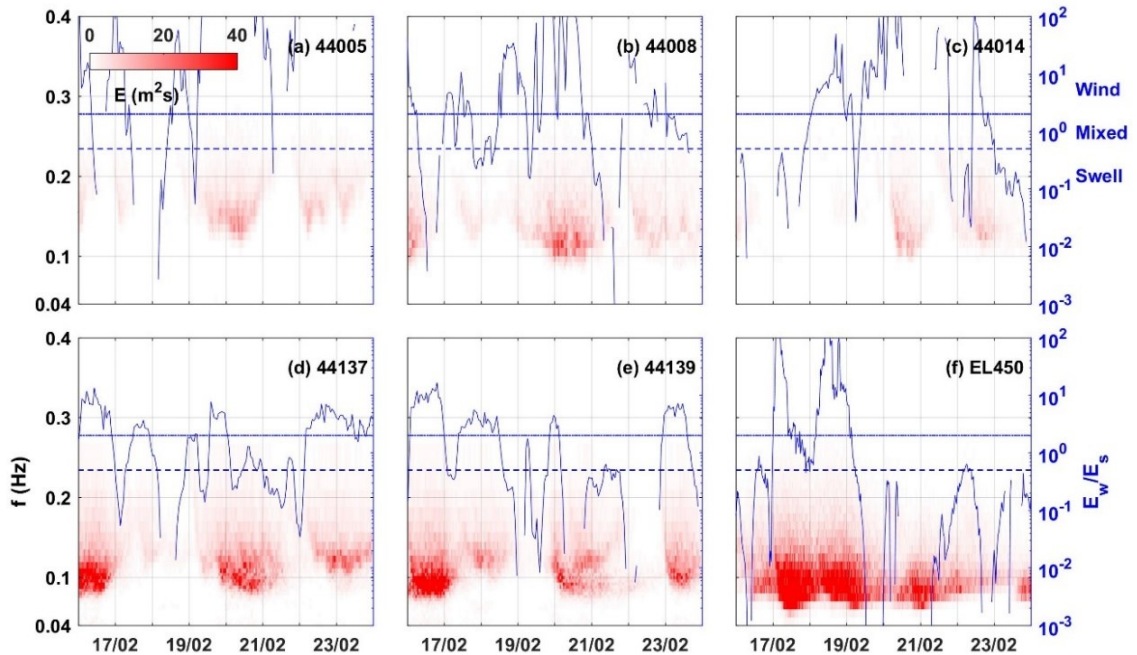
Figure 2.10: Observed 1D wave spectra (image) at six different buoy stations during the winter-storm period. Blue solid lines denote the wind wave ratio (E_w/E_s). Blue dotted lines ($E_w/E_s = 2.0$) denote the separation ratio between the wind-wave-dominated and mixed conditions. Blue dashed lines ($E_w/E_s = 0.5$) denote the separation ratio between the mixed and swell-dominated conditions. The values for the wind wave ratio are indicated by the y-axis on the RHS.
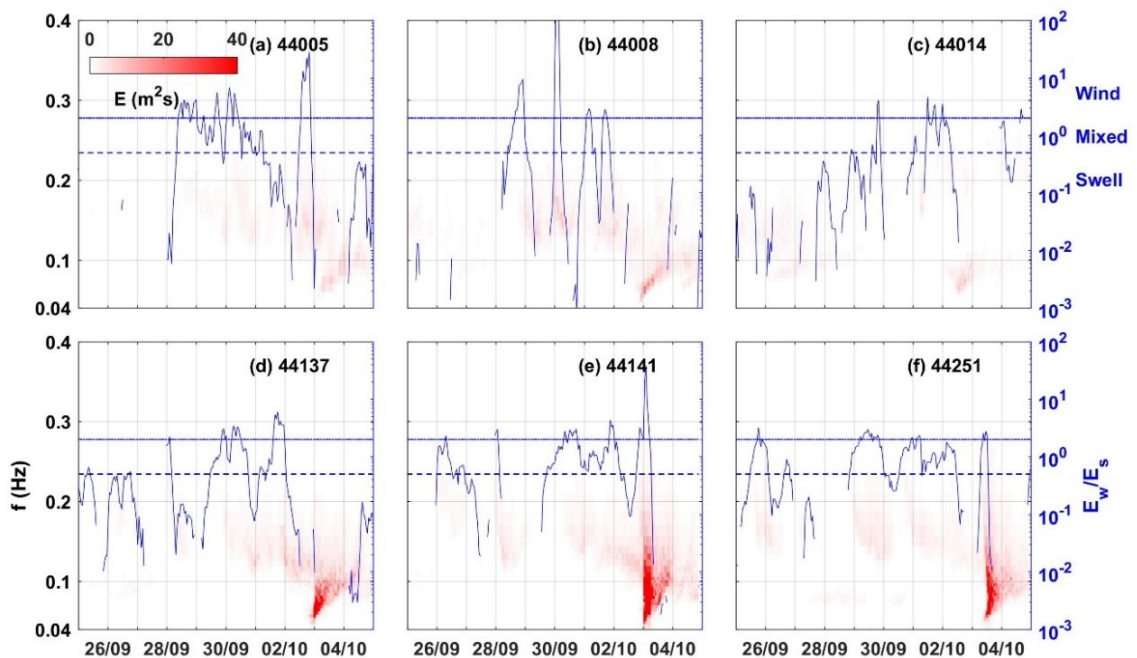
Figure 2.11: As in Fig. 2.10, but for the hurricane period.
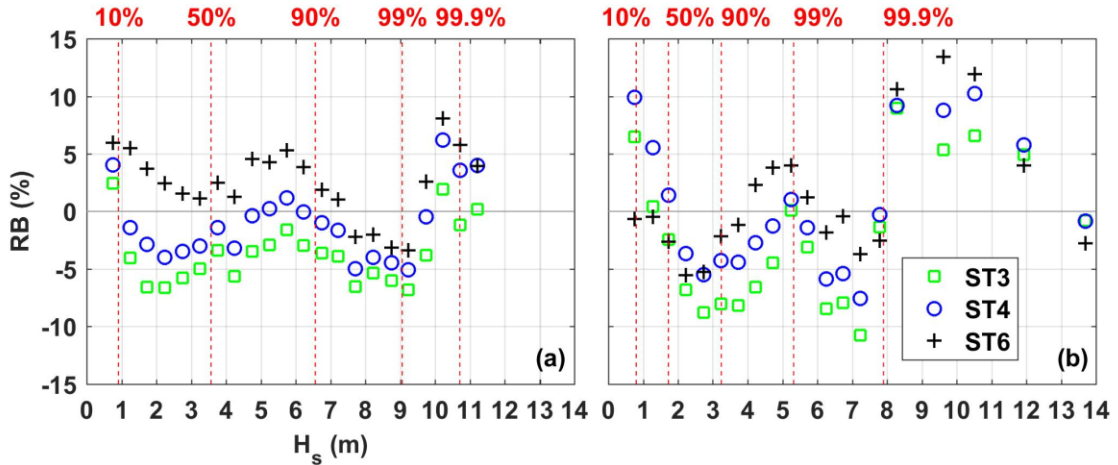
Figure 2.12: The relative bias (RB) for SWHs for model results with three different packages in terms of sea states (H_s) during (a) the winter-storm period and (b) the hurricane period. The SWHs at specific cumulative frequencies (10%-99.9%) are shown by the red dashed lines.

Dynamically, surface gravity waves are an integrated effect of winds in space and time. The performances of these four packages (ST2, ST3, ST4, and ST6) are highly related to the accuracy of the wind forcing (*Cavaleri,* 2009), as expected. Although the accuracy of the wind forcing can certainly affect model performance, problems associated with the source term parameterizations should not be overlooked. The different performances of these packages under different sea states and their strengths and weaknesses can be explained well in terms of the wave energy input and dissipation across the wave spectrum.

Wave spectra (E) and source terms for the wind input (S_{in}), wave dissipation (S_{ds}), nonlinear wave interactions (S_{nl}), and total wave energy gain (S_{tot}) predicted by the wave model using ST2, ST3, ST4, and ST6 at buoy 44137 over the southwestern Scotian Shelf Break during the winter-storm period and at buoy 44141 over the northeastern Scotian Shelf Break during the hurricane period in 2011 are shown in Figs. 2.13 and 2.14, respectively. At 2300 UTC 16 February, the wind input around the peak frequency is the strongest in ST3 followed by ST4 (Fig. 2.13b1). The input energy decays rapidly with increasing frequencies in ST3 and ST4. In comparison, ST6 has less input energy at the peak frequency but more energy at high frequencies. Wave spectra in ST6 thus have broader frequency bandwidths than ST2, ST3, and ST4 (Fig. 2.13a1). Package ST6 initially has strong wind input around the peak frequency but decays rapidly as waves become

mature. As a result, ST6 generates the largest wave energy at this time. Correspondingly, wave dissipation in ST6 is concentrated at high frequencies, and wave energy around the peak frequencies is strongly dissipated in ST3 and ST4 (Fig. 2.13c1). For nonlinear wave interactions (Fig. 2.13d1), a significant fraction of the wind input from the mid-range frequencies is transferred to lower frequencies and a small fraction to higher frequencies. Overall, wave energy is only slightly increased at the peak frequency but strongly dissipated at frequencies higher than the peak frequency (Fig. 2.13e1).
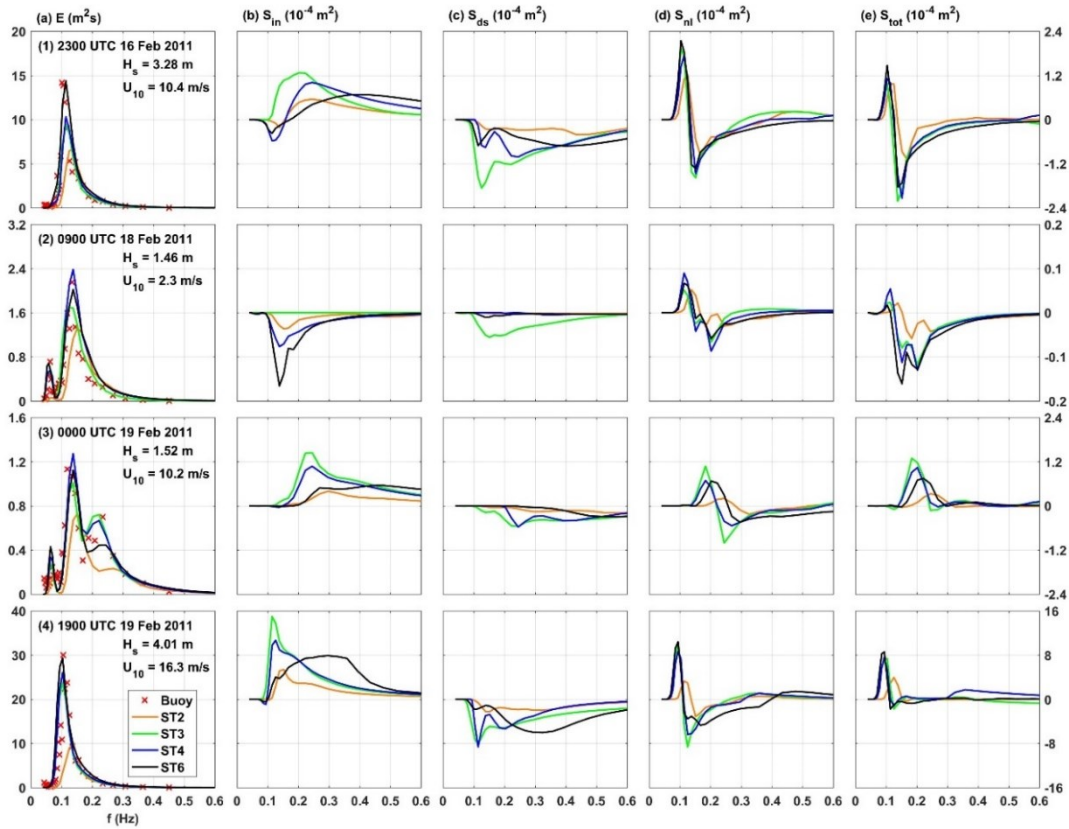
Figure 2.13: (a) Wave spectra and source terms for the (b) wind input, (c) wave dissipation, (d) nonlinear wave interactions, and (e) total wave energy gain or loss at buoy 44137 at different time (1-4) during the winter-storm period. Red crosses in (a) denote the observed wave spectra. Solid lines with different colors denote the model results using different packages (ST2/3/4/6). The values of wave spectra (a) are indicated by the y-axis on the LHS. The values for the source terms (b-e) are indicated by the y-axis on the RHS. The corresponding observed H_s and U_{10} are shown in (a).

At 0900 UTC 18 February (Fig. 2.13b2), ST6 generates the strongest negative wind input, followed by ST4 and ST2 because the wind decreased to 2.3 m/s and blew against the wave direction at buoy 44137. However, ST3 does not predict the negative wind input but has

extensive wave dissipation to compensate for the total wave energy loss. Overall, ST6 predicts the strongest energy loss, followed by ST3 and ST4 (Fig. 2.13e2). Therefore, in comparison with ST4, ST6 predicts larger SWHs under wind-wave-dominated conditions (Fig. 2.13a1) and smaller SWHs under swell-dominated conditions (Fig. 2.13a2).

The observed wind speed at buoy 44137 increased gradually to about 10.2 m/s at 2300 UTC 18 February. The wave spectra at this time had a tri-modal structure (Fig. 2.13a3) with a combination of bimodal swell energy and growth of wind waves at high frequencies. The wind speed at this time was comparable with that at 2300 UTC 16 February, and the wind direction similarly followed the wave direction. However, the growth of wind waves in the four packages at 2300 UTC 18 February concentrates at higher frequencies around 0.2 Hz (Fig. 2.13e3), in comparison with the counterpart at frequencies around 0.1 Hz at 2300 UTC 16 February (Fig. 2.13e1) because of the different behaviors of nonlinear wave interactions in the presence of swells. Physically, the presence of swells can reduce wave steepness and nonlinear wave interactions decrease accordingly (*Holthuijsen,* 2010).

The wind speed continuously increased and reached 16.3 m/s at 1900 UTC 19 February. The behaviors of different packages are similar to the situation at 2300 UTC 16 February but with overall energy gains (Fig. 2.13e4). Package ST6 has more input energy initially, mainly at higher frequencies compared with the other three packages. These features of ST6 can be attributed to the nonlinear behavior of the spectral saturation ($B_n \sim k^3$) in the parametrization of wind input. Package ST6 thus has fast and strong wind input under wind-wave-dominated conditions.

During the hurricane period, the main features of these four packages (Fig. 2.14) are similar to those during the winter-storm period. At 1300 UTC 29 September, the observed wave spectrum at buoy 44141 was bimodal and dominated by the swell peak (Fig. 2.14a1). The bimodal wave spectrum is reproduced reasonably well by the four packages but with underestimates of the swell peak and overestimates of the wind-wave peak, which are two important reasons for the underestimate of T_{m02} (Section 2.4.2). Of the four packages, ST3 has the strongest wind-wave growth followed by ST4 and ST6 (Fig. 2.14a1). Previous observations (e.g., *Chen and Belcher,* 2000; *Ardhuin et al.,* 2007) demonstrated that the

effect of swells on wind-wave growth is weak, with less than a 5% reduction in wind waves. However, ST3 amplifies the growth of wind waves in the presence of swells due to the excessive wind input (Fig. 2.14b1). This weakness of ST3 is addressed in ST4 by reducing the wind input at high frequencies through the reduction of the friction velocity (*Ardhuin et al.,* 2010). Moreover, *Rogers et al.* (2003) found that ST3 overpredicts the wave energy at the high-frequency tail in the presence of swells due to insufficient dissipation. As mentioned in Section 2.3.2, the dissipation term in ST3 is strongly weighted by the spectral mean wavenumber, which is sensitive to the presence of swells.
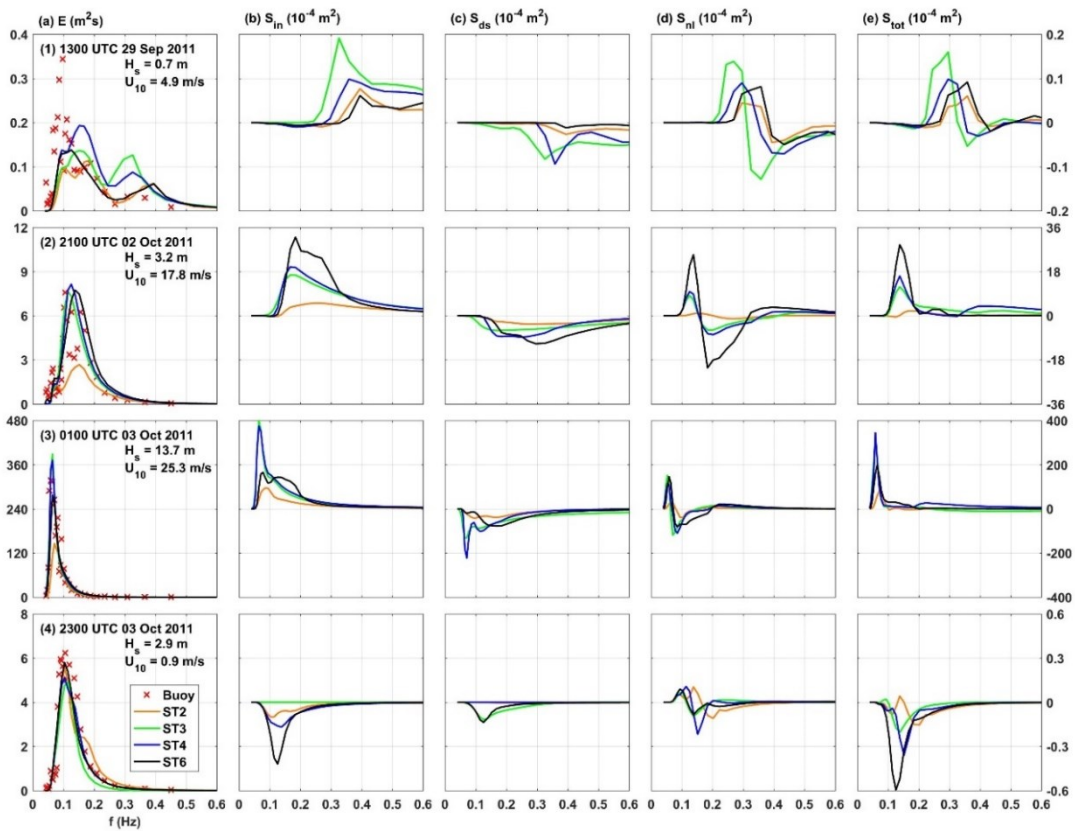
Figure 2.14: As in Fig. 2.13, but for buoy 44141 during the hurricane period.

As the hurricane center moved into the region, the wind speed at buoy 44141 increased sharply to 17.8 m/s at 2100 UTC 2 October and reached its maximum of 25.3 m/s at 0100 UTC 3 October. In comparison with the other three packages, ST6 has more energy input initially (Fig. 2.14b2) but saturates rapidly (Fig. 2.14b3). The behavior of different packages is also related to the different drag coefficients predicted by these four packages. Because ST3 and ST4 have larger drag coefficients than ST6 for high winds (discussed in

Section 2.5.2), ST3 and ST4 predict more energy input than ST6 and thus have larger SWHs (Fig. 2.8g). As the hurricane center passes by, waves are mainly affected by the wave dissipation process (Fig. 2.14b4). Similar to the situation shown in Fig. 2.13b2, ST6 has the strongest wave dissipation.

The main features of these four packages (ST2, ST3, ST4, and ST6) under different sea states are also shown in the comparisons of simulated and observed wave spectra (Fig. 2.15). The dashed lines in Fig. 2.15 represent the calculated splitting frequencies using the observed wave spectra based on Eq. 2.4. The observed sea states along the Scotian Shelf were dominated by wind waves at 0000 UTC 17 February (Figs. 2.15a-2.15c). At this time, ST6 predicts a higher wave energy than ST3 or ST4 and has the best agreement with observations with slight overestimates of wave energy. Before the approach of Hurricane Ophelia at 1500 UTC 1 October, the observed sea states along the Scotian Shelf were dominated by swells (Figs. 2.15d-2.15f). The common limitation of these four packages is the shifting of wave energy to higher frequencies. Therefore, swell energy is generally underestimated in these four packages. In comparison with ST3 and ST4, ST6 generates lower wave energy because of stronger swell dissipation, which is opposite to that under wind sea states.

Overall, the wind input predicted by ST2 is insufficient and shifted to higher frequencies during both study periods, which leads to the significant underestimates of H_s and T_{m02}. Under wind-wave-dominated sea states, the wind input supplying the growth of waves is the essential process for wave evolution, which becomes the swell dissipation and whitecapping dissipation when sea states are dominated by swells. Under wind-wave-dominated sea states, H_s, T_{m02}, and wave spectra predicted by ST6 agree best with observations (Table 2.2 and Fig. 2.15) as a result of the fast and strong wind input in ST6. However, ST4 predicts higher H_s than ST6 under the most energetic sea states because of the large drag coefficients at high winds in ST4 and the rapid saturation of wind input in ST6. Under swell-dominated sea states, ST4 and ST6 outperform the other two packages (Table 2.2 and Fig. 2.15). However, ST6 underestimates H_s and T_{m02} because of the strong swell dissipation in ST6.
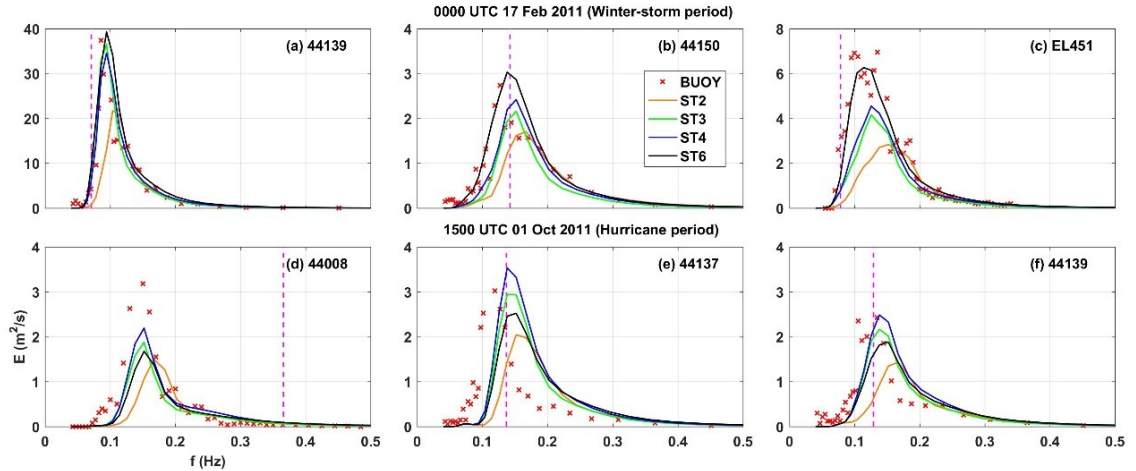
Figure 2.15: Observed (red crosses) and simulated wave spectra using four packages (solid lines) at buoy stations at 0000 UTC 17 February (a-c) and 1500 UTC 01 October (d-f) in 2011. The dashed lines represent the calculated splitting frequencies using the observed wave spectra based on Eq. 2.4.

2.5.2 Drag Coefficient and Wind Input

The growth and decay of surface gravity waves are significantly affected by the momentum transfer at the air-sea interface. The calculation of the momentum flux from winds to surface waves requires reliable estimates of the drag coefficient (or friction velocity) at the sea surface. The drag coefficient (C_d) has long been studied and has traditionally been considered as a monotonically increasing function of the wind speed (e.g., *Large and Pond,* 1981). The monotonic increase of the drag coefficient has been confirmed by previous measurements at moderate wind speeds. However, the drag coefficient has different features at low and high wind speeds. It was reported that the drag coefficient decreases with increasing wind speed at low wind speeds, based on observations in lakes (*Mitsuta and Tsukamoto,* 1978, *Wei et al.,* 2016), over the open ocean of the Southern Ocean (*Yelland and Taylor,* 1996), and over the north Indian Ocean (*Parekh et al.,* 2011). *Wei et al.* (2016) suggested that the increase in the turbulent intensity in the atmospheric boundary layer is the major cause for the increase in the drag coefficient at low wind speeds under unstable atmospheric conditions. At high wind speeds, on the other hand, the drag coefficient was found to level off or even decrease based on the field measurements (*Powell et al.,* 2003; *Jarosz et al.,* 2007), laboratory experiments (*Donelan et al.,* 2004), and theoretical studies (*Moon et al.,* 2004). Figure 2.16 presents the drag coefficient as a

function of the relative wind speeds (U_r) predicted by ST2, ST3, ST4, and ST6, as well as observational data from previous studies (*Black et al.,* 2007; *Garratt,* 1977; *Jarosz et al.,* 2007; *Large and Pond,* 1981; *Powell et al.,* 2003; *Smith and Banke,* 1975; *Wu,* 1982; *Bi et al.,* 2015; *Donelan et al.,* 2004; *French et al.,* 2007; *Vickery et al.,* 2009; *Zachry et al.,* 2013; *Holthuijsen et al.,* 2012; *Mitsuta and Tsukamoto,* 1978; *Wei et al.,* 2016; *Geernaert et al.,* 1988; *Bradley et al.,* 1991; *Xiao et al.,* 2013; *Yelland and Taylor,* 1996). Overall, previous observations convincingly demonstrated that the drag coefficient first decreases with the wind speed up to ~6 m/s then increases with the wind speed until it levels off or decreases at ~33 m/s. The saturation of the drag coefficient at high wind speeds has been implemented in numerical models of ocean circulation and surface waves (e.g., *Wang and Sheng,* 2016; *Xu et al.,* 2017).
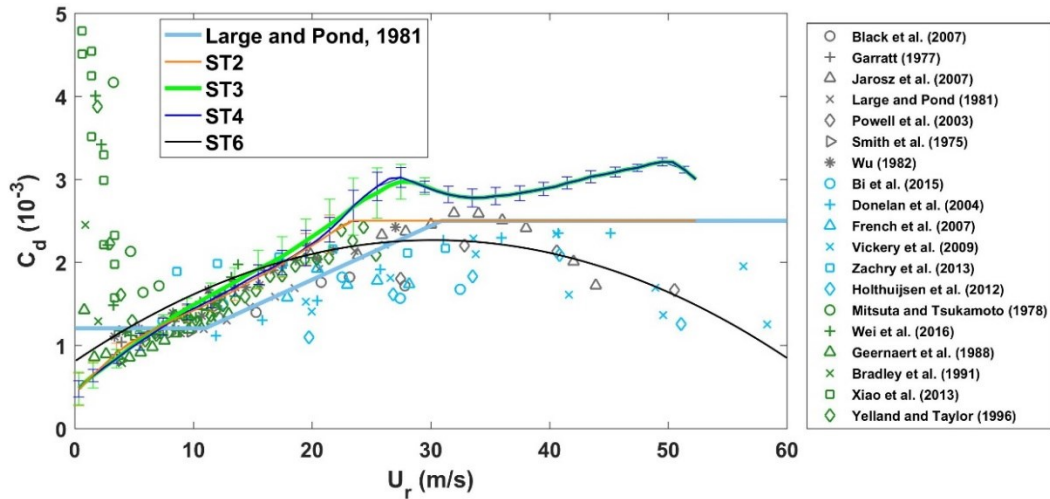
Figure 2.16: Values of the drag coefficient produced by four different source term packages as a function of the relative wind speed. The error bars represent the corresponding standard deviations. The widely-used formula for the drag coefficient suggested by *Large and Pond* (1981) with a maximum value (2.5×10^{-3}) at high winds is also shown for comparisons. Different markers represent the observed values of the drag coefficient from previous studies.

Different parameterizations for the drag coefficient are used in the four packages (ST2, ST3, ST4, and ST6). The drag coefficients in ST2, ST3, and ST4 are wave-state dependent and can be converted from the friction velocity based on $C_d = u_*^2/U_r^2$. Although the increasing drag coefficient with increasing wind speed at moderate winds is well represented by these four packages, none is able to generate the enhanced drag coefficient at low wind speeds. This can be part of the reason for the underestimates of SWHs in ST6

under swell-dominated sea states (Fig. 2.12b). Furthermore, the values of C_d in ST2, ST3, and ST4 (Fig. 2.16) are similar at low and moderate wind speeds ($U_r < 25$ m/s) but differ significantly at high wind speeds ($U_r > 25$ m/s). At high winds, C_d in ST2 is usually capped at a maximum value of 2.5×10^{-3}; however, ST3 and ST4 have values of C_d larger than 2.5×10^{-3} at high wind speeds. Package ST6 takes the drag coefficient as a parabolic function of wind speed as suggested by *Hwang* (2011) to account for the saturation at high winds. Compared with ST2, ST3, and ST4, the drag coefficients in ST6 have the lowest values at high winds.

The drag coefficient only affects wind stress at the ocean surface. The growth or decay of surface waves is determined by the net energy flux, which is defined as the wind-to-wave energy flux (F_{ww}) minus the wave-to-ocean flux (F_{wo}). Figure 2.17 presents snapshots of u_*, F_{ww}, ($F_{\mathrm{ww}} - F_{\mathrm{wo}}$), and H_s predicted by ST2, ST3, ST4, and ST6 at 0640 UTC 3 October 2011 during the hurricane period. As mentioned above, Hurricane Ophelia weakened to a tropical storm with a maximum wind speed of ~30 m/s by 0600 UTC 3 October before it approached the south coast of Newfoundland. The friction velocities shown in Fig. 2.17 demonstrate that four packages have large values of the drag coefficient (or u_*) over regions to the RHS of the hurricane track, with the maximum value of u_* being largest in both ST3 and ST4 and smallest in ST6 (Figs. 2.17a1-2.17d1). But ST6 produces a slightly larger u_* over areas away from the hurricane center with the contour line $u_* = 0.4$ m/s extending to a larger area than with ST2, ST3, or ST4. These are consistent with the comparisons of the drag coefficients in ST2, ST3, ST4, and ST6.

The wind input in the wave model is determined by not only the drag coefficient (u_*) but also the parametrization of the wave growth. Although the friction velocities in ST6 are weaker than those in ST2, ST6 predicts a much larger F_{ww}. Compared with ST3 and ST4, ST6 predicts a smaller F_{ww} at high winds but larger F_{ww} at moderate and low winds (Figs. 2.17a2-2.17d2) as a result of stronger wind input in ST6 (Figs. 2.13 and 2.14). The net energy fluxes ($F_{\mathrm{ww}} - F_{\mathrm{wo}}$) are similar in ST3 and ST4, with strong dissipation in the rear quadrants and strong input in the front quadrants. By comparison, the wave dissipation in ST6 is relatively weak (Fig. 2.17d3). Therefore, ST6 generates larger contour regions of SWHs for the contours $H_s = 4, 6$, and 8 m compared with its counterparts in ST3 and ST4

(Fig. 2.17d4). The corresponding observed SWHs from the satellite track are overlaid in Figs. 2.17a4-2.17d4. The simulated SWHs using ST4 and ST6 have the best agreement with the observed spatial variations of SWHs. On the other hand, swells propagating from the hurricane center travel a longer distance in ST4 than in ST6 because ST6 has strong swell dissipation, which is also shown in Figs. 2.13 and 2.14.
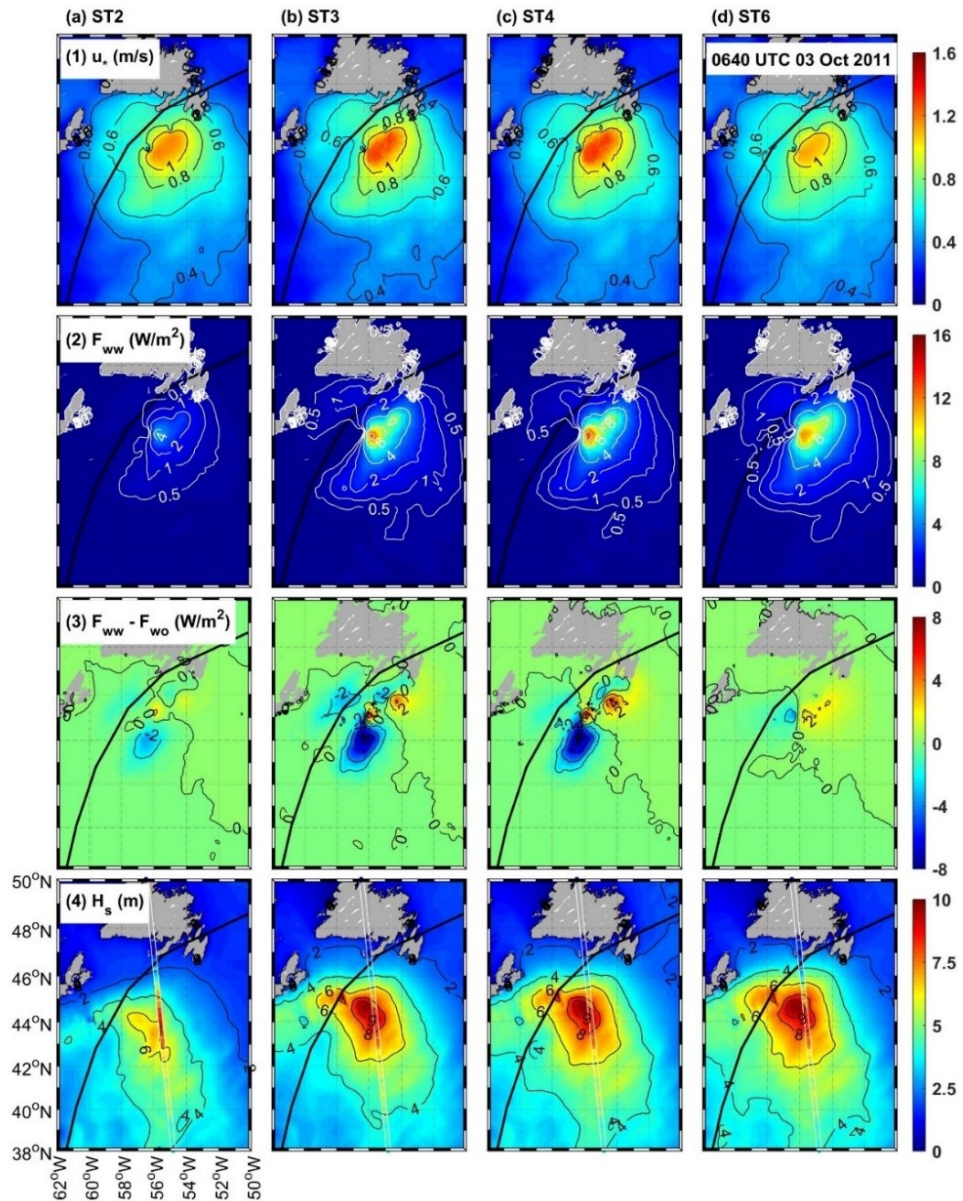
Figure 2.17: Snapshots of (first row) the friction velocity at the sea surface, (second row) wind-to-wave energy flux, (third row) net energy flux, and (fourth row) SWHs predicted by different packages (ST2/3/4/6) at 0640 UTC 3 October 2011. The corresponding observed SWHs along the satellite track are overlayered in the fourth row. Black lines denote the storm track of Hurricane Ophelia.

2.5.3   Effects of Currents on Waves

Strong ocean currents, such as the GS, can significantly affect ocean wave generation and propagation over the NWA (*Ardhuin et al.,* 2017). Figure 2.18 shows the effects of currents on the SWHs and wave directions at buoy 41001. Buoy 41001 is located to the east of Cape Hatteras and at the path of the GS with strong currents up to 1.2 m/s (blue line) during the winter-storm period. It is clear that the simulated SWHs using ST6 agree better with the observed values by considering the current effects (Fig. 2.18a). The simulated SWHs with currents (black solid line) are generally larger than those without currents (black dashed line). Wave model results using the other three packages (ST2, ST3, and ST4) are not shown because similar conclusions can be made.

As mentioned in Section 2.3.1, ocean currents can affect ocean surface gravity waves in terms of wave kinematics including wave spatial advection, wave refraction, and wavenumber shift. The effects of currents on the SWHs and MWPs over the NWA are shown in Fig. 2.19 together with the relative changes caused by currents. It is clear that currents can significantly increase the spatial variabilities of wave fields. The modulation of SWHs by currents is significant to the meanders and eddies of the GS with the maximum absolute and relative differences more than 1.5 m and 100% over the central GS. The absolute differences are small over shallow waters and in the ice because the SWHs are small. The modulation of the MWPs by currents is large over the central GS and in the Gulf of Maine, with the maximum absolute and relative differences more than 1.5 s and 50%. The effects of the GS on the waves are mainly a result of current-induced wave refraction (*Holthuijsen and Tolman,* 1991; *Ardhuin et al.,* 2017). The effect of current-induced wave refraction is to turn surface waves toward the area with lower group velocities causing the focusing or defocusing of wave energy. Surface waves propagating through the GS can be trapped as a result of wave refraction. Therefore, the SWHs at buoy 41001 generally increase when current effects on waves are taken into account (Fig. 2.18a). On the other hand, the effect of current-induced wavenumber shift depends on the spatial gradients of currents in the wave propagation directions. Waves (black line in Fig. 2.18b) at buoy 41001 mostly propagate in the opposite direction to currents (blue line in Fig.

2.18b). Waves propagating against accelerating currents experience an increase in wavenumber, which results in an increase in the SWHs.
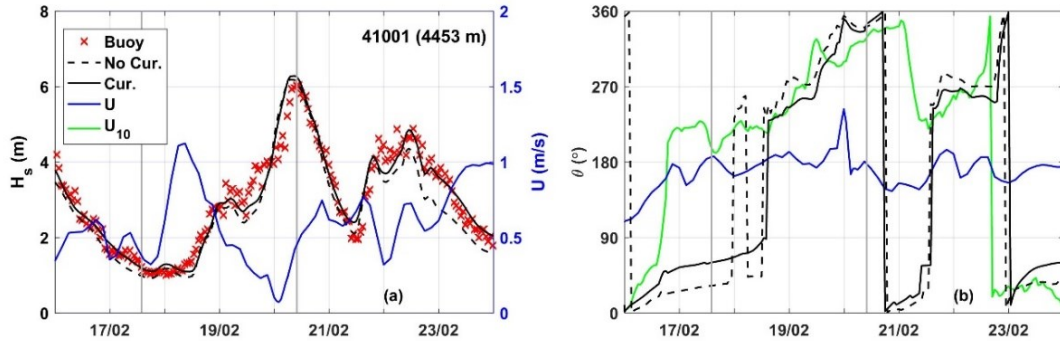
Figure 2.18: (a) Time series of the observed and simulated SWHs using ST6 with currents (black solid line) and without currents (black dashed line) at buoy station 41001 during the winter-storm period. (b) Time series of wind (green line), current (blue line) and simulated peak wave directions with currents (black solid line) and without currents (black dashed line). Surface currents from the HYCOM (blue line) are also indicated by the y-axis on the RHS in panel (a). The two gray lines represent the time for comparisons shown in Fig. 2.19.
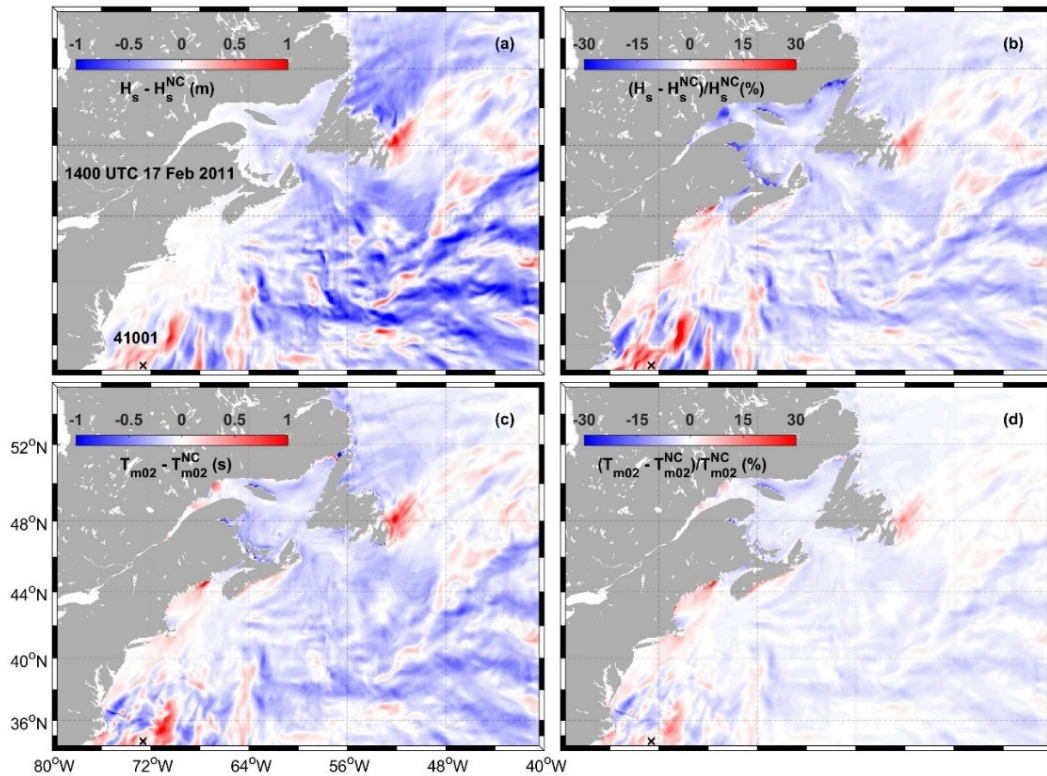
Figure 2.19: Differences in (a) SWHs (H_s) and (c) MWPs (T_{m02}) between model results with currents and without currents at 1400 UTC 17 February 2011. The corresponding relative differences are shown in (b) and (d), respectively. Black crosses denote the location of buoy 41001.

The linear kinematic effects of currents on waves can cause the redistribution of wave energy in the spatial and frequency domains (LHS of Eq. 2.1) but may not directly affect the wave energy gain and loss (RHS of Eq. 2.1). However, the modulation of wave spectra due to linear kinematic effects can have significant nonlinear dynamic consequences, such as the modulation of the nonlinear wave energy transfer (*Rapizo et al.,* 2016) and whitecapping (*Wang and Sheng,* 2018). The nonlinear dynamic effects are not explicitly implemented in the wave model (*WW3DG,* 2016), but the relative wind effect due to currents can directly affect the wind input and wave dissipation. Figure 2.20 shows the differences between the model results (E, S_{in}, S_{ds}, S_{nl} and S_{tot}) at buoy 41001, with currents and without currents using four different packages during the winter-storm period.

At 1400 UTC 17 February, waves at buoy 41001 experienced a decay of swell energy and growth of wind-wave energy (Figs. 2.20a1 and 2.20a2). In comparison with model results without currents (dashed lines), wave model results with ocean currents (solid lines) at this time have the following five important features. (i) The swell peak is stronger and in better agreement with observations because of linear kinematic current effects. (ii) Because the winds and currents are in the similar directions (Fig. 2.18b), the wind input decreases as a result of the relative wind effect (Figs. 2.20b1 and 2.20b2). Therefore, wave energy at high frequencies becomes lower. It should be noted that the wind input is also proportional to the wave energy; the negative wind input becomes stronger due to the stronger swell peak (Figs. 2.20a1 and 2.20a2). (iii) Wave dissipation becomes weaker due to the lower wave energy at high frequencies ($f > 0.2$ Hz), which represents the nonlinear dynamic effects of currents on waves (Figs. 2.20c1 and 2.20c2). In addition, the wave dissipation terms in ST2 and ST4 also depend on the friction velocity, which is lower because of the relative wind effect. (iv) Nonlinear wave interactions are concentrated at high frequencies ($f > 0.2$ Hz) and become weaker (Figs. 2.20d1 and 2.20d2). As mentioned in Section 2.5.1, the presence of stronger swell energy sharply reduces wave steepness and the nonlinear wave interactions decrease accordingly (*Holthuijsen,* 2010). The other possible reason is that the presence of currents could alter the four-wave resonance conditions and weaken energy transfer among different frequencies, as suggested by *Rapizo et al.* (2016). (v) Generally, ocean currents amplify the swell dissipation but weaken the growth of wind waves (Figs. 2.20e1 and 2.20e2).
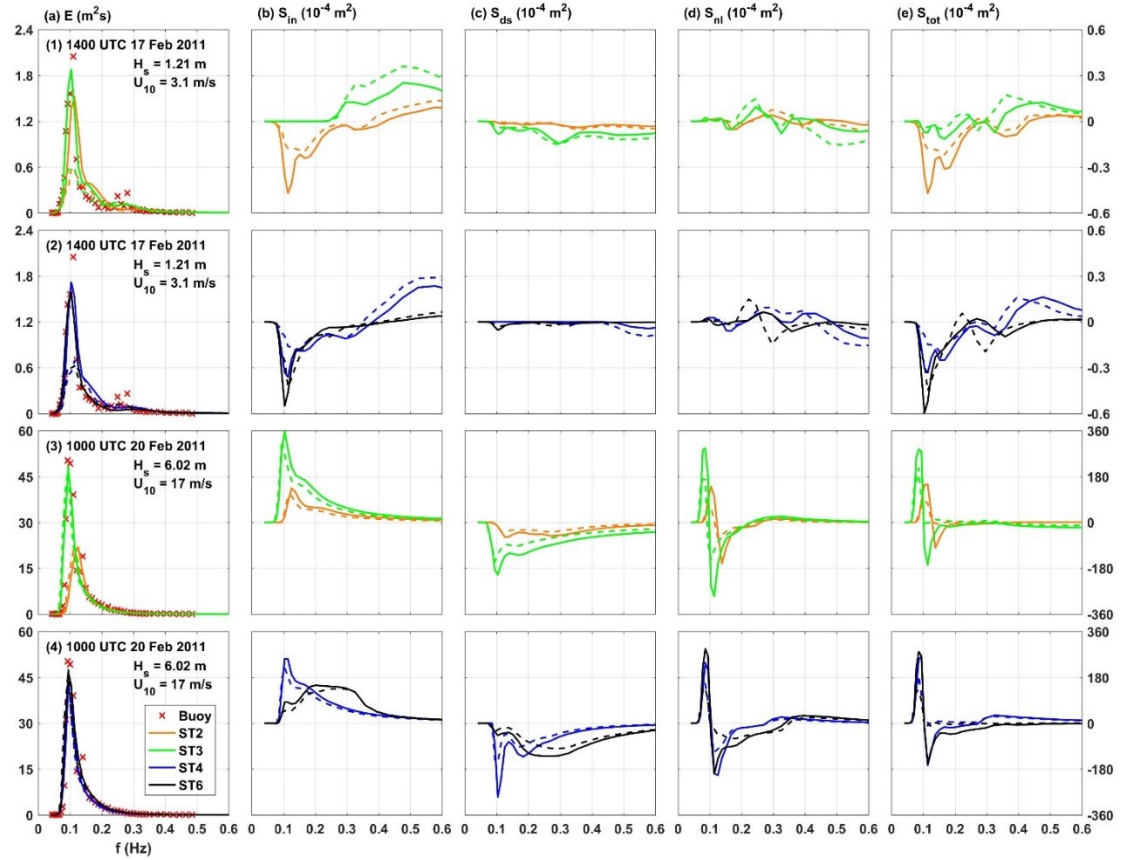
Figure 2.20: (a) Wave spectra and source terms for the (b) wind input, (c) wave dissipation, (d) nonlinear wave interactions, and (e) total wave energy gain or loss at buoy 41001 at 1400 UTC 17 February 2011 (1-2) and 1000 UTC 20 February 2011 (3-4). Solid (Dashed) lines with different colors denote the model results using different packages with (without) currents. Otherwise as Fig. 2.13.

At 1000 UTC 20 February, waves at buoy 41001 reached a maximum and propagated following surface winds and against ocean currents. In comparison with model results without currents, model results with currents at this time have the following four features. (i) Wave energy is slightly stronger and modulated toward higher frequencies as a result of current-induced wavenumber shift, which leads to an increase in wave steepness. (ii) Because the wind and current are in opposite directions (Fig. 2.18b), the wind input (Figs. 2.20b3 and 2.20b4) and wave dissipation (Figs. 2.20c3 and 2.20c4) become stronger as a result of the relative wind effect. The increase in wave steepness can also contribute to stronger wave dissipation. (iii) Nonlinear wave interactions become stronger (Figs. 2.20d3 and 2.20d4), which could be due to the increase in wave steepness. (iv) Ocean currents intensify the growth of wave energy (Figs. 2.20e3 and 2.20e4). This is consistent with the

46

study of *Holthuijsen and Tolman* (1991), who showed that one effect of opposing currents is to enhance the intensity of wave growth and dissipation near the center of the GS.

In summary, linear kinematic current effects on waves are similar in the four different packages (ST2, ST3, ST4, and ST6). However, the intensity of the nonlinear dynamic effects can be different because of different features of each package. For example, the increase or decrease of wave dissipation with ST3 resulting from ocean currents is generally more significant than with the other three packages.

2.5.4   Effects of Ice on Waves

The wave evolution over the ECS, particularly over the NLS and GSL, is affected by the presence of ice during the winter-storm period in February 2011. As shown in Fig. 2.4, there are five buoys (44235, 44251, 44258, SA1, and SA2) close to the ice edge. A comparison of observed SWHs and simulated values using four packages (Fig. 2.7) at these five buoys demonstrates that ST4 and ST6 have the smallest model bias. The same can be concluded based on a comparison between model results and altimeter observations over the NLS and GSL (not shown). Ice concentrations at buoy 44258 were around 0.05 during the winter-storm period. The low ice concentration at buoy 44258 has limited effects on wave evolution. Nevertheless, the effects of sea ice on waves can be investigated based on numerical wave model results.

Figure 2.21 presents differences between simulated wave variables (H_s and T_{m02}) with ice and without ice using ST4 at 0000 UTC 21 February. The presence of ice reduces SWHs (Fig. 2.21a) as a result of the wave attenuation in ice and the reduction in wind input. The MWPs generally increase in the presence of ice (Fig. 2.21b) because wave energy at higher frequencies decays more rapidly. The effects of ice on H_s and T_{m02} become stronger over regions with higher ice concentrations. It should be noted that the SWHs increase over the central GSL in the presence of ice (Fig. 2.21a) because of wave reflection and wave scattering in ice. In the marginal ice zone (MIZ), where the ice concentrations are relatively low and floe sizes are comparable with wavelength, wave scattering is more dominant than wave attenuation (*Boutin et al.,* 2018). During the winter-storm period, ice concentrations over the NLS and central GSL are around 0.1 with floe sizes being ~100 m. Thus, waves

propagating through the central GSL are scattered in different directions causing increasing local wave energy. Increased SWHs due to wave scattering in ice was also found in wave simulations in the Artic (*Boutin et al.,* 2018). A noticeable reduction in MWPs occurs over the northern GSL (Fig. 2.21b), which is due to the presence of ice blocking wave energy.

The effects of sea ice on waves can also be demonstrated by examining model results on a transect along 52°N (A1-A5, Fig. 2.4) at 0000 UTC 21 February. As shown in Fig. 2.22a, ice concentration increases from zero in the open ocean (A1) to 0.8 at the inner ice pack (A4), then decreases to 0.3 near the coast (A5). The variation of ice thickness along the transect is similar. The simulated SWHs using four different packages experience similar variations with a more rapid decay at higher ice concentrations (Fig. 2.22b). The wave directional spread (σ_θ), which represents the spreading of wave energy in different directions, is also shown in Fig. 2.21b. The value of σ_θ first increases at low ice concentrations (c_i < 0.4), then decreases in the inner ice pack with high ice concentrations. This demonstrates that wave scattering is the dominant process in the MIZ because wave energy is redistributed in different directions. When waves propagate into regions with high ice concentrations, wave attenuation becomes important, and wave energy in different directions is rapidly attenuated.

The values of E, S_{in}, and S_{ds} across the wave frequency at these five locations (A1-A5) are shown in Fig. 2.23. As waves propagate into ice, wave energy is dissipated with stronger dissipation occurring at the higher peak frequency (Fig. 2.23a). With an increase in ice concentration, the wind input in the inner ice pack is significantly reduced and shifts to higher frequencies compared with the situation in the open ocean (Fig. 2.23b). Wave dissipation becomes negligible at A3-A5, indicating significant suppression of wave dissipation in the inner ice pack (Fig. 2.23c). The presence of ice has a direct effect on the wind input and wave dissipation as a result of scaling by the open water fraction (*Roger et al.,* 2016). The modification of wave spectra resulting from the presence of sea ice has nonlinear effects on the wind input and wave dissipation. For example, wave energy can lie below the threshold spectrum and thus wave dissipation becomes negligible.
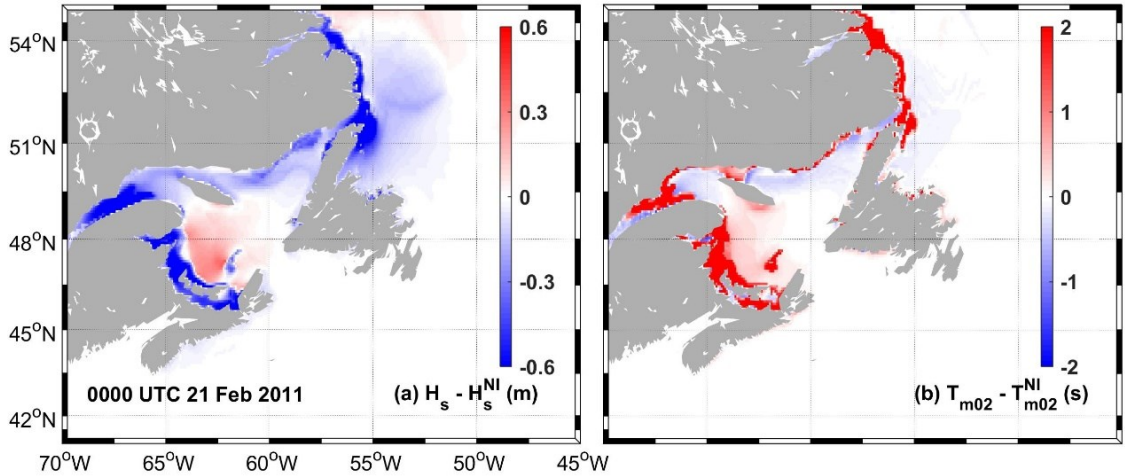
Figure 2.21: Differences in (a) SWHs (H_s) and (b) MWPs (T_{m02}) between model results with ice and without ice at 0000 UTC 21 February 2011.
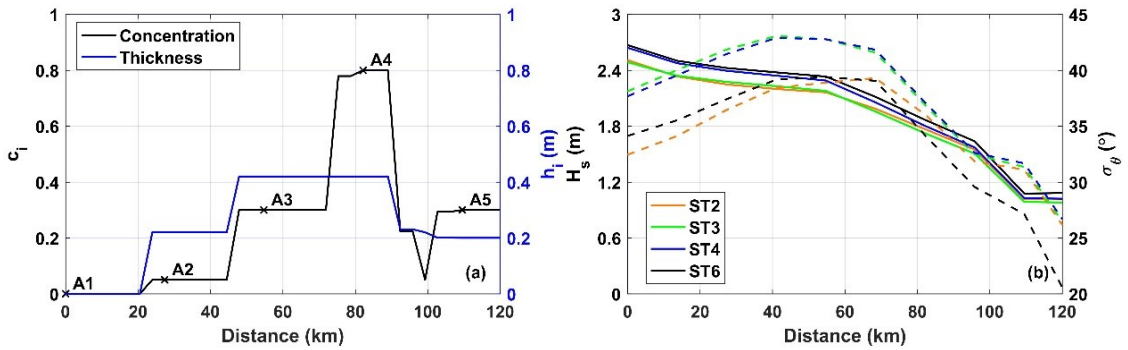
Figure 2.22: The (a) ice concentration and ice thickness, (b) SWHs (solid line) and wave directional spreads (dashed line) along the transect of 52°N (A1-A5, see Figure 2.4) at 0000 UTC 21 February 2011. The horizontal axis represents the distance to location A1 (54°W, 52°N).
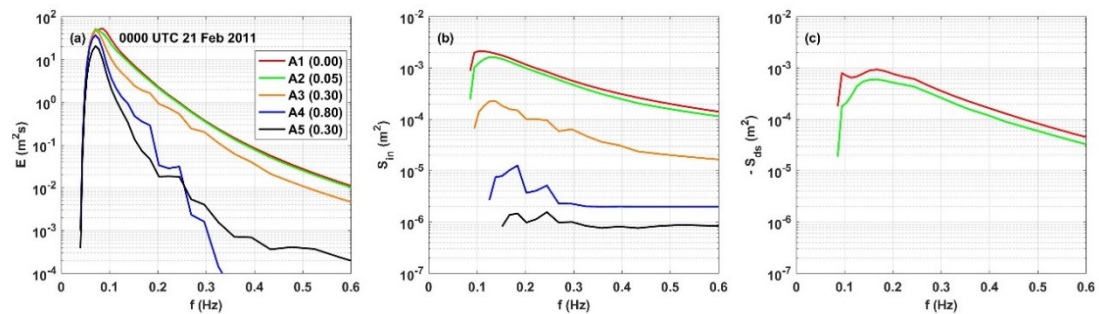
Figure 2.23: (a) Wave spectra and source terms for the (b) wind input and (c) wave dissipation predicted by ST4 at locations A1-A5 (Fig. 2.4) at 0000 UTC 21 February 2011 during the winter-storm period. The ice concentrations at A1-A5 are shown in brackets.

2.6 Conclusions

New parameterizations for the wind input and wave dissipation were incorporated in numerical models for ocean surface waves in recent years. Limited studies were, however, carried out on their performances in the presence of strong ocean currents and sea ice. In this study, the performances of different parameterizations for the wind input and wave dissipation in spectral wave models were assessed under dynamically complicated conditions with the presence of strong currents and sea ice over the NWA. The third-generation spectral wave model WW3 was used to evaluate four different source term packages (known as ST2, ST3, ST4, and ST6) for the wind input and wave dissipation. The observational data used in this study included satellite altimeter measurements from the GlobWave project, scatterometer measurements from RSS, and buoy measurements from NDBC, NERACOOS, SIO, ECCC, and SAA. Wave model results during the winter-storm period in February and the hurricane period associated with Hurricane Ophelia in September/October 2011 over the NWA were compared with available measurements. The wind fields extracted from CFSv2 and the ocean surface currents and elevations produced by HYCOM were used in wave simulations. A parametric vortex based on *Hu et al.* (2012) was inserted into the CFSv2 wind fields to improve the representation of hurricane winds. Ice concentration, ice thickness, and floe size from the CIS were used in wave simulations during the winter-storm period. The performances of ST2, ST3, ST4, and ST6 were assessed by examining the SWH (H_s), mean wave period (T_{m02}), wave spectrum, wind input, and wave dissipation. The model performances under different sea states, variations of drag coefficient from low to high wind speeds, and effects of currents and ice on waves were also investigated. The main findings can be summarized as follows:

(i)   Overall, ST4 and ST6 perform best in representing SWHs with the average SI lower than 19.0% in the presence of strong currents and sea ice under extreme weather conditions over the NWA. As for MWPs, all four packages have negative biases as a result of the underestimate of peak wave energy and the shifting of wave energy to high frequencies.

(ii) Package ST2 consistently underestimates the sea state because of insufficient wind input. Package ST3 amplifies the growth of wind waves in the presence of swells because

of excessive wind input. Package ST6 has stronger wind input and wave dissipation at high frequencies and yields faster wave growth for wind waves compared with ST2, ST3, and ST4.

(iii) The performances of ST2, ST3, ST4, and ST6 differ under different sea states. Under wind-wave-dominated sea states, ST6 generally overestimates H_s because of the strong wind input and fast wave growth; ST4 predicts smaller H_s than ST6 and has negative biases of H_s. However, ST4 could predict a larger H_s than ST6 under the most energetic sea states because of the large drag coefficients at high winds in ST4 and the rapid saturation of wind input in ST6. Under swell-dominated sea states, ST6 generally underestimates H_s because of the low drag coefficient and strong swell dissipation and ST4 generally overestimates H_s.

(iv) The drag coefficient at the sea surface decreases with the wind speed up to ~6 m/s then increases with the wind speed until it levels off or decreases at ~33 m/s. The enhanced drag coefficient at low winds is not captured by any of the four packages (ST2, ST3, ST4, and ST6).

(v) The linear kinematic effects of currents on waves can cause the redistribution of wave energy in the spatial and frequency domains and have significant nonlinear dynamic consequences including the modulation of wave dissipation and nonlinear wave interactions. The linear kinematic current effects on waves are similar in all four packages (ST2, ST3, ST4, and ST6). However, the intensity of the nonlinear dynamic effects can be different.

(vi) Wave scattering is the dominant process in the MIZ when floe sizes are comparable to the wavelength. Wave scattering increases the wave directional spread and may cause an increase in the SWHs. In the presence of ice, the wind input and wave dissipation are reduced as a result of scaling by the open water fraction. Moreover, wind input is shifted to higher frequencies and wave dissipation is suppressed.

CHAPTER 3

PERFORMANCES OF VISCOELASTIC MODELS FOR OCEAN WAVE DISSIPATION IN ICE-COVERED REGIONS[1]

3.1 Introduction

Ocean surface waves can penetrate great distances into the ice-covered regions, depending on the incident wave properties and ice conditions (e.g., *Meylan et al.,* 2014; *Kohout et al.,* 2014). Over the region between the open water and interior ice pack, which is referred to as the marginal ice zone (MIZ), the sea ice cover is inhomogeneous and highly dynamic. Several different types of ice appear in the MIZ, such as grease ice, pancake ice and continuous ice sheet. Intense wave-ice interactions occur over the MIZ with significant attenuation of wave energy. Ocean waves contribute to the ice breakage and affect the extent of the MIZ and floe size distribution (*Collins et al.,* 2015). Previous studies demonstrated that ocean surface waves can accelerate the ice retreat in the Arctic and Antarctic (e.g., *Stopa et al.,* 2016a; *Liu et al.,* 2016; *Kohout et al.,* 2014; *Ardhuin et al.,* 2018). The ice retreat, in turn, allows more energetic waves generated over the larger expanse of open water (*Thomson and Rogers,* 2014). Reliable predictions of wave propagations in ice are thus important for understanding surface wave and ice dynamics at high latitudes and assessing the climate change (*Squire,* 2020).

Wave energy attenuation in the MIZ results from the conservative scattering and non-conservative dissipation. Wave scattering redistributes wave energy in different directions, which results in the apparent decay of wave energy along the propagation direction. Wave

---

[1]Lin, S., Sheng, J., and Xing, J. (2021). A comparative study of viscoelastic models for ocean wave dissipation in ice-covered regions of the eastern Canadian shelf. *Cont. Shelf Res.* (in press).

measurements made by *Wadhams et al.* (1988) exhibited that wave scattering occurring at floe edges is the dominant mechanism for wave attenuation in the MIZ. However, wave scattering is only effective when floe sizes are comparable to wavelengths (e.g., *Bennetts and Squire,* 2012; *Ardhuin et al.,* 2016; *Boutin et al.,* 2018). *Ardhuin et al.* (2016) showed that wave scattering broadens the wave spectra but plays a negligible role in the attenuation of swells. *Boutin et al.* (2018) investigated the floe size effect on wave-ice interactions and showed that wave scattering is only effective to attenuate wave energy at short periods in the MIZ.

The non-conservative wave dissipation in ice includes a number of complex physical processes, such as wave breaking, turbulence, ice floe collisions, ice breakup and drifting (*Squire,* 2020). A wave dissipation rate (α) is commonly used to represent the exponential decay of wave energy due to all non-conservative dissipation processes in ice (*Rogers et al.,* 2016). The wave dissipation rate can be parameterized as empirical functions of wave and ice characteristics based on field measurements (e.g., *Wadhams et al.,* 1988; *Doble et al.,* 2015). Measurements of surface waves over the MIZs in the Arctic (e.g., *Wadhams et al.,* 1988; *Thomson et al.,* 2018) and Antarctic (e.g., *Meylan et al.,* 2014; *Doble et al.,* 2015) demonstrated that waves at higher frequencies are more rapidly dissipated in ice.

Mathematically, the propagation and dissipation of ocean surface waves in ice can be expressed using a complex wavenumber (k). The real part (k_r) of the wavenumber represents the change in wavelengths and propagation speeds, describing the effects of ice in ocean waves analogous to shoaling and refraction by bathymetry. The imaginary part (k_i) represents the exponential decay of wave amplitude (*Meylan et al.,* 2018). Since the wave energy density is proportional to the square of the wave amplitude, the wave energy dissipation rate is twice the amplitude dissipation ($\alpha = 2k_i$). Thus, the wave dissipation rate (α) can also be calculated by solving the dispersion relations of different theories for wave propagations in ice (e.g., *Zhao et al.,* 2015; *Collins et al.,* 2017).

Three general types of models were developed in the past for wave propagations in ice: (a) the mass loading model, (b) thin elastic plate model and (c) viscous layer model (e.g., *Weitz and Keller,* 1950; *Fox and Squire,* 1994; *Keller,* 1998). The effects of ice are included in

the mass loading model by adding the ice mass at the ice-ocean interface (*Weitz and Keller,* 1950). The thin elastic plate model assumes that the ice cover is a homogenous semi-infinite elastic plate (*Wadhams,* 1973; *Fox and Squire,* 1994). The original thin elastic plate model was later extended to include the wave dissipation by considering the water under the ice as a viscous fluid (*Liu and Mollo-Christensen,* 1988). The viscous layer model considers the ice as a layer of viscous fluid overlying an inviscid water body (*Weber,* 1987; *Keller,* 1998).

The mass loading model can be used in the disconnected pancake ice region where the elastic response of ice is negligible. The thin elastic plate model is applicable for a continuous ice sheet (*Zhao et al.,* 2015; *Collins et al.,* 2017). The viscous layer model was found to reproduce reasonably well the laboratory measurements of wave attenuation and dispersion in the grease ice, due to the fact that the dominant effect from the grease ice is viscous damping (*Newyear and Martin,* 1997). The three individual models mentioned above, however, may not be able to describe propagations of surface waves into different types of ice covers (*Zhao et al.,* 2015). Motivated by this need, *Wang and Shen* (2010) proposed a viscoelastic layer model by incorporating the elasticity of ice into the viscous model of *Keller* (1998) to describe propagations of waves into various types of ice covers. The model developed by *Wang and Shen* (2010) was shown to converge to above-mentioned three models under proper limiting conditions. More recently, *Mosig et al.* (2015) suggested an alternative viscoelastic model by introducing viscosity into the thin elastic plate model of *Fox and Squire* (1994). Both of these two viscoelastic theories attribute the wave dissipation entirely to the ice cover and show the dependence of dissipation rates on the ice thickness and wave frequency.

The viscoelastic models are used in this study since they are physically more applicable in different ice conditions than other models. The viscoelastic models have been shown to reasonably simulate wave propagations in ice in comparison with the field measurements taken in the Arctic and Antarctic (e.g., *Li et al.,* 2015; *Rogers et al.,* 2016; *Cheng et al.,* 2017; *Liu et al.,* 2020a; *Liu et al.,* 2020b). However, the viscoelastic models still cannot fully represent the complexity of wave propagations in the MIZ. The complexity of various physical processes for wave dissipation in ice hampers our understandings on wave

propagations in the MIZ. The lack of good knowledge about these physical processes means that all the existing theories for wave propagations in the MIZ are hypothetical and require more studies on their applicability. Furthermore, the ice rheological parameters (kinetic viscosity v and elasticity G) in the viscoelastic models have large uncertainties and their determination is still a great challenge (*Cheng et al.,* 2017). The large uncertainties in the ice field can also be a primary limitation on the accuracy of surface wave hindcasts in ice (*Rogers et al.,* 2018).

The main objective of this chapter is to examine propagations of surface waves in the ice-covered regions over the eastern Canadian shelf (ECS) using a nested-grid ocean surface wave model. The ECS considered here covers the coastal and continental shelf waters from the Labrador Sea in the north to the Scotian Shelf in the south. The ECS is seasonally affected by sea ice. It has been a great challenge to accurately predict surface waves in ice over this region. The representation of waves in ice over the ECS in previous studies was crude and far from satisfactory. *Ruest et al.* (2016) examined the wave climate over the Gulf of St. Lawrence. They applied a coarse post-processing method to the wave model results using a linear dissipation on the ice concentration to account for wave attenuation in ice. In several other studies on the wave climate over the ECS (e.g., *Guo and Sheng,* 2015; *Guo and Sheng,* 2017; *Wang et al.,* 2018), wave energy in ice was partially blocked according to ice concentrations in wave hindcasts and forecasts. These treatments of surface waves in ice can have large predictive errors for wave model results in ice, as shown in previous wave hindcasts in the Arctic and Antarctic (e.g., *Li et al.,* 2015; *Li et al.,* 2019; *Rogers et al.,* 2018). Until recently, *Lin et al.* (2020, Chapter 2) considered the processes of wave dissipation and scattering in ice. *Lin et al.* (2020, Chapter 2) showed the effects of ice on wave propagations by considering the wave attenuation rate α to be a step function of wave frequency based on the measurements of *Rogers et al.* (2016; known as IC4M6).

The second objective of this chapter is to assess the performances of two viscoelastic models in parameterizing the wave dissipation process in ice (*Wang and Shen,* 2010; *Mosig et al.,* 2015). For this objective, surface waves over the ECS are simulated during a winter storm in later March 2014. The values of key rheological parameters (v and G) in the two viscoelastic models are determined by comparing the simulated significant wave heights

(SWHs) with observations from buoys and altimeters. It should be noted that the viscoelastic models were applied for the regions with pancake ice or frazil slurries in many previous studies (e.g., *Li et al.,* 2015; *Rogers et al.,* 2016; *Cheng et al.,* 2017; *Liu et al.,* 2020b), with neglection of wave scattering. Wave scattering is included here in order to investigate the role of wave scattering in wave propagations in the ice-covered regions of the ECS.

This chapter is structured as follows. Section 3.2 introduces the methodology used in this study. Section 3.3 presents the validations of the nested-grid wave model for the ECS. Section 3.4 presents the surface waves over the ECS simulated by the nested-grid wave model using two different viscoelastic models for wave dissipation in ice. Section 3.5 discusses the challenge for numerical simulations of waves in ice. Section 3.6 is the conclusions.

3.2 Methodology

A nested-grid wave model based on WAVEWATCH III (WW3) is used in this study to determine the applicability of two viscoelastic models and examine wave propagations in ice over the ECS. The spectral wave model and parameterizations of wave dissipation in ice are introduced in Section 3.2.1. Wave model setup and model forcing are presented in Sections 3.2.2 and 3.2.3, respectively. The available observational data from satellite altimeters and in-situ buoys are introduced in Section 3.2.4. To investigate the dependences of wave dissipation rate on ice and wave properties, a one-dimensional (1D) idealized case is carried out and analyses of model results in this case are presented in Appendix C.

3.2.1   Spectral Wave Model and Wave Dissipation in Ice

The surface wave model used here is the third-generation spectral wave model WW3 (version 6.07, *WW3DG*, 2019), which is similar to that used in Chapter 2. There are several different schemes in WW3 to estimate wave dissipation in ice (S_{ice}) based on different theories or empirical functions. In this study, we assess two viscoelastic ice layer models for S_{ice} as mentioned in the introduction, namely (i) the viscoelastic fluid model of *Wang and Shen* (2010, hereafter referred as IC3) and (ii) the viscoelastic beam model suggested

by *Mosig et al.* (2015, hereafter referred as IC5). The key parameter to estimate S_{ice} is the wave dissipation rate α, which can be obtained by solving the wave dispersion relation. The wave dispersion relation for these two models is given as:

$$\sigma^2 = gkQtanh(kd) \tag{3.1}$$

where g is the gravitational acceleration of the Earth, d is the water depth, and Q is the coefficient accounting for the modification of dispersion relation due to the presence of ice.

The coefficient Q in Eq. 3.1 depends on the ice and wave properties but it takes different functions for these two models (*Wang and Shen,* 2010; *Mosig et al.,* 2015). For the IC3 model,

$$Q = 1 + \frac{\rho_i}{\rho_w} \frac{(g^2k^2 - N_1^4 - 16k^6a^2v_e^4)S_kS_a - 8k^3av_e^2N_1^2(C_kC_a - 1)}{gk(4k^3av_e^2S_kC_a + N_1^2S_aC_k - gkS_kS_a)} \tag{3.2}$$

and for the IC5 model,

$$Q = 1 + \frac{G_eh_i^3}{6\rho_wg}(1 + r_v)k^4 - \frac{\rho_ih_i\sigma^2}{\rho_wg} \tag{3.3}$$

where ρ_i and ρ_w are the densities of ice and water, respectively, h_i is the ice thickness, $v_e = v + iG/\rho_i\sigma$ is the complex equivalent kinematic viscosity, $G_e = G - iv\rho_i\sigma$ is the complex equivalent elasticity, $r_v = 0.3$ is the Poisson ratio of sea ice, $N_1 = \sigma + 2ik^2v_e$, $a^2 = k^2 - i\sigma/v_e$, $S_k = sinh\,(kh_i)$, $S_a = sinh\,(ah_i)$, $C_k = cosh\,(kh_i)$, and $C_a = cosh\,(ah_i)$. The dispersion relations in Eqs. 3.2 and 3.3 converge to the open water case ($Q = 1$) when the ice thickness vanishes. The wave dissipation rate in ice thus depends on the ice and wave properties:

$$\alpha \sim (v, G, h_i, f) \tag{3.4}$$

where f is the wave frequency, v and G are the kinematic viscosity and elasticity of the ice layer, respectively.

3.2.2   Wave Model Setup

A two-level nested-grid wave model is used for simulating ocean surface waves over the ECS integrating for March 2014. The outer model domain covers the region of 85°W-0° and 10°N-65°N, with a horizontal resolution of 1/4°. The inner model domain covers the ECS of 80°W-40°W and 34°N-55°N with a horizontal resolution of 1/12° (Fig. 3.1). Model results produced by the outer model are used to specify the open boundary conditions for

the inner model. The outer model domain is sufficiently large such that the swell energy propagating into the inner model domain is reasonably well simulated by the outer model. The wave model is initialized from 1 March and has a spin-up time of about three weeks. The inner model results during the winter storm period between 20 and 30 March 2014 are used in the following analyses.
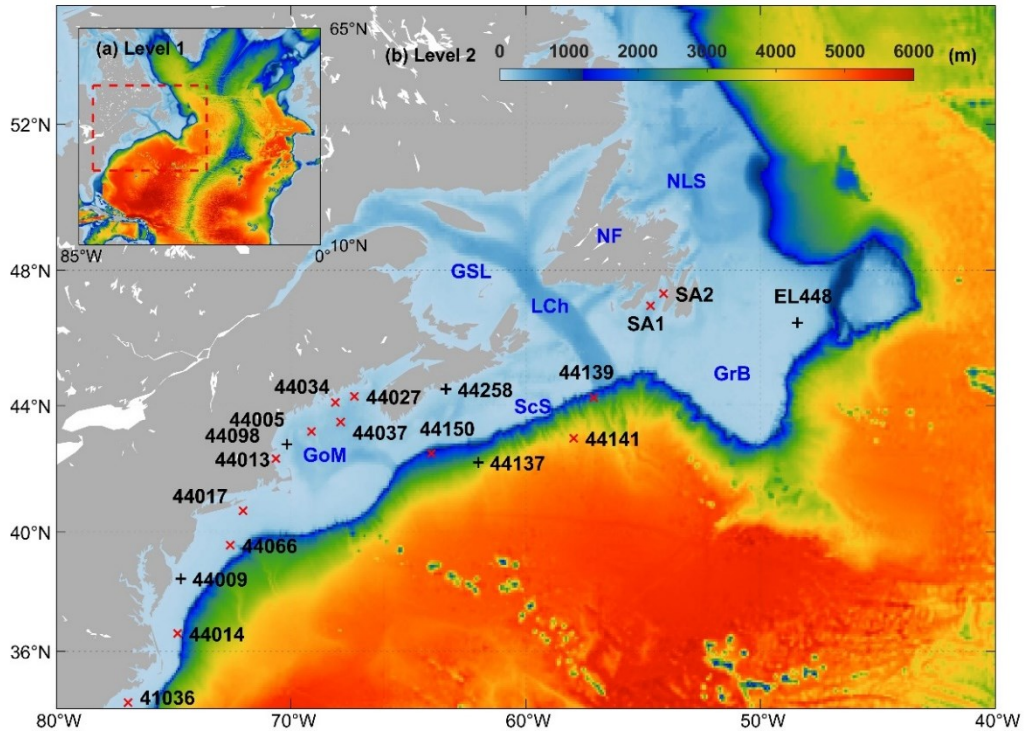
Figure 3.1: Domains and major topographic features of (a) the outer model for the north Atlantic and (b) the inner model for the northwest Atlantic. Black plus symbols denote buoy stations with wave observations. Red cross symbols denote buoy stations with wind and wave observations. Abbreviations are used for the Newfoundland and Labrador Shelves (NLS), Gulf of St. Lawrence (GSL), Laurentian Channel (LCh), Newfoundland (NF), Grand Banks (GrB), Scotian Shelf (ScS), and Gulf of Maine (GoM).

The model integrations are carried out in spherical coordinates with the discrete spectrum consisting of 36 directions ($\Delta\theta = 10°$) and 31 frequencies ranging from 0.04 to 0.70 Hz at a logarithmic increment of 0.1. The source term package known as ST6 (*WW3DG,* 2019) is used for the wind input and wave dissipation (*Lin et al.,* 2020). The nonlinear wave interactions (S_{nl}) are computed using the Discrete Interaction Approximation (DIA) of *Hasselmann et al.* (1985). Wave scattering in ice is parameterized using the floe-size dependent approach suggested by *Meylan and Masson* (2006, known as IS2), using the

scattering coefficient suggested by *Bennetts and Squire* (2012). Wave dissipation in ice can be parameterized based on two viscoelastic ice layer models (IC3/5) as introduced in Section 3.2.1. The values of two key rheological parameters (v and G) in IC3/5 determined previously have large uncertainties (*Cheng et al.,* 2017). Therefore, sensitivity studies are carried out in this study to determine their optimal values for wave propagations in ice over the ECS.

3.2.3 Model Forcing

The wave model is forced by hourly wind fields (U_{10}) extracted from the Climate Forecast System reanalysis dataset (CFSv2, Saha et al., 2014). The accuracy of the wind forcing over the study region will be validated in Section 3.3. Ocean surface currents and elevations extracted from the 3-hourly ocean circulation reanalysis dataset based on the Hybrid Coordinate Ocean Model (HYCOM; *Cummings and Smedstad,* 2013) are used in the wave model to account for the effects of ocean currents on waves. Previous studies demonstrated that the HYCOM dataset represents reasonably well the surface currents over the northwest Atlantic (e.g., *Chi et al.,* 2018) and has the advantage of an eddy-resolving horizontal resolution of 1/12°.

Accurate ice information is needed for reliable simulations of surface waves in ice, particularly over the MIZ. The daily ice data from the Canadian Ice Service digital archive (CISDA) are used in the wave simulations over the ECS. The CISDA is a unique and reliable dataset constructed integrating data from a variety of sources, including satellite remote sensing data, and ship and aircraft-based visual observations (*Galley et al.,* 2016). The CISDA provides the total and partial information for the ice concentrations, ice types and development stages using the World Meteorological Organization's egg code. The ice types and development stages can be interpreted as measurements of the ice floe size and thickness. More detailed information about the CISDA and associated uncertainties can be found in *CIS* (2005) and *Tivy et al.* (2011). In comparison with other sea ice products, overall, the CISDA provides the best estimations of ice conditions over the ECS (*Tivy et al.,* 2011), which will be discussed in Section 3.5. The viscoelastic models for wave dissipation require the input of the ice concentration and thickness, and the wave scattering

model requires the input of the maximum floe size. The digital daily ice data for the Gulf of St. Lawrence (GSL) and Newfoundland and Labrador Shelves (NLS) are gridded into a spatial resolution of 1/40° and combined together to provide the total ice concentration (c_i), weighted mean ice thickness (h_i), and maximum floe size (D_{max}) for the ECS.
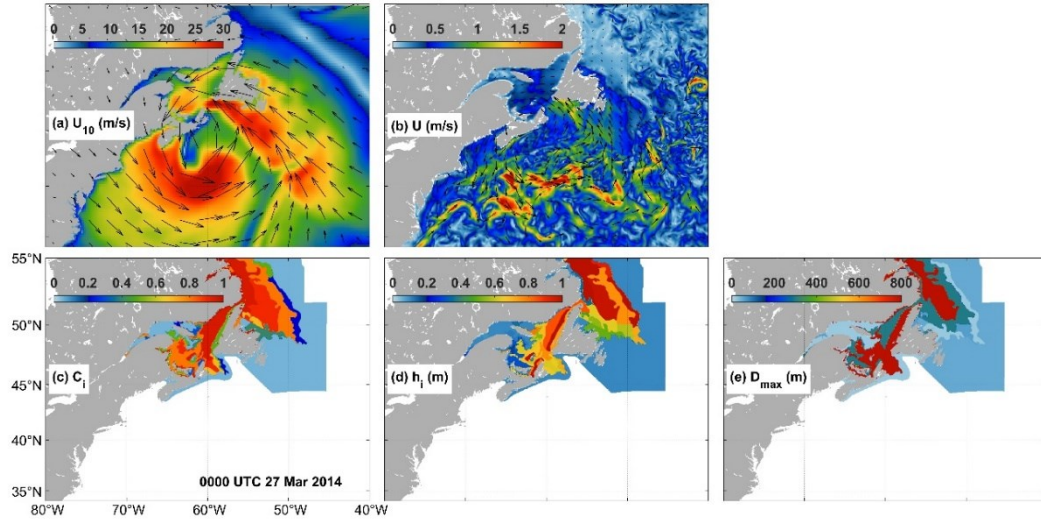
Figure 3.2: Distributions of (a) wind fields (U_{10}) from the CFSv2, (b) ocean surface currents (U) from the HYCOM, and (c) total ice concentrations, (d) mean ice thicknesses and (e) maximum floe sizes from the CISDA at 0000 UTC 27 March 2014. Arrows and colour image in (a) and (b) represent the wind vectors and ocean surface current vectors and associated magnitudes, respectively.

Figure 3.2 presents the wind fields, surface currents and the total ice concentration, mean ice thickness and maximum floe size at 0000 UTC 27 March 2014 during the winter storm in March 2014 (known as March 2014 Nor'easter). This Nor'easter was the most powerful winter storm during the North American winter storm season in 2013-2014. The March 2014 Nor'easter emerged off the southeast US coast on 25 March and began to undergo explosive intensification late that day. The winter storm then moved toward the northeast and had a peak sustained wind speed of about 39.7 m/s before it made landfall on Nova Scotia on 27 March (Fig. 3.2a). This large-scale winter storm resulted in large surface waves over the ECS as expected. The surface waves were affected by strong surface currents and sea ice in the region. The wind-driven surface currents and the Gulf Stream were up to 2.5 m/s during the storm period (Fig. 3.2b). Sea ice in late March 2014 mostly occurred in the GSL and NLS. Over a large portion of the eastern and southeastern

Newfoundland waters, sea ice had low concentrations less than 0.1 during this period (Fig. 3.2c). The mean ice thicknesses at this time were generally less than one meter (Fig. 3.2d). The ice floe sizes at this time varied significantly from dozens to hundreds meters (Fig. 3.2d). Small ice floes with sizes of several dozen meters mostly spread around the areas with ice concentrations of about 0.15. Over areas with higher ice concentrations, there were mostly medium and big floes with sizes of several hundred meters. The sea ice conditions over the ECS at other times in March 2014 had some temporal and spatial variabilities but with large-scale patterns similar to those shown in Fig. 3.2.

3.2.4   Wind and Wave Observations

The observational wind and wave data used in this study include remote sensing measurements from satellite altimeters and in-situ observations from buoys. These observational data are used here to assess the accuracy of wind forcing and wave model results. The altimeter data were extracted from the database constructed by the GlobWave project using data from nine satellite missions (*GlobWave Product User Guide,* 2013, www.globwave.org). The measured SWHs (H_s) and wind speeds (U_{10}) inferred from satellite data were calibrated using in-situ buoy measurements and have satisfactory accuracy with typical errors less than 5% (*Gavrikov et al.,* 2016). The calibrated H_s and U_{10} have reduced discrepancies between measurements from different satellite missions and provide additional quality flags (good, acceptable and bad measurements) and estimated errors.

Although the GlobWave data have been extensively used in the past for validations of surface wave model results and the studies of wave and wind climates (e.g., *Shanas et al.,* 2017; *Young and Ribal,* 2019; *Stopa et al.,* 2019), the altimeter measurements in the partially ice-covered areas should be used with caution. Several previous studies (e.g., *Kudryavtseva and Soomere,* 2016; *Tuomi et al.,* 2019) demonstrated that the altimeter data have good agreement with in-situ data over the areas with ice concentrations less than 0.3. To ensure the quality of altimeter data, similar to the criteria used in *Young et al.* (2017), we use the following four quality control criteria in this study for the calibrated U_{10} and H_s: (i) the data with bad quality are excluded, (ii) the data with ice concentrations larger

than 0.3 are excluded, (iii) the ratio of the standard deviation to the mean value should be less than 20%, and (iv) the data should be over open waters more than 50 km offshore.

The in-situ wind and wave observations at 19 buoy stations within the model domain (Fig. 3.1) were obtained from the National Data Buoy Center (NDBC), Environment and Climate Change Canada (ECCC), and SmartAtlantic Alliance (SAA). The SWHs and peak wave periods (PWPs) were measured at all buoys. The observed wind speeds and directions were made only at 14 buoy stations indicated by the red cross symbols in Fig. 3.1.

3.3 Model Validations

3.3.1   Wind Forcing

The performance of spectral wave models is affected by the accuracy of the wind forcing (*Cavaleri*, 2009). In this session, the accuracy of wind fields is assessed by comparing the wind fields with observations from altimeters and buoys (Fig. 3.3). We use four statistical error metrics for the assessment (see definitions in Appendix A), which include the root mean square error (RMSE), relative bias (RB), scatter index (SI), and correlation coefficient (R). These four metrics are widely used in previous studies (e.g., *Lin and Sheng,* 2017; *Lin and Sheng,* 2020).
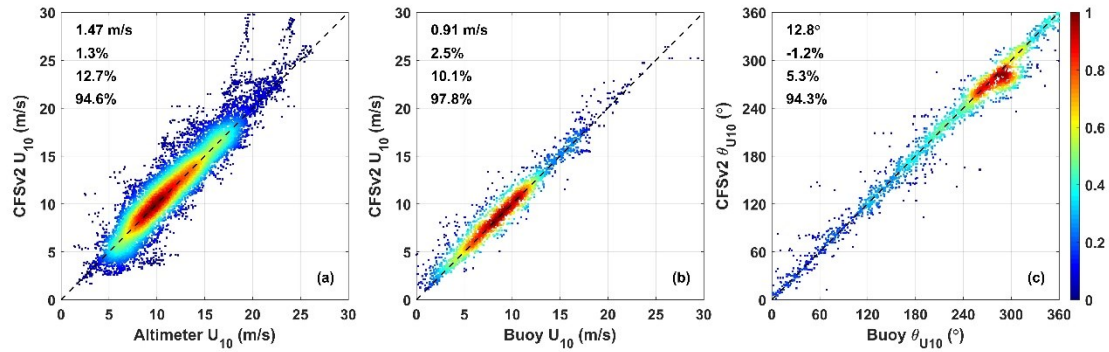
Figure 3.3: Scatter plots for wind speeds (U_{10}) between the CFSv2 and observed values from (a) satellite altimeters and (b) buoy stations, and (c) for the wind directions between the CFSv2 and observed values from buoy stations during 20-30 March 2014. Colors represent the density of data points. Values of four error metrics (RMSE, RB, SI and R from top to bottom) are also shown in each panel.

During 20-30 March 2014, the CFSv2 wind speeds agree well with the wind measurements from altimeters, with a RMSE of ~1.47 m/s and a SI of ~12.7% (Fig. 3.3a). In comparison

with the buoy observations, the CFSv2 wind speeds have a RMSE of ~0.91 m/s and a SI of ~10.1% (Fig. 3.3b). The wind directions from the CFSv2 agree well with the buoy observations with a SI of ~5.3% (Fig. 3.3c). Overall, the CFSv2 winds agree well with the observations in terms of both the wind speeds and directions.

3.3.2   Significant Wave Height

Figure 3.4 presents the observed SWHs inferred from satellite altimeters (Fig. 3.4a) and differences between model results and observed values (Fig. 3.4b) along different satellite tracks during 20-30 March 2014. Before the March 2014 Nor'easter, the observed sea states were generally calm and affected mainly by swells over the study region. During the passage of this winter storm, large wind waves were generated by the large-scale strong winds with the SWHs up to 14.5 m. The inner wave model reproduces reasonably well the observed SWHs, with some underestimations of large waves. On average, the simulated SWHs are highly correlated with the observed values and have small errors with an average RB of ~-3.3% and an average SI of ~11.5% (Fig. 3.4b). The model errors can partially be attributed to the wind biases and the parameterization for the wind input and wave dissipation (*Lin and Sheng,* 2020).

Figure 3.5 presents time series of simulated and observed SWHs at 12 buoy stations during 20-30 March 2014. Before the passage of the March 2014 Nor'easter, the observed sea states at these buoy stations were under calm conditions with SWHs less than 4 m. During the storm, the observed SWHs were large and up to 6 m near the eastern US coast (Figs. 3.5a-3.5c). In the Gulf of Maine (GoM), the observed SWHs had a peak value around 7 m (Figs. 3.5d-3.5f). Over the Scotian Shelf (ScS) region, sea states were energetic with the observed SWHs up to 16 m (Figs. 3.5g-3.5j). The observed SWHs near the Grand Banks (GrB) (Fig. 3.5k) and the coast of southern Newfoundland (Fig. 3.5l) were also large, with peak values around 9 m. The comparisons of simulated and observed SWHs demonstrate that the inner wave model reproduces reasonably well the observed temporal and spatial variability of the SWHs during the winter storm. Overall, the simulated SWHs at all 19 buoy stations have a high correlation coefficient (R = 96.6%) and small errors (RMSE = 0.27 m, SI = 13.2% and RB = -0.9%) in comparison with the observed values. It should

be noted that the peak SWHs observed at some buoys are slightly underestimated, which is mostly due to the negative biases of the wind speeds at high winds (Fig. 3.3b).
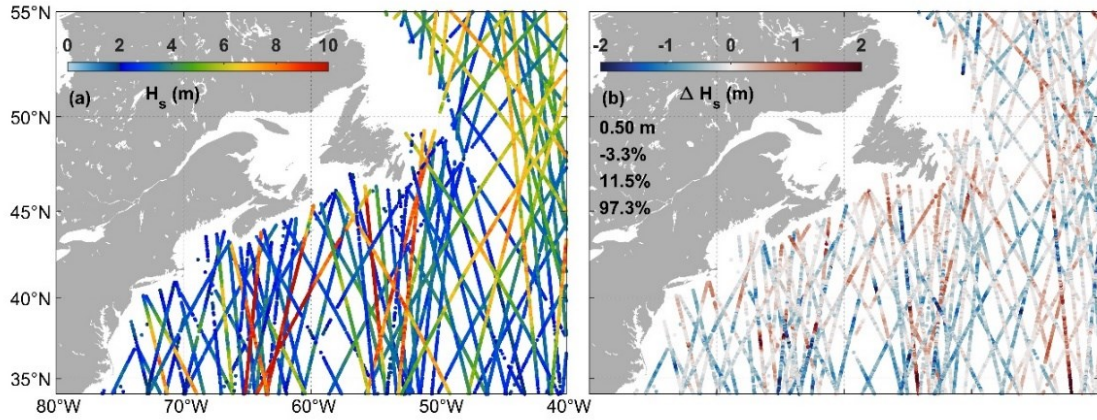
Figure 3.4: (a) Observed SWHs inferred from satellite altimeters and (b) the difference between simulated and observed values along satellite tracks during 20-30 March 2014. Values of four error metrics (RMSE, RB, SI and R) are shown in panel (b).
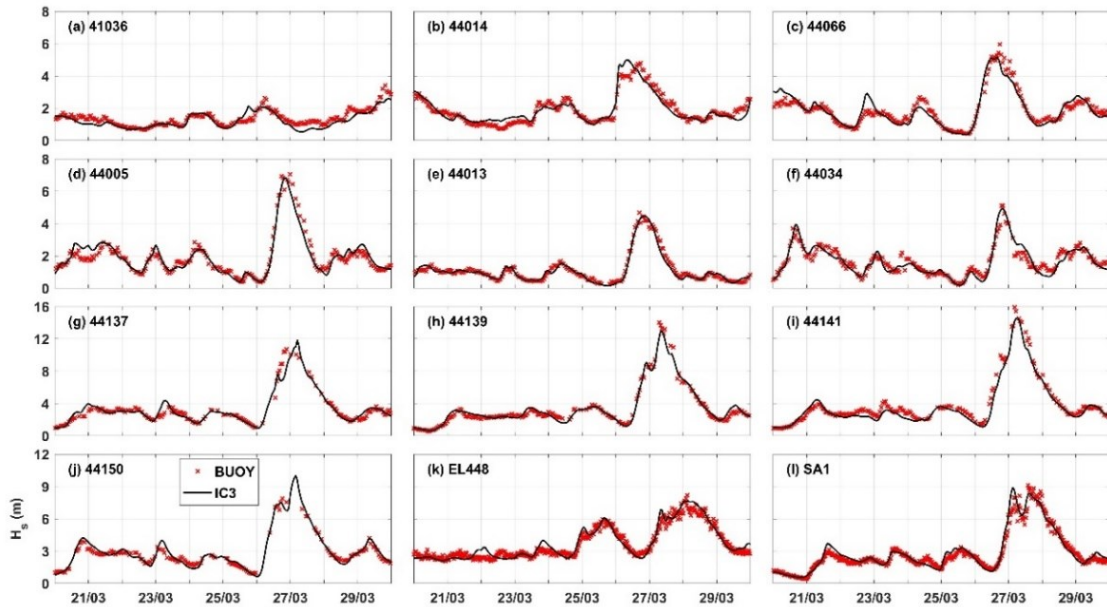
Figure 3.5: Time series of simulated SWHs using IC3 with the optimal parameters against the observed values at 12 buoy stations during 20-30 March 2014. The name of each buoy station is shown in each panel and positions of these buoys are shown in Fig. 3.1.

3.3.3 Peak Wave Period

Figure 3.6 presents time series of simulated and observed peak wave periods (PWPs) at 12 buoy stations during 20-30 March 2014. The observed sea states near the eastern US coast

were dominated by swells with long PWPs and low SWHs (Figs. 3.6a-3.6c) before 23 March. Large waves with long PWPs were generated by the winter storm over the GoM (Figs. 3.6d-3.6f), ScS (Figs. 3.6g-3.6i) and GrB (Figs. 3.6j-3.6l) after 26 March. The observed temporal and spatial variations of PWPs are well simulated by the inner wave model, except for some model deficiencies in simulating occasional shift of observed PWPs to higher or lower values (e.g., Figs. 3.6e-3.6f). The observed shift of PWPs is likely due to the variations of the swell peak and wind wave peak for the bimodal wave spectra. Statistically, the simulated PWPs at all 19 buoy stations have an average RMSE of ~1.6 s and an average SI of ~19.9%.
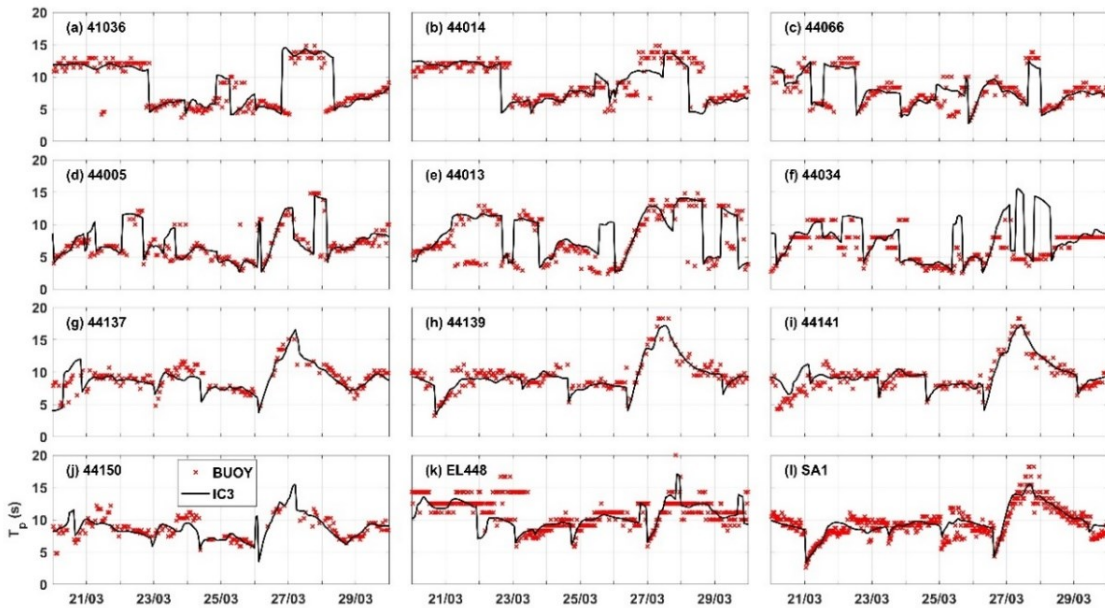
Figure 3.6: As in Fig. 3.5 but for the peak wave periods.

The wave model results presented here are produced using IC3 (the viscoelastic model) with the optimal values of v and G for wave dissipation in ice. The optimal values of v and G will be determined in Section 3.4.1. It should be noted that the choice of different parameterizations for wave dissipation in ice only affects surface waves in and near the ice-covered regions. The pre-condition for reliable predictions of wave propagations in ice is accurate representations of the incident waves in the open waters. Overall, the inner wave model is robust and accurate to predict the SWHs and PWPs in the open waters over the ECS during the March 2014 Nor'easter.

3.4 Results

As mentioned in Section 3.1, the kinetic viscosity (v) and elasticity (G) for the ice layer used in the two viscoelastic models (IC3/5) are two key parameters for wave dissipation in ice, and their determinations remain highly debatable in the community (*Cheng et al.,* 2017). In this section, the calibration and validation processes for v and G are performed. The optimal values of v and G for wave propagations in ice are calibrated in Section 3.4.1 and validated in Section 3.4.2. The important role of wave scattering for wave propagations in ice is examined in Section 3.4.3, based on the model results using IC3 with the calibrated optimal ice rheological parameters.

In the calibration process, the effects of different values of v and G on the wave model results are first examined (Sections 3.4.1.1 and 3.4.1.2). The optimal values of v and G are then determined by requiring the model bias for the simulated SWHs in comparison with observations to be the smallest (Section 3.4.1.3). A series of numerical experiments is carried out using different values of v and G, i.e., $0 \leq G \leq 10^{12} \ Pa$ and $0.002 \leq v \leq 1.4 \ m^2 \ s^{-1}$ for IC3 and $5.0 \times 10^6 \leq G \leq 5.0 \times 10^{12} \ Pa$ and $5.0 \times 10^{-1} \leq v \leq 5.0 \times 10^7 \ m^2 \ s^{-1}$ for IC5. The use of different values of v and G only affects the wave model results in and near the ice-covered regions. Therefore, only the observations in and near the ice-covered regions are used in the following comparisons, including buoy observations at four stations (44258, EL448, SA1 and SA2) and altimeter measurements within 70°W-45°W and 43°N-55°N during 20-30 March. In the validation process, the wave model results using IC3/5 with the calibrated values of v and G in this and previous studies are compared with the observations in terms of the SWHs, PWPs and wave spectra.

3.4.1   Determination of Ice Rheological Parameters

3.4.1.1   Kinetic Viscosity

Figure 3.7a presents distributions of simulated SWHs and mean wave periods (MWPs) over the northwest Atlantic at 1800 UTC 27 March 2014, produced by the inner wave model using IC3 with $v = 0.05 \ m^2 \ s^{-1}$ and $G = 10^5 \ Pa$. The black contour lines in Fig. 3.7 denote the ice edge with a concentration of 0.15. The model results demonstrate that

sea states are energetic with large waves propagating long distances into ice at this time. When waves propagate into ice, wave energy at high frequencies is rapidly decayed. This leads to decreases of SWHs and increases of MWPs along the wave propagation directions into ice. Figures 3.7b-3.7d show the corresponding differences between model results using different values of v ($v = 0.2$, 0.6 and $1.4\ m^2\ s^{-1}$) and model results using $v = 0.05\ m^2\ s^{-1}$ (Fig. 3.7a). Physically, wave dissipation due to the viscosity effect of the ice layer becomes stronger for larger v. Thus, the simulated SWHs (MWPs) using IC3 are lower (higher) for larger v. Large differences in SWHs between different model runs occur mainly near the ice edge, and MWPs have large differences in the inner ice pack.
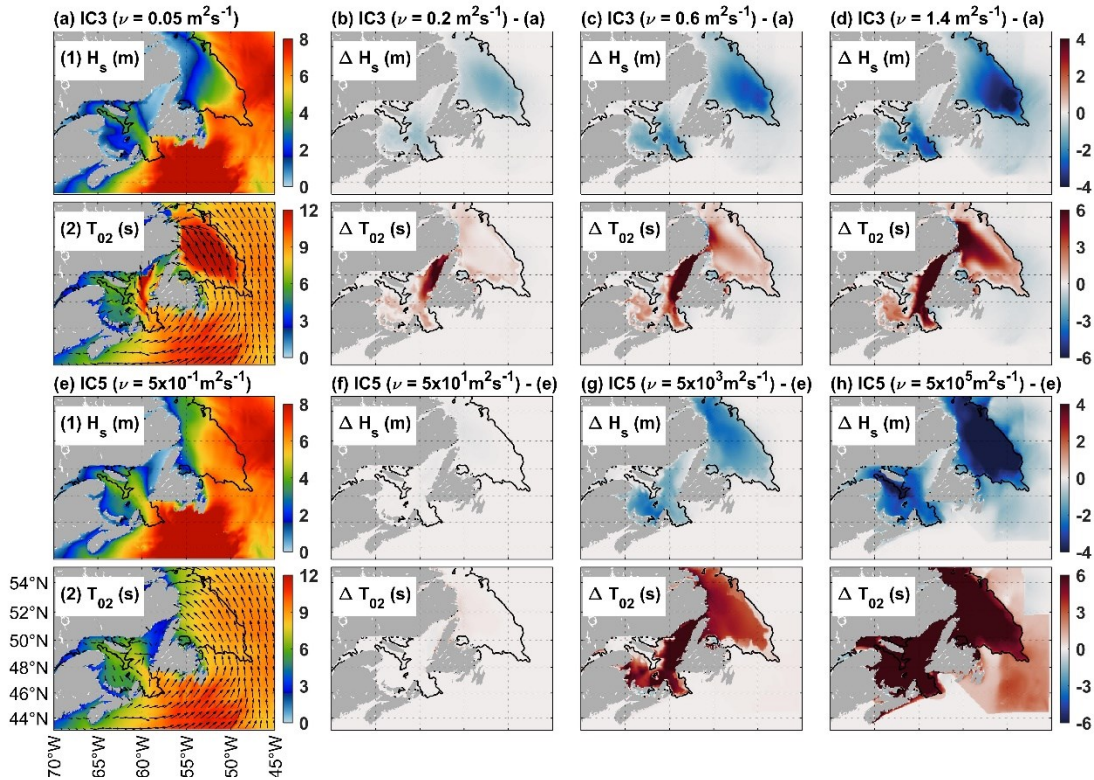
Figure 3.7: Spatial distributions of SWHs (row 1) and MWPs (row 2) at 1800 UTC 27 March 2014 produced by the inner wave model using IC3 (columns a-d) with the same elasticity ($G = 10^5\ Pa$) but different values of kinematic viscosity ($0.05 \leq v \leq 1.4\ m^2 s^{-1}$). Columns e-h show the same results but for IC5 with $G = 5 \times 10^8\ Pa$ and $5 \times 10^{-1} \leq v \leq 5 \times 10^5\ m^2 s^{-1}$. Black contours denote the ice edge ($c_i = 0.15$). Arrows represent mean wave directions with the length showing the MWPs.

The similar conclusion can be made for wave model results using IC5 with $G = 5.0 \times 10^8\ Pa$ and different values of v in the range of $5.0 \times 10^{-1} \leq v \leq 5.0 \times$

$10^5 \ m^2 \ s^{-1}$ (Figs. 3.7e-3.7h). The wave dissipation rates produced by IC5 have small values at low viscosity regimes and then gradually increase with the increasing viscosity values, as shown in Appendix C (Fig. C3a). Thus, wave model results using IC5 with different values of v are basically the same at low viscosity regimes (Figs. 3.7e-3.7f). The simulated SWHs (MWPs) using IC5 become lower (higher) at relatively higher viscosity regimes (Figs. 3.7g-3.7h). It should be noted that wave model results using low values of viscosity ($v \le 50 \ m^2 \ s^{-1}$) are not realistic with large waves persisting in the inner ice pack near the coastal regions of the NLS.

3.4.1.2 Elasticity

We next examine the sensitivity of wave model results to the ice elasticity (G) used in IC3/5. Figure 3.8a presents distributions of SWHs and MWPs over the study region at 1800 UTC 27 March 2014 produced by the inner wave model using IC3 with $v = 0.05 \ m^2 \ s^{-1}$ and $G = 10.0 \ Pa$. Figures 3.8b-3.8d show the corresponding differences between model results using different values of G ($G = 10^3$, 10^5 and $10^{10} \ Pa$) and model results using $G = 10 \ Pa$ (Fig. 3.8a). Wave dissipation due to the ice elasticity arises from the energy storage ability of the flexible ice floes (*Cheng et al.,* 2017). At low elasticity regimes, the wave model using IC3 generates highly similar SWHs and MWPs (Figs. 3.8a-3.8b) as wave dissipation rates have similar values, which is consistent with the analysis in Appendix C (Fig. C3b). Surface waves propagating into ice with higher elasticity generally experience weaker dissipation and thus have higher (lower) SWHs (MWPs), as shown in Figs. 3.8b-3.8d. The use of different values of ice elasticity not only affects the wave dissipation locally but may have nonlinear effects on wave propagations over different regions. For example, the use of higher elasticity leads to lower SWHs in the inner ice pack (Fig. 3.8c). At higher elasticity regimes, wave dissipation is weaker and simulated waves have lower MWPs near the ice edge (Fig. 3.8c). Surface waves with lower MWPs generally have more energy at high frequencies, which can lead to stronger wave dissipation. Wave dissipation in the inner ice pack is thus determined by the balance between both effects.

The wave model results using IC5 with $v = 50.0 \ m^2 \ s^{-1}$ but different values of G are shown in Figs. 3.8e-3.8h. The effect of ice elasticity on wave dissipation in IC5 is similar

to the effect in IC3. As shown in Appendix C (Fig. C3b), the wave dissipation rates predicted by IC5 have similar values at low elasticity regimes and then gradually reduce to slightly lower values at high elasticity regimes. Thus, the simulated SWHs (MWPs) at higher elasticity regimes have higher (lower) values in IC5, although the differences of model results become negligible at high elasticity regimes (Figs. 3.8g-3.8h).
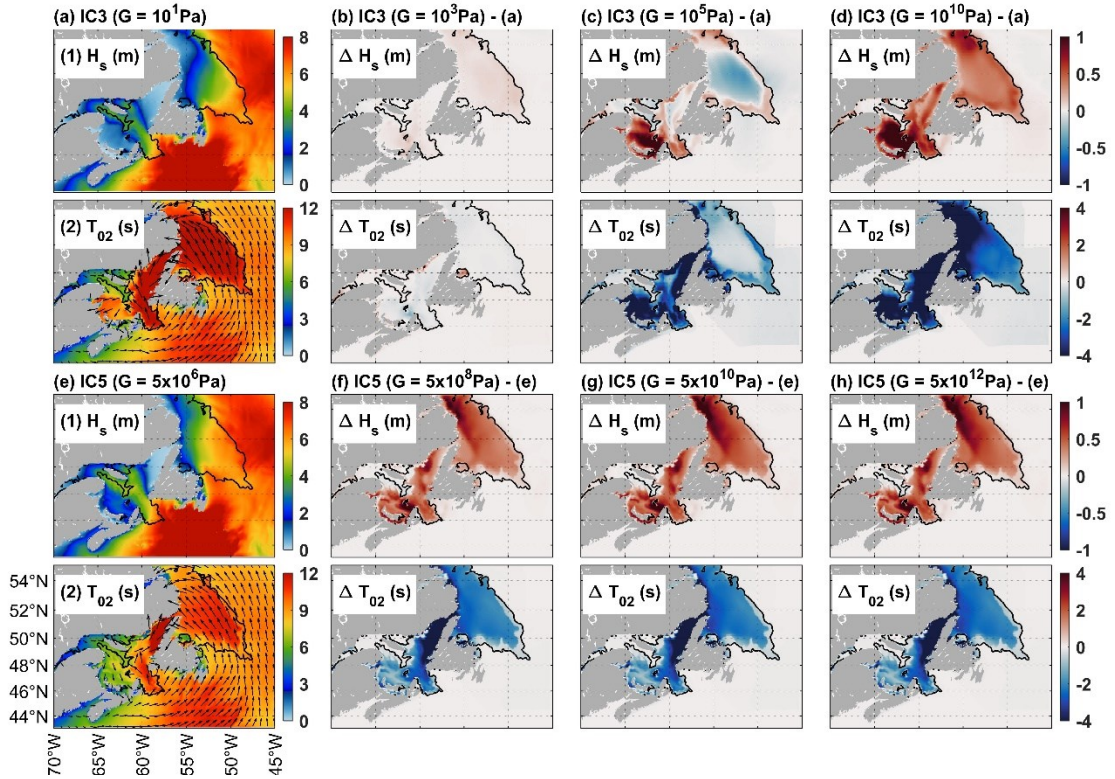
Figure 3.8: Spatial distributions of SWHs (row 1) and MWPs (row 2) at 1800 UTC 27 March 2014 produced by the inner wave model using IC3 (columns a-d) with the same kinematic viscosity ($v = 0.05 \, m^2 s^{-1}$) but different values of elasticity ($10^1 \leq G \leq 10^{12} \, Pa$). Columns e-h show the same results but for IC5 with $v = 50 \, m^2 s^{-1}$ and $5 \times 10^6 \leq G \leq 5 \times 10^{12} \, Pa$.

3.4.1.3 Calibrations of Kinetic Viscosity and Elasticity

In this section, we examine the model errors for simulated SWHs in a series of numerical experiments to calibrate v and G. Figure 3.9 presents values of SI and RB for simulated SWHs as functions of v and G in IC3/5. As shown in Figs. 3.7 and 3.8, the SWHs predicted by IC3/5 generally become lower (higher) with the increasing values of viscosity (elasticity). Therefore, the RB values for SWHs predicted by IC3/5 vary from positive to negative with the increasing viscosity, which is opposite with the increasing elasticity. It

should be noted that the SWHs predicted by IC3/5 are insensitive to the viscosity and thus have similar errors at low viscosity regimes (Figs. 3.9a and 3.9c). By comparison, the SWHs predicted by IC3/5 have large negative biases at high viscosity regimes. For example, the SWHs using IC5 with $v = 5.0 \times 10^7 \ m^2 \ s^{-1}$ have a large negative RB more than -20.0% (Fig. 3.9c). This indicates the important role of ice viscosity causing strong wave dissipation in ice at high viscosity regimes. At low elasticity regimes ($G \leq 10^4 \ Pa$), the model results using IC3 have similar negative biases for the SWHs with an average RB of ~-0.5% (-1.7%) compared with altimeter (buoy) observations. At high elasticity regimes ($G \geq 10^6 \ Pa$), the model results using IC3 have similar positive biases for the SWHs (Fig. 3.9b). The model errors for the SWHs predicted by IC5 show similar variations. This is due to that wave dissipation rates predicted by IC3/5 remain no change at low elasticity regimes and then gradually decrease until they level off at low values at high elasticity regimes (Fig. C3b).
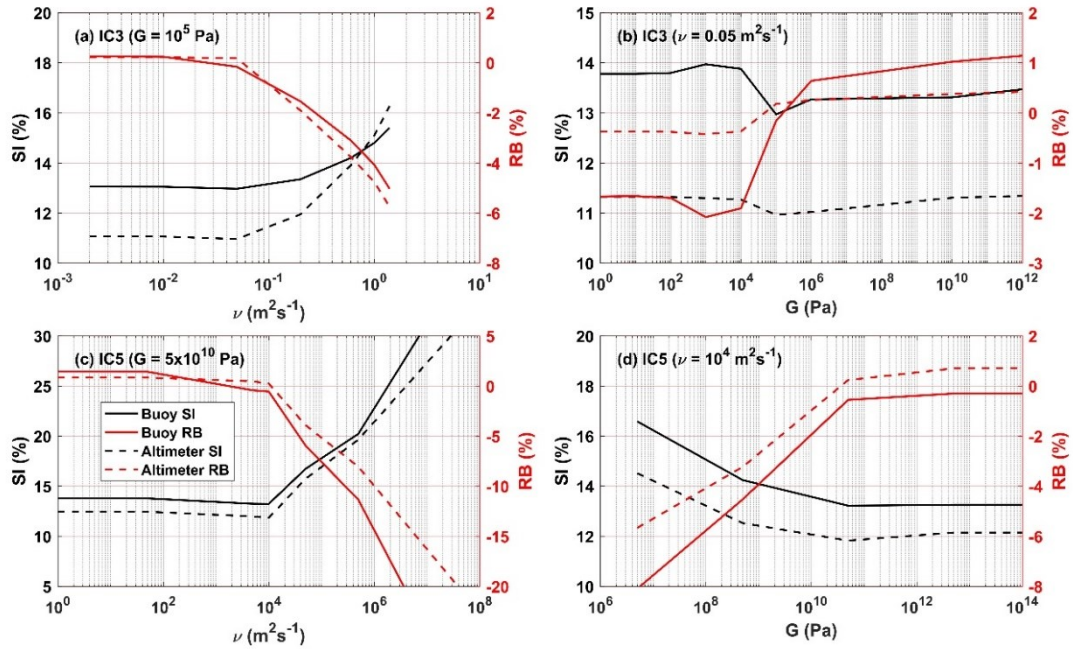
Figure 3.9: Variations of wave model errors (SI and RB) for the SWHs in terms of ice kinetic viscosity (a and c) and elasticity (b and d) in IC3/5 in comparison with observations from buoys (solid lines) and altimeters (dashed lines). The black (red) lines represent the SI (RB) with values shown by the y-axis on the left (right).

There are some intermediate values for these two rheological parameters (v and G) used in IC3/5 that can produce the least errors with an average RB around zero. Figure 3.9 only

shows the errors for the SWHs using IC3 with $v = 0.05\ m^2\ s^{-1}$ or $G = 10^5\ Pa$ and IC5 with $v = 10^4\ m^2\ s^{-1}$ or $G = 5.0 \times 10^{10}\ Pa$. Different model runs with a wide range values of v and G were also conducted and examined. Overall, the SWHs using IC3 have the best performance for $v = 0.05\ m^2\ s^{-1}$ and $G = 10^5\ Pa$ with an average SI of ~12.0% and an average RB around zero (Figs. 3.9a-3.9b). The best rheological parameters for IC5 are calibrated as $v = 10^4 m^2\ s^{-1}$ and $G = 5.0 \times 10^{10}\ Pa$ with an average SI of ~12.5% (Figs. 3.9c-3.9d).

One may notice that the optimal values of ice rheological parameters in IC3 are several orders of magnitudes smaller than those in IC5. Although both the viscosity and elasticity effects of ice are included in IC3/5, the underlying assumptions for these two viscoelastic models are different. The former (IC3) incorporates elasticity into the viscous model of *Keller* (1998) and assumes the ice as an incompressible, viscoelastic and non-Newtonian fluid (*Wang and Shen,* 2010). The latter (IC5) introduces viscosity into the thin elastic plate model of Fox and Squire (1994) and assumes the ice layer as an isotropic viscoelastic thin beam (*Mosig et al.,* 2015). The derived wave dispersion relations from the governing equations and boundary conditions are thus different for IC3/5 (Eqs. 3.2 and 3.2). Therefore, IC5 requires much larger values of ice rheological parameters to obtain similar wave dissipation rates. This is also clearly shown in the idealized case (Fig. C3).

3.4.2   Comparisons of Two Viscoelastic Models for Wave Dissipation

In this section, the optimal ice rheological parameters (v and G) are validated by comparing the model results with observations in terms of the SWHs, PWPs and wave spectra. Model results in four numerical experiments are analyzed to examine main features of the two different viscoelastic models (IC3/5). These four experiments consist of model runs using IC3/5 with the optimal parameters (v and G) determined in this study and two previous studies (*Li et al.,* 2015; *Mosig et al.,* 2015). Configurations of these four model runs are listed in Table 3.1, with the corresponding average error metrics (RMSE, RB, SI and R) for the SWHs compared with altimeter and buoy measurements in and near the ice-covered regions. In comparison with the altimeter measurements, the SWHs produced by IC3 with the optimal values of rheological parameters (IC3A) have the best performance

with a RB of ~0.2% and a SI of ~10.9%. Using IC3 with $v = 0.2\ m^2\ s^{-1}$ and $G = 2.0 \times 10^4\ Pa$ suggested by *Li et al.* (2015, IC3B), the wave model overall underestimates the SWHs with a RB of ~-2.9% and a SI of ~12.0%. This is due to the fact that the wave dissipation rates in run IC3B are generally larger than those in run IC3A. The wave model using IC5 with the optimal values of rheological parameters (IC5A) also have a good performance with a SI of ~11.8%. The using of $v = 5.0 \times 10^7\ m^2 s^{-1}$ and $G = 4.9 \times 10^{12}\ Pa$ suggested by *Mosig et al.* (2015, IC5B) produces strong wave dissipation. Therefore, run IC5B significantly underestimates the SWHs with a RB of ~-9.3% and a SI of ~17.2%.

Table 3.1: Summary of four error metrics for the SWHs predicted by the wave model using two viscoelastic models (IC3/5) with different values of ice kinetic viscosity (v) and elasticity (G). The simulated SWHs are compared with observations from altimeters (buoy stations) during 20-30 March 2014. The error metrics includes root mean square error (RMSE), relative bias (RB), scatter index (SI), and correlation coefficients (R). Wave scattering (WS) is taken into account in all model runs except for IC3C. The best error metrics are shown in bold.

Run	Reference	v $(m^2\ s^{-1})$	G (Pa)	RMSE (m)	RB (%)	SI (%)	R (%)
IC3A	*This study*	0.05	1.0×10^5	**0.43 (0.34)**	**0.2 (-0.2)**	**10.9 (13.0)**	**97.9 (98.2)**
IC3B	*Li et al.* (2015)	0.2	2.0×10^4	0.48 (0.35)	-2.9 (-3.4)	12.0 (13.4)	97.5 (98.1)
IC5A	*This study*	1.0×10^4	5.0×10^{10}	0.47 (0.35)	0.2 (-0.3)	11.8 (13.2)	97.5 (98.1)
IC5B	*Mosig et al.* (2015)	5.0×10^7	4.9×10^{12}	0.69 (0.44)	-9.3 (-11.5)	17.2 (18.6)	96.1 (97.8)
IC3C	*This study*	0.05	1.0×10^5	0.46 (0.35)	0.7 (0.4)	11.5 (13.2)	97.4 (97.6)

Figures 3.10a1-3.10d1 present time series of simulated and observed SWHs at four buoy stations. At buoy 44258 near the Halifax Harbour (Fig. 3.10a), the observed SWHs reached the peak value at around 1800 UTC 26 March 2014. Afterward, the storm moved northeastward and large waves were generated over the GrB (EL448, Fig. 3.10b1) and near the Placentia Bay (SA1 and SA2, Figs. 3.10c1 and 3.10d1). The observed SWHs at these three buoy stations reached the peak values at around 1800 UTC 27 March. These four buoy stations are located in the region with low ice concentrations (c_i < 0.1) and thus the effects of ice on surface waves are very limited. Runs IC3A, IC3B and IC5A produce similar SWHs for large wind waves generated by the winter storm (27-29 March) but run IC5B generates lower SWHs than other runs associated with stronger wave dissipation in

ice due to viscosity in run IC5B than other runs. As a result, the simulated SWHs in run IC5B have the largest errors as expected, with an average SI of ~18.6% in comparison with buoy observations. The differences between different model runs are larger before and after the winter storm (i.e., periods of 20-27 March and 29-30 March respectively), in comparison with the counterparts during the storm. The simulated SWHs in run IC5A generally have the largest values followed by runs IC3A and IC3B. Overall, run IC3A has the best performance in comparison with buoy observations under both swell-dominated and wind-wave-dominated sea states with an average SI of ~13.0%.
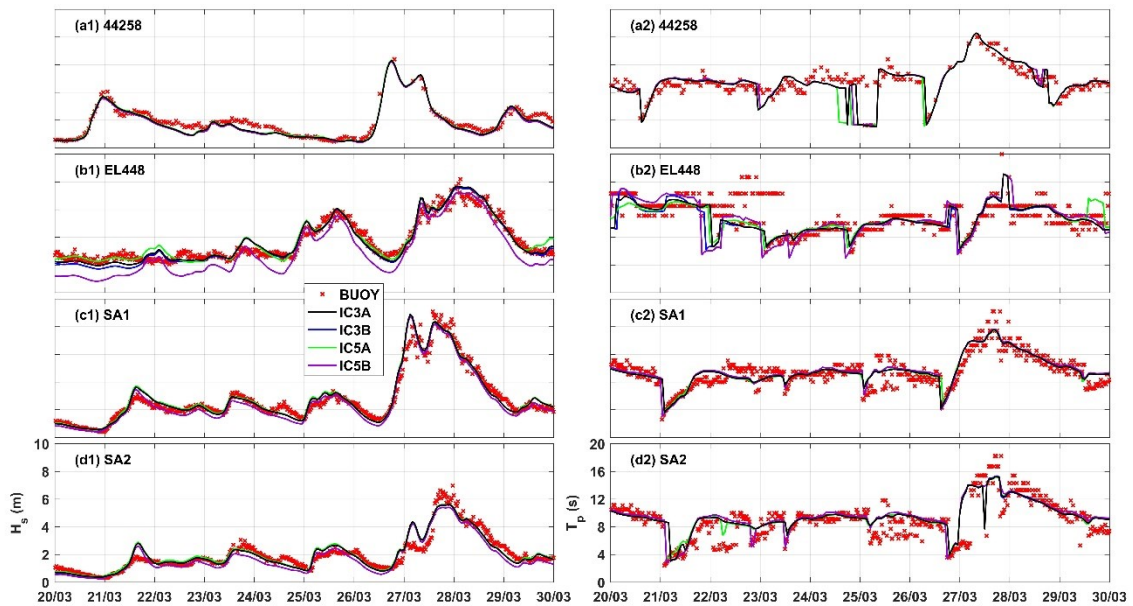
Figure 3.10: Time series of simulated SWHs (a1-d1) and PWPs (a2-d2) predicted by IC3/5 with different values of v and G (Table 3.1) against the observed values at four buoy stations during 20-30 March 2014.

The performances of IC3/5 using the optimal rheological parameters are also examined in terms of the PWPs. Figure 3.10a2-3.10d2 present time series of simulated and observed PWPs at four buoy stations. The observed PWPs at these four buoys increased from low values at young seas to high values under the strong winds during 26-28 March. With the passage of the winter storm, wave energy became lower with the spectral peak moving toward higher frequencies as the winds became relatively weaker. The observed variations of PWPs are reasonably reproduced in runs IC3A and IC5A with the calibrated rheological parameters in this study. The occasional shift of PWP is also reproduced in runs IC3A and IC5A, such as at buoy SA2 at around 1400 UTC 27 March. The comparisons of PWPs

show large differences in different model runs at buoy EL448. The simulated PWPs in runs IC3B and IC5B at buoy EL448 show some underestimations before the winter storm during 20-25 March. The average error metrics for the PWPs in different model runs in comparison with buoy observations are shown in Table 3.2. Overall, the simulated PWPs in run IC3A have the best performance with an average SI of ~14.5% in comparison with those larger than ~15.1% in other model runs.

Table 3.2: As in Table 3.1 but the error metrics for the PWPs using buoy observations.

Name	RMSE (*s*)	RB (%)	SI (%)	R (%)
IC3A	**1.42**	**0.3**	**14.5**	**80.7**
IC3B	1.48	-0.1	15.1	78.8
IC5A	1.51	-0.1	15.5	78.3
IC5B	1.55	1.1	15.8	78.0
IC3C	1.50	0.4	15.2	78.7

We next examine the wave spectra produced by two different viscoelastic models (IC3/5) with the observed counterparts at buoy EL448 (Fig. 3.11). Model results in both runs IC3A and IC5A reproduce reasonably well the observed swell energy before and after the storm and the strong wind wave energy during the storm. In comparison with model results in run IC3A, the model results in run IC5A have larger wave energy under the swell-dominated sea states before and after the storm, leading to overestimations of the SWHs (Fig. 3.10b). The main difference between the two viscoelastic models (IC3/5) is the wave dissipation rate derived from different wave dispersions and thus wave dissipation in ice (S_{ice}). Wave spectra are modified by wave dissipation in ice, which can have significant nonlinear effects on other processes, such as the wind input. That is the main reason for the stronger SWHs produced in run IC5A in comparison with those in run IC3A before and after the storm. This will be discussed in the following analyses.

Figure 3.12 presents spatial distributions of the wind-to-wave flux (F_{ww}), wave-to-ice flux (F_{wi}), SWHs and MWPs at 1800 UTC 27 March 2014 in different runs. As expected, the ice insulates the air-sea momentum flux with much lower wind input in the ice-covered regions (Fig. 3.12a1) than that in the open waters. In the MIZ with relatively low ice concentrations ($0.15 < c_i < 0.6$), wind input energy however is comparable or even larger

than wave dissipation in ice under strong wind conditions (Fig. 3.12a2). Waves propagating into ice are slightly dissipated near the ice edge of $c_i = 0.15$ and then rapidly decayed further into the inner ice pack until waves diminish near the coast (Fig. 3.12a3). Meanwhile, the MWPs increase with distances into ice due to the rapidly dissipation of wave energy at high frequencies (Fig. 3.12a4). In comparison with run IC3A, wind input produced in run IC5A is similar in the open water but much stronger in the MIZ with $0.15 < c_i < 0.6$ (Figs. 3.12b1 and 3.12c1). In the MIZ, the wind-to-wave flux can be one order of magnitudes larger than the wave-to-ice flux in run IC5A (Fig. 3.12b2). The accumulated wave energy then propagates into the inner ice pack, resulting in the unrealistic high SWHs and low MWPs near the coast of NLS. In run IC5A, the SWHs can be more than 4.0 m and the MWPs become lower with values less than 6 s in the inner ice pack (Figs. 3.12b3 and 3.12b4). In comparison with run IC3A, the higher (lower) values of SWHs (MWPs) produced in run IC5A (Figs. 3.12c3 and 3.12c4) are thus mostly due to the stronger wind input (Fig. 3.12c1) rather than the difference in wave dissipation in ice (Fig. 3.12c2).
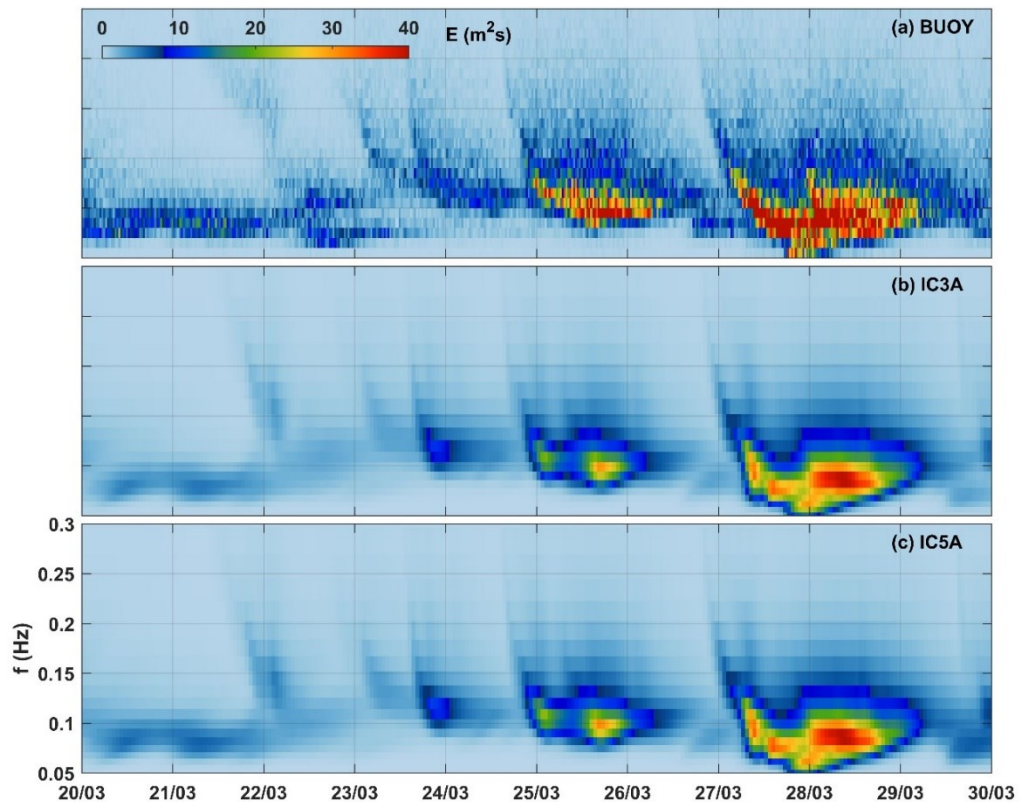
Figure 3.11: Time series of (a) observed and simulated wave energy density simulated by the wave model in runs (b) IC3A and (c) IC5A during 20-30 March 2014.
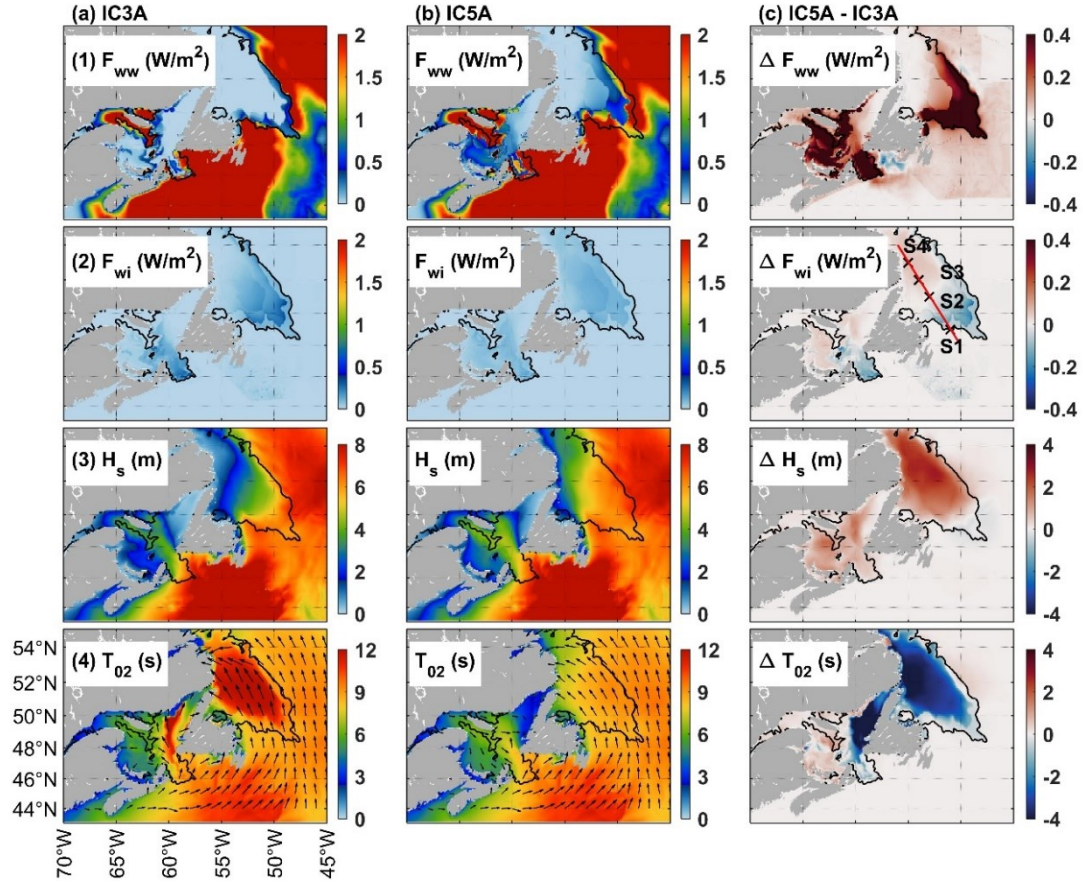
Figure 3.12: Spatial distributions of (1) wind-to-wave fluxes, (2) wave-to-ice fluxes, (3) SWHs and (4) MWPs predicted in (a) run IC3A and (b) run IC5A at 1800 UTC 27 March 2014. Column c shows the corresponding differences. Black contours represent the ice edge with a concentration of 0.15. Black crosses and the red line in panel (c2) represent the transect along the wave propagation directions, which is used in Fig. 3.13. Arrows in panel (a4) represent mean wave directions with the length showing the MWPs.

The surface wave spectra along transect S1-S4 over the NLS (marked in Fig. 3.12c2) at 1800 UTC 27 March 2014 in different model runs are examined in Fig. 3.13. Transect S1-S4 is roughly in parallel to the main wave propagation direction into the inner ice pack at this time (Fig. 3.12a4). The wave spectra predicted by the wave model in runs IC3A and IC5A are basically the same at location S1 (51.0°W, 49.0°N). However, the differences between two runs become larger with distances into ice, particularly at high frequencies. For example, wave energy at S4 (55.0°W, 53.0°N) in run IC5A can be more than three orders of magnitude larger than that in run IC3A for $f > 0.3$ Hz. This arises from the lower wave dissipation in ice but is mostly due to stronger wind input in run IC5A. As shown in Figs. 3.13a2 and 3.13b2, the wind input in run IC5A is much larger than that in run IC3A

at S2-S4. This demonstrates the significant nonlinear effect of wave dissipation in ice on other physical processes.

The main differences between these two viscoelastic models (IC3/5) result from different dispersions with different dependences on the wave frequency. Using the calibrated values of ice rheological parameters (v and G), IC3A has a power law relation between the wave dissipation rate and frequency given as $\alpha \sim f^7$ and IC5A has a relationship of $\alpha \sim f^{1.5}$. Therefore, waves produced in run IC3A are more rapidly decayed particularly at high frequencies in comparison with those in run IC5A (Fig. 3.13). The power law dependences of the wave dissipation rate on the frequency for these two models (IC3/5) are consistent with the theoretical analyses in previous studies (e.g., *Wang and Shen,* 2010; *Mosig et al.,* 2015; *Meylan et al.,* 2018). It should be noted that the IC5 viscoelastic model has a relationship of $\alpha \sim f^{11}$ for low elasticity and low frequency regimes (*Liu et al.,* 2020b).
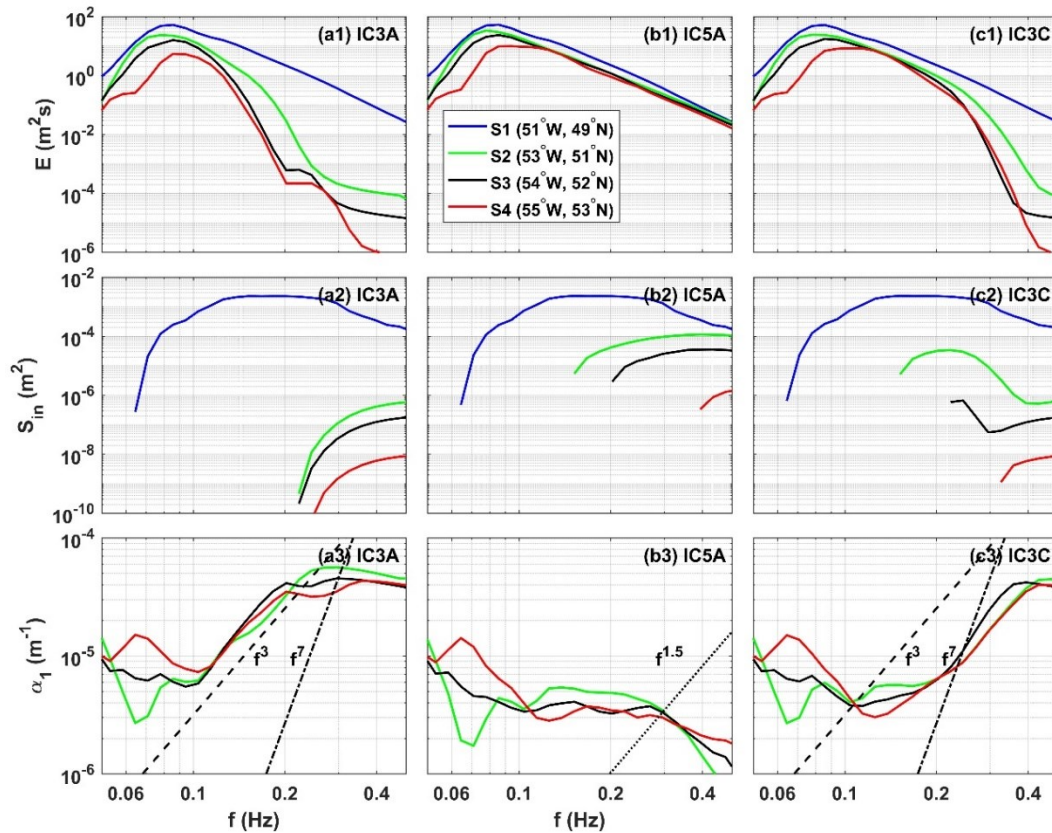
Figure 3.13: Variations of (first row) wave spectra, (second row) wind input and (third row) apparent wave attenuation rate along transect S1-S4 (Fig. 3.12c2) in the wave propagation direction predicted by the wave model in runs (a1-a3) IC3A, (b1-b3) IC5A and (c1-c3) IC3C at 1800 UTC 27 March 2014.

We next calculate the apparent wave attenuation rate (α_1) at locations S2-S4 for the incident wave from location S1 at 1800 UTC 27 March 2014 (Figs. 3.13a3-3.13c3). The apparent wave attenuation rate (α_1) is defined in Appendix C (Eq. C2) representing the energy difference between two locations. In theory, the apparent attenuation rate is identical to the wave dissipation rate if other physical processes are excluded. However, α_1 deviates significantly from the theoretical wave dissipation rates, indicating the effects of other physical processes on wave dissipation in ice. The wind input to surface waves in the MIZ can be comparable or even larger than wave dissipation in ice (Fig. 3.12). Wave energy is transferred among different frequencies through nonlinear wave interactions and dissipated through whitecapping and swell dissipation. The conservative wave scattering can also affect wave propagations in ice, which will be discussed in Section 3.4.3. The effects of other physical processes on the apparent wave attenuation were also discussed in several recent studies (e.g., *Li et al.,* 2015; *Li et al.,* 2017; *Liu et al.,* 2020b; *Cheng et al.,* 2020). *Li et al.* (2017) suggested that the wave attenuation rates at high frequencies are lower than expected values as the wind input and nonlinear energy transfer can offset the damping caused by ice. *Liu et al.* (2020b) showed that the apparent wave attenuation can be noticeably reduced at high frequencies (see their Fig. 9) by including other source terms. This is also shown in our analysis. Due to the wind input at high frequencies at locations S2-S4, α_1 has lower values than the theoretical wave dissipation rates at high frequencies ($f > 0.3$ Hz) in run IC3A ($\alpha \sim f^7$) and run IC5A ($\alpha \sim f^{1.5}$).

Due to the strong wind input for low and intermediate frequencies at location S1, larger values of α_1 are obtained compared with the theoretical wave dissipation rates. In particular, α_1 has a power law of $\alpha_1 \sim f^3$ at intermediate frequencies ($0.1 < f < 0.2$ Hz) in run IC3A, which is consistent with field measurements (e.g., *Doble et al.,* 2015; *Cheng et al.,* 2017; *Meylan et al.,* 2018). *Meylan et al.* (2018) found that the apparent attenuation has a power law dependence of $\alpha_1 \sim f^n$ with n between 2 and 4 based on field measurements in the Arctic and Antarctic. In comparison with run IC3A, α_1 in run IC5A has much lower values at high frequencies as a result of the stronger wind input. Overall, IC5A is less sensitive to the frequency and produces unrealistic large waves in the inner ice pack.

3.4.3   Effects of Wave Scattering on Wave Propagations

The effects of wave scattering on wave propagations in ice are examined in Fig. 3.14, which shows distributions of SWHs, MWPs and mean wave directions predicted by the wave model using IC3 ($v = 0.05 \ m^2 \ s^{-1}$ and $G = 10^5 \ Pa$) with (IC3A) and without (IC3C) wave scattering at 1800 UTC 27 March 2014. The strong winter storm generates large waves in the open waters over the ScS, GrB and NLS. These large waves propagate great distances into the ice fields in the GSL and NLS. Along the wave propagation directions, waves are largely decayed in ice with the SWHs approaching zero in the northeast GSL and coastal regions of NLS (Fig. 3.14a1). As wave energy at high frequencies is rapidly decayed in ice, the MWPs thus are largely increased in the inner ice pack with the MWPs up to 13.0 s (Fig. 3.14b1).

Figures 3.14a3-3.14c3 show the corresponding differences between model results with and without wave scattering. Waves propagating into ice in the NLS experience reflection, which leads to the increase of SWHs near the ice edge (black contour). The SWHs over other regions, such as the inner ice pack and lee side of ice, become lower due to wave scattering. The decrease of SWHs (Fig. 3.14a3) and increase of MWPs (Fig. 3.14b3) due to wave scattering are significant, which can be up to 2.5 m and 8.0 s respectively. Without wave scattering (IC3C), waves in the GSL and coast regions of NLS are unrealistically large with the SWHs up to 5.0 m (Fig. 3.14a2). Therefore, the exclusion of wave scattering (IC3C) enlarges the model errors, as shown in Table 3.1.

The arrows in Figs. 3.14b1 and 3.14c1 represent the wind directions and wave directions, respectively. As shown in Fig. 3.14c1, ocean surface waves generally follow the wind directions in the open water. The presence of sea ice, however, greatly modulates wave propagations. Waves propagate northwestward from the deep waters into the GSL through the Laurentian Channel (LCh), although the wind directions are opposite (southeastward). These waves then propagate northward with scattering into the southwest and northeast GSL as a result of the wave scattering process. If wave scattering is not considered (Fig. 3.14c2), the incident waves in the LCh continuously propagate toward the northern GSL without scattering. Meanwhile, waves in the southwest and northeast GSL are generated

locally following the wind directions (southeastward). Therefore, wave scattering can significantly modulate wave directions in the GSL such that waves can propagate in completely opposite directions. Waves in the ice fields over the NLS are also slightly modulated toward north (~20°) by wave scattering (Fig. 3.14c3).
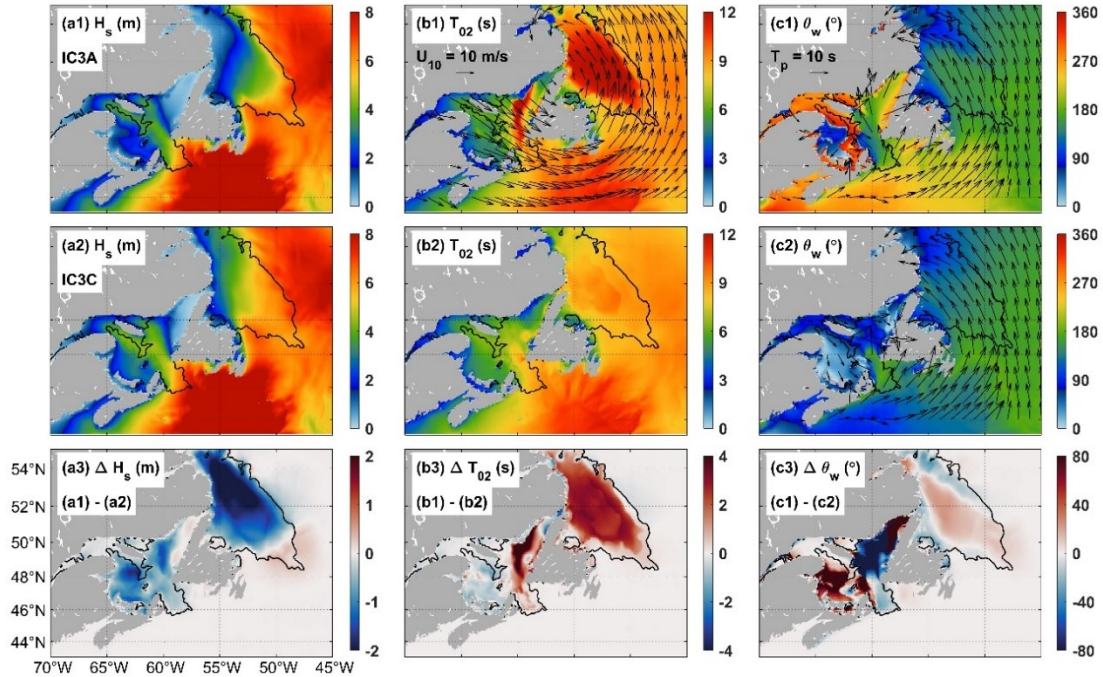
Figure 3.14: Spatial distributions of (a1-a2) SWHs, (b1-b2) MWPs and (c1-c2) mean wave directions at 1800 UTC 27 March 2014 simulated by in runs IC3A (with scattering) and IC3C (without scattering). The bottom panels show the corresponding differences. Arrows in panel (b1) represent wind directions with the length showing the wind speeds. Arrows in panels (c1-c2) represent mean wave directions with the length showing the PWPs.

Wave scattering is conservative such that wave energy is only redistributed in different directions but not dissipated. The significant decrease of SWHs in Fig. 3.14a3 thus is not directly due to the wave scattering process but the nonlinear effects of wave scattering on other physical processes. Figure 3.15 shows distributions of the wind-to-wave flux (F_{ww}), wave-to-ice flux (F_{wi}) and wave directional spread (σ_θ) at the same time as in Fig. 3.14. In response to the winter storm (Fig. 3.14b1), strong energy fluxes from winds to waves occur over the ScS and GrB. The wind input over the GSL and NLS is mostly insulated by the presence of ice in spite of the strong winds (Fig. 3.15a1). Wave scattering has a strong nonlinear effect on the wind input, which is largely reduced over the MIZ (Fig. 3.15a3). As shown in Fig. 3.15b1, wave energy is mostly attenuated in the MIZ. The amount of

attenuated wave energy becomes slightly lower due to the nonlinear effect of wave scattering (Fig. 3.15b3).
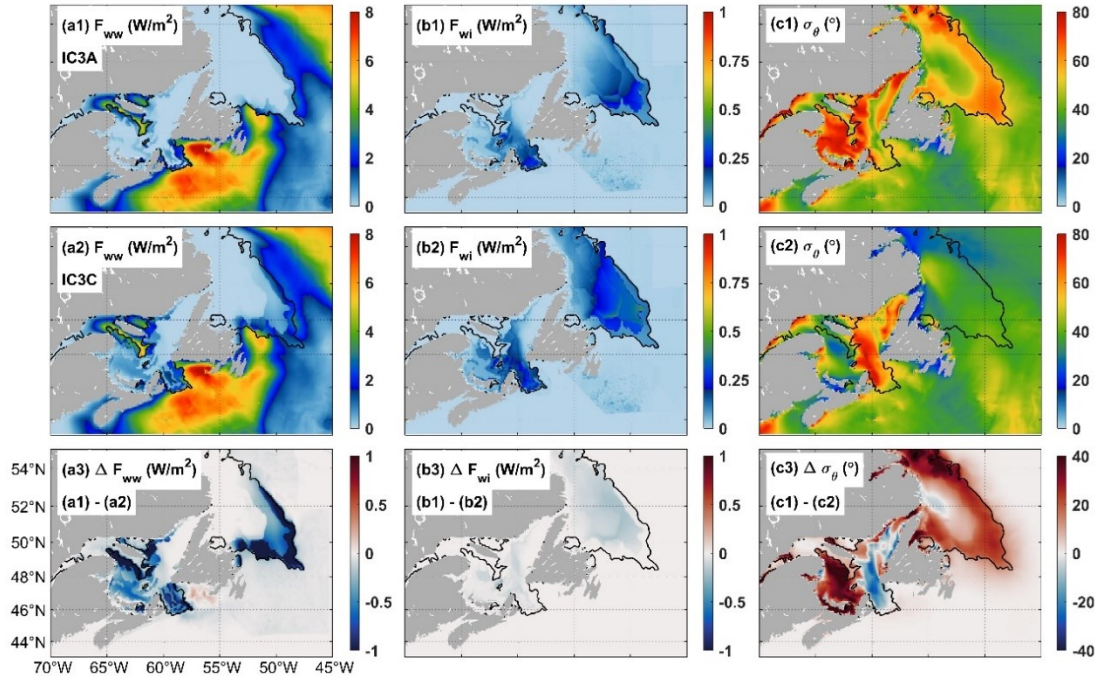
Figure 3.15: As Fig. 3.14 but for (a1-a3) the wind-to-wave fluxes, (b1-b3) wave-to-ice fluxes and (c1-c3) wave directional spread.

The significant decrease in SWHs due to wave scattering, therefore, mostly comes from the lower wind input in the MIZ (Fig. 3.15a3). Wind input for ocean surface waves strongly depends on the directional spread of wave energy. The energy transfer from winds to waves becomes more efficient, when the directional spectra are narrower (*Zieger et al.,* 2015). Wave scattering redistributes wave energy and significantly enlarges the directional spread, as shown in Figs. 3.15c1-3.15c3. The broadening of directional spreads due to wave scattering can be up to 60° in the MIZ. Therefore, wind input becomes much weaker due to the nonlinear effect of wave scattering over the regions where wave spectra are broadened, winds are sufficient strong and ice concentrations are relatively low (Fig. 3.15a3).

The nonlinear effect of wave scattering in wave propagations is also examined based on the wave spectra and wind input along the transect S1-S4, as shown in Figs. 3.13c1-3.13c3. In comparison with model results with wave scattering (IC3A), the simulated wave spectra

81

without wave scattering (IC3C) for S2-S4 are similar at low and high frequencies ($f < 0.1$ Hz and $f > 0.4$ Hz), but much stronger at medium frequencies ($0.1 < f < 0.4$ Hz). This is attributed to the stronger wind input at medium frequencies for S2-S4 in IC3C (Fig. 3.13c2). The spatial distributions of differences in the wind input due to different viscoelastic models (Fig. 3.12c1) and wave scattering (Fig. 3.15a3) are very similar. However, these two nonlinear effects result from different physical processes. The former is due to the stronger wave energy arising from less wave dissipation and affects the entitle frequency range (Fig. 3.13b2). The latter is due to the broadening of wave directional spreads and occurs mainly at medium frequencies (Fig. 3.13c2).

The effect of wave scattering in the apparent wave attenuation (α_1) is only significant at intermediate and high frequencies (Fig. 3.13c3). This is consistent with previous studies (*Ardhuin et al.,* 2016; *Boutin et al.,* 2018) that scattering is negligible for swells. If wave scattering is excluded in the wave simulation (Fig. 3.13c3), lower values of α_1 are obtained in run IC3C due to the stronger wind input. Overall, wave scattering plays a very important role for wave propagations in ice over the ECS and should be included in wave simulations.

It should be noted that the above analyses of the nonlinear effects are based on numerical wave model results. One of the drawbacks of the third-generation spectral wave models is their ad-hoc formulations for source terms accounting for different wave evolution processes. Particularly, wave dissipation due mostly to whitecapping is one of the least known parts and often considered as a tuning knob to balance the residual energy of other source terms (*Cavaleri et al.,* 2007). There are several different source term packages for the most important processes of the wind input and whitecapping. In this study, the source term package known as ST6 is used for the wind input and whitecapping (Section 3.2.2). *Lin et al.* (2020) suggested that ST6 has fast and strong wind input focusing mainly at higher frequencies compared with other packages. Therefore, the use of different source terms may change the intensity of nonlinear effects of wave dissipation and scattering in ice on the wind input. Nevertheless, package ST6 includes several important new physical features for the wind-wave exchange and has the best performance for wave simulations over the northwest Atlantic (*Lin et al.,* 2020). It is justified to infer that the nonlinear effects

of wave dissipation and wave scattering in ice are qualitatively reasonable but may vary quantitatively.

3.5 Discussion

The optimal values of rheological parameters (v and G) for IC3/5 presented in this study differ from those used in previous studies (Table 3.3), which deserves further discussions. It should be noted that a wide range of values were suggested in the past for these two rheological parameters. Field experiments were carried out in recent years for the measurements of waves in the MIZ, such as the Marginal Ice Zone field program (*Wang et al.,* 2016), the Arctic Sea State program (*Thomson et al.,* 2018) in the Beaufort and Chukchi Seas, and the Sea Ice Physics and Ecosystem Experiment in the Antarctic MIZ (*Kohout et al.,* 2014). These field measurements were used to determine the rheological parameters (v and G) in the viscoelastic models and also to evaluate the performances of different wave dissipation models in previous studies (e.g., *Li et al.,* 2015; *Liu et al.,* 2020b). Table 3.3 summarises these applications, including values of rheological parameters and the used ice fields.

The main challenge for accurate simulations of ocean surface waves in ice mostly arises from large uncertainties with the ice fields and parameterizations of wave dissipation in ice (*Rogers et al.,* 2018). Although the local conditions of the atmospheric, oceanic and sea ice conditions can be observed during field experiments, accurate wave hindcasts require simultaneous representations of these conditions in a larger scale (*Squire,* 2020). The ice concentrations used in previous studies were typically taken from satellite microwave measurements or numerical ice model results. The ice thicknesses in the previous studies were taken from the ice model results or based on the assumption of a constant ice thickness (Table 3.3). The microwave measurements for the ice concentrations, however, should be used with caution (*Galley et al.,* 2016). Considerable discrepancies were found between different sea ice products (*Agnew and Howell,* 2003; *Meier et al.,* 2014) and that the microwave-based ice concentrations may not well represent the in-situ observations of ice concentrations (*Wang et al.,* 2019; *Alekseeva et al.,* 2019). One of main limitations is that the microwave-based ice concentrations over regions with low ice concentrations or thin

ice floes are underestimated (*Meier et al.,* 2015). The sea ice models still have large model errors in reproducing the ice concentrations and thicknesses in daily and shorter time scales (*Stroeve et al.,* 2014; *Hebert et al.,* 2015). Although it is reasonable to modify the modeled ice thickness based on observations (*Li et al.,* 2015) or use a constant ice thickness in some studies (*Liu et al.,* 2020b), which can certainly introduce additional uncertainties in wave hindcasts.

Accurate simulations of surface wave dissipation in the MIZ require information on not only the ice concentration and thickness but also the ice floe size. In addition to the non-conservative wave dissipation in the MIZ, surface waves also experience the conservative process of scattering, which depends on the ice floe size (*Rogers et al.,* 2016; *Boutin et al.,* 2018). Information on the ice floe size, however, was not included in the sea ice data used in previous studies (Table 3.3). Wave scattering thus was not taken into account in these previous wave hindcasts (e.g., *Li et al.,* 2015; *Liu et al.,* 2020a), although wave scattering in ice is not important when floe sizes are smaller than wavelengths. In this study, the ice data from the CISDA are used in wave simulations. As mentioned in Section 3.2, the use of reliable ice data reduces the possible model errors for wave simulations over the ECS and allows the consideration of wave scattering in the wave model, which are shown to play an important role in this region (Section 3.4.3).

Different ice data used in this and previous studies can be one of the reasons for different values of the optimal ice rheological parameters (v and G) in IC3/5. The different values are also attributed to differences between the sea ice conditions over the ECS in March 2014 and those in the Arctic/Antarctic MIZ considered in previous studies. The ice conditions encountered in the Antarctic MIZ (*Li et al.,* 2015; *Li et al.,* 2017) and the Arctic MIZ (*Cheng et al.,* 2017; *Liu et al.,* 2020a) in spring and autumn were mostly pancake ice with floe sizes less than 20 m (Table 3.3). As shown in Fig. 3.2, the ice floe sizes over the ECS in March 2014 range from dozens to hundreds meters, which are comparable to the wavelengths of surface waves. Physically, the ice viscosity property comes from the small ice floes, since interactions of waves and surrounding water with small ice floes create an effective viscosity for the ice layer. The elasticity property comes from the rigidity of ice

floes in which larger floe sizes are less flexible and dissipate less wave energy (*Wang and Shen,* 2010).

As sea ice over the ECS in March 2014 mostly consists of large ice floes, it is reasonable that the calibrated viscosity for IC3 ($v = 0.05\ m^2\ s^{-1}$) in this study is smaller than those used for small ice floes, such as $v = 0.2\ m^2\ s^{-1}$ in *Li et al.* (2015) and $v = 2.0\ m^2\ s^{-1}$ in *Cheng et al.* (2017). The elasticity property can be negligible for small ice floes, thus small values for the ice elasticity were used for IC3 previously, such as $G = 2.0 \times 10^4\ Pa$ in *Li et al.* (2015) and $G = 0\ Pa$ in *Cheng et al.* (2017). By comparison, a larger value $G = 1.0 \times 10^5\ Pa$ is used for IC3 in this study. It is similar that the optimal value of viscosity in IC5 in this study is smaller than those used in previous studies (Table 3.3). The calibrated value of elasticity in IC5 in this study is comparable with previous values as the wave dissipation rate in IC5 is insensitive to ice elasticity at high elasticity regimes (Fig. 3.9d).

The other important reason for different values of ice rheological parameters between our study and previous studies is that wave scattering is included in our wave simulations. As discussed in Section 3.4.3, wave scattering redistributes wave energy in different directions causing the decrease of SWHs along the main wave direction. When wavelengths of surface waves are appreciably longer than the floe sizes, wave scattering however is negligible (e.g., *Dumont et al.,* 2011; *Ardhuin et al.,* 2016). Thus, it could be reasonable to ignore the wave scattering process in previous wave hindcasts (Table 3.3). However, wave scattering plays an important role for wave propagations in ice over the ECS in March 2014 due to different ice floe sizes. In comparison with previous studies, the optimal rheological parameters for IC3/5 used here generate lower wave dissipation rates, allowing less wave dissipation in ice. The other part of wave energy along the wave propagation direction is dissipated due to wave scattering or reduced by other physical processes due to the nonlinear effect of wave scattering.

Table 3.3: Summary of previous and current applications of two viscoelastic model (IC3/5) with values of ice kinetic viscosity (v) and elasticity (G) using different ice data for the ice concentration (c_i), thickness (h_i) and maximum floe size (D_{max}). Abbreviations are used for the Marginal Ice Zone Field Program (MIZFP), Arctic Sea State Program (ASSP), Sea Ice Physics and Ecosystem Experiment (SIPEE), Near-Real-Time DMSP SSMIS Daily Polar Gridded Sea Ice Concentrations (NRTSI), Los Alamos Community Ice Code (CICE), Climate Forecast System Reanalysis (CFSR), NOAA OI SST V2 High Resolution Dataset (OISST), National Centers for Environmental Prediction (NCEP), Advanced Microwave Scanning Radiometer 2 (AMSR2) and Special Sensor Microwave Imager (SSMI).

Model	Reference	v $(m^2 s^{-1})$	G (Pa)	Program, location and time	Ice data and ice conditions
IC3	*Wang et al.* (2016)	1.0	0	MIZFP, Beaufort and Chukchi Seas, Aug.-Sep. 2014	c_i: microwave (NRTSI)
	Cheng et al. (2017)	2.0~10.0	0	ASSP, Beaufort and Chukchi Seas, Oct. 2015	c_i and h_i: model (CICE) Pancake and frazil ice 1-2 m
	Li et al. (2015)	0.2	2.0×10^4	SIPEE, Antarctic MIZ Sep.-Oct. 2012	c_i: microwave (SSMI) h_i: analysis (CFSR) Pancake ice 2-20 m
	Li et al. (2017)	0.5	5.0×10^3	Weddell Sea Apr. 2000	c_i: microwave (ASISSMI) h_i: analysis (CFSR) Pancake ice
	Li et al. (2019)	0.03	5.0×10^3	Wave hindcast, Arctic, 2007-2018	c_i: microwave (ASISSMI) h_i: analysis (NCEP)
	Liu et al. (2020a)	0.328	31318	Field experiment, Barents Sea, Apr.-May 2016	c_i: analysis (OISST) h_i: analysis (CFSv2) Small floe around 10 m
	This study	0.05	1.0×10^5	Wave hindcast, ECS, Mar. 2014	c_i: observations (CISDA) h_i: observations (CISDA) D_{max}: observations (CISDA)
IC5	*Mosig et al.* (2015)	5.0×10^7	4.9×10^{12}	SIPEE, Antarctic MIZ, Sep. 2012	
	Liu et al. (2020b)	1.6×10^7	4.0×10^{12}	SIPEE, Antarctic MIZ, Sep. 2012	c_i: microwave (AMSR2) h_i: 0.75 m Pancake ice 2-20 m
	Liu et al. (2020b)	3.2×10^4	1.0	ASSP, Beaufort and Chukchi Seas, Oct. 2015	c_i: microwave (SSMI) h_i: 0.75 m Pancake and frazil ice 1-2 m
	This study	1.0×10^4	5.0×10^{10}	Wave hindcast, ECS, Mar. 2014	c_i: observations (CISDA) h_i: observations (CISDA) D_{max}: observations (CISDA)

The above discussions demonstrate the ice rheological parameters for IC3/5 determined in this study are physically reasonable. However, the optimal values of ice rheological parameters in this study are based on limited observational data in regions with relatively low ice concentrations. Large differences are found between model results using two viscoelastic models in the inner ice pack. Although we do not expect significant changes of calibrated ice rheological parameters under similar ice conditions, additional observations for waves in higher ice concentrations would help to further verify wave propagations in the inner ice pack. More importantly, substantial observations for waves in a range of ice conditions are needed to examine the applicability of these optimal values under different ice conditions.

The other limitation is that v and G are assumed to be constants in space and time. Although the viscoelastic ice layer model is physically more advanced than several other models, it still cannot properly represent all processes accounting for wave dissipation in ice. The ice rheological parameters cannot be measured directly as they do not represent observable physical processes (*Mosig et al.,* 2015; *Cheng et al.,* 2017). Therefore, v and G are effective ice rheological parameters determined by adjusting the parameters to match observations and represents the overall wave dissipation induced by ice. However, this does not hamper the fact that v and G are strongly affected by the ice conditions. Physically, the viscosity originates from ice floes much smaller than the wavelength and the elasticity from ice floes larger than the wavelength. The values of v and G should be determined based on local ice conditions and vary in time and space, when the precise ice data (including concentration, thickness, floe size and ice type) with sufficient spatial and temporal resolutions from the ice model or observations become available in the future. At the current stage, the assumption of constant ice rheological parameters has to be used to calibrate their values and test the viscoelastic models.

From the operational forecast perspective, it is not limited to use the viscoelastic models accounting for wave dissipation in ice, the applicability of other models or empirical formulas should also be examined in the future study. For the viscoelastic models, in comparison with IC5, IC3 better reproduces the observed wave variables near the ice edge and has more realistic waves in the inner ice pack. Moreover, the calibrated ice rheological

parameters in IC3 and the dependence of wave dissipation rate on the frequency are physically more reasonable (Section 3.4.2). The major drawback associated with IC3 is that the wave dispersion relation is complicated and may have many solutions representing different wave modes (*Mosig et al.,* 2015). This forced *Wang and Shen* (2010) to introduce criteria to select the primary propagating wave mode in IC3. The complexity of IC3 may arise the concern for the computational efficiency. Based on our numerical tests, the running time is only slightly increased by using IC3, as other processes account for most of the computational costs such as the whtiecapping and nonlinear wave interactions. Despite the great challenging for wave simulations in ice, this viscoelastic model IC3 is certainly more advanced than the partial-blocking approach used in most wave simulations for the ECS (e.g., *Guo and Sheng,* 2015; *Guo and Sheng,* 2017; *Wang et al.,* 2018).

3.6 Conclusions

Several theories were developed in recent years for wave dissipation in ice, including two physical-based viscoelastic models (known as IC3 and IC5). Many important issues, however, remain to be addressed, including the applicability of these viscoelastic models for wave dissipation in ice. In this study, a nested-grid ocean surface wave model based on WW3 for the NWA was used to investigate wave propagations in ice during a winter storm in March 2014. The nested-grid wave model was demonstrated to have good performances in the open water in comparison with observations from altimeters and buoys. The model accuracy in simulating surface waves in ice was found to depend largely on the input ice fields and parameterizations of wave dissipation in ice (*Rogers et al.,* 2018). The reliable ice data set from the CISDA was used in this study, including the ice concentration, thickness and floe size.

The optimal values of two key ice rheological parameters (v and G) in IC3/5 were determined by comparing the simulated SWHs with observations from altimeters and buoys over the study region. Both viscoelastic models (IC3/5) were found to represent reasonably well wave propagations in ice with an average scatter index for the SWHs less than 12.5% near the ice edge. The two viscoelastic models were, however, found to perform differently in the inner ice pack. The model using IC5 produces unrealistic large

waves in the inner ice pack. These large model differences between IC3 and IC5 arise from the nonlinear effect of different wave dissipation rates on the wind input. The wave dissipation rates (α) in IC3 and IC5 using the optimal values of rheological parameters have different dependences on the wave frequency (f), predicting a power law of $\alpha \sim f^7$ and $\alpha \sim f^{1.5}$, respectively. The calculated apparent wave attenuation (α_1) using the IC3 model has a power law of $\alpha_1 \sim f^3$ at intermediate frequencies, which is consistent with field measurements (*Meylan et al.,* 2018).

Different from most of previous studies in the Arctic and Antarctic (Table 3.3), the use of ice data from the CISDA minimizes the model errors introduced by the input ice field and allows the consideration of wave scattering in ice over the ECS. Wave scattering significantly alters wave propagations and results in the strong decreases of SWHs and increases of MWPs in the inner ice pack. This is due to the nonlinear effect of wave scattering on the wind input in the MIZ arising from the broadening of the wave directional spread. Wave scattering thus plays a very important role for wave propagations in ice, particularly when ice floe sizes are comparable with wavelengths. The exclusion of wave scattering enlarges the model errors for surface waves in ice over the ECS during the March 2014 Nor'easter (Table 3.1).

To our knowledge, this was the first study on wave simulations over the ECS using the physical-based parameterizations for wave dissipation and wave scattering in ice, with optimal values of rheological parameters in IC3/5 determined by comparing model results and observations. Future studies are needed to examine the applicability of these optimal values to other coastal and shelf waters at high latitudes. Physically, the rheological parameters should depend on local ice conditions and should vary in space and time. Therefore, efforts can be devoted to include the dependences of rheological parameters on the ice conditions if the precise ice data become available in the future. The other limitation of this study is that the in-situ observations in ice used in this study were made in regions with low ice concentrations. Further investigations with additional field observations in a wide range of ice concentrations will improve our understandings of wave-ice interactions and predictive skills of numerical models.

CHAPTER 4

DEPENDENCES OF DRAG COEFFICIENT ON WIND SPEED AND WAVE STATE[1]

4.1 Introduction

Good knowledge about the momentum flux at the air-sea interface is needed for numerical modelling of atmospheric and oceanic dynamics, weather forecasting, climate studies, and remote sensing of the ocean environment (*Yu,* 2019). Wind stress at the sea surface is the primary driving force for many oceanographic phenomena including surface gravity waves, storm surges, and ocean currents. During the past several decades, significant efforts have been made to estimate the wind stress based on laboratory and field observations and theoretical analyses (e.g., *Charnock,* 1955; *Yelland and Taylor,* 1996; *Drennan et al.,* 2003; *Edson et al.,* 2013). Wind stress (τ) is normally estimated from the wind speed using the bulk formula in terms of a drag coefficient (C_{dz}),

$$\tau = \rho_a u_*^2 = \rho_a C_{dz} U_z^2 \tag{4.1}$$

where ρ_a is the air density, u_* is the friction velocity, U_z is the mean wind speed at the height of z m above the mean sea level (MSL), and C_{dz} is the drag coefficient at the same height. The drag coefficient is usually parameterized as a function of the mean wind speed (e.g., *Large and Pond,* 1981; *Hwang,* 2011). Wind stress, however, is also determined by the structure and physics of the marine atmospheric boundary layer (MABL) and sea surface wave states (*Soloviev et al.,* 2014). The physical processes in the MABL is traditionally described by the Monin-Obukhov similarity theory (hereafter MOST, *Monin*

---

[1]Lin, S., and Sheng, J. (2020). Revisiting dependences of the drag coefficient at the sea surface on wind speed and sea state. *Cont. Shelf Res.,* 207, 104188. doi:10.1016/j.csr. 2020.104188

and Obukhov, 1954), which assumes stationary and homogenous conditions and a constant momentum flux in the surface layer.

Based on the MOST, the drag coefficient can be related with the sea surface roughness (Section 4.2). The wave-dependent drag coefficient is usually determined by taking the nondimensional sea surface roughness as a function of wave age (e.g., *Smith et al.,* 1992; *Johnson et al.,* 1998; *Oost et al.,* 2002; *Drennan et al.,* 2003; *Gao et al.,* 2006) or wave steepness (e.g., *Anctil and Donelan,* 1996; *Taylor and Yelland,* 2001). It was found that the drag coefficient has larger values for younger waves and steeper waves under developing sea states. However, the scatter of experimental data for such dependences is very significant (*Drennan et al.,* 2005). Moreover, many previous studies demonstrated that the presence of swells has significant influences on the wind stress (e.g., *Drennan et al.,* 1999; *Potter,* 2015; *Jiang et al.,* 2016) and obscures the relationship between the roughness and sea states (*Drennan et al.,* 2005). The main difficulty lies in the fact that the dynamics of the MABL are related with the wave states, which may not be simply represented by the wave age or wave steepness.

In this study, the performances of eight existing parameterizations of the drag coefficient are assessed using field observations in a wide range of wind and surface wave conditions. Analyses of these field observations provide a valuable insight into the momentum exchange under different sea states. A new wave-dependent parameterization of the drag coefficient is then proposed to better represent the wind stress under different sea states in comparison with the existing schemes. The applicability of the new parameterization is examined using a nested-grid wave model for the northwest Atlantic (NWA). Ocean surface waves over the NWA during a winter storm in March 2014 are simulated with the wind stress using the new and three existing parameterizations of the drag coefficient. The model results are compared with the available measurements from in-situ buoys and satellite altimeters.

The chapter is structured as follows. Section 4.2 introduces the existing and a new parameterizations for the drag coefficient. Section 4.3 describes observational data for the wind stress and wave parameters from eight field experiments. Section 4.4 presents the

analyses of the observational data and a new wave-dependent parameterization for the drag coefficient. Section 4.5 investigates the applicability of different parameterizations of the drag coefficient in predicting ocean surface waves during the winter storm in March 2014 over the NWA. Section 4.6 is the discussion and conclusions.

4.2 Drag Coefficient at the Sea Surface

The drag coefficient (C_{dz}) and sea surface roughness (z_0) are two important parameters to compute the wind stress (τ) from the wind speed (U_z). The estimation of C_{dz} relies on the assumption of the logarithmic wind profile in the MABL given as:

$$U_{zN} = \frac{u_*}{\kappa} \ln\left(\frac{z}{z_0}\right) = U_z + \left(\frac{u_*}{\kappa}\right) \psi_m\left(\frac{z}{L_1}\right) \tag{4.2}$$

where U_{zN} is the wind speed under neutral atmospheric conditions, $\kappa = 0.4$ is the von Karman constant, and ψ_m is a dimensionless function of the Obukhov length L_1 to account for the effect of the atmospheric stability (*Drennan et al.*, 2003). In practice, wind speeds at different heights are converted to the standard height at 10 m above the MSL based on the logarithmic law. The corresponding neutral drag coefficient C_{dN} can be related to the sea surface roughness through:

$$C_{dN} = \left(\frac{u_*}{U_{10N}}\right)^2 = \kappa^2 \left[\ln\left(\frac{10}{z_0}\right)\right]^{-2} \tag{4.3}$$

The sea surface roughness can be decomposed to a smooth flow component (z_0^s) due to the viscosity and a rough flow component (z_0^r) driven by the surface gravity waves (*Fairall et al.*, 2003):

$$z_0 = z_0^s + z_0^r \tag{4.4}$$

In an aerodynamically smooth flow, the surface roughness is given as (*Fairall et al.*, 2003):

$$z_0^s = 0.11 \upsilon / u_* \tag{4.5}$$

where υ is the kinematic viscosity of the air, which depends on the air temperature (T_{air}) and is 1.48×10^{-5} m² s⁻¹ at $T_{air} = 15°C$. *Charnock* (1955) suggested the following parameterization for the rough flow component based on a dimensional analysis:

$$z_0^r = \alpha_c u_*^2 / g \tag{4.6}$$

where $\alpha_c = g z_0^r / u_*^2$ is the nondimensional roughness known as the Charnock parameter, and g is the gravitational acceleration of the Earth.

The Charnock parameter α_c was taken to be a constant in many previous studies, although α_c was found to vary significantly between 0.012 and 0.035 (e.g., *Charnock, 1955; Wu, 1980*). A constant Charnock parameter implies that the drag coefficient increases monotonically with the wind speed. Physically, the drag coefficient should depend on the wind speed and other factors such as the wave age or wave steepness. In the wave age formulation, the nondimensional roughness is set to be an exponential function of the wave age (e.g., *Drennan et al., 2003; Smith et al., 1992*) given as:

$$\alpha_c = gz_0^r/u_*^2 = m_1\,(c_p/u_*)^{m_2} \tag{4.7}$$

where m_1 and m_2 are coefficients. The wave age (c_p/u_*) is defined as the phase speed of the spectral peak (c_p) divided by the friction velocity (u_*).

The nondimensional roughness was alternatively scaled by the significant wave height (e.g., *Donelan, 1990; Oost et al., 2002; Drennan et al., 2003*) given as:

$$z_0^r/H_s = n_1\,(c_p/u_*)^{n_2} \tag{4.8}$$

where n_1 and n_2 are coefficients. Different values of m_1, m_2, n_1 and n_2 were suggested in the past based on various laboratory and field observations, which are summarized in Table 4.1. The values of m_1 were found to vary between 0.114 (*Edson et al., 2013*) and 49.9 (*Oost et al., 2002*) and the values of n_1 range from 0.09 (*Edson et al., 2013*) to 3.35 (*Drennan et al., 2003*), which indicates large uncertainties involved in these existing parameterizations. Several studies (e.g., *Anctil and Donelan, 1996; Taylor and Yelland, 2001; Takagaki et al., 2012*) suggested the following wave steepness formula as an alternative to the classical wave age formulation:

$$z_0^r/H_s = A_1(H_s/L_p)^{A_2} \tag{4.9}$$

where L_p is the wavelength of the spectral peak, A_1 and A_2 are coefficients shown in Table 4.1.

In this study, a new parameterization of the drag coefficient is suggested based on analyses of field observations of wind and wave data (Section 4.3). In the new parameterization, the sea surface roughness (z_0^r) depends on the significant wave height (SWH or H_s) and wave age (c_p/u_*) based on Eq. 4.8. The main difference of the new parameterization from previous ones is the different values of n_1 and n_2 under different sea states instead of

constant values suggested in previous studies. The new values of n_1 and n_2, together with new values of m_1 and m_2, will be presented in Section 4.4.3.

Table 4.1: Values for coefficients for exponential functions in Eqs. 4.7-4.9

Reference	m_1	m_2	Reference	n_1	n_2
Donelan (1990)	0.42	-1.03	*Donelan* (1990)	0.46	-2.53
Drennan et al. (2003)	1.70	-1.70	*Drennan et al.* (2003)	3.35	-3.40
Pan et al. (2008)	0.942	-1.40	*Pan et al.* (2008)	0.745	-2.82
Edson et al. (2013)	0.114	-0.622	*Edson et al.* (2013)	0.09	-2.00
Maat et al. (1991)	0.86	-1.01	*Hsu* (1974)	0.16	-2.00
Smith et al. (1992)	0.48	-1.00	Reference	A_1	A_2
Monbaliu (1994)	2.87	-1.69	*Anctil and Donelan* (1996)	639	6.76
Vickers and Marht (1997)	2.90	-2.00	*Taylor and Yelland* (2001)	1200	4.5
Johnson et al. (1998)	1.89	-1.59	*Takagaki et al.* (2012)	10.9	3.0
Oost et al. (2002)	49.9	-2.52			

4.3 Observational Data

Observational data used in this study include wind stresses and wave parameters from eight field experiments. The measured and estimated variables (Table 4.2) include the measurement height (z), fetch (X), water depth (d), stability parameter (z/L_1), wind speed (U_{10N}), friction velocity (u_*), significant wave height (H_s) and wave age (c_p/u_*). The observed fetches and wave ages listed in Table 4.2 have a wide range of values, indicating the complexity of sea states in these eight field experiments. Wave parameters were estimated based on the measured directional wave spectra. Wind stress for each field experiment was measured using the direct eddy correlation method (*Fairall et al.,* 2003). The friction velocity was then calculated using the wind stress measurements based on Eq. 4.1. The neutral wind speed was converted from the measured wind speed at different heights based on Eq. 4.2 taking account of the atmospheric stability. The corresponding neutral drag coefficient (C_{dN}) and surface roughness (z_0) were calculated based on Eq. 4.3.

In this study, sea states are classified as the wind-sea-dominated and swell-dominated conditions based on the relative energy of swell (E_s) and wind waves (E_w) for all datasets except for the GOTEX and North Sea experiments. For these two field experiments, the

classifications of sea states are made based on the values of wave age, since the wave spectra are not available. Swell is characterized by the peak wave phase speed exceeding the local wind speed. The sea state is characterized as the swell-dominated conditions if $c_p/u_* \geq 30$, and the wind-sea-dominated conditions if $c_p/u_* < 30$ (*Smith et al.,* 1992; *Wu et al.,* 2016). The datasets are briefly described below.

4.3.1 FETCH

The flux, sea state, and remote sensing in conditions of variable fetch (FETCH) experiment was conducted in the Gulf of Lion of the Mediterranean Sea during the early spring of 1998 (*Hauser et al.,* 2003). Wind stress data were observed at 7 m above the MSL using a sonic anemometer. Wave data were measured from an Air-Sea Interaction Spar (ASIS) buoy moored at about 50 km offshore with the water depth of about 100 m. A more detailed overview of the FETCH experiment was given in *Hauser et al.* (2003) and *Drennan et al.* (2003). A total of 831 runs from wind-sea-dominated and swell-dominated sea conditions are used in this study. The FETCH data are available at http://seaflux.org/seaflux_data/ INSITU/ALBATROS/FETCH/.

4.3.2 GOTEX

Wind and wave measurements were collected using an aircraft during the Gulf of Tehuantepec Experiment (GOTEX) in February 2004 (*Romero and Melville,* 2010). The data presented in *Romero and Melville* (2010) are used in this study, which consist of 67 runs under offshore wind conditions with the fetch between 6 km and 509 km.

4.3.3 Grand Banks Experiment

This experiment took place over the Grand Banks off Newfoundland in November 1991 for the validation of the ERS-1 SAR wave spectra (*Dobson et al.,* 1994). Wind stress measurements were made from the research vessel CSS Hudson using a Gill propeller-vane anemometer at 14 m above the MSL. Wave data were collected from two directional buoys and one non-directional buoy at the water depth of 79-96 m. The data presented in *Dobson et al.* (1994) are used in this study. The observational data consist of 41 runs, of which 8 are classified as the wind-sea-dominated conditions.

4.3.4 HEXMAX

The Humidity Exchange over the Sea Main Experiment (HEXMAX) was conducted from a Dutch offshore platform at the water depth of about 18 m in October-November 1986 (*Smith et al.,* 1992). The observational data from *Janssen* (1997) representing the wind-sea-dominated sea conditions (50 runs) are used in this study by averaging the wind measurements from the sonic and pressure anemometers at about 6 m above the MSL.

4.3.5 North Sea Experiment

In this experiment, wind measurements were collected using a sonic anemometer at ~33 m above the MSL from the North Sea platform at the water depth of about 30 m in December 1985. A total of 116 observational data published by *Geernaert et al.* (1987) are used here.

4.3.6 RASEX

The Risø Air-Sea Exchange experiment (RASEX) was carried out in 1994 at the water depth of about 4 m off Denmark. Wind stress data were collected using a sonic anemometer at 3 m above the MSL. The corresponding mean wind data were obtained from a cup anemometer located at 7 m above the MSL. The observational data published by *Johnson et al.* (1998) are used here, representing wind-sea-dominated conditions (74 runs).

4.3.7 SWADE

The Surface Wave Dynamics Experiment (SWADE) was conducted in 1990-1991 from a ship in the mid-Atlantic coastal region (*Donelan et al.,* 1997). Wind data were collected using a Gill anemometer at 12 m above the MSL, and directional wave spectra were obtained from a bow-mounted wave staff array. The observational data published by *Donelan et al.* (1997) are used here. The observational data consist of 126 runs, of which 27 are classified as wind-sea-dominated conditions.

4.3.8 WAVES

The Water-Air Vertical Exchange Study (WAVES) experiment was carried out from a tower at the water depth of about 12 m in Lake Ontario during the autumn seasons of 1985-

1987 (*Drennan et al.,* 1999). Wind stress measurements were made from a bivane anemometer at 12 m above the MSL and directional wave spectra were obtained from an array of wave gauges. The observational data published by *Drennan et al.* (1999) and *Terray et al.* (1996) are used in this study.

Table 4.2: Summary of observed variables in eight field experiments, including the measurement height (z), fetch (X), water depth (d), stability parameter (z/L_1), wind speed (U_{10N}), significant wave height (H_s), wave age (c_p/u_*), and number of data points for each experiment (NA refers to not available).

Data	Reference	z (m)	Fetch X (km)	Depth d (m)	z/L_1	U_{10N} (m/s)	H_s (m)	c_p/u_*
FETCH	*Drennan et al.* (2003)	7	>50	100	-12-0.8	1.5-18.9	0.35-2.91	11-115
GOTEX	*Romero and Melville* (2010)	40/50	6-509	NA	NA	11.0-20.4	0.44-3.96	8-34
Grand Banks	*Dobson et al.* (1994)	14	NA	79-96	NA	7.0-16.8	0.61-4.16	13-28
HEXMAX	*Janssen* (1997)	6	> 175	18	NA	7.2-20.2	1.66-4.18	9-38
North Sea	*Geernaert et al.* (1987)	33	40-100	30	-0.05-0.12	3.8-24.4	1.02-7.08	9.7-66
RASEX	*Johnson et al.* (1998)	7	15-25	4	-0.25-0.07	4.1-16.4	0.19-0.71	6.6-23
SWADE	*Donelan et al.* (1997)	12	NA	NA	-9.23-0.33	3.5-14.2	0.72-3.41	11-79
WAVES	*Drennan et al.* (1999); *Terray et al.* (1996)	12	1-200	12	NA	3.8-15.6	0.1-2.53	4-114

4.4 Analyses of Observational Wind Stress and Wave Data

Observational data mentioned in Section 4.3 are used in this section to examine the dependences of the drag coefficient on the wind speed and sea state. Discussions on variations of the drag coefficient in terms of the wind speed and sea state are presented in Sections 4.4.1 and 4.4.2, respectively. The new parameterization of the drag coefficient based on features of the sea surface roughness under different sea states is presented in Section 4.4.3. The performances of the new and eight existing parameterizations are assessed in Section 4.4.4.

4.4.1   Wind-speed-dependent Drag Coefficient

The measured values of the drag coefficient (C_{dN}) in the neutral atmospheric conditions from eight field experiments (Table 4.2) are shown in Fig. 4.1 as a function of the wind

speed (U_{10N}). The sea state for each observational data point is classified as either the wind-sea-dominated (circle) or swell-dominated (cross) conditions based on the methodology mentioned in Section 4.3. The black dots in Fig. 4.1 represent the bin-averaged values of observed C_{dN} with the bin width of 1.0 m/s in U_{10N}. The bin-averaged values of observed C_{dN} decrease first with wind speeds at low winds ($U_{10N} < 6$ m/s) and then increase at moderate winds ($6 < U_{10N} < 25$ m/s). *García-Nava et al.* (2009) suggested that very large values of the drag coefficient at low winds are partially due to the effect of opposing swell and associated with the wind gustiness (more discussion in Section 4.6).
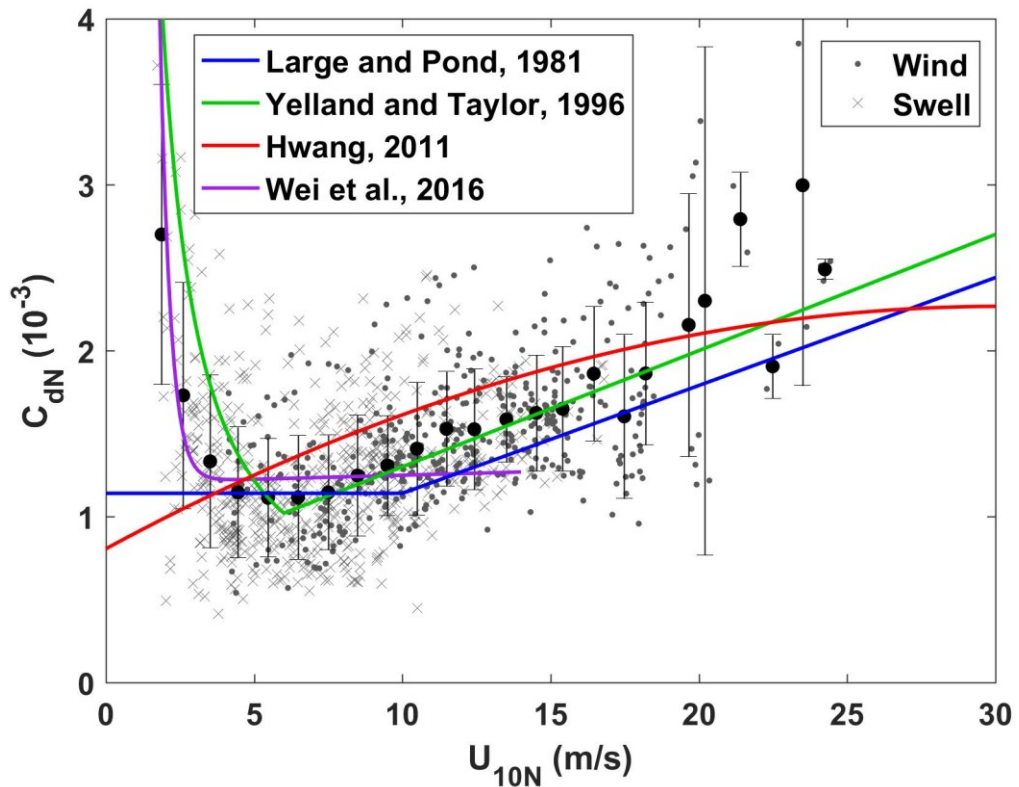
Figure 4.1: The drag coefficient versus the wind speed at 10 m above the mean sea level in neutral atmospheric conditions. The circles and crosses represent data from wind-sea-dominated and swell-dominated conditions, respectively. The error bars represent two standard deviations about the mean. The formulations from *Large and Pond* (1981, LP81, blue line), *Yelland and Taylor* (1996, YT96, green line), *Hwang* (2011, HW11, red line) and *Wei et al.* (2016, WM16, purple line) are also shown for comparisons.

To demonstrate the adequacy of existing parameterizations for the drag coefficient, four wind-speed-dependent parameterizations are also shown in Fig. 4.1. The drag coefficient suggested by *Large and Pond* (1981, LP81) is a linear function of U_{10N} for $U_{10N} \geq 11$

m/s and a constant of ~1.2×10^{-3} for U_{10N} < 11 m/s. The drag coefficient suggested by *Hwang* (2011, HW11) is a parabolic function of U_{10N} with a maximum value of ~2.3×10^{-3} at U_{10N} = 30.2 m/s. The observational data used here were those collected at low and moderate winds. It was found in previous studies (e.g., *Powell et al.,* 2003; *Donelan et al.,* 2004; *Bi et al.,* 2015) that the drag coefficient levels off at high winds. At moderate winds, both the LP81 and HW11 schemes reproduce the general trend of the bin-averaged values of observed C_{dN}, with some underestimations by the LP81 scheme and overestimations by the HW11 scheme. It should be noted that both the LP81 and HW11 schemes fail to generate the enhanced value of the drag coefficient at low winds. The enhanced drag coefficient at low winds is reproduced in the schemes suggested by *Yelland and Taylor* (1996, YT96) and *Wei et al.* (2016). One major issue of these four existing parameterizations is that they do not well represent the significant scatter of observed C_{dN} shown in Fig. 4.1. This indicates the drag coefficient at the sea surface depends on not only the wind speed but also other factors such as the sea state.

4.4.2   Wave-dependent Drag Coefficient

In this section, we examine the dependence of the drag coefficient on ocean surface waves based on observations. The wave-dependent drag coefficient is usually expressed using the relationship between the nondimensional roughness and the wave age (c_p/u_*) or wave steepness (H_s/L_p). Figure 4.2 shows the nondimensional roughness (gz_0^r/u_*^2 and z_0^r/H_s) in terms of the wave steepness (a and b) and inverse wave age (c and d) respectively, using the observational data under the wind-sea-dominated conditions. Five widely-used parameterizations for the sea surface roughness summarized in Table 4.3 are also shown in Fig. 4.2. One of important features in Fig. 4.2 is that both gz_0^r/u_*^2 and z_0^r/H_s have stronger correlations with the inverse wave age (u_*/c_p) than wave steepness (H_s/L_p), which is consistent with the finding made by *Drennan et al.* (2005). *Drennan et al.* (2005) found that the parameterization suggested by *Taylor and Yelland* (2001, TY01) underestimates the roughness for H_s/L_p < 0.02. In this study, the observational data have wider ranges of wave steepness and wave age in comparison with previous studies (e.g., *Drennan et al.,* 2005; *Edson et al.,* 2013). It is shown in Fig. 4.2c that the TY01 scheme

can predict the observed values with the medium wave steepness ($0.03 <$ H_s/L_p < 0.06), but performs poorly for the observational data with relatively lower and higher wave steepness.
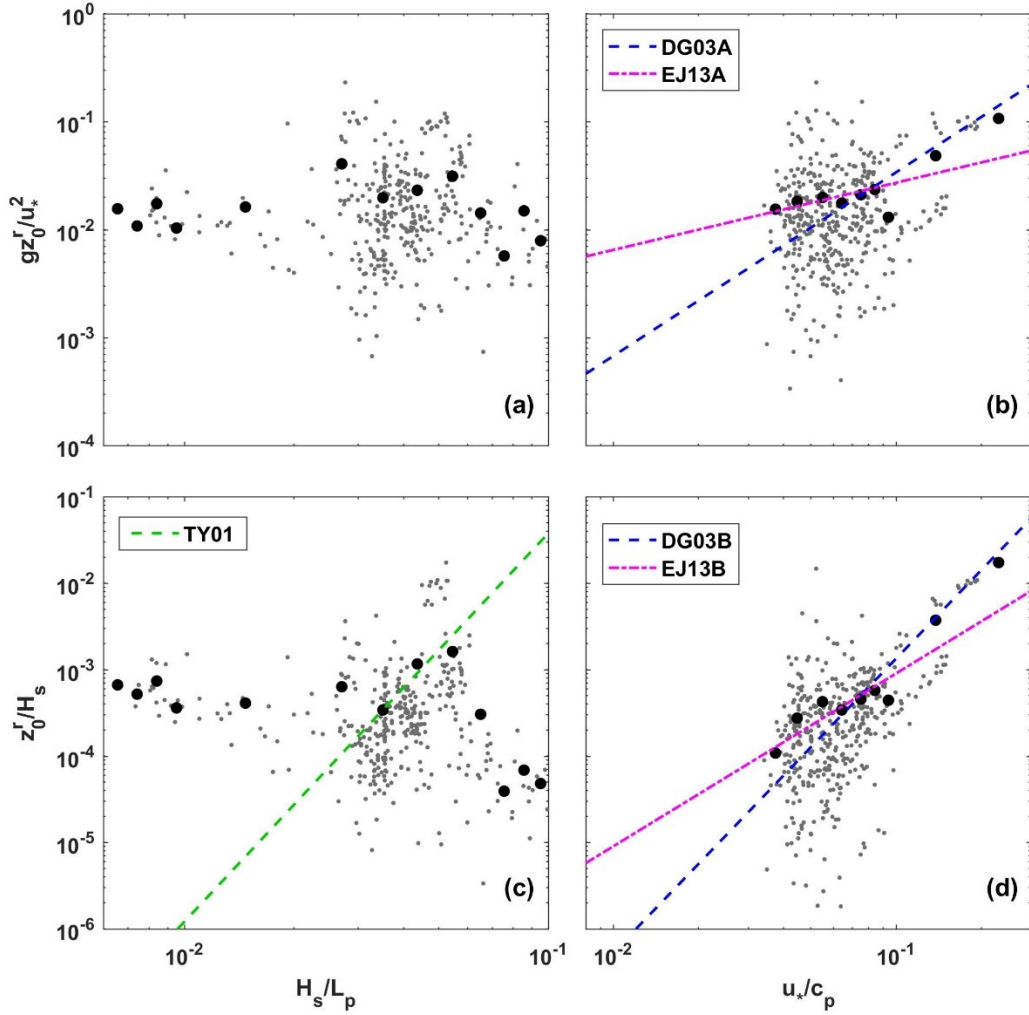
Figure 4.2: Nondimensional roughness gz_0^r/u_*^2 (a and b) and z_0^r/H_s (c and d) versus the wave steepness (a and c) and inverse wave age (b and d). Only observational data under wind-sea-dominated sea states are used here. The black dots show the bin-averaged values.

Figure 4.2 also demonstrates that the parameterizations for the sea surface roughness suggested by *Drennan et al.* (2003, DG03A and DG03B) and *Edson et al.* (2013, EJ13A and EJ13B) can predict the general mean behavior of the nondimensional roughness. Physically, younger waves have larger values of the sea surface roughness (or drag coefficient) and thus extract a larger amount of momentum from the atmosphere. Both the DG03A and DG03B schemes predict reasonably well the roughness under developing sea

states (u_*/c_p > 0.05) but underestimate the roughness under developed sea states (u_*/c_p < 0.05). By comparison, the EJ13A and EJ13B schemes have good estimations for the sea surface roughness under developed sea states but underestimate the roughness under developing sea states. This is reasonable since both the DG03A and DG03B schemes were developed using observational data under the developing sea states, while both the EJ13A and EJ13B schemes were developed without observational data for the very young waves (u_*/c_p > 0.11). Overall, gz_0^r/u_*^2 and z_0^r/H_s have stronger dependences on the wave age for the developing waves than for developed waves. It is expected that the relationship between the nondimensional roughness and the wave age is not unique under different sea states.

4.4.3   A New Parameterization of the Drag Coefficient

Most of the existing parameterizations were developed for wind-sea-dominated sea states excluding the effect of swells. The presence of swells was found to modify the logarithmic wind profile above the MSL (e.g., *Drennan et al,* 2003; *García-Nava et al.,* 2009; *Jiang et al.,* 2016), and the MOST is generally invalid under swell-dominated sea states. Therefore, the calculated values based on the logarithmic law (Eqs. 4.2 and 4.3) may not well represent the sea surface roughness under swell-dominated sea states. In this case, z_0 can be taken as an apparent roughness, which is an integration parameter for the calculation of the drag coefficient (*Smedman et al.,* 2003).

As mentioned in Section 4.4.2, the nondimensional roughness gz_0^r/u_*^2 and z_0^r/H_s are correlated more significantly with the wave age than wave steepness. In this section, we present new regressions for the nondimensional roughness in terms of the wave age for all sea states. The observed values of gz_0^r/u_*^2 and z_0^r/H_s under all sea states are shown in Fig. 4.3 in terms of the inverse wave age. The observational data under swell-dominated sea states, which were mostly collected at low wind speeds, spread over a wider range and hardly follow the existing parameterizations. This suggests that the presence of swells modifies the wind stress and further complicates the variation of the roughness. The observed values of gz_0^r/u_*^2 and z_0^r/H_s are generally larger for older waves under the swell-dominated sea states, which corresponds to the large drag coefficient values at low

winds as discussed in Section 4.4.1. The relationships between the nondimensional roughness and the wave age under the swell-dominated sea states differ significantly from those for the developing and developed wind waves. It should be noted that the non-dimensional sea surface roughness gz_0^r/u_*^2 and z_0^r/H_s have strong dependences on the wave age for developing waves but relatively weaker dependences for developed waves.

Considering different dependences of the sea surface roughness under different sea states, the sea states are further classified into three groups, namely the wind-sea-dominated ($c_p/u_* < 12$), mixed ($12 \le c_p/u_* < 30$) and swell-dominated ($c_p/u_* \ge 30$) sea states. For the accurate classification of sea states, the relative energy of swell and wind waves should be used, which requires the data of the wind speeds, wind and wave directions and wave spectra (e.g., *Smedman et al., 2003; Potter, 2015; Lin et al., 2020*). As wave spectra in the eight field experiments are not always available, sea states are empirically classified using the wave age here by following previous studies (e.g., *Smith* et *al., 1992; Edson et al., 2007*). Based on the least squares regression, we have following regressions using observational data under three different sea states:

$$
gz_0^r/u_*^2 = \begin{cases} 1.63\,(c_p/u_*)^{-1.98}, & c_p/u_* < 12 \\ 1.43 \times 10^{-2}\,(c_p/u_*)^{-0.008}, & 12 \le c_p/u_* < 30 \\ 4.03 \times 10^{-5}\,(c_p/u_*)^{1.59}, & c_p/u_* \ge 30 \end{cases} \tag{4.10}
$$

$$
z_0^r/H_s = \begin{cases} 4.54\,(c_p/u_*)^{-3.90}, & c_p/u_* < 12 \\ 5.61 \times 10^{-3}\,(c_p/u_*)^{-1.20}, & 12 \le c_p/u_* < 30 \\ 1.57 \times 10^{-5}\,(c_p/u_*)^{0.50}, & c_p/u_* \ge 30 \end{cases} \tag{4.11}
$$

The regressions shown in Eqs. 4.10 and 4.11 are made using all individual observational data points instead of the bin-averaged values to represent characteristics of all the observational data.

As shown in Eq. 4.10 (Eq. 4.11), different values are used for m_1 and m_2 (n_1 and n_2) under different sea states instead of constant values suggested by previous studies (e.g., *Drennan et al., 2003; Edson et al., 2013*). Under the wind-sea-dominated sea states, the coefficients in Eqs. 4.10 and 4.11 are close to the values suggested by *Drennan et al. (2003)*. Under the mixed sea states, the new parameterizations for gz_0^r/u_*^2 and z_0^r/H_s have lower dependences on the wave age with lower values of coefficients, in comparison with

those under the wind-sea-dominated sea states. The coefficients m_2 and n_2 are positive under the swell-dominated sea states, indicating that older waves have larger values of the drag coefficient. It should be noted that the observational data shown in Fig. 4.3 remain significant scatter with respect to the new parameterizations. This is most likely due to the sampling variability and highly-varying large-scale atmospheric features (*Chen et al.,* 2001; *Drennan et al.,* 2003).
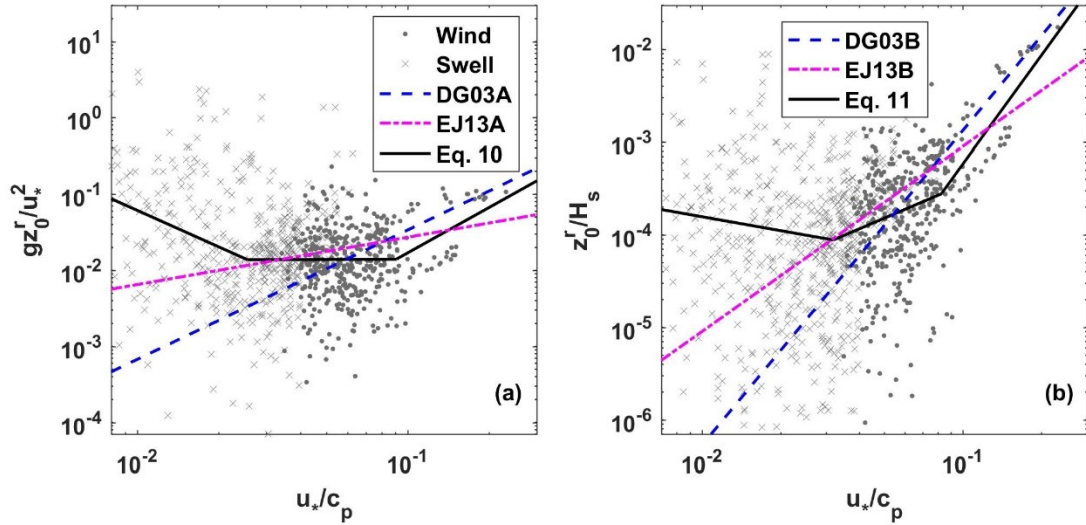
Figure 4.3: Nondimensional roughness gz_0^r/u_*^2 (a) and z_0^r/H_s (b) versus the inverse wave age. Observational data under both wind-sea-dominated and swell-dominated sea states are used here.

4.4.4   Assessment of Existing and New Parameterizations

The features of the new parameterizations for the sea surface roughness are further examined by comparing the predicted values of the drag coefficient with the existing parameterizations. The drag coefficient is calculated based on Eqs. 4.3-4.5 using different parameterizations for z_0^r (Table 4.3). The computed values of the drag coefficient for six different schemes are shown in Fig. 4.4. In the existing schemes of DG03A and EJ13A and the new scheme based on Eq. 4.10, C_{dN} depends on U_{10N} and c_p/u_*. Both DG03A and EJ13A (Figs. 4.4a and 4.4b) yield larger values of C_{dN} for higher wind speeds (or older waves). In comparison to the EJ13A scheme, the DG03A scheme has larger values of C_{dN} for young waves at high winds but smaller values for older waves at low winds. With the development of surface waves, the values of C_{dN} predicted by Eq. 4.10 first rapidly

decrease with increasing c_p/u_* and then remain almost constants and finally increase for swells (Fig. 4.4c).
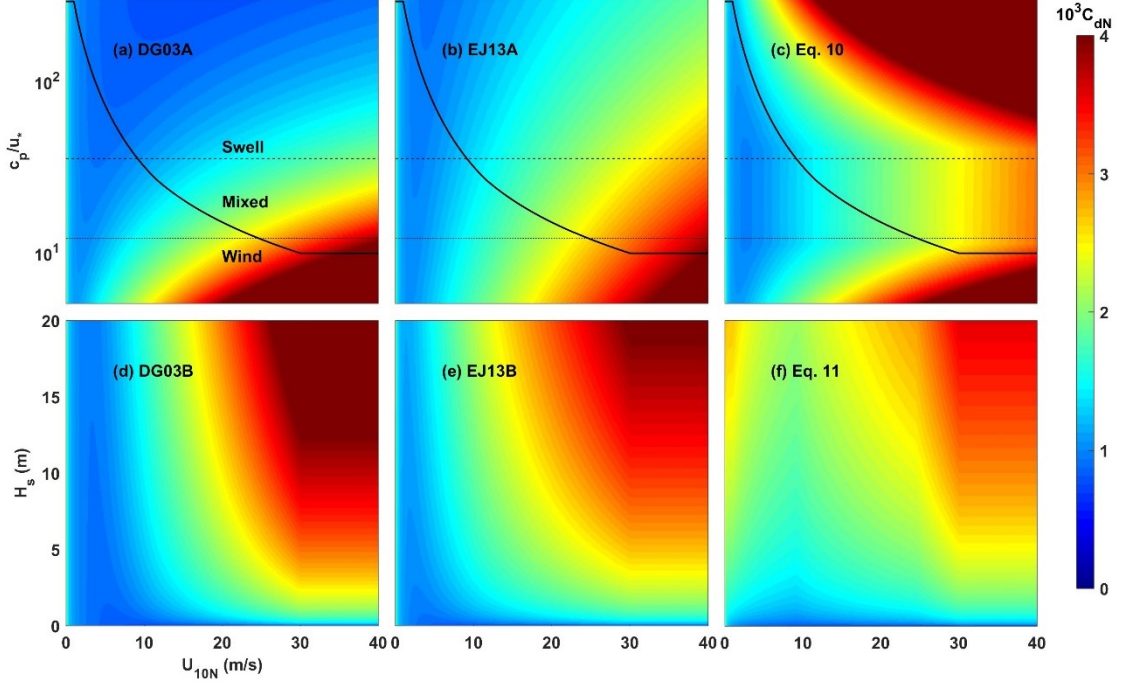
Figure 4.4: Predicted values of the drag coefficient using existing parameterizations suggested by *Drennan et al.* (2003, DG03A and DG03B), *Edson et al.* (2013, EJ13A and EJ13B), and the new parameterizations based on Eqs. 4.10 and 4.11.

In addition to U_{10N} and c_p/u_*, H_s is also important for the estimation of C_{dN} for the existing schemes of DG03B and EJ13B and the new scheme based on Eq. 4.11. Figures 4.4d-4.4f show C_{dN} as a function of U_{10N} and H_s, computed by the existing schemes of DG03B and EJ13B and the new scheme based on Eq. 4.11, considering c_p/u_* is a linear function of U_{10N} (black lines in Figs. 4.4a-4.4c) suggested by *Edson et al.* (2013, their Fig. 9):

$$c_p/u_* = 1/(0.0035 U_{10N} - 0.0023), \qquad 1 \leq U_{10N} \leq 30 \text{ m/s} \qquad (4.12)$$

The wave age for Eq. 4.12 is limited for the range of $1 \leq U_{10N} \leq 30$ m/s to avoid the unrealistic values. Both the DG03B and EJ13B schemes (Figs. 4.4d and 4.4e) suggest that larger waves have larger values of C_{dN}. The values of C_{dN} predicted by Eq. 4.11 (Fig. 4.4f) are smaller than those in the existing schemes of DG03B and EJ13B and more reasonably represent the saturation of C_{dN} at high winds. As mentioned in Section 4.4.1,

the drag coefficient levels off or even decreases at high winds based on the field and laboratory measurements (e.g., *Powell et al.,* 2003; *Donelan et al.,* 2004). In comparisons, the drag coefficient predicted by the existing schemes of DG03A and EJ13A and the new scheme based on Eq. 4.10 has very large values since waves at high winds are generally young with low values of c_p/u_*. Moreover, the new parameterization based on Eq. 4.11 is the only one to yield the enhanced drag coefficient at low winds. Thus, the drag coefficient predicted by the new scheme based on Eq. 4.11 at different sea states are more realistic than the existing schemes.

Another useful assessment of the new and existing parameterizations is to investigate their performances in predicting the measured friction velocity. Figure 4.5 shows the comparisons between measured values of u_* from eight field experiments and the predicted values using ten different parameterizations (listed in Table 4.3). To quantify their performances, four error metrics are introduced. These four metrics (*Lin and Sheng,* 2017) include the root mean square error (RMSE), relative bias (RB), scatter index (SI), and correlation coefficient (R). The values of the error metrics for u_* are summarized in Table 4.3.
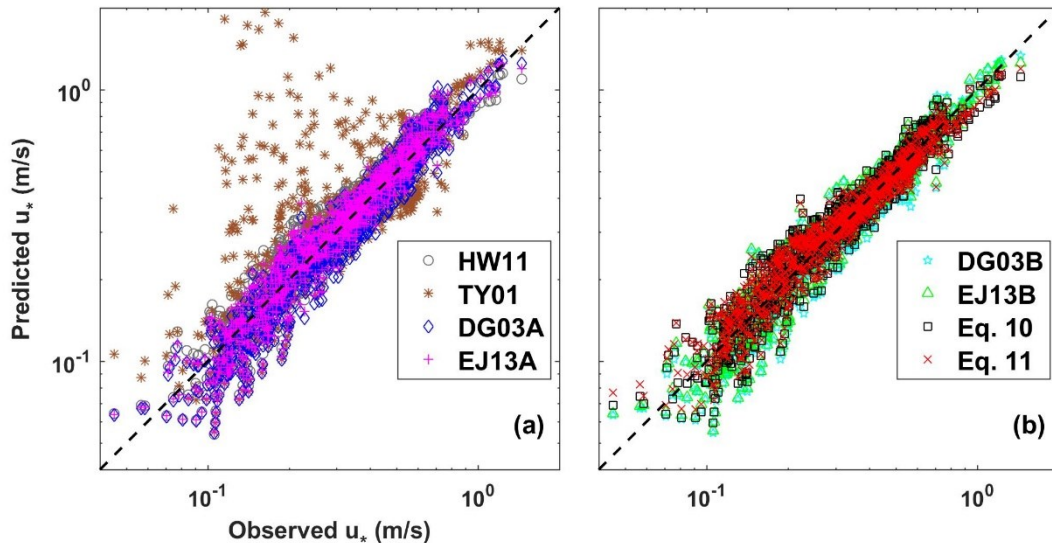
Figure 4.5: Predicted values of the friction velocity using different parameterizations (Table 4.3) for the drag coefficient versus the observed values in eight field experiments.

Table 4.3: Different parameterizations for the drag coefficient at the sea surface and corresponding error metrics for the predicted friction velocity.

Abbr.	Reference	Formulation	u_*			
			RMSE (cm/s)	RB (%)	SI (%)	R (%)
LP81	*Large and Pond*	$10^3 C_{dN} = 0.49 + 0.065 \max(U_{10N}, 11)$	5.7	-4.0	16.3	96.4
HW11	*Hwang* (2011)	$10^4 C_{dN} = 8.058 + 0.967 U_{10N} - 0.016 U_{10N}^2$	6.0	6.2	17.1	96.4
YT96	*Yelland and Taylor* (1996)	$10^3 C_{dN} = 0.29 + 3.1 U_{10N}^{-1} - 7.7 U_{10N}^{-2}$, $3 \leq U_{10N} \leq 6 m/s$ $10^3 C_{dN} = 0.7 + 0.07 U_{10N}, 6 \leq U_{10N} \leq 26 \, m/s$	5.3	0.3	14.9	96.6
TY01	*Taylor and Yelland* (2001)	$z_0^r / H_s = 1200 (H_s/L_p)^{4.5}$	51.4	27.1	146.0	31.1
DG03A	*Drennan et al.* (2003)	$\alpha_c = 1.7 \, (c_p/u_*)^{-1.7}$	5.4	-2.5	15.3	96.8
DG03B	*Drennan et al.* (2003)	$z_0^r / H_s = 3.35 \, (c_p/u_*)^{-3.4}$	5.2	-2.7	14.8	96.9
EJ13A	*Edson et al.* (2013)	$\alpha_c = 0.114 \, (c_p/u_*)^{-0.622}$	5.2	2.3	14.8	96.9
EJ13B	*Edson et al.* (2013)	$z_0^r / H_s = 0.09 \, (c_p/u_*)^{-2}$	5.0	1.4	14.1	96.9
Eq. 4.10	*This study*	$\alpha_c = m_1 \, (c_p/u_*)^{m_2}$	5.2	2.2	14.8	96.7
Eq. 4.11	*This study*	$z_0^r / H_s = n_1 \, (c_p/u_*)^{n_2}$	**4.6**	**-0.4**	**13.1**	**97.5**

The traditional wind speed formula suggested by LP81 shows systematic underestimations of u_* with negative RB values. The HW11 scheme underestimates u_* at low winds but overestimates u_* at moderate winds with overall positive RB values. Due to the undesirable representations of z_0^r for waves with low and high wave steepness, the wave steepness formula in TY01 has the largest errors. The wave age formulas in the existing schemes of DG03A, DG03B, EJ13A and EJ13B reasonably represent u_* with the SI values less than 15.3%. Among them, the wave height scaling parameterizations (DG03B and EJ13B) have better performances than the Charnock parameterizations (DG03A and EJ13A), since the former group includes the dependences of C_{dN} on $c_p/u_*, U_{10N}$ and H_s. A comparison between Eq. 4.10 and Eq. 4.11 further demonstrates the importance of including the dependence of C_{dN} on H_s. The data points computed by the new scheme based on Eq. 4.11 (red cross) spread close to the perfect-fitting line (black dashed line) and reduce the underestimations of the observed large values of u_* at low winds. Overall, the new scheme based on Eq. 4.11 has the best performance with the smallest SI value (13.1%) and the best correlation value (97.5%). Thus, the new scheme based on Eq. 4.11 is

qualitatively and quantitatively more reasonable than the existing schemes and the new scheme based on Eq. 4.10.

4.5 Wave Simulations Using Different Drag Coefficient Parameterizations

To examine the applicability of the new scheme and three widely-used schemes (DG03A, DG03B, HW11) for the drag coefficient at the sea surface, these four schemes are implemented in a nested-grid ocean wave modelling system for the northwest Atlantic (NWA). The nested-grid modelling system and setup are introduced in Section 4.5.1. Model forcing and available wave observations are presented in Sections 4.5.2 and 4.5.3, respectively. The wave model results during the winter storm in March 2014 are examined using observational data from in-situ buoys and satellite altimeters in Section 4.5.4.

4.5.1   Spectral Wave Model and Setup

The wave model used here is the third-generation spectral wave model WAVEWATCH III (WW3, version 5.16), which consists of all physical processes for wave growth and decay. A nested-grid setup is used with two sub-models. The outer sub-model domain covers the region between 85°W and 0°W and between 10°N and 65°N, with a spatial resolution of 1/4°. The inner sub-model domain covers the NWA between 82°W and 40°W and between 25°N and 55°N, with a spatial resolution of 1/12° (Fig. 4.6). The nested-grid ocean wave modelling system is integrated for March 2014. The results produced by the outer sub-model are used to specify the open boundary conditions for the inner sub-model. The inner sub-model results during the period between 20 and 30 March 2014 are used in the following analyses.

The wave model uses the spherical coordinates and the discrete spectrum consisting of 36 directions ($\Delta\theta$ = 10°) and 31 frequencies ranging from 0.04 to 0.70 Hz at a logarithmic increment of 0.1. The source term package known as ST6 (*WW3DG,* 2016) is used to compute the wind input and wave dissipation (*Lin et al.,* 2020). Package ST6 uses the wind-speed-dependent drag coefficient suggested by *Hwang* (2011, HW11). In addition to HW11, two existing schemes (DG03A and DG03B) and the new scheme based on Eq. 4.11 (hereafter NEW) are used to compute the drag coefficient in wave simulations.

Parameterizations for the nonlinear wave interactions, bottom friction, and wave dissipation in ice are the same as in *Lin et al.* (2020).
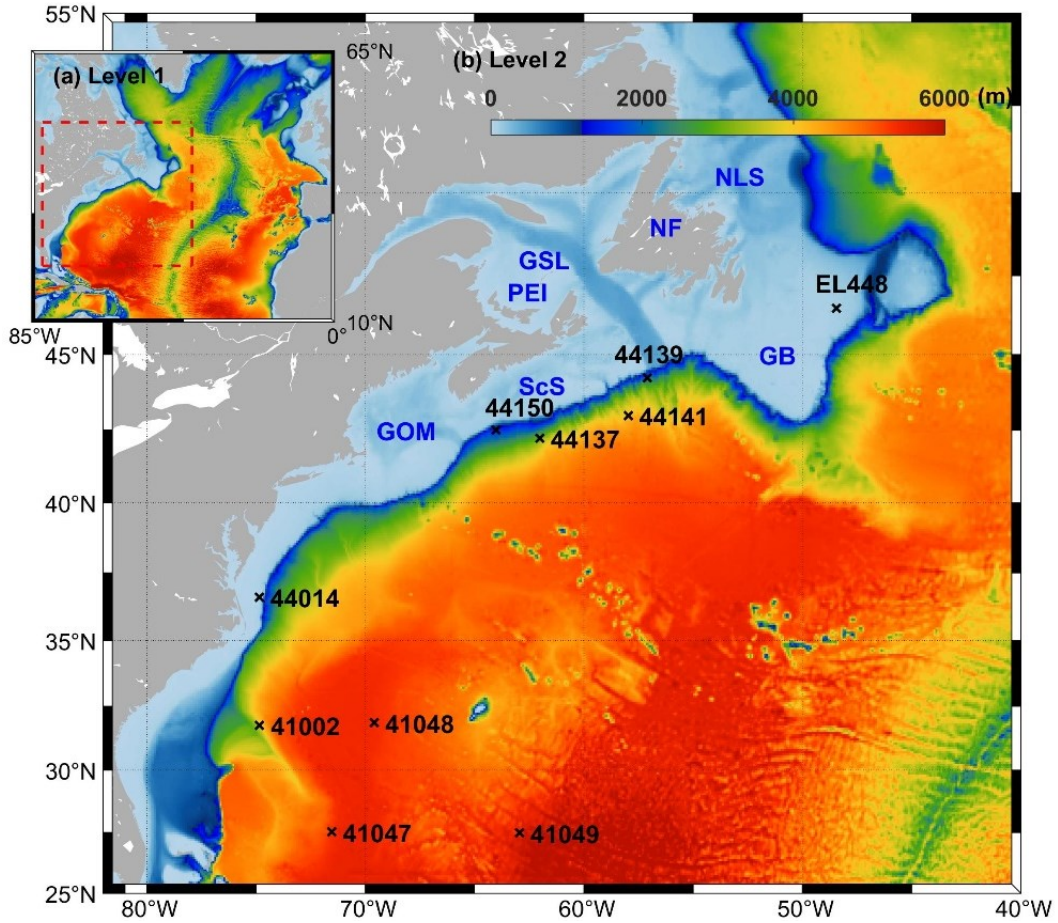
Figure 4.6: Domains and major topographic features of (a) the outer sub-model for the north Atlantic and (b) the inner sub-model for the northwest Atlantic. Black crosses denote buoy stations with wind and wave observations.

4.5.2   Model Forcing

The forcing fields used to drive the wave model include the hourly wind fields (U_{10}) extracted from the Climate Forecast System reanalysis version 2 (CFSv2, *Saha et al.,* 2014). The ocean surface currents and sea surface elevations extracted from 3-hourly HYCOM global reanalysis dataset (*Cummings and Smedstad,* 2013) are used in the wave modelling system to account for the effects of currents on surface gravity waves. The presence of sea ice during the winter storm affects the air-sea fluxes and dissipates wave energy. In this

study, the observed daily ice data from the Canadian Ice Service (CIS), including the ice concentration, thickness and floe size, are used in the wave modelling system.

A strong winter storm known as the March 2014 nor'easter had peak sustained winds of about 39.7 m/s (about 143 km/h) and was the most powerful winter storm in the North American winter storm seasons of 2013-2014. Figure 4.7 shows the wind fields, surface currents and ice concentrations at 2100 UTC 26 March 2014. The massive nor'easter reached its peak intensity at this time with strong winds affecting New England, Nova Scotia and Newfoundland (Fig. 4.7a). Figure 4.7b shows that the Gulf Stream and surface currents during this winter storm were strong and up to 2.5 m/s. The sea ice on 26 March 2014 occurred over the Labrador and northern Newfoundland shelves and in the Gulf of St. Lawrence (Fig. 4.7c).
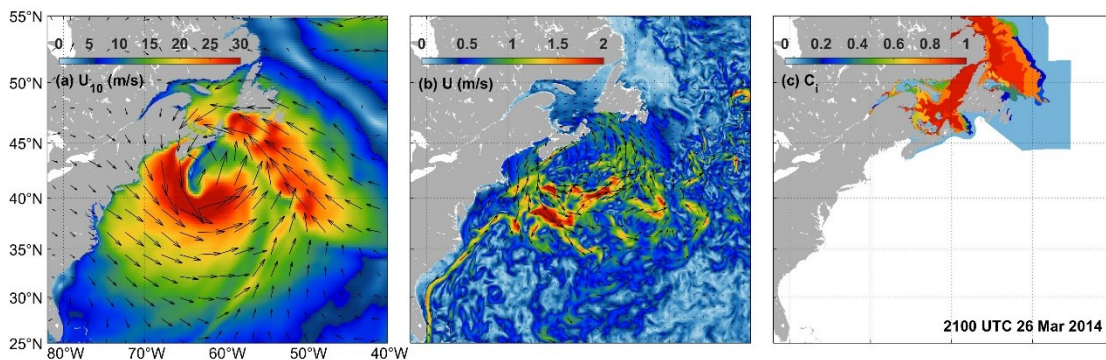
Figure 4.7: Snapshots of (a) wind fields (U_{10}) at 10 above the mean sea level from the CFSv2, (b) surface currents (U) from the HYCOM and (c) ice concentrations from the CIS at 2100 UTC 26 March 2014. Arrows in (a) and (b) represent the wind directions and current directions, respectively.

4.5.3   Wind and Wave observations

The observational wind and wave data used in this study include the in-situ observations from buoys and remote sensing measurements from satellite altimeters. These observational data are used to assess the accuracy of wind forcing and wave model results. The in-situ wind and wave observations at ten offshore buoy stations within the model domain (Fig. 4.6) were obtained from the National Data Buoy Center (NDBC) and Environment and Climate Change Canada (ECCC). The altimeter data were obtained from

the database constructed by the GlobWave project (*GlobWave Product User Guide,* 2013). More details about the observational data are described in *Lin et al.* (2020).

4.5.4 Wave Model Results

Four schemes (DG03A, DG03B, HW11 and NEW) for the drag coefficient at the sea surface are examined using the inner wave sub-model. Figure 4.8 presents the calculated drag coefficient as a function of the relative wind speed ($U_r = U_{10} - 0.7U_{oc}$, where U_{oc} is the ocean surface current) and wave age (c_p/u_*). The drag coefficients in three schemes of DG03A, DG03B and NEW are wave-state dependent and can be converted from the friction velocity based on $C_d = u_*^2/U_r^2$. It should be noted that only C_d values over the deep waters (> 500 m) are used here to exclude the effects of strong nonlinearity waves over the coastal areas (*Babanin and Makin,* 2008). One of the key features of the HW11 scheme is that C_d reaches a maximum value of 2.3×10^{-3} at U_r = 30.2 m/s and decreases at higher winds. As mentioned in Section 4.4, the observational data indicated that the drag coefficient C_d does not increase continuously but levels off or even decreases at high winds (e.g., *Powell et al.,* 2003; *Donelan et al.,* 2004).

The average C_d in the DG03A and DG03B schemes has small values around 9.0×10^{-4} at low winds (U_r < 8 m/s) and then increases rapidly with values large than 3.0×10^{-3} at high winds (U_r > 32 m/s). Overall, the drag coefficients in the DG03A and DG03B schemes are too small at low and moderate winds but too large at high winds. The new scheme based on Eq. 4.11 has two important features that the averaged C_d has larger values for lower winds at low winds and levels off at around 2.5×10^{-3} at high winds. In comparison with the HW11 scheme, the average C_d in the new scheme has larger values at low winds, smaller values at moderate winds and slightly larger values at high winds. The formulas LP81 and YT96 are also shown in Fig. 4.8a for comparisons. The drawbacks of these two formulas are that LP81 shows low values of C_d at moderate winds and YT96 produces too large values of C_d at low winds. The more important reason for not using these two formulas in wave simulations is that C_d only depends on the wind speed in these two formulas and thus the variations of C_d under different sea states cannot be represented.

The differences of these four parameterizations are also shown in Fig. 4.8b in terms of the wage age. The averaged C_d in the DG03A and DG03B schemes decreases rapidly as waves become older until levels off at 9.0×10^{-4} for $c_p/u_* > 60$, which corresponds to low values of the averaged C_d at low winds. Although C_d in the HW11 scheme only depends on the wind speed, the averaged C_d in the HW11 scheme has lower values for older waves as waves at lower winds are generally older. In comparison with the HW11 scheme, the averaged C_d in the new scheme has larger values for young waves ($c_p/u_* <$ 15), smaller values for relatively old waves ($15 < c_p/u_* < 50$) and larger values for old waves ($c_p/u_* > 50$). The averaged C_d in the new scheme slightly increases as waves become older for $c_p/u_* > 50$, which corresponds to the enhanced values of the averaged C_d at low winds.
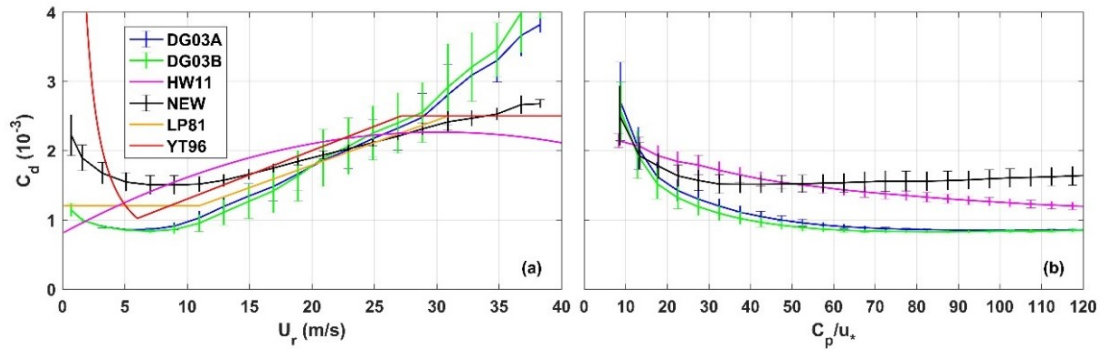
Figure 4.8: Values of the drag coefficient predicted by different parameterizations as a function of (a) the relative wind speed and (b) wave age. The error bars represent the corresponding standard deviations. The formulas for the drag coefficient suggested by *Large and Pond* (1981, LP81) and *Yelland and Taylor* (1996, YT96) with a maximum value (2.5×10^{-3}) at high winds are also shown for comparisons.

The use of different schemes of C_d leads to different wind stresses at the ocean surface and thus different sea states. Figure 4.9 shows snapshots of the friction velocities (u_*) and SWHs (H_s) at 2100 UTC 26 March 2014. The corresponding observed SWHs from the altimeter track are overlaid in Figs. 4.9a2-4.9d2 bounded by the white lines. In comparison with the HW11 scheme and the new scheme, both the DG03A and DG03B schemes generate larger values of u_* at strong winds of the winter storm but smaller values of u_* elsewhere. This is consistent with distributions of C_d shown in Fig. 4.8 that the DG03A and DG03B schemes generate small values of C_d at low and moderate winds but large

values at high winds. Therefore, both the DG03A and DG03B schemes overestimate H_S at high winds but underestimate H_S at low and moderate winds. The HW11 scheme has better agreement with the observed H_S but generally overestimates H_S for $H_S > 8$ m. Overall, the simulated H_S using the new scheme has the best agreement with the observed spatial variations.
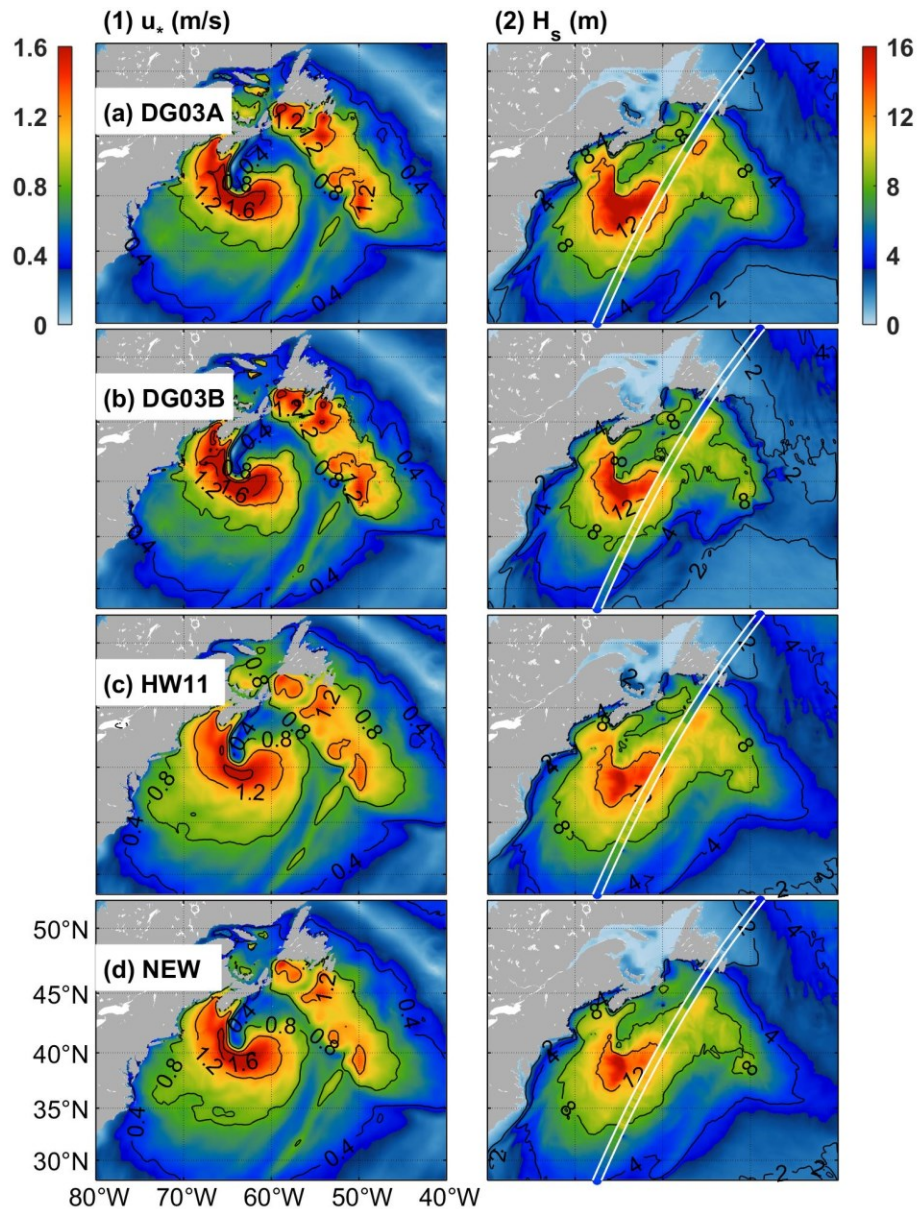
Figure 4.9: Snapshots of (first column) the friction velocity at the sea surface and (second column) SWHs predicted by the inner wave model using four different parameterizations for the drag coefficient (DG03A, DG03B, HW11 and NEW, rows a-d) at 2100 UTC 26 March 2014. The corresponding observed SWHs along the satellite track are overlaid in the second column bounded by white lines.
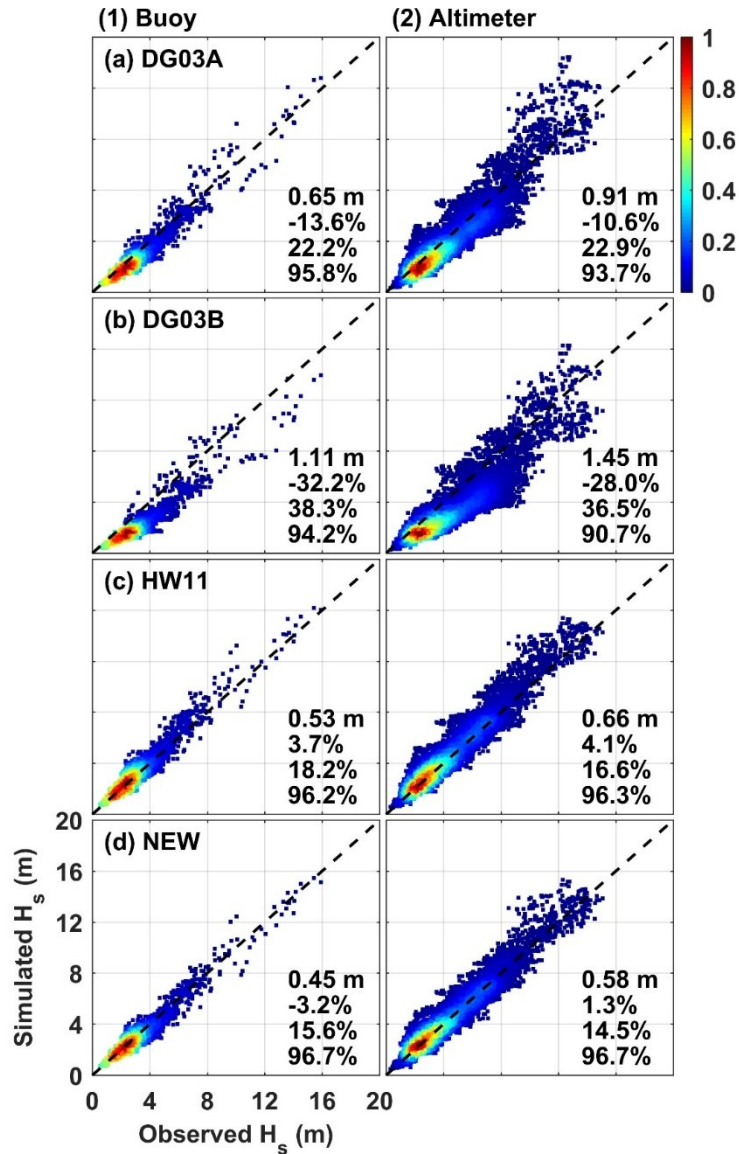
Figure 4.10: Scatter plots for SWHs between simulated values using four different parameterizations for the drag coefficient (DG03A, DG03B, HW11 and NEW, rows a-d) and observed values from (first column) buoys and (second column) satellite altimeters during the winter storm in March 2014. Values for the RMSE, RB, SI and R are shown in sequence in each panel.

We now compare the inner wave model results using four different schemes of the drag coefficient (DG03A, DG03B, HW11 and NEW) with observations from buoys and altimeters introduced in Section 4.5.3. The simulated SWHs are compared with observed values in terms of scatter plots shown in Fig. 4.10. The corresponding error metrics (RMSE, RB, SI and R) are also shown. Among the four schemes, the DG03A and DG03B schemes perform less well with significant underestimations of the observed SWHs with a RB up

to -32.2% (Figs. 4.10a1, 4.10a2, 4.10b1 and 4.10b2). This is due to the fact that the DG03A and DG03B schemes have low values of C_d at low winds when the SWHs are generally small. Moreover, the DG03A scheme overestimates H_s for the most energetic sea states as it has high values of C_d at high winds. The HW11 scheme performs better than the DG03A and DG03B schemes with an average SI of ~17.4% (Figs. 4.10c1 and 4.10c2). In comparison, the new scheme has the best performance with data points closely following the perfect-fitting line with an average SI of ~15.0% (Figs. 4.10d1 and 4.10d2). This is attributed to that the new scheme has more accurate prediction of the drag coefficient than the HW11 scheme by taking account of the different dependences on the wave age and SWH at different sea states.

The performances of these four schemes are further examined under different sea states. The bin-averaged values of the RB for SWHs in terms of the wind speed and wave age are shown in Fig. 4.11 based on observations from both buoys and altimeters. Both the DG03A and DG03B schemes have large negative bias for majority wave conditions with a RB up to -40% but overestimate large waves at high winds ($U_r > 20$ m/s). In comparison, the HW11 scheme also overestimates large waves but has relatively small biases for low and moderate winds ($U_r < 20$ m/s) and for relatively older waves ($c_p/u_* > 15$) with RB values within $\pm 10\%$. The new scheme has the best performance, which reduces the underestimations of H_s at low winds (or old waves) and the overestimations of H_s at moderate and high winds (or young waves) associate with the other three existing schemes.
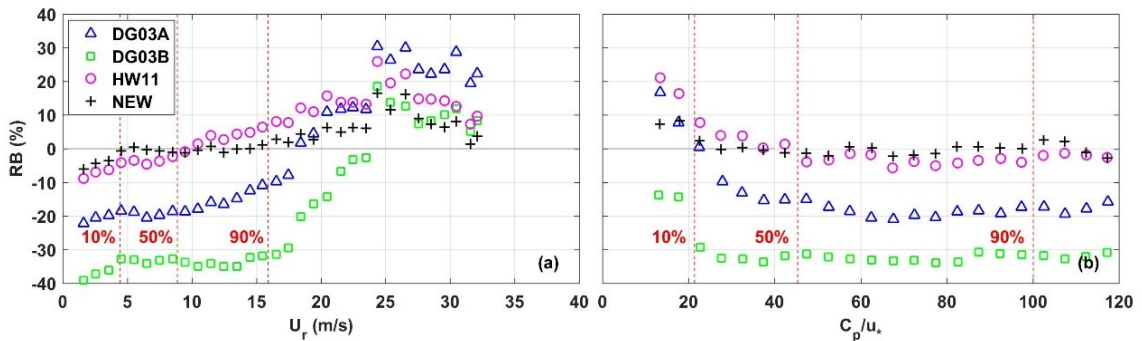
Figure 4.11: The relative bias (RB) for SWHs for model results using four different schemes for the drag coefficient (DG03A, DG03B, HW11 and NEW) in terms of (a) the relative wind speed and (b) wave age during the March 2014 nor'easter. The SWHs at specific cumulative frequencies (10%-90%) are shown by the red dashed lines.

4.6 Discussion and Conclusions

Accurate estimation of wind stress at the sea surface is still a great challenge, due partially to insufficient high-quality field observations and partially to complicated atmospheric and oceanic processes affecting the sea surface roughness. Field measurements of wind stress require precise measurements of wind turbulent fluctuations in the atmospheric boundary layer above the wavy ocean surface. However, the scatter of observational data with respect to previous and new parameterizations should not blame solely on the errors of measurements. The main difficulties arise from a wide rang of aspects (*Babanin and Makin,* 2008). It has long been recognized that wave states can strongly affect the air-sea momentum transfer (e.g., *Smith et al.,* 1992; *Drennan et al.,* 2003). However, wave states may not be simply represented by the wave steepness, wave age and significant wave height as used in many previous and the new parameterizations for the drag coefficient. Wave steepness is a geometric parameter measuring the wave nonlinearity. Wave age represents the relative speed between waves and winds and determines the ability of momentum transfer (*Zhao and Li,* 2019). The wave effects on the wind stress is controlled by a full wave spectrum instead of several wave parameters (e.g., *Takagaki et al.,* 2012; *Donelan et al.,* 2012; *Thomson et al.,* 2013; *Reichl et al.,* 2014). *Takagaki et al.* (2012) and *Thomson et al.* (2013) showed a strong correlation between the drag coefficient and spectral levels of both the equilibrium range and the swell range. *Donelan et al.* (2012) and *Reichl et al.* (2014) calculated the wind stress based on the full wave spectrum and suggested that the drag coefficient magnitude is very sensitive to the spectral tail.

The presence of swells further complicates the estimation of the drag coefficient and thus the surface wind stress. Wave states can be better represented by the relative energy of swell and wind waves (E_s/E_w) based on the wave spectra in comparison with the wave age. *Smedman et al.* (2003) quantified the swell contribution to the wind stress by introducing the dependence of the drag coefficient on E_s/E_w. A similar approach to estimate the swell contribution is to use the partition SWHs of swell components, as suggested by *Högström et al.* (2015).

Wave directionality also plays an important role in modifying the wind stress. *Ting et al.* (2012) showed the dependence of the drag coefficient on the directional spreading of surface waves. It was shown that the drag coefficient can increase by almost a quarter in narrow wave spectra for the same wind speed and wave age. *Holthuijsen et al.* (2012) also identified the effects of wave directional spreading on the drag coefficient and showed large differences for the drag coefficient in different quadrants of hurricanes. In additional to the wave directional spreading, this is also due to that the rotated hurricane winds can blow in the opposing, cross and following directions of swells in different quadrants. It was found that the drag coefficient generally increases in the presence of opposing swells but decreases for following swells (e.g., *Drennan et al.,* 1999; *García-Nava et al.,* 2009; *Potter,* 2015). This is part of the reason that the drag coefficient can have low values at low winds although the averaged values are enhanced at low winds (Fig. 4.1).

As mentioned in Section 4.4.1, the enhanced drag coefficient at low winds is due to the opposing swells and wind gustiness, which is also shown in previous studies (e.g., *Janssen,* 1989, *Li et al.,* 2016; *Wei et al.,* 2016). The wind gustiness is primarily produced by the large-scale turbulence as the wind speed approaching the free convective condition (*Drennan,* 2006). Wind gustiness can cause the wind to vary widely in both magnitude and direction with respect to the mean values particularly at low winds. Uncertainty in predicting the stress at low winds thus is associated with the largely varying magnitude and direction of winds (*Babanin and Makin,* 2008).

The other difficulty lies in estimations of wind stress at high winds. Measurements of wind stress in extreme wind conditions are relatively limited due to the adverse sea states. At high winds, the drag coefficient was found to level off or even decrease based on the field measurements (e.g., *Powell et al.,* 2003; *Jarosz et al.,* 2007; *Bi et al.,* 2015; *Holthuijsen et al.,* 2012), laboratory experiments (e.g., *Donelan et al.,* 2004; *Takagaki et al.,* 2016) and theoretical studies (e.g., *Moon et al.,* 2004). This saturation behavior at high winds can be attributed to the air-flow separation and sea spray droplets generated by intensive wave breaking (*Powell et al.,* 2003; *Takagaki et al.,* 2016). The new parameterization for the drag coefficient presented in this study (Eq. 4.11) can produce this saturation behavior with

the drag coefficient leveling off at ~2.5×10^{-3} at high winds (Fig. 4.8), which is consistent with many previous studies (e.g., *Powell et al.,* 2003; *Donelan et al.,* 2004).

Moreover, the drag coefficient can be different in the open ocean and coastal waters. Previous observations demonstrated that the drag coefficient in coastal waters is typically larger than that in the open ocean (e.g., *Drennan et al.,* 1999; *Oost et al.,* 2002; *Smith et al.,* 1992). The enhancement of the drag coefficient at coastal water is mainly caused by wave steepening and reduction of the wave phase speed in finite depth (*Chen et al.,* 2020). *Chen et al.* (2020) suggested that enhancement of the drag coefficient in shallow waters is within 25%-40% and it is sensitive to the bottom slope with a larger increase on a steeper bottom slope.

The above-mentioned effects, however, have not been considered yet in many previous and the new parameterizations for the drag coefficient, indicating limitations of these parameterizations. There are other factors can also contribute to the wind stress. *Babanin and Makin* (2008) summarized a series of physical properties and phenomena that can affect the wind stress. Incorporation of these factors in addition to the wind speed, SWH and wave age in the new parameterization can further reduce the scatter of observational data with respect to the parameterization. Furthermore, the estimation of the wind stress using the new parameterization for the drag coefficient still has relatively large errors at low and high winds (Figs. 4.8 and 4.11). With additional observations, the new parameterization proposed in this study is expected to be improved by quantitively addressing some of these effects on the wind stress. Nevertheless, it has been demonstrated that the new parameterization for the drag coefficient overall reproduces well the field observations of wind stress and significantly improves the accuracy of wave simulations over the NWA.

In summary, a new parameterization was presented here for the sea surface roughness in terms of the wind speed and sea state. The new parameterization was based on analyses of observed wind stress and wave parameters from eight field experiments under a wide range of wind and wave conditions. It was found that the nondimensional roughness (gz_0^r/u_*^2 and z_0^r/H_s) is more significantly correlated with the wave age than wave steepness. In

comparison with previous parameterizations, one important feature for the new parameterization is that the nondimensional roughness has different dependences on the wave age under different sea states, which shows the enhanced drag coefficient at low winds. The other important feature is that the new parameterization includes the dependences on not only the wave age (c_p/u_*) and wind speed (U_{10N}) but also the SWH (H_s), which allows the saturation of drag coefficient at high winds. The new parameterization (Eq. 4.11) can be used to quantitively estimate the drag coefficient under different sea states. In comparison with previous schemes, the new parameterization significantly improves the estimations of the wind stress with an average SI of ~13.1% for the friction velocity, in comparison with the SI values large than 14.1% from several existing schemes. Moreover, the new parameterization is the only parameterization which can well represent the observed variations of the drag coefficient from low to high wind conditions (Fig. 4.8).

Considering the importance of the air-sea momentum flux, the applicability of different parameterizations for the nondimensional roughness and drag coefficient was investigated using a nested-grid ocean wave modelling system based on WW3. Wave model results using the new and three existing parameterizations for the drag coefficient during a powerful winter storm in March 2014 over the NWA were compared with the available measurements from in-situ buoys and satellite altimeters. It was found that the uniform dependence of the nondimensional roughness on the wave age (DG03A and DG03B) has small values of the drag coefficient at low and moderate winds but large values at high winds. Therefore, the SWHs predicted by the existing schemes of DG03A and DG03B are overestimated at high winds but overall have large negative bias with an average RB up to -32.2%. By comparison, the new parameterization has different dependences on the wave age and SWH under different sea states. The new parameterization thus performs the best in predicting the SWHs with an average SI of ~15.0%, which surpasses the default parameterization of the drag coefficient (HW11) in WW3 with an average SI of ~17.4%.

CHAPTER 5

PERFORMANCES OF WAVE BREAKING PARAMETERIZATIONS IN THE SPECTRAL WAVE MODEL[1]

5.1 Introduction

Wind-generated surface gravity waves are the most prominent feature at the ocean surface. The development of ocean waves is determined mainly by the balance between the wind momentum transfer and energy dissipation due to wave breaking. In deep waters, whitecapping, which is the steepness-induced wave breaking, accounts for the most significant energy dissipation for the ocean waves. As waves move into increasingly shallow waters, depth-induced wave breaking becomes the primary dissipation mechanism. In coastal waters, depth-induced wave breaking has been of particular interest due to its important role in many scientific and engineering applications, such as coastal engineering design, beach morphology and surf zone hydrodynamics. Breaking waves exert large forces on coastal structures, drive sediment transport, and generate ocean currents and turbulence in the surf zone. The physical processes associated with depth-induced wave breaking in shallow waters, however, have not been fully understood (*Salmon et al.,* 2015).

Depth-induced wave breaking is normally parameterized in wind wave models. The most widely-used parameterization for depth-induced wave breaking was suggested by *Battjes and Janssen* (1978, BJ78). In fact, BJ78 is the default parameterization for depth-induced wave breaking specified in most spectral wave models. BJ78 combines the wave breaking probability within a random wave field and an individual breaking wave height calculated

---

[1]Lin, S., and Sheng, J. (2017). Assessing the performance of wave breaking parameterizations in shallow waters in spectral wave models. *Ocean Modell.,* 120, 41-59. doi:10.1016/j.ocemod.2017.10.009

from the breaker index. Since BJ78, various parameterizations have been proposed for the breaker index or wave breaking probability (e.g. *Thornton and Guza,* 1983; *Nelson,* 1987; *Battjes and Stive,* 1985; *Ruessink et al.,* 2003; *Goda,* 2010).

Most of these parameterizations are empirical or semi-empirical. *Rattanapitikon* (2007) investigated the applicability of eight existing parameterizations for depth-induced wave breaking and showed the improvement of the wave prediction accuracy by using recalibrated coefficients in the existing parameterizations. *Apotsos et al.* (2008) assessed nine existing parameterizations using field observations and also showed the reduction of model errors by tuning the breaker index in the existing parameterizations. *Salmon et al.* (2015, SA15) recently examined the performances of twelve different wave breaking parameterizations and identified their limitations using laboratory and field observations. They found that BJ78 performs well in a wide range of situations, but has a problem of overestimating the significant wave heights (SWHs) over flat bottoms when waves are remotely generated and underestimating the SWHs in locally generated wave conditions. The assessment made by SA15 confirmed earlier findings made by *Nelson* (1987), *Katsardi* (2007), *van der Westhuysen* (2010) and *Bottema and van Vledder* (2009) about the drawbacks of BJ78. The parameterization suggested by *Thornton and Guza* (1983) was found to predict extensive dissipation in the outer surf zone and thus underpredict the wave heights. To overcome these limitations, SA15 suggested a dependence of the breaker index on both the local bottom slope and normalized water depth. The parameterization suggested by SA15 was shown to improve the model performance of simulating SWHs with an average error of ~11%, in comparison with the model errors between 13% and 43% for other twelve parameterizations. SA15 significantly reduces the model error in simulating SWHs over flat bottoms, but performs less well over sloping bottoms in comparison with BJ78. Although major limitations of existing wave breaking parameterizations were identified, physical interpretations of these parameterizations were not well described.

In this study, the performances of six commonly-used parametrizations for depth-induced wave breaking in spectral wave models are assessed using laboratory and field observations, which include 882 cases from 14 sources of published observational data. We interpret the underlying physics contributing to different performances of these parameterizations and

demonstrate the dependences of the breaker index on the bottom slope and normalized water depth. We then follow the methodology suggested by SA15 and develop a new parameterization to improve the performance of spectral wave models for depth-induced wave breaking over both flat and sloping bottoms.

This chapter is structured as follows. Section 5.2 presents a brief description of the third-generation spectral wave model and introduces six existing parameterizations and a new parameterization for depth-induced wave breaking used in spectral wave models. Section 5.3 describes the laboratory and field observational data, the numerical wave model setup, and the method used to analyze the results. Section 5.4 presents comparisons between model results and observations using six existing and the new parameterizations for depth-induced wave breaking. Section 5.5 is a summary and conclusion.

5.2 Model Description and Depth-induced Wave Breaking Parameterizations

5.2.1   Spectral Wave Model

The spectral wave model Simulating Waves Nearshore (SWAN, version 41.01) is used in this study to assess different parameterizations for depth-induced wave breaking. SWAN has been developed for simulating the growth, decay, and transformation of wind-generated ocean surface gravity waves, particularly over coastal areas, lakes and estuaries (*Booij et al.,* 1999; *SWAN Team,* 2013). SWAN is based on the wave action balance equation, in which the evolution of ocean surface gravity waves is described by the wave action density N (e.g. *Hasselmann et al.,* 1973):

$$\frac{\partial N}{\partial t} + \nabla \cdot (\boldsymbol{c}_g + \boldsymbol{U})N + \frac{\partial}{\partial \sigma}(c_\sigma N) + \frac{\partial}{\partial \theta}(c_\theta N) = \frac{S_{tot}}{\sigma} \qquad (5.1)$$

$$S_{tot} = S_{in} + S_{ds} + S_{nl4} + S_{nl3} + S_{bot} + S_{db} \qquad (5.2)$$

This is similar to the spectral wave model WW3 used in Chapters 2-4 but using the relative radian frequency σ to represent the wave energy in frequency domain instead of the wavenumber. The right-hand side (RHS) of Eq. 5.2 represents the effects of the generation and dissipation of waves. Wave dissipation due to bottom friction (S_{bot}) and depth-induced wave breaking (S_{db}) become important in shallow waters.

5.2.2 Existing Parameterizations for Depth-induced Wave Breaking

In this section, we briefly review six commonly-used parameterizations (Table 5.1) for depth-induced wave breaking in shallow waters. An extensive overview of recent advances in parameterizing depth-induced wave breaking can be found in *van der Westhuysen* (2010) and *Salmon et al.* (2015). By assuming that the total energy dissipation is distributed over the wave spectrum in proportion to the spectral density, the source term S_{db} in Eq. 5.2 can be calculated based on (*Battjes and Beji,* 1992):

$$S_{db}(\sigma, \theta) = \frac{D_{tot}}{E_{tot}} E(\sigma, \theta) \tag{5.3}$$

where E_{tot} is the total wave energy, and D_{tot} is the mean rate of total energy dissipation due to depth-induced wave breaking. In the widely-used parameterization of BJ78, the energy dissipation rate is estimated using an analogy between the dissipation in breaking waves and a one-dimensional (1D) turbulence bore (*Stoker,* 1957):

$$D_{tot} = -\frac{1}{4} \alpha_{BJ} Q_b \bar{f} H_{max}^2 \tag{5.4}$$

where α_{BJ} is a tunable parameter, $\bar{f}$ is the mean frequency, Q_b is the fraction of breaking waves and H_{max} is the maximum individual wave height defined as a proportion of the local water depth (d):

$$H_{max} = \gamma d \tag{5.5}$$

where γ is the breaker index. BJ78 combines a maximum individual wave height calculated from the breaker index with the wave breaking probability for random wave heights. For a random wave field, the fraction of breaking waves is determined by a truncated Rayleigh distribution at an upper limit with the maximum wave height. This yields the following implicit expression for the fraction of breaking waves:

$$\frac{1 - Q_b}{-\ln Q_b} = \left(\frac{H_{rms}}{H_{max}}\right)^2 \tag{5.6}$$

where H_{rms} is the root-mean-square wave height.

The breaker index given in Eq. 5.5 is one of important parameters in the energy dissipation formulation. BJ78 suggested a constant breaker index of 0.8 based on the average of several wave breaking observations. An averaged value of 0.73 determined from extensive data sets is used as the default value in the current third-generation wave models. Subsequent studies demonstrated that the breaker index should be a function of the local bottom slope

and normalized water depth (*Nelson, 1987; Goda, 2010; Ruessink et al., 2003; Salmon et al., 2015*). *Nelson* (1987, NE87) suggested a positive dependence of the breaker index on the local bottom slope *m* as:

$$\gamma = 0.55 + 0.88\exp\left(-0.012/m\right) \tag{5.7}$$

Based on field observations on a barred beach, *Ruessink et al.* (2003, RU03) found only a weak correlation between the breaker index and the local bottom slope and proposed a linear dependence of the breaker index on a normalized water depth $k_p d$:

$$\gamma = 0.29 + 0.76 k_p d \tag{5.8}$$

where k_p is the local peak wave number. Using several sets of field and laboratory observations, *Goda* (2010, GO10) proposed a breaker criterion by considering the local bottom slope and a normalized water depth defined as the ratio of the local water depth over the deep-water wavelength L_0, given as:

$$\gamma = \frac{0.17}{d/L_0}\left\{1 - \exp\left[-1.5\pi\frac{d}{L_0}(1 + 11m^{4/3})\right]\right\} \tag{5.9}$$

Salmon et al. (2015, SA15) suggested a new parameterization for the breaker index by considering effects of both the local bottom slope and normalized water depth kd (where k is the lower-order mean wave number defined in SA15) in a joint scaling, but with different dependencies in deep waters $(kd > 1)$ and shallow waters $(kd < 1)$. In order to achieve a smooth transition from deep to shallow waters, SA15 suggested a hyperbolic tangent defined as:

$$\gamma = \gamma_1(m)/\tanh\left[\gamma_1(m)/\gamma_2(kd)\right] \tag{5.10}$$

where γ_1 and γ_2 are two different linear dependencies on the local bottom slope and normalized water depth given as:

$$\gamma_1(m) = \gamma_0 + a_1 m \tag{5.11}$$

$$\gamma_2(kd) = a_2 + a_3 kd \tag{5.12}$$

where γ_0 represents the breaker index for flat bottoms, and γ_0, a_1, a_2 and a_3 are all tunable coefficients. SA15 suggested that $\gamma_0 = 0.54$, $a_1 = 7.59$, $a_2 = -8.06$ and $a_3 = 8.09$. In very deep waters, $kd \to \infty$, Eq. 5.10 is reduced to $\gamma \to \gamma_2(kd)$, and a very large value of the breaker index is obtained. It should be noted that depth-induced wave breaking does not occur in very deep waters where the breaker index takes very large values. As waves propagate into increasingly shallow waters, by comparison, $kd \to 0$, Eq. 5.10 is

reduced to $\gamma \rightarrow \gamma_1(m)$, and the breaker index is independent of the normalized water depth. In the very shallow waters, wave breaking is only determined by the local bottom slope. In the intermediate water depths, wave breaking is affected by both the local bottom slope and normalized water depth. To prevent unrealistic large values of $\gamma_1(m)$ over steep slopes, an upper limit of slope $m = 1:10$ was suggested for Eq. 5.11.

The above-mentioned five parameterizations (Table 5.1) for depth-induced wave breaking are differentiated in terms of different formulations for the breaker index with a truncated Rayleigh distribution at an upper limit for random wave heights. There are other representations for the statistics of breaking wave height distributions. *Baldock et al.* (1998) suggested a Rayleigh distribution with truncation at a lower limit of $H_b = \gamma d$. The breaker index of RU03 was originally calibrated based on the dissipation model of *Baldock et al.* (1998). However, *van der Westhuysen* (2010) found the good agreement between the breaker index of RU03 and the optimal values of the breaker index based on the dissipation model of BJ78. Thus, the breaker index of RU03 is applied with the dissipation model of BJ78 without further calibration in this study. *Thornton and Guza* (1983, TG83) considered a different description of the breaking wave height probability in contrast to that in BJ78. TG83 (Table 5.1) shifts the Rayleigh distribution for the breaking waves to larger wave heights with a weighting function $W(H)$. Thus, the mean rate of energy dissipation is formulated as:

$$D_{tot} = -\frac{B^3 \bar{f}}{4d} \int_0^\infty H^3 W(H) p(H) dH \qquad (5.13)$$

Where B is a tunable coefficient accounting for the intensity of breaking, $p(H)$ is the Rayleigh wave height probability density function defined as:

$$p(H) = \frac{2H}{H_{rms}^2} \exp\left[-\left(\frac{H}{H_{rms}}\right)^2\right] \qquad (5.14)$$

and the weighting function $W(H)$ is defined as follow with a breaker index $\gamma_{TG} = 0.42$:

$$W(H) = Q_b = (H_{rms}/\gamma_{TG} d)^4 \qquad (5.15)$$

It should be noted that the breaker index has been related with the local bottom slope, normalized water depth, and deep-water wave steepness. The last varies spatially in both the longshore and offshore directions and cannot be used in a two-dimensional (2D) wave simulations. In this section, we reviewed six parameterizations with the dependences of

breaker index only on the local parameters. Among them, five parameterizations are based on a truncated Rayleigh distribution of breaking waves (the dissipation model of BJ78), with the breaker index to be a constant in BJ78, an exponential dependence of the local bottom slope in NE87, a linear dependence of the normalized water depth in RU03, and a joint dependence of the local bottom slope and normalized water depth in GO10 and SA15. GO10 is included since the deep-water wavelength used in this parameterization can be converted to the local wavelength (see Section 5.3.2). We also considered TG83 that is based on a different wave breaking probability for comparisons. These six parameterizations were selected in this study since they have been shown to have reasonable performances in parameterizing depth-induced wave breaking (e.g. *Rattanapitikon,* 2007; *Apotsos et al.,* 2008; *Zheng et al.,* 2008; *Salmon et al.,* 2015).

Table 5.1: Summary of the breaker index and fraction of breaking waves in six existing and the new parameterizations for depth-induced wave breaking.

Parameterization	Breaker index γ	Fraction of breaking waves Q_b	Reference
BJ78	$\gamma = 0.73$		*Battjes and Janssen* (1978)
NE87	$\gamma = 0.55 + 0.88\exp\left(-0.012/m\right)$		*Nelson* (1987)
RU03	$\gamma = 0.29 + 0.76k_p d$		*Ruessink et al.* (2003)
GO10	$\gamma = \frac{A}{d/L_0}\left\{1 - \exp\left[-1.5\pi\frac{d}{L_0}(1 + 11m^{4/3})\right]\right\}$	$\frac{1-Q_b}{-\ln Q_b} = \left(\frac{H_{rms}}{H_{max}}\right)^2$	*Goda* (2010)
SA15	$\gamma = \gamma_1(m)/\tanh\left[\gamma_1(m)/\gamma_2(kd)\right]$ $\gamma_1(m) = \gamma_0 + a_1 m$ $\gamma_2(kd) = a_2 + a_3 kd$		*Salmon et al.* (2015)
NEW	$\gamma = \gamma_1(m)/\tanh\left[\gamma_1(m)/\gamma_2(kd)\right]$ $\gamma_1(m) = b_0 + b_1\exp\left(-b_2/m\right)$ $\gamma_2(kd) = a_2 + a_3 kd$		*This study*
TG83	$\gamma_{TG} = 0.42$	$Q_b = (H_{rms}/\gamma_{TG} d)^4$	*Thornton and Guza* (1983)

5.2.3   A New Parameterization for Depth-induced Wave Breaking

In this study, we follow SA15 and use a similar scaling of the breaker index in terms of both the bottom slope and normalized water depth, but with a nonlinear dependence of the breaker index on the bottom slope in shallow waters. This nonlinear slope dependency will be further justified in Section 5.4. In this new parameterization, the original linear dependence on the bottom slope (Eq. 5.11) in shallow waters is modified with a nonlinear

dependence given as:

$$\gamma_1(m) = b_0 + b_1 \exp(-b_2/m) \tag{5.16}$$

where b_0, b_1 and b_2 are tunable coefficients. In term of the effect of normalized water depth, this new parameterization uses the same coefficient for γ_2 defined in Eq. 5.12, but has the new nonlinear dependence on the bottom slope for γ_1 (Eq. 5.16) to form a similar joint scaling with Eq. 5.10. The calibration and validation of this new parameterization, together with the six existing parameterizations mentioned in Section 5.2.2, will be presented in Section 5.4.

5.3 Observational Data and Methodology

5.3.1   Laboratory and Field Observations

The laboratory and field observations in 882 cases taken from 14 different data sources are used in this study to assess the performances of six existing and the newly-developed parameterizations discussed in Section 5.2. The bottom profiles and positions of wave gauges in the 14 data sources are shown in Figs. 5.1 and 5.2. These laboratory and field observations were made under a variety of wave conditions with different bottom profiles. In these observations, the SWHs were measured in all cases. Only a small percentage of these observations, however, had measurements of wave periods and wave-induced setup. Table 5.2 provides a summary of laboratory and field observations in 14 different data sources (*Baldock et al.,* 2002; *Baldock et al.,* 1998; *Battjes and Janssen,* 1978; *Allsop et al.,* 1998; *Stive,* 1985; *Ruessink et al.,* 2013; *Mai et al.,* 1999; *Arcilla et al.,* 1994; *Boers,* 1997; *Jensen,* 2004; *Bottema and van Vledder,* 2009; *Jafari and Cartwright,* 2012; *Birkemeier et al.,* 1997).

To assess the performances of parameterizations for depth-induced wave breaking under various dynamic conditions, the observational data in the 882 cases are separated into four types based on different types of bottom profiles. These four types consist of (a) the plane sloping bottom type, (b) barred beach type, (c) sandy beach type in the field, and (d) flat bottom type. The bottom profiles in the plane slope type to be considered in this study vary from a steep slope of 1:10 to a relative gentle slope of 1:80. The main feature of bottom profiles in the barred beach type is a bar-trough system, in which wave breaking often

occurs over the bar before heading to the shoreline. The flat bottom type includes a shallow lake data set and a reef flat data set. The main feature of the flat bottom type (Indices 13 and 14 in Table 5.2) is the relative uniform and high values of the normalized water depth over the reef flat or across the lake. For the remaining cases, the normalized water depth varies from large values at deep waters (Column 7 in Table 5.2) to zero approaching the shoreline.
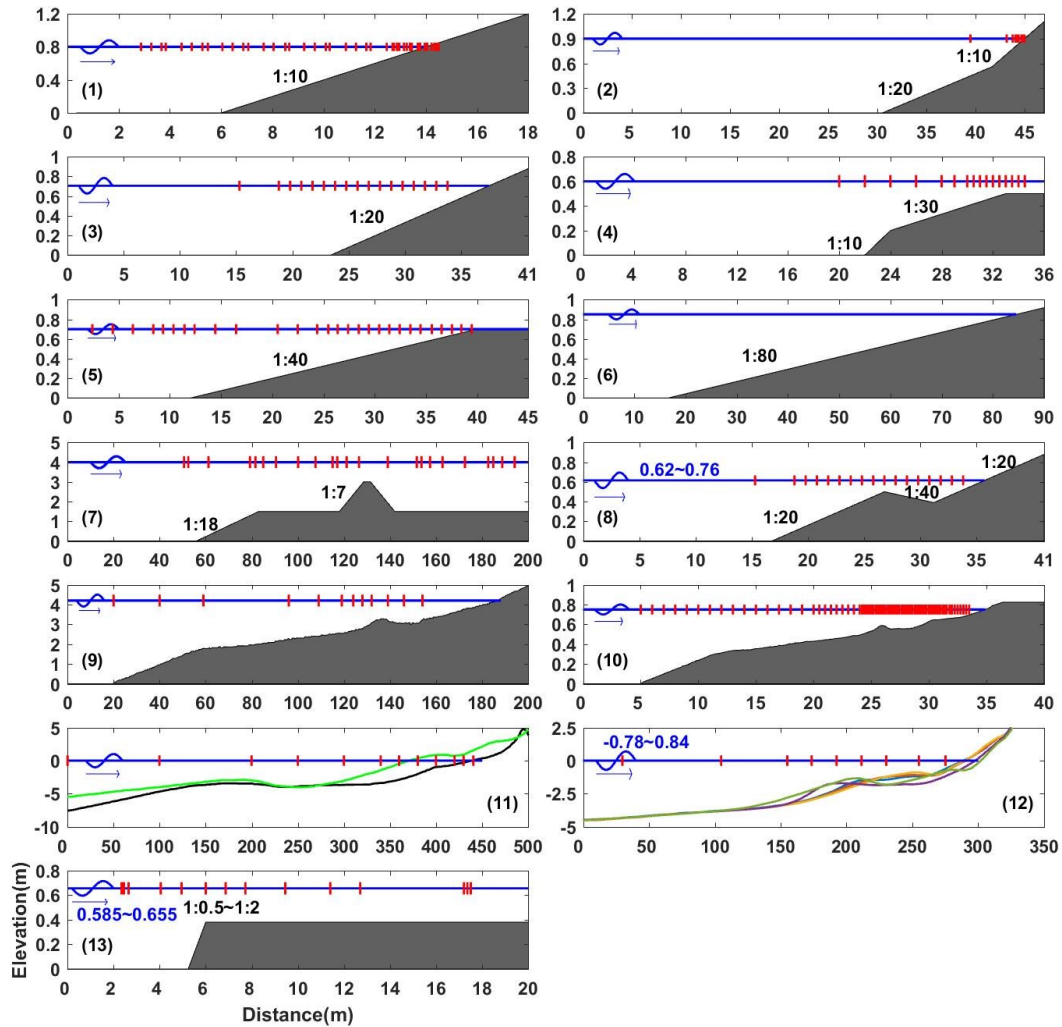
Figure 5.1: Bottom profiles and positions of wave gauges in 13 different data sets (Index 1-13 in Table 5.2). In each panel, the blue solid line indicates the still water level, and the arrow represents the incident wave direction. The red vertical lines mark locations of wave gauges. It should be noted that 190 wave gauges were deployed by *Ruessink et al.* (2013) in the wave tank and are not marked in panel 6. For field data collected on the sandy beach, the bottom profiles are shown in different colors in panels 11 and 12.
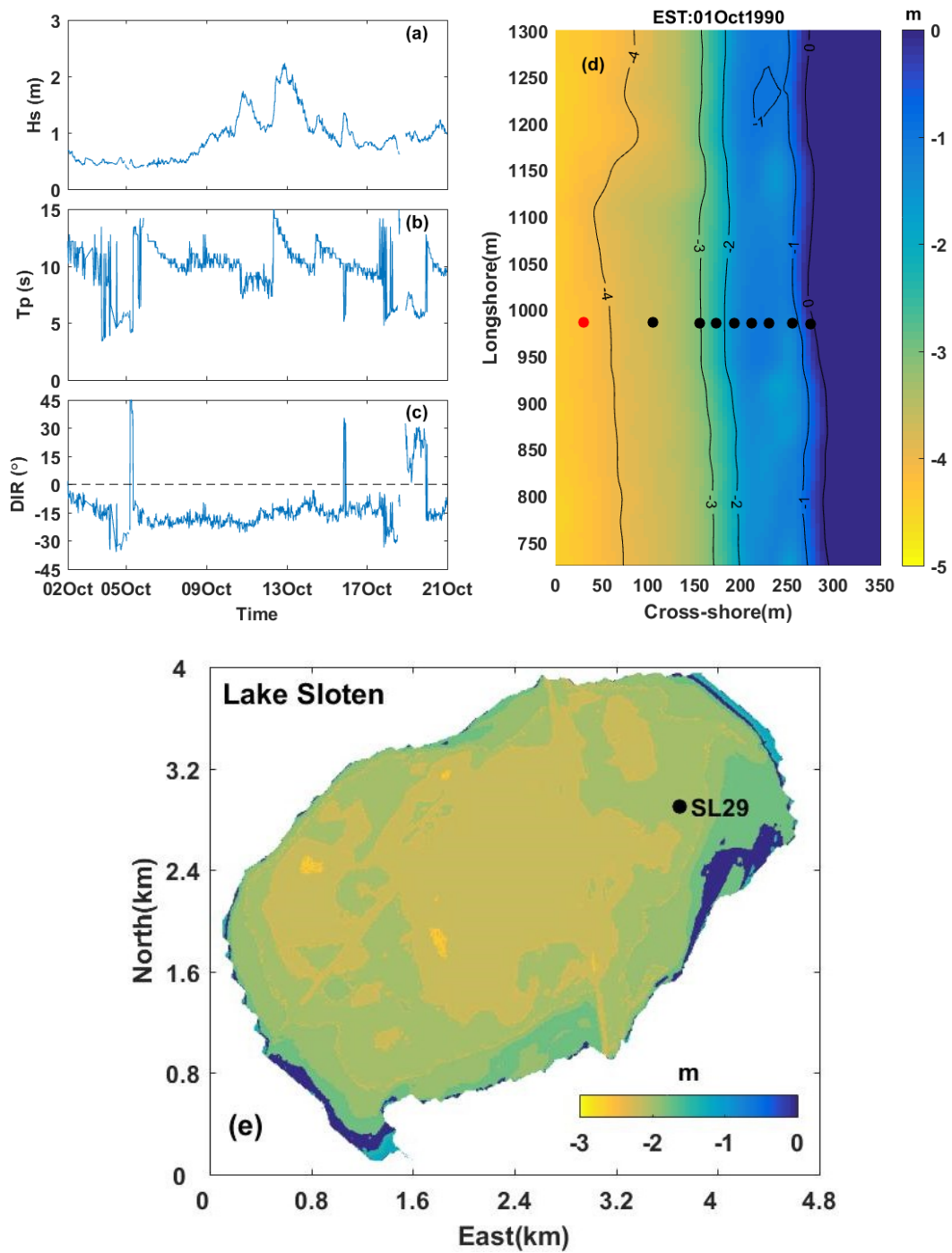
Figure 5.2: Incident wave conditions (a, significant wave height; b, peak wave period; c, incident wave angle) at the deep-water pressure sensor (indicated by red solid dot) and two-dimensional bathymetry (d, on 1 October, 1990) for the DELILAH nearshore experiment (Index 12 in Table 5.2). (e) Bottom topography with respect to the Normal Amsterdams Peil datum in Lake Sloten (Index 14 in Table 5.2). The solid dots mark the observation locations.

Table 5.2: Summary of laboratory and field observational data taken from 14 sources. The observational data in 882 cases from 14 data sources are categorized into four general types. Column 1 refers to types. Column 2 refers to indices for 14 data sources. Column 3 refers to references for the 14 data sources. Column 4 refers to the total number of cases in each data source. Column 5 refers to a brief description of bottom profiles. Column 6 shows the range of the incident SWHs in m. Column 7 refers to the normalized water depth ($k_p d$) at deep waters. Column 8 refers to the apparatus for each data source.

Type (1)	Index (2)	Data Source (3)	No. of Cases (4)	Bottom Profile (5)	Incident H_s (m) (6)	$k_p d$ (7)	Apparatus (8)
Sloping	1	*Baldock et al.* (2002)	6	Slope, 1:10	0.071-0.141	1.32	Small-scale
	2	*Baldock et al.* (1998)	3	Slope, 1:10	0.065-0.127	1.72-3.63	Small-scale
	3	*Battjes and Janssen* (1978)	2	Slope, 1:20	0.171-0.204	0.60-0.84	Small-scale
	4	*Allsop et al.* (1998)	6	Slope, 1:30	0.107-0.19	0.48-1.85	Small-scale
	5	*Stive,* (1985)	2	Slope, 1:40	0.192-0.195	0.48-1.85	Small-scale
	6	*Ruessink et al.* (2013)	3	Slope, 1:80	0.1-0.2	0.93-1.51	Small-scale
Barred	7	*Mai et al.* (1999)	3	Barred beach	0.8-1.0	0.52-0.66	Large-scale
	8	*Battjes and Janssen* (1978)	2	Barred beach	0.147-0.202	0.75-0.79	Small-scale
	9	*Arcilla et al.* (1994)	1	Barred beach	0.58	0.54	Large-scale
	10	*Boers* (1996)	3	Barred beach	0.103-0.206	0.55-0.98	Small-scale
Field	11	*Jafari and Cartwright* (2012)	2	Sandy beach	0.85-3.25	0.63-0.73	Field
	12	*Birkemeier et al.* (1997)	730	Sandy beach	0.36-2.25	0.26-1.83	Field
Flat	13	*Jensen* (2004)	110	Reef flat	0.1-0.21	0.73-1.49	Small-scale
	14	*Bottema and van Vledder* (2009)	9	Lake Sloten	0.23-0.7	0.88-1.44	Field

Among the total 14 data sources, 11 data sets are laboratory observations (Table 5.2). These 11 laboratory observations were made in wave flumes in three different types of bottom profiles: plane sloping bottoms, barred beaches and flat bottoms. Laboratory experiments were primarily conducted in small-scales under random wave conditions with incident SWHs ranging from 0.065 m to 0.21 m and some observations made in large-scales with incident SWHs ranging from 0.58 m to 1.0 m.

The other 3 data sources are in-situ field observations (Table 5.2). The first set of field data was collected on the Spit of Gold Coast in Australia during 2009 and 2010 (*Jafari and Cartwright,* 2012). Over this coastal water, an array of manometer tubes was deployed at 12 locations from 500 m offshore through the inner surf zone for measuring both the mean water level and surface wave heights. Two wave conditions from this data set are considered in this study, including a moderate wave condition with an incident SWH of

~0.85 m and a storm condition with an incident SWH of ~3.25 m. The cross-shore sandy beach profiles for these two cases are presented in panel 11 of Fig. 5.1.

The second set of field data was acquired by a field program known as the DELILAH nearshore experiment (*Birkemeier et al.,* 1997). This field program was conducted on a barred beach in Duck, North Carolina of the US in October 1990, with a cross-shore array of nine pressure sensors from 4.5 m to the shoreline for measuring the cross-shore variation of wave heights. The wave heights, wave periods, wave directions, cross-shore bathymetry and tidal evaluation measurements during 2-21 October were made at about every 34 minutes (http://frf.usace.army.mil/delilah/start.stm). Figures 5.2a-5.2c show the observed incident wave conditions at deep-water pressure sensors. In-situ observations of 730 cases in Duck (83% of the total 882 cases in this study) are used with observed incident SWHs ranging from 0.36 m to 2.25 m (Fig. 5.2a). These cases are selected under the conditions of observed incident wave angles less than 30° (Fig. 5.2c) so as to have relatively consistent cross-shore incident wave energy. Figure 5.2d shows 2D bathymetry during the experiment. The depth contour lines can be regarded as parallel for majority of cases, so that longshore differences can be neglected. Furthermore, the changing bar profiles were well documented in the experiment representing the simultaneous bathymetry associated with the wave observations. Thus, we conduct 1D wave simulations for this data set using the changing bar profiles to represent the variations of bathymetry. Several typical beach profiles are shown in panel 12 of Fig. 5.1. It should be noted that the mean offshore slope of 1:150 was not substantially modified by the incident wave conditions. The bar location, however, was significantly affected by wave breaking behaviors with the foreshore slope varying between 1:10 and 1: 40.

The third set of field data was collected in Lake Sloten in the Netherlands (*Bottema and van Vledder,* 2009). Lake Sloten is a shallow lake of about 4.5 km by 3 km, and its bottom is nearly flat with the mean water depth of ~1.7 m. A ten-year data set for wind and wave measurements during the period of 1997-2007 was made at station SL29 (Fig. 5.2e), with 9 stationary cases identified by *Bottema and van Vledder* (2009). These 9 stationary cases are considered in this study, in which wind speeds ranged between 11 m/s and 23 m/s. Due to its horizontal dimension and shallow water depth in Lake Sloten, the wave growth in

this Lake was fetch-limited and the wave transformation is highly depth-limited. Of special interest is that waves in the Lake were locally generated by the wind. For all the other data sets, by comparison, waves were not generated by local winds but arrived from offshore deep waters.

5.3.2   Wave Model Setup

Surface wave simulations in all 882 cases are conducted using SWAN (Section 5.2.1) in stationary mode. A special consideration is given for wave simulations in Lake Sloken, as waves in the lake are driven by the wind field. A two-dimensional regular computational grid is used with a spatial resolution of 40 m for nine cases in Lake Sloken, with winds and water levels in the model set to spatially uniform and same as the observations at station SL29. Formulations proposed by *Komen et al.* (1984) are used for wind input (S_{in}) and whitecapping (S_{ds}) in wave simulations in the Lake, with the wind drag coefficient suggested by *Zijlema et al.* (2012). The quadruplet wave-wave interactions (S_{nl4}) are considered using the Discrete Interaction Approximation (DIA) of *Hasselmann et al.* (1985). The wave model uses the bottom friction dissipation term (S_{bot}) derived from the JONSWAP results (*Hasselmann et al.,* 1973) with friction coefficient 0.038 $m^2 s^{-3}$ and the triad wave-wave interactions term (S_{nl3}) based on the Lumped Triad Approximation (LTA) method of *Eldeberky* (1996). The wave-induced setup, which is only an approximation in SWAN, is included in wave simulations, since the water depth near the shoreline could be affected by the setup. The wave directionality is considered with a directional spread of $\sigma_\theta = 25°$ (*Salmon et al.,* 2015) for all the parameterizations. The effects of ambient currents are not included in this study. A logarithmic frequency distribution with frequency increment of $\Delta f = 0.1f$ ranging from 0.01 Hz to 2.5 Hz and directional resolution $\Delta\theta = 6°$ are used. All the other settings followed the default physics or numerical schemes in SWAN model version 41.01.

The wave simulations in other cases are conducted in one-dimension and forced by incident waves in the offshore. The incident wave conditions are implemented based on offshore wave parameters in each case in terms of observed wave heights, frequencies, and the shape of the incident wave spectrum. The source terms for wind energy input (S_{in}), wave energy

dissipation due to whitecapping (S_{ds}) and quadruplet wave-wave interactions (S_{nl4}) are not used in these cases. The wave directionality, which has no effect on the 1D wave simulations, is not included for these cases as well. The other settings for the source terms remain the same with the cases in Lake Sloken. However, a frequency ranging from 0.01 Hz to 2.5 Hz with increment of $0.05f$ and a directional resolution $\Delta\theta = 1°$ are used for these cases.

The depth-induced wave breaking term (S_{db}) is computed using the six existing and newly developed parameterizations mentioned in Section 5.2 for all cases. Among the six existing parameterizations, five parameterizations (BJ78, NE87, RU03, SA15 and TG83) have already been implemented in version 41.01 of SWAN. For this study, GO10 is incorporated into SWAN. It should be noted that GO10 is parameterized in terms of incident wave parameters (deep-water wavelength), which is not suitable for 2D wave simulations (*Salmon et al.,* 2015). In this study, the deep-water wavelength L_0 used in the formulation is converted into the local wavelength L based on the linear wave dispersion relation (*Stoker,* 1957), given by:

$$L_0 = L / \tanh(k_p d) \tag{5.17}$$

In addition, a constant value of 0.73 for the breaker index is used for a negative bottom slope for the NE87 and GO10. For the SA15 and new parameterizations, the absolute values of the bottom slope are used, as a default set in version 41.01 of SWAN.

5.4 Results and Discussion

We assess the performances of six existing parameterizations for depth-induced wave breaking in simulating SWHs in Section 5.4.1. Section 5.4.2 examines the effects of the bottom slope and local water depth on the wave breaking over coastal waters. Section 5.4.3 calibrates and validates the newly-developed parameterization based on Eq. 5.16.

5.4.1 Performances of Six Existing Parameterizations

For each of 882 cases of laboratory and field observations, six different model runs are conducted using SWAN with the same model setup and the same external forcing except for different parameterizations (BJ78, TG83, NE87, RU03, GO10 and SA15) for depth-

induced wave breaking. Four metrics are used in this study to quantify the performances of the wave model using different parameterizations for depth-induced wave breaking. These four metrics consist of the relative bias (RB), scatter index (SI), root mean square error (RMSE) and correlation coefficient (R) (see definitions in Appendix A). In terms of SI values, the performances of different parametrizations are ranked in five ranges in this study: excellent for SI $\leq$ 6.0%; very good for 6.0% < SI $\leq$ 10.0%; good for 10.0% < SI $\leq$ 15.0%; fair for 15.0% < SI $\leq$ 25.0%; and poor for SI > 25.0%.

Values of the RB, RMSE, SI and R for the SWHs in each run (total 5292 runs) are calculated using the simulated and observed SWHs at observation locations based on definitions given in Appendix A. Figure 5.3 presents RB-SI scatter plots for 5292 runs categorized into four different bottom types, in which different colored symbols represent different parameterizations. The dash black line in each panel of this figure represents the positive linear relation of RB = SI with model errors (i.e., differences between simulated and observed SWHs) to be positive at all observation locations (indicating systematic overpredictions), and the dotted black line represents the negative linear relation of RB = - SI with model errors to be negative at all observation locations (indicating systematic underpredictions). These two lines intersect at the origin with RB = 0 and SI = 0. Less errors occur if the SI-RB points are closer to the origin.

The three parameterizations of SA15, BJ78 and GO10 perform very well in the barred bottom type (Fig. 5.3b), with all the SI-RB points occupying over areas very close to the intersection of the two lines (i.e., dash and dotted black lines in Fig. 5.3). These three parameterizations perform also well in the sloping bottom type (Fig. 5.3a). In the sandy beach type, these three parameterizations perform poorly, however, with the SI-RB points scattered over a larger area bounded by the two lines with some data points very close to the dotted line (Fig. 5.3c), indicating systematic underpredictions in these cases. In the flat bottom type, SA15 performs better than BJ78 and GO10, with the SI-RB points spreading closer to the origin. The SI-RB points of BJ78 and GO10 mostly spread along the dash or dotted lines, indicating systematic overpredictions or underpredictions of the model.

In comparison with SA15 and BJ78, TG83 and RU03 perform less well in terms of SI-RB

distributions (Figs. 5.3e-5.3h). In the sloping and barred bottom types, most of the SI-RB points in TG83 and RU03 spread along the dotted line, indicating systematic underpredictions of SWHs in these cases. The similar underpredictions can be found in the sandy beach type for these two parameterizations as well. In the flat bottom type, RU03 shows a tendency of overpredictions of the SWHs, which is different from its performances in the other three bottom types. The SI-RB distributions shown in Figs. 5.3e-5.3h demonstrate that NE87 performs slightly better than TG83 and RU03. Overall, SA15 and BJ78 appear to have better performances than the other four parameterizations in terms of the SI-RB distributions.
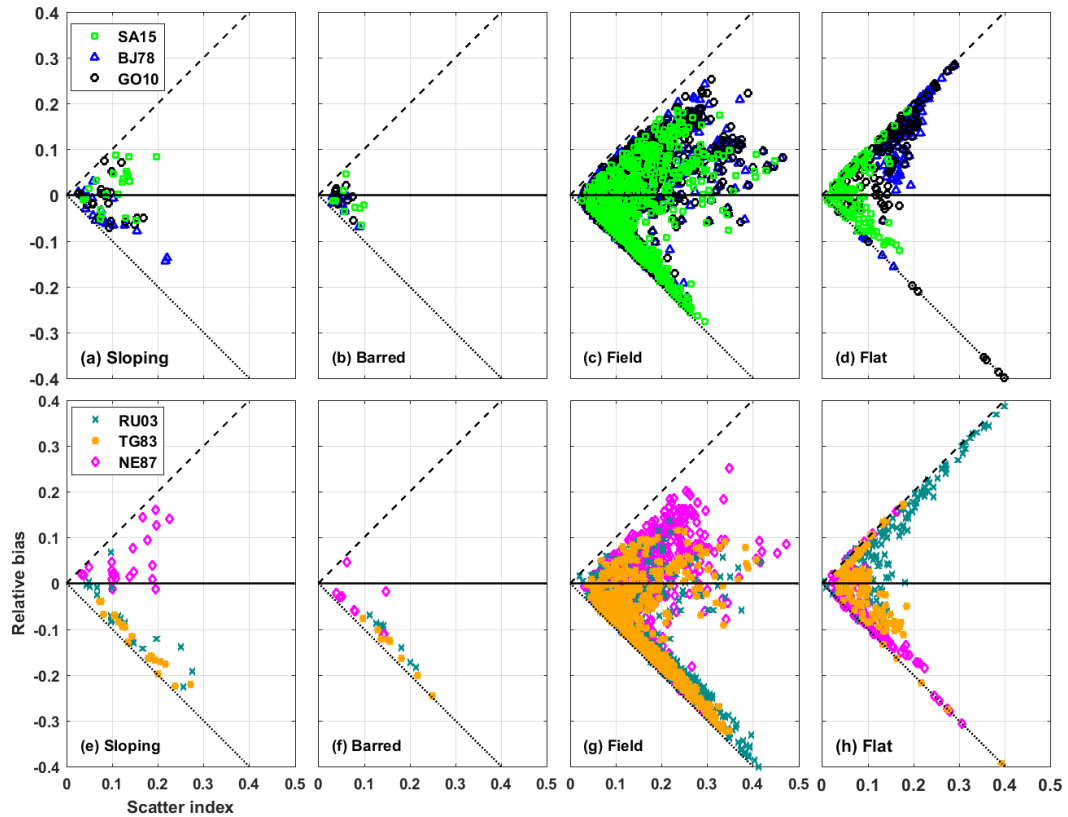
Figure 5.3: Scatter plots of the relative bias versus the scatter index calculated from observed and simulated SWHs in the type of sloping bottom, barred beach, sandy beach, and flat bottom. The simulated SWHs are generated by SWAN using (a-d) SA15, BJ78 and GO10 and (e-h) TG83, NE87 and RU03 for depth-induced wave breaking.

As mentioned above, field observations of 730 cases under different wave conditions in the DELILAH nearshore experiment (Index 12 in Table 5.2) are used in this study to assess the performances of different parameterizations. The model results and field observations

of these cases are separated into different subsets in terms of incident wave directions, normalized water depths and wave ages at deep waters. As shown in Appendix D, there are no systematic differences in the characteristic distributions of points in the SI-RB plots for different wave conditions.

To further quantify the performances of these six existing parameterizations in each bottom type, the above-mentioned four error metrics are averaged arithmetically for the same parameterization for depth-induced wave breaking in different cases but in the same bottom type to obtain the average values of these four metrics for each data source in each bottom type (Tables 5.3 and 5.4). The magnitudes of the error metrics are also indicated by the background color of each cell. Table 5.3 shows that, for the plane sloping bottom type, the average SI values are generally small and less than 19% and the average RB values in the range between -6% and 10% for SA15, BJ78 and GO10 (except for the cases of index 2 using BJ78), while RU03, TG73, and NE87 have relatively large average SI (up to 28%) and RB (between -24% and 15%) values. For the barred bottom type, the average SI values are smallest among four bottom types and less than 8% and the average RB values are small and in the range between -4% and 3% for SA15, BJ78, and GO10, while the RU03 and TG83 have relatively large average SI (up to 21%) and RB (between -19% and -10%) values. For the flat bottom type, SA15 also has relatively small average SI values of less than 8% and small average RB values in the range between 0.4% and 4%, while TG83 and GO10 have relatively large average SI (up to 32%) and RB (between -32% and 10%) values. In the sandy beach type, the average SI values are less than 16% and the average RB values are in the range between -8% and -0.4% for SA15, BJ78 and GO10, while RU03 and TG83 have relatively large average SI (up to 22%) and RB (between -18% and -9%) values. The RB values for the field cases are consistently negative on average, indicating wave energy is generally underestimated during the simulations. The discrepancies can be explained by the incident wave angle and the application of 1D simulations. On the other hand, it should be noted that the effects of wind energy input and ambient currents are not included in numerical simulations for the sandy beach type, which may also explain significantly large SI and RB values in this bottom type. In terms of RMSE values for the SWHs shown in Table 5.4, similar characteristics can be found for these six existing parameterizations as the SI values.

The overall mean values of four metrics for the six existing parameterizations are computed from the average values discussed above and presented in the bottom rows of Tables 5.3 and 5.4. Although the performances of the six existing parameterizations differ for different cases, the average performance in each bottom type is satisfactory, with the average SI values between 5.3% and 20.8%. In the sloping, barred and sandy bottom types, BJ78 and GO10 have the best performance, while SA15 performs slightly worse. Both RU03 and TG83 perform the worst and systematically underpredict the SWHs in these three bottom types, as demonstrated in Figs. 5.3e-5.3g. In the flat bottom type, SA15 performs well with the average SI of 6.7%, while the other five parameterizations have the relatively large average SI values between 12% and 20.8%.

Table 5.3: Summary of the relative bias and scatter index for the SWHs using six existing parameterizations. The red background colors in cells represent smaller relative bias, scatter index, root mean square error and higher correlation coefficient, indicating good performances of the parameterizations. The blue colors represent the relatively poor performance.

Type	Index	Relative Bias (%)							Scatter Index (%)					
		SA15	BJ78	RU03	TG83	NE87	GO10		SA15	BJ78	RU03	TG83	NE87	GO10
Sloping	1	3.3	-5.7	-7.9	-8.0	1.2	0.2		12.9	8.0	11.4	10.9	10.3	8.6
	2	9.1	-16.5	-20.2	-23.7	4.2	-5.8		19.0	22.7	28.0	26.3	17.5	15.2
	3	8.5	-1.9	-12.5	-16.3	14.3	7.3		12.3	5.5	14.5	16.7	19.7	10.2
	4	-0.9	-3.0	-6.5	-14.8	5.5	-4.6		9.6	8.5	12.0	17.8	18.0	9.7
	5	-2.5	-2.1	-6.7	-16.2	9.5	0.1		8.1	9.0	14.9	18.2	13.3	8.4
	6	-1.6	0.7	-1.2	-6.5	2.4	-0.5		5.1	3.1	5.9	9.7	4.1	3.8
Barred	7	-1.6	-1.7	-10.8	-10.7	-9.4	-0.1		7.5	4.6	15.1	13.3	12.3	3.8
	8	1.3	-3.6	-13.8	-18.5	1.4	-0.7		8.0	7.7	17.7	20.3	10.5	6.9
	9	-1.3	0.2	-10.1	-10.1	-3.1	2.1		3.7	4.3	13.0	13.0	4.6	6.1
	10	-3.8	-1.9	-10.9	-16.3	-3.6	-2.2		6.1	4.4	14.7	17.9	5.6	5.2
Field	11	-7.6	-5.7	-12.3	-17.5	-5.0	-5.5		15.3	14.2	15.0	21.3	17.4	14.6
	12	-3.7	-1.0	-11.9	-9.9	-2.2	-0.4		15.2	14.9	17.8	16.8	16.0	15.1
Flat	13	0.4	13.8	13.4	-0.7	-5.3	9.4		7.9	18.5	18.8	9.4	9.4	14.3
	14	3.1	-5.3	2.7	-31.9	-16.7	-27.4		5.5	9.1	5.2	31.9	17.9	27.4
Average	Sloping	2.6	-4.7	-9.2	-14.3	6.2	-0.6		11.2	9.5	14.5	16.6	13.8	9.3
	Barred	-1.3	-1.8	-11.4	-13.9	-3.7	-0.2		6.3	5.3	15.1	16.1	8.3	5.5
	Field	-5.7	-3.4	-12.1	-13.7	-3.6	-3.0		15.3	14.6	16.4	19.1	16.7	14.9
	Flat	1.7	4.2	8.0	-16.3	-11.0	-9.0		6.7	13.8	12.0	20.6	13.6	20.8
	Overall	**-0.7**	**-1.4**	**-6.2**	**-14.5**	**-3.0**	**-3.2**		**9.9**	**10.8**	**14.5**	**18.1**	**13.1**	**12.6**

Table 5.4: Summary of the root mean square error (RMSE) and correlation coefficient (R) for the SWHs using six existing parameterizations. Otherwise as in Table 5.3.

Type	Index	Root mean square error (cm)							Correlation coefficient (%)					
		SA15	BJ78	RU03	TG83	NE87	GO10		SA15	BJ78	RU03	TG83	NE87	GO10
Sloping	1	1.2	0.8	1.1	1.1	1.0	0.8		82.2	99.4	98.8	95.1	89.4	92.1
	2	1.4	1.7	2.1	1.9	1.3	1.1		95.0	94.0	92.4	90.6	95.2	96.0
	3	1.9	0.7	2.2	2.5	3.0	1.5		93.7	98.9	98.9	99.0	85.1	95.6
	4	0.9	0.8	1.2	1.8	1.8	0.9		95.7	97.7	96.9	95.0	86.1	96.9
	5	1.2	1.3	2.2	2.7	2.0	1.2		99.3	99.1	97.9	98.0	97.0	99.4
	6	0.7	0.4	0.7	1.2	0.5	0.4		98.7	99.4	98.8	97.3	99.4	99.2
Barred	7	6.6	4.1	13.2	11.7	10.9	3.4		91.8	97.4	94.5	92.2	92.2	97.7
	8	1.1	1.0	2.4	2.7	1.4	0.9		89.6	90.6	92.6	93.1	85.4	90.5
	9	2.3	2.6	8.0	8.0	2.8	3.7		89.8	82.8	82.7	82.7	91.0	67.6
	10	1.2	1.0	2.1	2.6	1.2	0.9		96.9	96.7	90.8	91.2	96.9	97.4
Field	11	18.9	15.1	18.8	27.5	20.1	15.0		89.3	94.2	97.1	95.9	83.1	91.4
	12	12.5	10.9	16.9	15.4	13.2	11.7		76.0	65.2	85.2	81.6	70.6	62.7
Flat	13	0.9	2.1	2.1	1.1	1.1	2.0		99.3	91.6	83.2	98.6	99.0	97.6
	14	2.8	5.3	2.5	19.2	11.3	17.0		99.1	97.1	98.9	95.1	93.5	92.5
Average	Sloping	1.2	1.0	1.6	1.9	1.6	1.0		94.1	98.1	97.3	95.8	92.0	96.5
	Barred	2.8	2.2	6.4	6.3	4.1	2.2		92.0	91.9	90.1	89.8	91.4	88.3
	Field	15.7	13.0	17.9	21.5	16.7	13.4		82.7	79.7	91.2	88.8	76.9	77.1
	Flat	1.8	3.7	2.3	10.1	6.2	9.5		99.2	94.4	91.1	96.8	96.3	95.1
	Overall	**5.4**	**5.0**	**7.0**	**9.9**	**7.1**	**6.5**		**92.0**	**91.0**	**92.4**	**92.8**	**89.1**	**89.2**

For the overall performances of the six existing parameterizations (see the bottom rows of Tables 3 and 4), SA15 and BJ78 have the lowest average SI values (<12%), smallest amplitudes of the average RB values (< 2%), smallest average RMSE values (< 6 cm), and relatively high average correlation coefficient values (> 0.91). Although BJ78 and GO10 perform well in the sloping, barred and sandy bottom types, their relatively poor performances in the flat bottom type result in the slightly worse overall performances than SA15. SA15 performs the best with an overall SI of 9.9%, due partially to its satisfactory performances in both the flat and barred bottom types. Our findings are consistent with previous study made by *Salmon et al.* (2015, see their Fig. 10), who showed that, the average SI value of SA15 (11%) is larger than that of BJ78 (9%) in the sloping bottom type, while SA15 has smaller average SI value (15%) compared with BJ78 (18%) in the flat bottom type.

5.4.2   Effect of Bottom Slope and Normalized Water Depth

As discussed in Section 5.4.1, the six existing parameterizations perform differently in the study cases, due mainly to different expressions used for the breaker index. A large value of the breaker index yields a large maximum breaking wave height (H_{max}), indicating small fraction of breaking waves and low wave energy dissipation. Overestimations (underestimations) of the SWHs discussed in Section 5.4.1 are, therefore, mainly associated with unrealistically high (low) values of the breaker index. The features of the breaker index in five existing parameterizations (SA15, BJ78, RU03, NE87 and GO10) are presented in terms of the bottom slope (Fig. 5.4) and normalized water depth (Fig. 5.5). The normalized water depth used in SA15 is calculated using a mean wave number. To compare the breaker indices in different parameterizations, the mean wave number is converted into the peak wave number using an empirical relationship of $k = 1.33k_p$ suggested by *Komen et al.* (1996) under the assumption of idealized JONSWAP spectra.

As mentioned above, the breaker index is set to a constant value of 0.73 in BJ78 (Figs. 5.4 and 5.5, see also Section 5.2.2). The breaker index in RU03 is independent of the bottom slope (Fig. 5.4) but is set to a positive dependence on the normalized water depth (Fig. 5.5), with very small values (~0.3) in shallow waters and large values (~1.0) in finite water depths ($k_p d \approx 1$, Fig. 5.5). The breaker index in NE87 is a nonlinear function of the bottom slope only, with values between 0.55 and 1.43. The breaker index in GO10 has a positive nonlinear dependence on the bottom slope and a negative nonlinear dependence on the normalized water depth (Figs. 5.4 and 5.5). Thus, GO10 provides larger values (~1.2) of the breaker index over steep bottom slopes in shallow waters (Fig. 5.5a) and small values (~0.6) over gentle bottom slopes in finite water depths (Fig. 5.5c). In shallow waters (Fig. 5.4a), the breaker index in SA15 is a linear positive function of the bottom slope (Fig. 5.4), with values between 0.54 and 1.3. In coastal waters with finite water depths (Fig. 5.4b), the breaker index in SA15 depends on both the bottom slope and normalized water depth with large values (> 1.6).
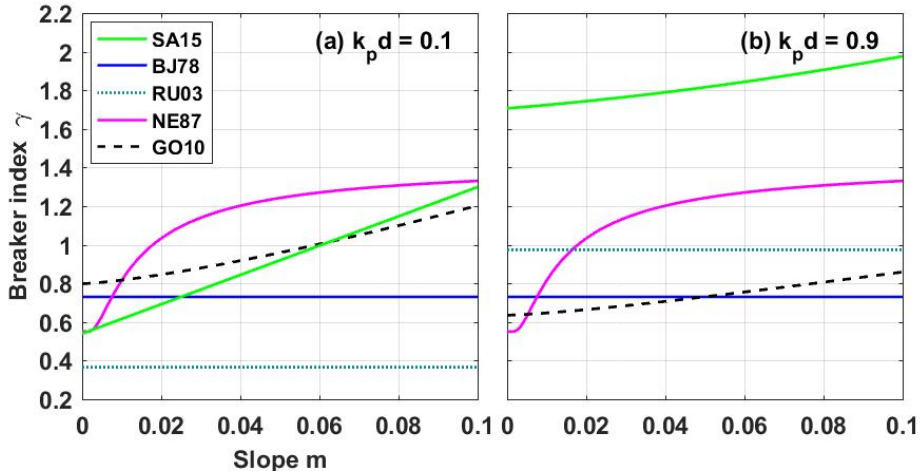
Figure 5.4: Comparisons of breaker indices in five existing parameterizations as a function of bottom slope (m) for (a) shallow waters ($k_p d = 0.1$) and (b) relative deep waters ($k_p d = 0.9$).
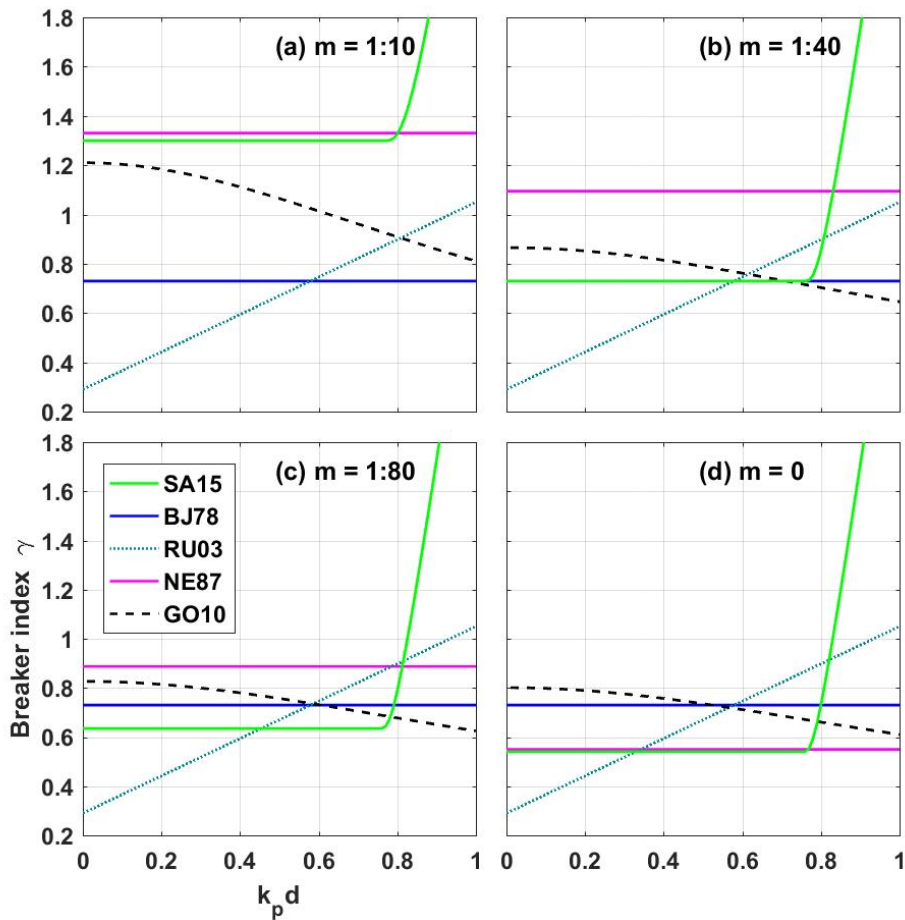
Figure 5.5: Comparisons of breaker indices in five existing parameterizations as a function of the normalized water depth for four different bottom slopes of (a) $m = 1:10$, (b) $m = 1:40$, (c) $m = 1:80$, and (d) $m = 0$.

To further illustrate the effect of breaker index variations, the performances of the six existing parameterizations over four different plane sloping bottoms are examined (Fig. 5.6). For steep bottom slopes in shallow waters, SA15, NE87 and GO10 have large values of the breaker index of greater than 0.73, while RU03 has lower values of the breaker index of less than 0.73 in relatively shallow waters ($k_p d < 0.58$, Figs. 5.4a and 5.5a). As a result, the use of SA15, NE87 and GO10 in SWAN over these steep bottom slopes leads to larger SWHs than BJ78, and the use of RU03 leads to lower SWHs ($m = 1:10$ and $m = 1:20$, Figs. 5.6a and 5.6b). Over the relatively gentle slope of $m = 1:40$ in shallow waters, by comparison, NE87 and GO10 have values of the breaker index greater than 0.73, and SA15 and RU03 have values of the breaker index around 0.73 and lower than 0.73, respectively (Figs. 5.4a and 5b). Consequently, the use of NE87 and GO10 in SWAN over this relatively gentle slope results in simulated SWHs greater than BJ78, the use of SA15 results in the similar performance with BJ78, and the use of RU03 gives lower SWHs (Fig. 5.6c). For the gentle bottom slope of $m = 1:80$, NE87 still has larger values of the breaker index than 0.73, and SA15 and RU03 have the values lower than 0.73 in shallow waters (Fig. 5.4a and 5.5c). Thus, the use of NE87 predicts larger SWHs than BJ78 and the use of SA15 and RU03 predicts lower SWHs over this gentle bottom slope (Fig. 5.6d).

Figure 5.6 demonstrates that SA15, BJ78 and GO10 are overall the three best performing parameterizations for depth-induced wave breaking in the four bottom slope cases. Some noticeable differences, however, occur in the performances of these three parameterizations. The use of SA15 in SWAN leads to overpredictions of SWHs in the steep bottom slope case and underpredictions in the relatively gentle bottom slope case, which indicates its overestimation of the breaker index in steep bottom slopes and underestimation in relatively gentle bottom slopes. On the other hand, BJ78 performs well in the relatively gentle bottom slope case, but this parameterization tends to generate underpredictions of SWHs in the steep bottom slope case, indicating underestimation of the breaker index by BJ78 in the latter case.
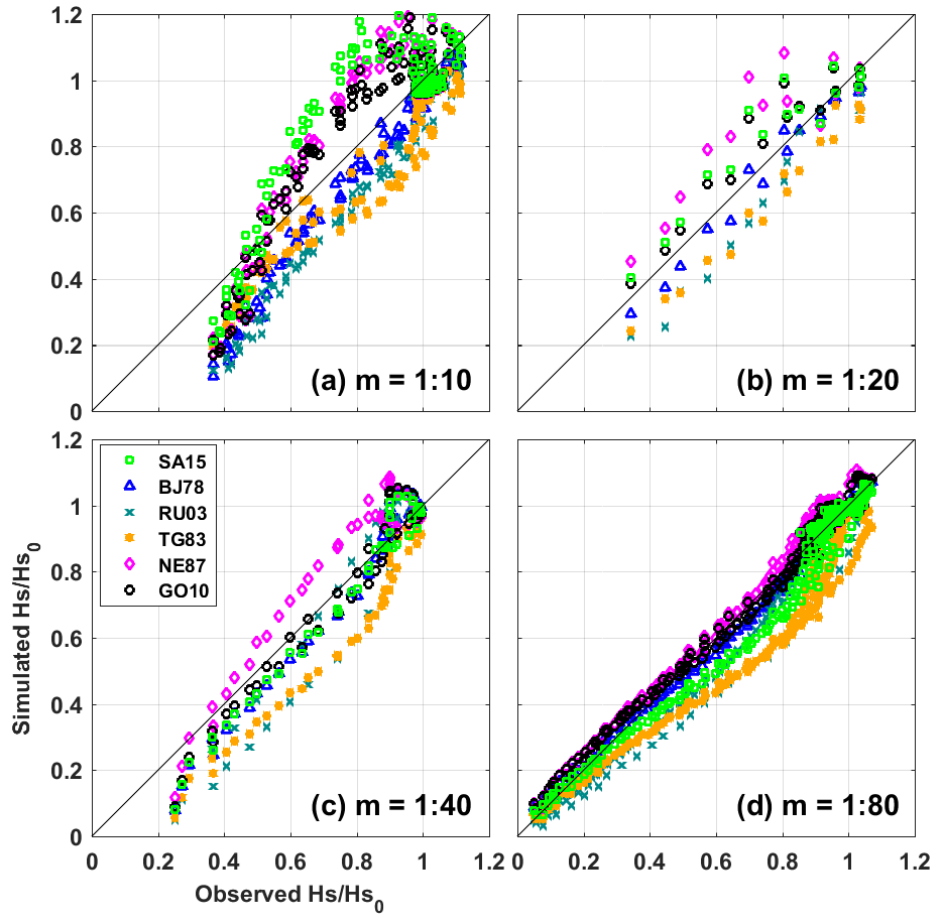
Figure 5.6: Scatter plots of observed and simulated SWHs normalized by corresponding incident SWHs in four bottom slopes of (a) $m = 1:10$ (*Baldock et al.,* 2002; Index 1), (b) $m = 1:20$ (*Battjes and Janssen,* 1978; Index 3), (c) $m = 1:40$ (*Stive,* 1985; Index 5) and (d) $m = 1:80$ (*Ruessink et al.,* 2013; Index 6). The simulated SWHs are generated by SWAN using six existing parameterizations for depth-induced wave breaking.

Figure 5.7 presents a comparison of simulated and observed SWHs in the flat bottom cases based on laboratory observations made over a reef flat (*Jensen,* 2004) and field observations made in Lake Sloten (*Bottema and van Vledder,* 2009). The bathymetry of the reef flat is characterized by steep bottom slopes with an abrupt transition at the reef crest to a flat platform connected to the shoreline. For this type of bottom profiles, the onset of the wave breaking process typically happens at the reef crest, and then the waves evolve into turbulent bores losing energy on the reef flat. Thus, the wave breaking process happens most likely on a flat bottom but with rapid and strong nonlinear processes ahead (*Jensen,* 2004). Depending on the incident wave conditions and water depths over the reef flat, the normalized water depths in these cases are small with the values up to 0.6. The breaker

index over flat bottoms for remotely-generated incident waves was reported to be relatively low ($0.45 < \gamma < 0.65$) by various previous observations (e.g. *Nelson,* 1987; *Katsardi,* 2007). SA15 has the value of the breaker index to be around 0.54 in the flat bottom with relatively shallow water depths (Fig. 5.5d), which is very close to the reported values. Thus, SA15 shows a superior performance for this data set (Fig. 5.7a). The constant breaker index value of 0.73 in BJ78 leads to overpredictions of SWHs on the reef flat. Furthermore, the use of GO10 and RU03 leads to overpredictions of SWHs, and the use of NE87 leads to underpredictions of SWHs.
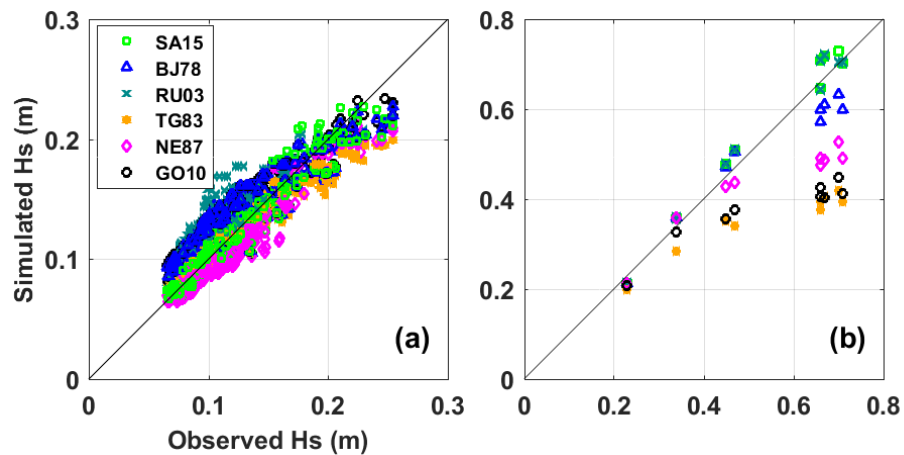
Figure 5.7: Scatter plots of observed and simulated SWHs in cases of (a) reef flat (*Jessen,* 2004; Index 13) and (b) Lake Sloten (*Bottema,* 2007; Index 14). The simulated SWHs are generated by SWAN using six existing parameterizations for depth-induced wave breaking.

The surface gravity waves in Lake Sloten are locally generated by winds. A distinguishing feature of wave breaking in this Lake is that the local shallow water depths result in relatively high values of the normalized water depth ($0.88 < k_p d < 1.44$), in comparison with the values over other surf zones. Figure 5.7b demonstrates that the use of BJ78 results in underpredictions of SWHs in Lake Sloten, which is consistent with previous findings made by *Bottema and van Vledder* (2009) and *van der Westhuysen* (2009). Both of these papers documented that the use of BJ78 underestimates the wave heights for locally generated wind waves over a nearly flat bathymetry. It can be anticipated that the realistic value of the breaker index in the lake should be greater than 0.73. Figure 5.5d indicates that, for large values of normalized water depths ($k_p d > 0.8$), both SA15 and RU03 have large values of the breaker index of greater than 0.73, while NE87 and G010 have low

values of the breaker index less than 0.73. This explains why the use of SA15 and RU03 results in satisfactory model performances in simulating SWHs, while the use of NE87 and GO10 results in underpredictions of SWHs in Lake Sloten (Fig. 5.7b). The results suggest that the increasing of the breaker index with increasing normalized water depth in SA15 and RU03 is more realistic than the opposite tendency in GO10.

Wave transformations over steep and gentle bottom slopes have some distinct features, particularly in the intensity of wave nonlinearity. As waves propagating shoreward to the shoreline, the nonlinear wave dynamics become increasingly important for both steep and gentle bottom slopes. The cross-shore distributions of the SWHs normalized by corresponding incident SWHs (H_s/H_{s0}), breaking wave fraction (Q_b), wave energy dissipation rate (D_{tot}), and wave-induced force per unit area (F_x) over steep and gentle bottom slopes are presented in Fig. 5.8. The wave-induced force is defined as the gradient of radiation stress (*Longuet-Higgins and Stewart*, 1962):

$$F_x = -\frac{\partial S_{xx}}{\partial X} - \frac{\partial S_{xy}}{\partial y} \tag{5.18}$$

where subscripts *x* and *y* refer to geographical directions, and *S* is the radiation stress tensor calculated from the wave spectrum.

The cross-shore distributions of the normalized SWHs shown in Figs. 5.8a1 and 5.8b1 further demonstrate the satisfactory performances of BJ78 and GO10 and undesirable performances of the other four parameterizations over sloping bottoms. In particular, the use of TG83 in SWAN leads to significant underpredictions of the SWHs, since this parameterization generates relatively large values of the breaking wave fraction (Figs. 5.8a2 and 5.8b2). It should be noted that the wave-induced forces generated by SWAN with the use of different parameterizations differ significantly, which should have a significant effect on the simulation of the ambient wave-induced currents and setup. The narrow surf zone on a steep beach (Figs. 5.8a1-5.8a4), on the other hand, results in very strong nonlinear processes to occur locally and on a short time scale. On a gentle bottom slope (Figs. 5.8b1-5.8b4), by comparison, the wide surf zone allows the nonlinearity to build up gradually over a long distance, the wave energy dissipation rate and wave-induced force are relatively small and spatially smooth, and the wave shape changes gradually with

slowly increasing wave steepness. Although the incident wave heights are similar in the two cases shown in Fig. 5.8, the energy dissipation rate and wave-induced force on the steep slope are roughly an order of magnitude larger than that on the gentle slope.
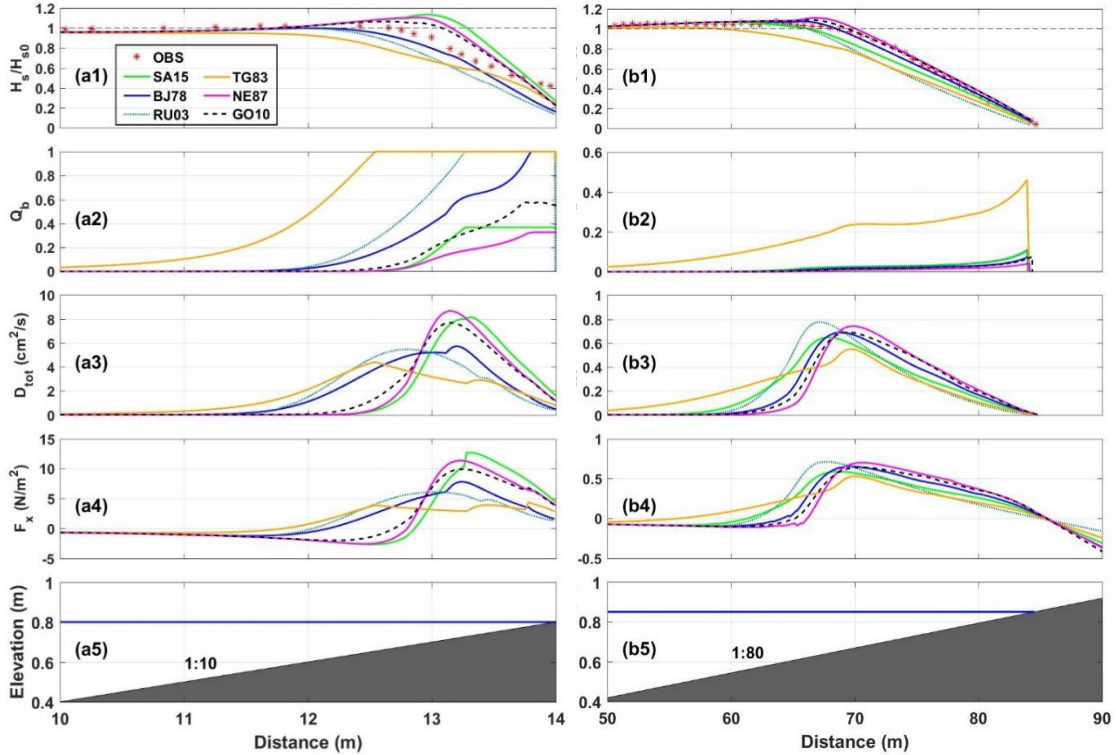
Figure 5.8: Cross-shore distributions of the normalized SWHs (H_s/H_{s0}), breaking wave fraction (Q_b), wave energy dissipation rate (D_{tot}), and wave-induced force (F_x) over a steep bottom (a1-a5; *Baldock et al.,* 2002; $H_s = 0.106$ m, $T_p = 1.67$ s) and a gentle bottom (b1-b5; *Ruessink et al.,* 2013; $H_s = 0.1$ m, $T_p = 2.25$ s). The red stars refer to observation data. The model results from six parameterizations are shown in different colors. The bathymetry profiles are shown at the bottom (a5 and b5) with water level indicated by blue lines.

5.4.3 Calibration and Validation of the New Parameterization

As discussed above, the six existing parameterizations have reasonable performances in representing the depth-induced wave breaking in shallow waters, but with their own limitations and drawbacks. It was discussed in Section 5.4.2 that these can be explained by the undesirable representations of the breaker index. The linear dependence of the breaker index on the bottom slope in shallow waters specified in SA15 (Eq. 5.11) leads to overpredictions of the breaker index over steep bottom slopes and underpredictions over gentle bottom slopes in shallow waters. Considering the performances of the six existing

parameterizations, we expect a nonlinear dependence of the breaker index on the bottom slope in shallow waters as discussed in Section 5.2.3. The nonlinear slope dependency has long been recognized. NE87 has an exponential dependence of the breaker index on the bottom slope. Several previous studies (e.g., *Rattanapitikon and Shibayama, 2000; Le Roux, 2007*) also suggested parabolic functions of bottom slope for the breaker index. Apart from the pure nonlinear slope dependency, there are several joint nonlinear dependences of the breaker index on the bottom slope and other parameters presented in previous studies as well (e.g., *Camenen and Larson, 2007; Goda, 2010; Rattanapitikon, 2007*). Our analysis of the model results demonstrates the nonlinear slope dependency, which is consistent with previous findings. Thus, we simply follow NE87 and use an exponential function (Eq. 5.16) to replace the linear function (Eq. 5.11).

In this section, the three tunable coefficients for the new parameterization (b_0, b_1 and b_2) defined in Eq. 5.16 are first determined and the performance of the new parameterization is then assessed using the observed SWHs in both laboratories and fields discussed in Section 5.3.1. For these purposes, the cases in each date set are almost evenly separated into calibration and validation subsets. The division is made such that the two subsets contain representative cases from all types of bottom profiles and incident wave conditions. The large data sets for the DELALAH project and reef flat (Table 5.2, index 12 and 13) are equally divided into calibration and validation parts, respectively, based on values of the deep-water normalized water depth ($k_p d$). For the remaining data sets with small number of cases, each of them is randomly divided into the calibration and validation subsets. For the calibration, the optimum values of three tunable coefficients are determined by considering the minimum values of the average SI between the simulated and observed SWHs.

The following two major steps are taken to determine the three tunable coefficients of the new parameterization. The first step is to determine the optimum value of b_0 by minimizing the average SI value defined for the simulated and observed SWHs in the flat bottom cases of *Jensen* (2004) and Lake Sloten within the calibration subset. For these flat bottom cases, Eq. 5.16 reduces to $\gamma_1(m) = b_0$, and the breaker index in Eq. 5.10 is given by $\gamma_1(m) = b_0/\tanh[b_0/(a_2 + a_3 kd)]$ with $a_2 = $ -8.06 and $a_3 = $ 8.09 (see Section

5.2.2). Figure 5.9a presents variations of average SI values over the range of $0.46 < b_0 <$ 0.62 during the calibration. The average SI value reaches a minimum of ~6.73% at $b_0 =$ 0.54. This optimum value of b_0 (0.54) represents the breaker index over flat bottoms in shallow waters, which is the same as the value of γ_0 in SA15. The second step is to determine the optimum values of b_1 and b_2 by minimizing the average SI value based on simulated and observed SWHs in all the cases of the above-mentioned calibration subset. Figure 5.9b demonstrates that the average SI value reaches a minimum of ~9.65% at $b_1 =$ 0.47 and $b_2 = 0.018$.
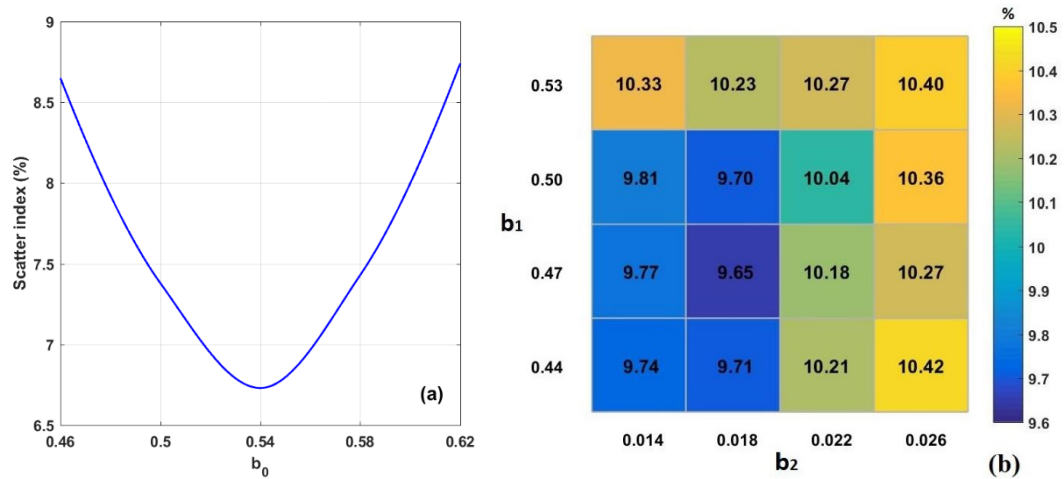
Figure 5.9: Distributions of the average scatter index for the SWHs during the calibration of parameters in the new parameterization. (a) Calibration of b_0 using the flat bottom cases of *Jensen* (2004). (b) Calibration of b_1 and b_2. In (b), the values of the average scatter index are marked by the color and the numbers.

Figure 5.10a presents a comparison of the new parameterization for the breaker index with SA15 and BJ78 as a function of the bottom slope (m) in shallow waters with $kd < 1$. Both the SA15 and BJ78 are the best among the six existing parameterizations as discussed in Section 5.4.1. In shallow waters ($kd < 1$) with gentle bottom slopes ($m < 0.05$), the breaker indices in the new parameterization have highly comparable values as in SA15, except that the breaker indices in the new parameterization and SA15 increase nonlinearly and linearly with the bottom slope. At the flat bottom case ($m = 0$) in shallow waters, the breaker indices in both the SA15 and new parameterizations are identical and equal to 0.54 (Fig. 5.10a). The breaker index in BJ87, by comparison, is constant and equal to 0.73 regardless of bottom slopes and water depths. For steep bottom slopes with $0.04 < m <$

0.15 in the shallow waters, the breaker indices in the new parameterization increase gradually with the bottom slope, which differs from the counterparts in SA15 and BJ78 (Fig. 5.10a). For very steep bottom slopes with $m > 0.15$ in the shallow waters, the breaker indices in the new parameterization approach nearly a constant value of 0.96, which differs from 1.30 in SA15 and 0.73 in BJ78.

Figure 5.10a also compares the nonlinear slope dependency in the new parameterization with the joint nonlinear slope dependencies of the breaker index suggested by *Camenen and Larson* (2007, CL07, see their Eqs.13-19) and *Goda* (2010, GO10, Eq. 5.9). The observed breaker indices collected by *Camenen and Larson* (2007, see their Figs. B.2a-B.2c) are also presented for comparisons. The breaker indices of CL07 and GO10 are also affected by the deep-water wave steepness (λ_0) and normalized water depth (kd), respectively. For small wave steepness ($\lambda_0 = 0.01$, cyan solid line) or shallow water ($kd = 0.2$, black solid line), both generally predict higher values of the breaker index than those from the conditions of large wave steepness ($\lambda_0 = 0.08$, cyan dash line) or relatively deep water ($kd = 0.9$, black dash line). The main feature of GO10 is that the breaker index monotonously increases with increasing bottom slope. However, CL07 shows a different tendency of the breaker index. The breaker indices of CL07 level off or even decrease for large slopes ($m > 0.1$), which is more realistic compared with the extensive date sets with a wide range of bottom slopes ($0.01 < m < 2$) collected in CL07. The saturation of the breaker index at large bottom slopes is well represented in the new parameterization. The breaker indices in the new parameterization are basically bounded by the breaker indices in CL07 for small and large wave steepness (cyan lines) and agrees well with the observed values. This further justifies the nonlinear slope dependency in the new parameterization in shallow waters. These findings reveal the fact of nonlinear effect of bottom slope on the wave breaking behaviors. Considering the significant differences in wave transformations over gentle and steep bottom slopes (as presented in Fig. 5.8), the nonlinear effect of the bottom slope may not limited in the wave breaking behaviors but also in other physical processes, such as the triad wave-wave interactions (e.g. *Toledo and Agnon,* 2012).

Figure 5.10b presents variations of breaker indices in the new parameterization in comparison with SA15 and BJ78 as a function of normalized water depths at four different

bottom slopes. The breaker indices in the new parameterization differ significantly from the indices in SA15 and BJ78 in shallow waters ($kd < 1$) with steep bottom slopes ($m > 1:20$). The differences in the breaker indices between the new parameterization and SA15 are, however, small in relatively deep waters with $kd > 1.1$ (Fig. 5.10b).
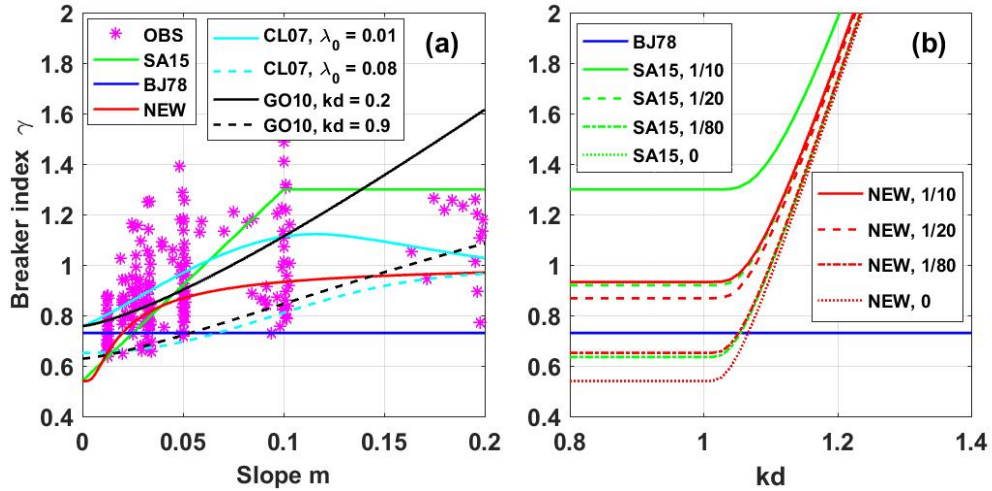
Figure 5.10: Comparisons of breaker indices in the new parameterization and two existing parameterizations (SA15 and BJ78) as a function of the (a) bottom slope (m) for shallow waters ($kd < 1$) and (b) normalized water depth. In panel (a), the observed values (OBS) of the breaker indices collected in *Camenen and Larson* (2007) are presented. The cyan lines represent the nonlinear slope dependency of the breaker index suggested by *Camenen and Larson* (2007, CL07) under the small ($\lambda_0 = 0.01$) and large ($\lambda_0 = 0.08$) deep-water wave steepness. The black lines represent the nonlinear slope dependency of the breaker index suggested by *Goda* (2010, GO10) under the shallow water ($kd = 0.2$) and deep water ($kd = 0.9$). In panel (b), different line colors represent different parameterizations and the line styles represent the breaker indices over different bottom slopes.

We next assess the performance of the new parameterization for depth-induced wave breaking by comparing the observed SWHS in the verification subset with the simulated SWHs produced by SWAN using the new parameterization with the same modelling settings as described in Section 5.3.2. We also compute the values of four metrics (i.e., the RB, RMSE, SI and R) for the observed and simulated SWHs in the verification subset (441 cases) based on the same definitions given in Section 5.3.3 for a quantitative comparison with the values in other parameterizations.

Figure 5.11 presents a comparison of SI-RB values in the new parameterization with those in the three best existing parameterizations (SA15, BJ78 and GO10) in four different

bottom types. In the sloping, barred and sandy bottom types (Figs. 5.11a-5.11c), most of the SI-RB points in the new parameterization are closer to the origins of the coordinates than those in SA15, indicating the better performance of the new parameterization than SA15. In the flat bottom type, the new parameterization and SA15 have highly comparable performances (Fig. 5.11d), which is expected since both the new parameterization and SA15 have the same value of the breaker index for the flat bottoms. In comparison with BJ78 and GO10, the new parameterization performs better over the sloping, sandy and flat bottom types, particularly in the flat bottom type.
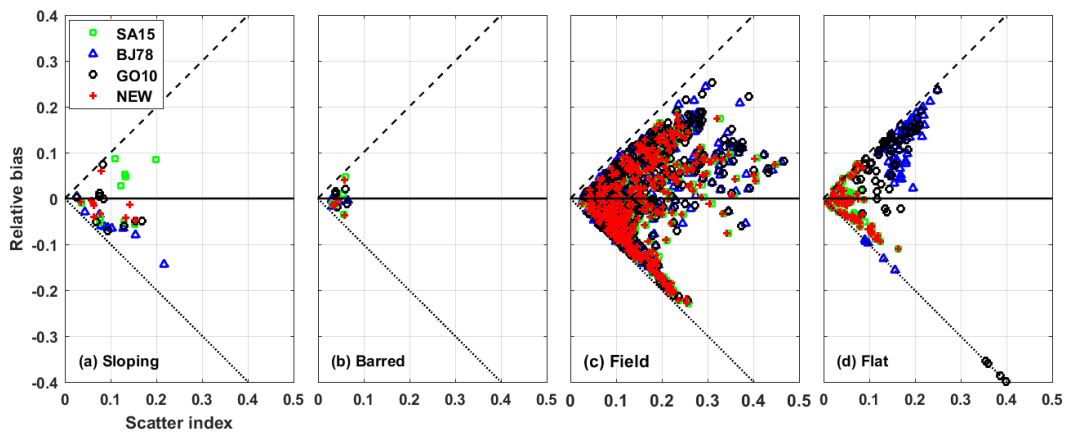
Figure 5.11: As in Fig. 5.3 but for the verification subset.

The four error metrics for the SWHs using the SA15, BJ78, GO10, and new parameterizations in the verification subset are presented in Table 5.5. In the sloping bottom type, the average SI values are relatively small and less than 12.7% and the average RB values are also relatively small in the range between -4.1% and 5.9% for the new parameterization, in comparison of the larger average SI (up to 22.3%) and larger average RB (between -5.2% and 11.9%) for SA15. In the barred and sandy bottom types, the average SI values for the new parameterization are slightly smaller (between 3.7% and 15.1%) than the corresponding values for SA15 (between 3.7% and 15.3%).

In terms of the average performances in each bottom type, the new parameterization shows a better performance over sloping bottoms with an average RMSE of 0.92 cm compared to 1.29 cm for SA15. The improvement of the RMSE seems minor and could be even within the range of the measurement or subsampling uncertainties. However, the small

improvement in the average RMSE may not impede a significant improvement of the new parameterization for a particular case. Furthermore, the SI value, which is generally more meaningful than the RMSE value, shows a significant reduction for the new parameterization with an average SI of 8.1% compared to 11.6% for SA15 over sloping bottoms. The new parameterization also shows slight improvements in the barred and sandy bottom types and remains a superior performance over flat bottoms with the same average SI value (5.3%) with SA15. The systematic overpredictions or underpredictions of the SWHs in the wave model are reduced by using the new parameterization in SWAN with the values of RB between -2.2% and 0.5%, in comparison of the RB values between -2.8% and 2.3% for SA15. Overall, the new parameterization has the lowest mean SI value (8.2%), smallest mean RMSE values (4.7 cm), and highest mean correlation coefficient values (0.93), in comparison with three best performing existing parameterizations.

Table 5.5: Summary of the error metrics for the SWHs using the SA15, BJ78, GO10 and new parameterizations in the verification subset. Otherwise as in Table 5.3.

Type	Index	Relative Bias (%)				Scatter Index (%)				RMSE (cm)				R (%)			
		SA15	BJ78	GO10	NEW	SA15	BJ78	GO10	NEW	SA15	BJ78	GO10	NEW	SA15	BJ78	GO10	NEW
Sloping	1	4.2	-6.3	0.5	-1.0	12.9	9.4	7.9	6.1	1.47	1.08	0.89	0.69	86.5	99.5	95.0	97.4
	2	11.9	-17.9	-5.5	-0.9	22.3	23.0	15.4	12.7	1.84	1.93	1.30	1.05	95.5	96.5	97.8	96.9
	3	8.7	-3.0	7.4	5.9	10.9	5.7	8.3	8.0	1.67	0.87	1.27	1.22	97.3	99.7	99.1	98.2
	4	-4.9	-6.8	-6.0	-4.1	12.0	12.1	12.6	12.2	1.21	1.21	1.23	1.22	93.2	96.6	95.3	92.3
	5	-5.2	-3.4	-5.0	-4.1	7.5	7.6	6.9	6.4	1.11	1.13	1.01	0.94	99.7	99.7	99.6	99.6
	6	-1.0	0.5	0.3	-0.8	3.7	2.6	2.6	3.4	0.44	0.28	0.29	0.41	99.0	99.5	99.5	99.2
Barred	7	1.0	-0.3	1.5	-0.5	5.5	3.0	3.9	4.4	4.24	2.33	3.78	3.43	95.6	97.4	97.4	95.8
	8	4.7	-0.4	-1.1	4.9	6.1	6.5	6.4	6.8	0.86	0.91	0.89	0.95	82.2	81.7	82.2	76.7
	9	-1.3	0.2	2.1	-1.5	3.7	4.3	6.1	3.7	2.26	2.65	3.72	2.26	89.8	82.8	67.6	90.1
	10	-2.3	-1.2	-0.5	-2.6	4.4	3.8	4.0	4.4	1.09	1.01	0.67	1.11	96.1	95.6	96.7	99.2
Field	11	-2.0	-4.5	-2.5	-2.5	14.9	14.0	14.2	14.3	16.7	15.7	15.9	16.0	87.8	94.1	90.9	90.1
	12	-3.6	-1.0	-0.4	-2.0	15.3	15.5	16.3	15.1	12.6	12.9	13.3	12.2	75.6	64.1	62.8	79.9
Flat	13	-2.2	11.8	6.7	-2.2	6.2	17.5	12.2	6.2	0.71	2.02	1.99	0.71	99.6	96.8	98.6	99.6
	14	3.1	-11.4	-38.4	3.1	4.4	11.4	38.4	4.4	2.97	7.78	26.1	2.97	99.1	97.1	92.5	99.1
Average	Sloping	2.3	-6.2	-1.4	-0.8	11.6	10.1	8.9	8.1	1.29	1.08	1.00	0.92	95.2	98.6	97.7	97.3
	Barred	0.5	-0.4	0.5	0.1	4.9	4.4	5.1	4.8	2.11	1.72	2.26	1.94	90.9	89.4	86.0	90.4
	Field	-2.8	-2.7	-1.4	-2.2	15.1	14.8	15.3	14.7	14.6	14.3	14.6	14.1	81.7	79.1	76.9	85.0
	Flat	0.5	0.2	-15.8	0.5	5.3	14.4	25.3	5.3	1.84	4.90	14.1	1.84	99.3	96.9	95.6	99.3
	Overall	**0.1**	**-2.3**	**-4.5**	**-0.6**	**9.2**	**10.9**	**13.6**	**8.2**	**4.97**	**5.50**	**7.98**	**4.70**	**91.8**	**91.0**	**89.0**	**93.0**

The satisfactory performances of the new parameterization over sloping and flat bottoms are further demonstrated in scatter plots shown in Figs. 5.12 and 5.13 for the verification subset. Figure 5.12 indicates that the use of the new parameterization in SWAN performs

better than SA15 in the four sloping bottom types, particularly in the steep bottom slope of $m = 1:10$ (Fig. 5.12a). However, it should be noted that the new parameterization performs worse than BJ78 and GO10 over the gentle bottom slope of $m = 1:80$ (Fig. 5.12d). For the flat bottom cases, Fig. 5.13 demonstrates that the new parameterization has the similar performance with SA15 with the data points generally following the ideal fitting line over flat bottoms, and they show much better performances than BJ78 and GO10. Therefore, with the inclusion of the nonlinear dependency of the breaker index on the bottom slope in shallow waters, the new parameterization significantly improves the performances of SWAN in simulating SWHs over various bottom slopes and remains very good performances over flat bottoms.
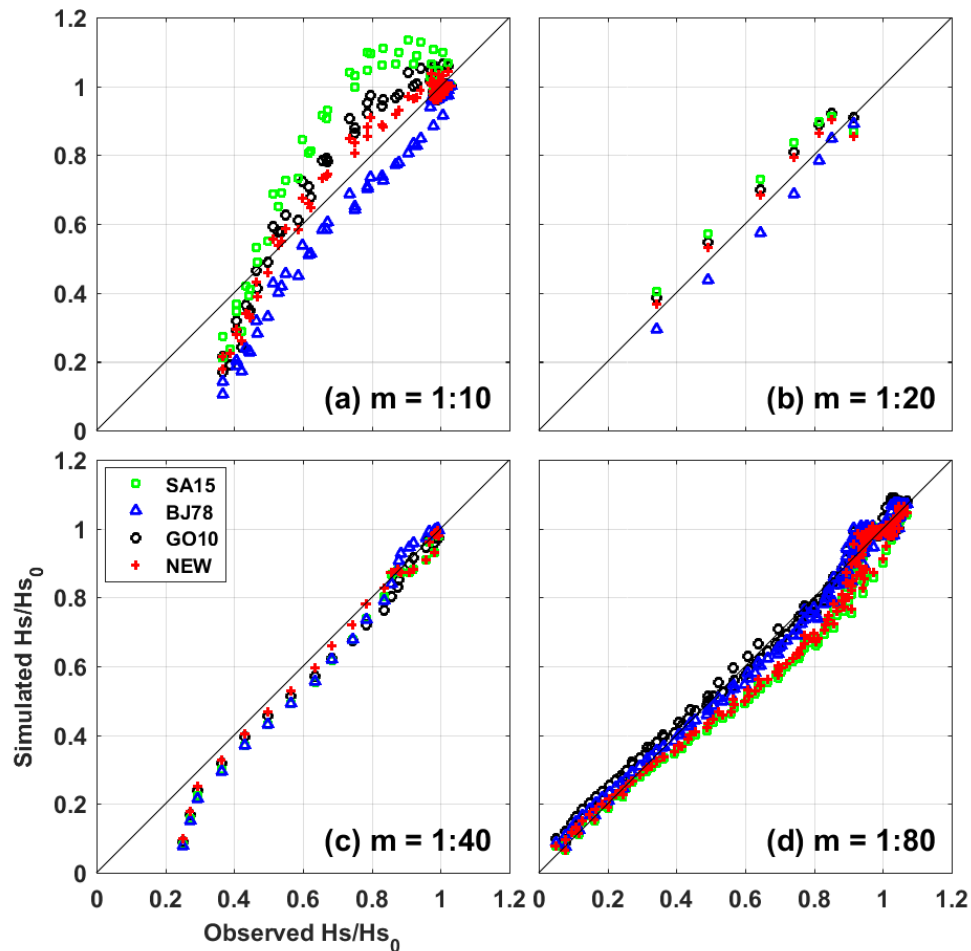
Figure 5.12: Scatter plots of observed and simulated SWHs normalized by corresponding incident SWHs in four bottom slopes of (a) $m = 1:10$ (Index 1), (b) $m = 1:20$ (Index 3), (c) $m = 1:40$ (Index 5) and (d) $m = 1:80$ (Index 6) in the verification subset.
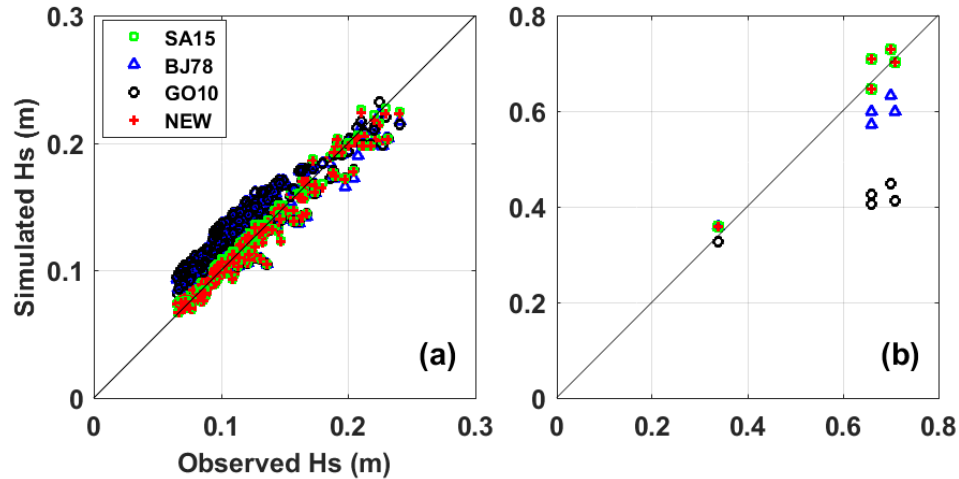
Figure 5.13: Scatter plots of observed and simulated SWHs in cases of (a) reef flat (Index 13) and (b) Lake Sloten (Index 14) in the verification subset.

5.5 Conclusions

The main objectives of this study were to assess the performances of six existing parameterizations for depth-induced wave breaking in spectral ocean wave models and to introduce a new parameterization to improve the performance of the spectral ocean wave model in simulating significant wave heights (SWHs) in coastal waters. The main differences between the six existing parameterizations are different representations of the breaker index or breaking wave fraction. The new parameterization was modified from the parameterization suggested by *Salmon et al.* (2015) by using a nonlinear dependence of the breaker index on the bottom slope to replace the piecewise linear dependence in the original SA15 parameterization.

The laboratory and field observations in 882 cases taken from 14 different data sources were used in this study to assess the performances of seven parameterizations including six existing and the new parameterizations. The observations were obtained under a wide range of wave conditions and bottom profiles, which were categorized into four bottom types in this study for the simplicity of analysis. The performances of the seven parameterizations were quantified using four error metrics, including the scatter index, relative bias, root mean square error and correlation coefficient. We demonstrated that these six existing parameterizations have reasonable performances in parameterizing depth-induced wave breaking in shallow waters, but with their own limitations and drawbacks. These

limitations together with the improvement of the new parameterization are summarized as follow:

(i)   The use of the parameterization suggested *Thornton and Guza* (1983, TG83) in SWAN leads to excessive wave energy dissipation due to the overestimation of breaking wave fraction, resulting in its underestimations of SWHs in all bottom types. The parameterization suggested by *Ruessink et al.* (2003, RU03) has relative low values of the breaker index in shallow waters, leading to its underestimations of SWHs in all bottom types except the flat bottom type. The use of the parameterization suggested by *Nelson* (1987, NE87) in SWAN results in overestimations of SWHs over relatively steep bottom slopes, since this parameterization has unrealistically large values of the breaker index.

(ii) The parameterizations suggested by *Goda* (2010, GO10), *Battjes and Janssen* (1978, BJ78) and *Salmon et al.* (2015, SA15) are the best among the six existing parameterizations. The use of the parameterization suggested by *Goda* (2010, GO10) leads to satisfactory simulations of SWHs in the sloping and barred bottom types, but this parameterization has large errors of SWHs over flat bottoms. The undesirable performance of GO10 in flat bottoms results in a higher overall scatter index of 12.6% compared to that of 9.9% for SA15. The commonly-used default parameterization of BJ78 shows reliable performances under a wide range of bottom profiles. BJ78, however, generates underpredictions of SWHs in the locally-generated wave conditions and overpredictions in the remotely-generated conditions over flat bottoms. The undesirable performance of BJ78 in flat bottoms results in a slightly higher overall scatter index of 10.8% compared to that of 9.9% for SA15. The drawbacks of BJ78 can be addressed in SA15, but SA15 has relatively larger errors in SWHs than BJ78 over sloping, barred and sandy bottoms.

(iii) The newly developed parameterization for depth-induced wave breaking in shallow waters has three tunable coefficients for the nonlinear dependence of the breaker index on the bottom slope (Eq. 5.16). The laboratory and field observations were used to determine these three coefficients. These three coefficients were found to be $b_0 = 0.54$, $b_1 = 0.47$ and $b_2 = 0.018$. The newly developed parameterization was demonstrated to improve the performances of the spectral ocean wave model in simulating SWHs over sloping, sandy

and flat bottom types. Overall, the new parameterization has the best performance with an overall average scatter index of ~8.2% in comparison with the three best performing existing parameterizations with the average scatter index between 9.2% and 13.6%.

(iv) It should be noted that significant differences occur in the radiation stress gradients produced by the six existing parameterizations and the newly developed parameterization. As spectral ocean wave models have increasingly been used to study the wave-current interactions, an appropriate estimation of the radiation stress gradients is important for representing wave-induced currents and associated sediment transport over coastal waters. One of future research directions is to address the accuracy of the newly developed parameterization for depth-induced wave breaking in terms of not only wave heights but also other parameters, such as radiation stress and wave-induced setup. More studies are needed to determine coefficients of the newly developed parameterization (Eq. 5.16) simultaneously for all cases either by brute force sampling of parameter space (e.g., *Zamora-Sillero et al.,* 2011), or by using for instance a genetic optimization approach (e.g., *Altiparmak et al.,* 2006).

CHAPTER 6

WAVE-CURRENT INTERACTIONS DURING HURRICANES EARL AND IGOR[1]

6.1 Introduction

Ocean surface gravity waves are generated by winds, representing the most energetic motion in the ocean. The effects of surface waves on ocean currents, however, are often left out from the ocean general circulation and climate models (*Babanin et al.,* 2017). Wave-current interactions (WCIs) over the coastal and shelf waters and in the deep oceans have been an important research topic in recent decades. Surface waves can affect ocean currents through mainly four physical mechanisms. At the sea surface, surface waves can affect the air-sea fluxes by changing the sea surface roughness (*Niu and Xia,* 2017; *Lin and Sheng,* 2020). In the upper ocean, waves can enhance the turbulent mixing through the interaction between the Stokes drift and Coriolis force, Langmuir circulation, breaking and nonbreaking waves (*Wu et al.,* 2015). In coastal waters, the interactions of surface waves with the seabed can enhance the bottom shear stress (*Dalyander et al.,* 2013; *Mao and Xia,* 2018). The additional momentum flux from surface waves to currents can generate longshore and rip currents (*Kumar et al.,* 2011) and escalate surge elevations (*Huang et al.,* 2010). Wave-induced setup can have large effects on the sea level variations during storms (*Zou and Xie,* 2016; *Liu and Huang,* 2020). Moreover, surface waves can affect the river plume and circulations in estuaries (*Gong et al.,* 2018). Therefore, accurate representations of wave-dependent wind stress, wind input to waves, whitecapping, depth-induced wave

---

[1]Lin, S., Sheng, J., Ohashi, K., and Song, Q. (2021). Wave-current interactions during Hurricanes Earl and Igor in the northwest Atlantic. To be submitted.

breaking are important for the study of WCIs. These important physical processes are investigated in our previous studies (*Lin and Sheng, 2017*; *Lin and Sheng, 2020*; *Lin et al., 2020*). Ocean currents, in turn, can affect the horizontal advection of surface waves and change the absolute frequencies of surface waves as a result of the Doppler shift (*Wang and Sheng, 2018*). When surface waves encounter spatially varying currents, currents can modify the wave frequency and cause wave refraction. Ocean currents also modify the relative speed of the air above the sea surface and affect the air-sea momentum flux, which is known as the relative wind effect (*Ardhuin et al., 2012*).

The study region of this research is the northwest Atlantic (NWA). The circulation and associated variability in this region are dynamically complicated, with meanders and eddies associated with the Gulf Stream and Labrador Current (*Wu et al., 2012*). The strong tidal currents in the Gulf of Maine (GoM) and adjacent waters contributes to the complexity of circulation in the region (*Chen et al., 2011*). The large river discharge from the St. Lawrence River (SLR) affects the circulation in the Gulf of St. Lawrence (GSL) and over the Scotian Shelf (ScS) (*Ohashi and Sheng, 2013*). The NWA is also frequently subjected to storms and hurricanes. Intensive WCIs occur during storms or hurricanes over areas ranging deep waters to coastal regions. The interactions between surface waves and currents, including larger-scale circulations, tides, buoyancy-driven currents, and wind-driven currents, contribute greatly to the complexity of hydrodynamics in this region. WCIs are therefore of significant importance and should be carefully studied in order to gain a comprehensive understanding of physical environments and associated variability in the NWA.

Previous studies have shown some effects of WCIs on coastal circulations, surface cooling, storm surges, and wave propagations (e.g., *Xie et al., 2001*; *Perrie et al., 2003*; *Olabarrieta et al., 2011*; *Sun et al., 2013*; *Zou and Xie, 2016*; *Wang and Sheng, 2016*; *Sun et al., 2018*). *Xie et al.* (2001) showed that waves can significantly affect coastal ocean currents in the South Atlantic Bight through wave-dependent wind stress and wave-induced bottom stress based on the results of a coupled wave-current model driven by uniform surface winds. *Perrie et al.* (2003) demonstrated that wave-induced currents due to Stokes drift and wave-breaking dissipation can exceed 40% of the usual Ekman current over the Labrador Sea

during a winter storm. *Olabarrieta et al.* (2011) examined the effects of WCIs on the sea surface elevations and currents in an inlet-estuary system and suggested that the acceleration induced by wave breaking is one of the leading terms for the momentum balance in the inlet area. *Sun et al.* (2013) investigated the responses of coastal regions to Hurricane Bob in 1991 over the GoM and New England, and showed that the impact of WCIs on surge elevations varied in space and time. *Zou and Xie* (2016) investigated the WCIs in the GoM during the extratropical storm on Patriot's Day of 2007. They found that wave-induced currents at the storm peak can account for 17% of the total depth-mean currents over Georges Bank (GeB) and wave heights were modulated by tides and surges along the coast. *Wang and Sheng* (2016) investigated the WCIs over the eastern Canadian shelf (ECS) during a winter storm and Hurricanes Juan (2003) and Bill (2009). They found that surface cooling can be enhanced by up to 1.2°C due to the WCIs during hurricanes. They also showed that the significant wave heights (SWHs) generated by hurricanes can be reduced by more than 11% on the right-hand side (RHS) of the storm track and increased by about 5% on the left-hand side (LHS). This finding was also confirmed by *Sun et al.* (2018), who showed a reduction of SWHs of ~10% due to the WCIs during Hurricanes Juan and Bill.

The previous studies certainly improved our understandings of the WCIs but mostly focused on coastal regions. Considering the complicated circulation patterns in the NWA associated with tides, river runoff, storms and large-scale circulations, it is necessary to investigate the WCIs on different spatiotemporal scales and in different environmental conditions. Moreover, some of the important physical processes in the WCIs were not included or not well represented in the coupled wave-circulation models used in these previous studies, such as the effects of waves on the wind stress and bottom stress. Physical processes in the WCIs are far from being well understood. Quantifying the effects from different physical processes in the WCIs will greatly deepen our knowledge on the WCIs. The main objective of this chapter is to examine the roles of different WCI mechanisms on the response of ocean surface waves and circulations during Hurricanes Earl and Igor in September 2010. A three-dimensional (3D) coupled wave-circulation model is developed and validated for the NWA based on the Coupled Ocean-Atmosphere-Wave-Sediment Transport (COAWST) modeling system (*Warner et al.* 2010).

This chapter is structured as follows. Section 6.2 introduces the coupled wave-circulation model for the NWA. Section 6.3 presents the observational data used in this study. Section 6.4 describes Hurricanes Earl and Igor in the NWA. The effects of currents on waves during these two hurricanes in terms of the SWHs, peak wave periods, and wave spectra are investigated in Section 6.5. The effects of waves on the sea level, current, salinity and temperature are discussed in Section 6.6. Conclusions are presented in Section 6.7.

6.2 The Coupled Wave-Circulation Model

A coupled wave-circulation model is developed to investigate the ocean responses to Hurricanes Earl and Igor over the NWA based on the COAWST modeling system (*Warner et al.* 2010). The COAWST modelling system is skillful at simulating ocean surface wave fields, sea surface properties, and WCIs (e.g., *Olabarrieta et al.* 2011; *Chen et al.* 2019; *Prakash and Pant,* 2020; *Hegermiller et al.,* 2019). In this study, only the Simulating Waves Nearshore model (SWAN; version 41.31) and the Regional Ocean Modeling System (ROMS; version 3.8) are used and other components are deactivated. In the COAWST modelling system, ROMS and SWAN are two-way coupled using the Model Coupling Toolkit (*Larson et al.,* 2005) at a user-specified coupling interval. Details on the coupled model, model configurations and design of numerical experiments are provided below.

6.2.1 Ocean Wave Model

SWAN is a third-generation spectral wave model that solves the wave action balance equation written as (*Booij et al.,* 1999):

$$\frac{\partial N}{\partial t} + \nabla \cdot (\dot{\boldsymbol{X}} N) + \frac{\partial}{\partial \sigma}(c_\sigma N) + \frac{\partial}{\partial \theta}(c_\theta N) = \frac{S_{tot}}{\sigma} \tag{6.1}$$

$$\dot{\boldsymbol{X}} = \boldsymbol{c_g} + \boldsymbol{U} \tag{6.2}$$

$$c_\sigma = -\frac{\partial \sigma}{\partial d}\frac{\partial d}{\partial s} - \boldsymbol{k} \cdot \frac{\partial \boldsymbol{U}}{\partial s} \tag{6.3}$$

$$c_\theta = -\frac{1}{k}\left(\frac{\partial \sigma}{\partial d}\frac{\partial d}{\partial q} + \boldsymbol{k} \cdot \frac{\partial \boldsymbol{U}}{\partial q}\right) \tag{6.4}$$

where N is the wave action density, σ is the relative wave frequency, θ is the wave direction, d is the total water depth, $\boldsymbol{k}$ is the wavenumber vector, k is the wavenumber magnitude, S_{tot} is the total wave energy source or sink, $\boldsymbol{c_g}$ is the wave group velocity,

c_σ and c_θ are the propagation speeds in frequency space and directional space, s is a coordinate in the wave direction, q is a coordinate perpendicular to s, $\boldsymbol{U}$ is the depth-weighted mean ocean current integrating over a depth controlled by the wavenumber to allow vertically sheared currents (*Kirby and Chen,* 1989). The effects of currents on waves are incorporated in the third-generation spectral wave models, including the horizontal current advection of surface waves ($\boldsymbol{c_g} + \boldsymbol{U}$), the change of wavenumber (Eq. 6.2) as a result of the Doppler shift and the current-induced refraction (Eq. 6.3). The relative wind effect is also included by using the modified wind velocity vector ($\boldsymbol{U_{10}} - \boldsymbol{U}$) in driving the coupled model. In addition, the sea surface elevations calculated by the ocean circulation model modifies the total water depth used in the wave model.

6.2.2   Ocean Circulation Model

ROMS is a free surface, terrain-following numerical model, which solves the 3D Reynolds-averaged Navier-Stokes (RANS) equations using the hydrostatic and Boussinesq assumptions (*Haidvogel et al.,* 2000). The effects of waves on currents in the ROMS are incorporated through mainly four mechanisms, including the 3D wave forces on currents, wave-dependent wind stress, wave-induced bottom stress and wave-enhanced vertical mixing. The 3D wave forces on currents are specified in terms of the radiational stress (RS) formulation (*Mellor,* 2008) or the vortex force (VF) formulation (*McWilliams et al.,* 2004; *Uchiyama et al.,* 2010; *Kumar et al.,* 2012). Following previous studies (*Uchiyama et al.,* 2010; *Kumar et al.,* 2012), the momentum equations based on the VF formulation are used here, written as:

$$\frac{\partial \boldsymbol{u}}{\partial t} + \boldsymbol{u} \cdot \nabla_h \boldsymbol{u} + w \frac{\partial \boldsymbol{u}}{\partial z} + f_c \hat{\boldsymbol{z}} \times \boldsymbol{u} + \nabla_h \varphi - \boldsymbol{F} = -\nabla_h \mathcal{R} + \boldsymbol{J} + \boldsymbol{F_w} \quad (6.5)$$

$$\frac{\partial \varphi}{\partial z} + \frac{\rho g}{\rho_o} = -\frac{\partial \mathcal{R}}{\partial Z} + K \quad (6.6)$$

and the continuity equation is written as:

$$\nabla_h \boldsymbol{u} + \frac{\partial w}{\partial z} = 0 \quad (6.7)$$

and the tracer equation (for temperature and salinity) is written as:

$$\frac{\partial c}{\partial t} + (\boldsymbol{u} \cdot \nabla_h)c + w \frac{\partial c}{\partial z} - C_{source} = -(\boldsymbol{u_s} \cdot \nabla_h)c - w_s \frac{\partial c}{\partial z} + \frac{1}{2} \frac{\partial}{\partial z} \left(\epsilon \frac{\partial c}{\partial z} \right) \quad (6.8)$$

where $(\boldsymbol{u}, w)$ are components of the quasi-Eulerian mean velocity and $(\boldsymbol{u}_s, w_s)$ are components of the Stokes drift in the horizontal (x, y) and vertical (z) directions, respectively. The quasi-Eulerian mean velocity is defined as the Lagrangian mean velocity minus the Stokes drift. Here ∇_h is the horizontal Laplace operator, f_c is the Coriolis parameter, $\hat{\boldsymbol{z}}$ is the unit vector in the vertical direction, ρ and ρ_o are the total and reference densities of sea water, g is the gravitational acceleration, $\varphi = p/\rho_o$ is the dynamic pressure, p is the hydrostatic pressure, $\boldsymbol{F}$ represents the non-wave forces, $\mathcal{R}$ is the Bernoulli-head, $(\boldsymbol{J}, K)$ are the horizontal and vertical components of the vortex force, and $\boldsymbol{F_w}$ represents the wave forces due to non-conservative wave dissipation processes, including whitecapping, depth-induced wave breaking and wave rollers. In the tracer equation, c is any material tracer concentration, C_{source} is the tracer source or sink, and ϵ is the wave-induced tracer diffusivity. Terms on the RHS of Eqs. 6.5-6.8 corresponds to the effects of waves on currents. When the 3D wave forces are not considered, these terms will be excluded in the simulations. Additional information about the formulas for calculating these terms can be found in *Uchiyama et al.* (2010) and *Kumar et al.* (2012).

The air-sea momentum flux is affected by surface waves through the variation of sea surface roughness (z_0), which has a smooth flow component (z_0^s) due to the viscosity and a rough flow component (z_0^r) driven by surface gravity waves (Eq. 4.4). In this study, two different parameterizations are used for z_0^r. When the wave effect on the wind stress is not considered, z_0^r is estimated using the formulation suggested by *Charnock* (1955) given as:

$$z_0^r = \alpha_c u_*^2 / g \tag{6.9}$$

$$\alpha_c = \frac{g z_0^r}{u_*^2} = 0.011 + 0.007 \min\left(max\left(\frac{U_{10}-10}{8}, 0\right), 1.0\right) \tag{6.10}$$

where α_c is the nondimensional roughness and varies between 0.011 and 0.018 at different wind speeds (*Smith,* 1988). This equation implies that the sea surface roughness increases monotonically with the wind speed. When the wave effect on the wind stress is included, the newly-developed formula by *Lin and Sheng* (2020) is used for z_0^r. In the new formula (Eq. 5.11), z_0^r is scaled by the SWH and has different dependencies on the wave age under three different sea states (i.e., the wind-wave-dominated, mixed, and swell-dominated sea states). The reason for using this new formula is that many existing formulas have some drawbacks in representing the wind stress (e.g., *Drennan et al.,* 2005; *Lin and*

Sheng, 2020). Based on the suggestion by *Davis et al.* (2008), the sea surface roughness (z_0) is limited with a maximum value of 2.85×10^{-3} m for all the model runs, which corresponds to a maximum value of 2.4×10^{-3} for the drag coefficient. This is consistent with many other studies in that the drag coefficient levels off at high winds (e.g., *Powell et al.,* 2003; *Donelan et al.,* 2004).

The bottom-boundary layer (BBL) model suggested by *Madsen* (1994) is used to account for the enhancement of the apparent bed roughness due to WCIs. For the cases without wave effects on the bottom stress, the logarithmic formulation is used in the ROMS assuming a logarithmic profile in the BBL (*Warner et al.,* 2008).

There are several different methods for the calculation of vertical mixing in the ROMS (*Warner et al.,* 2005). In this study, the $k - \varepsilon$ turbulence closure model is used through the Generic Length Scale (GLS) scheme (*Umlauf and Burchard,* 2003). Wave-enhanced vertical mixing is accomplished by introducing the contribution of wave dissipation as a surface flux of turbulent kinetic energy (TKE) in the GLS scheme. The TKE is proportional to the wave energy dissipation during wave breaking (*Feddersen and Trowbridge,* 2005) and the surface roughness is proportional to the SWH (*Stacey,* 1999). For the cases without wave effects on the vertical mixing, the TKE in the GLS scheme is calculated based on the wind stress (*Warner et al.,* 2005).

6.2.3   Model Configurations

The coupled wave-circulation model covers the northwest Atlantic between 80°W and 40°W and between 34°N and 55°N (Fig. 6.1). The model bathymetry is based on the General Bathymetric Chart of the Oceans (GEBCO) gridded bathymetric data set (www.gebco.net), which is a global terrain model with a resolution of 1/120°. The circulation model ROMS has a horizontal resolution of 1/12° and 40 vertical sigma levels with higher resolution close to the surface to resolve the vertical system dynamics.

The atmospheric forces used to drive the ROMS are extracted from the fifth generation of the European Center for Medium-Range Weather Forecasts reanalysis (ERA5), which is available on one-hour intervals with a horizontal resolution of 1/4° (*C3S,* 2017). The

specified atmospheric fields include the wind velocity, sea level pressure, shortwave radiation, long wave radiation, humidity, precipitation, air temperature, and cloud cover. To have good representations of the fine wind structure associated with Hurricanes Earl and Igor, the tropical cyclone data from the Hurricane Wind Analysis System (HWIND) is blended into the ERA5 wind forcing. The HWIND provides an objective analysis of hurricane winds that integrates wind measurements from a variety of observation platforms (*Powell et al.,* 1998). Because direct temporal and spatial interpolation may result in the distortion of hurricane wind fields, we use the method suggested by Fan et al. (2009) to interpolate the HWIND wind fields during Hurricanes Earl and Igor into the model grid at 0.5-hour intervals. The modified ERA5 winds are made by first interpolating the original ERA5 winds into the model grid (1/12°) and then inserting the HWIND wind fields into the interpolated ERA5 winds. The atmospheric forces are used to calculate the wind stress and heat flux in ROMS using the bulk flux algorithms (*Fairall et al.,* 2003).

The total sea level and velocity at the open boundary conditions of the circulation model (ROMS) are divided into the tidal and subtidal components. The tidal components are obtained from the Oregon State University Tidal Inversion Software (OTIS). The regional tidal solutions for the Atlantic Ocean are used, which have 11 tidal constituents (P1, Q1, O1, K1, M2, S2, N2, K2, M4, MS4 and MN4) and a spatial resolution of 1/12° (*Egbert and Erofeeva,* 2002). The initial and open boundary conditions for the subtidal components are interpolated from the daily Global Ocean Reanalysis and Simulation (GLORYS) data set with a horizontal resolution of 1/12° (*Fernandez and Lellouche,* 2018). The initial and open boundary conditions for the active tracers (i.e., temperature and salinity) are also interpolated from the GLORYS data set. At the open boundaries, a radiation boundary condition with nudging is imposed for the temperature, salinity and baroclinic velocities (*Marchesiello et al.,* 2001). The Shchepetkin boundary condition is imposed for the barotropic currents, allowing for the free propagation of wind-generated currents and tides (*Mason et al.,* 2010). Meanwhile, a sponge layer is imposed near the open boundaries, in which the model temperature and salinity are nudged to the GLORYS data with a resorting time scale of one day. The freshwater discharges for 49 rivers within the model domain are specified using the monthly-mean climatology data from Environment and Climate Change Canada (ECCC) and U.S. Geological Survey (USGS), except for the SLR. For the SLR,

the monthly-mean discharge values at Quebec City in 2010 published by the St. Lawrence Global Observatory (SLGO) are used. The SLR's discharge is estimated from the observed water level using the regression model of *Bourgault and Koutitonsky* (1999).

The wave model (SWAN) uses the same model grid and wind force as the circulation model (ROMS). The sea surface elevations and currents used in the SWAN are provided by the ROMS. The boundary conditions for the SWAN are interpolated from the global WAVEWATCH III (WW3) model provided by the French Research Institute for Exploitation of the Sea (IFREMER, ftp://ftp.ifremer.fr/ifremer/ww3/HINDCAST/). The global WW3 model was run using the ST4 source term package for the wind input and wave dissipation (*Ardhuin et al.,* 2010), which was extensively validated against observations (*Stopa et al.,* 2016b). The WW3 model output data have a spatial resolution of 1/2° and a temporal resolution of 3 hours. Spectral partition data from WW3 are used to create two-dimensional (2D) wave spectra along the open boundary of the SWAN.

The wave model integrations are carried out in spherical coordinates with a discrete spectrum consisting of 36 directions ($\Delta\theta$ = 10°) and 34 frequencies ranging from 0.04 to 1.0 Hz at a logarithmic increment of 0.1. The source term package known as ST6 is used to compute the wind input and wave dissipation (*Babanin,* 2011; *Zieger et al.,* 2015). The wind input and wave dissipation are important processes for wave evolution. Package ST6 includes new physical features for the wind-wave exchange (*Babanin,* 2011) and was shown to have the best performance for wave simulations over the NWA (*Lin et al.,* 2020). The nonlinear wave interactions are computed in the wave model using the Discrete Interaction Approximation (DIA) of *Hasselmann et al.* (1985). The wave model uses the eddy-viscosity model of *Madsen et al.* (1988) to estimate the bottom friction. The depth-induced wave breaking parametrization is computed using the scheme suggested by *Lin and Sheng* (2017), in which the breaker index is not a constant value but depends on the bottom slope and water depth.

In the coupled model, different time steps are used for the ROMS and SWAN. ROMS uses a 120 s baroclinic time step with a mode-splitting ratio of 20. SWAN is run with a time step of 300 s. The time interval for data exchange between models is set to 1200 s. ROMS

provides current velocity components and sea surface elevations to SWAN. SWAN, in turn, transfers wave dissipation source terms (including whitecapping, bottom friction and depth-induced wave breaking), surface and bottom wave parameters (including wave height, period, direction, wavelength, orbital velocity, Stokes drift and Bernoulli-head) to ROMS. This study focuses on September 2010, when two hurricanes passes over the NWA. The coupled model is initialized at 0000 UTC 1 August 2010 and the model results in September will be used in the following analyses.

Model results in seven different model simulations are used in this study to quantify the roles of different physical processes in the WCIs. Three basic numerical experiments are designed to examine the effects of the WCIs on ocean currents and surface gravity waves over the NWA, which include the wave-only model, circulation-only model, and fully-coupled model runs. Furthermore, four additional process-oriented experiments are designed to quantify different effects of waves on currents, including the wave-dependent wind stress, wave-induced bottom stress, wave-enhanced vertical mixing and 3D wave forces. Model configurations for the seven numerical experiments are summarized in Table 6.1.

Table 6.1: Model configurations for the seven numerical experiments

Run	Case description	Wave-dependent wind stress	Wave-induced bottom stress	Wave-enhanced vertical mixing	Wave forces
WO	Wave-only model	**Off**	**Off**	**Off**	**Off**
CO	Circulation-only model	**Off**	**Off**	**Off**	**Off**
FC	Fully-Coupled model	On	On	On	On
NWS	Coupled model no wave effects on wind stress	**Off**	On	On	On
NBS	Coupled model no wave effects on bottom stress	On	**Off**	On	On
NVM	Coupled model no wave effects on vertical mixing	On	On	**Off**	On
NWF	Coupled model no wave forces on currents	On	On	On	**Off**
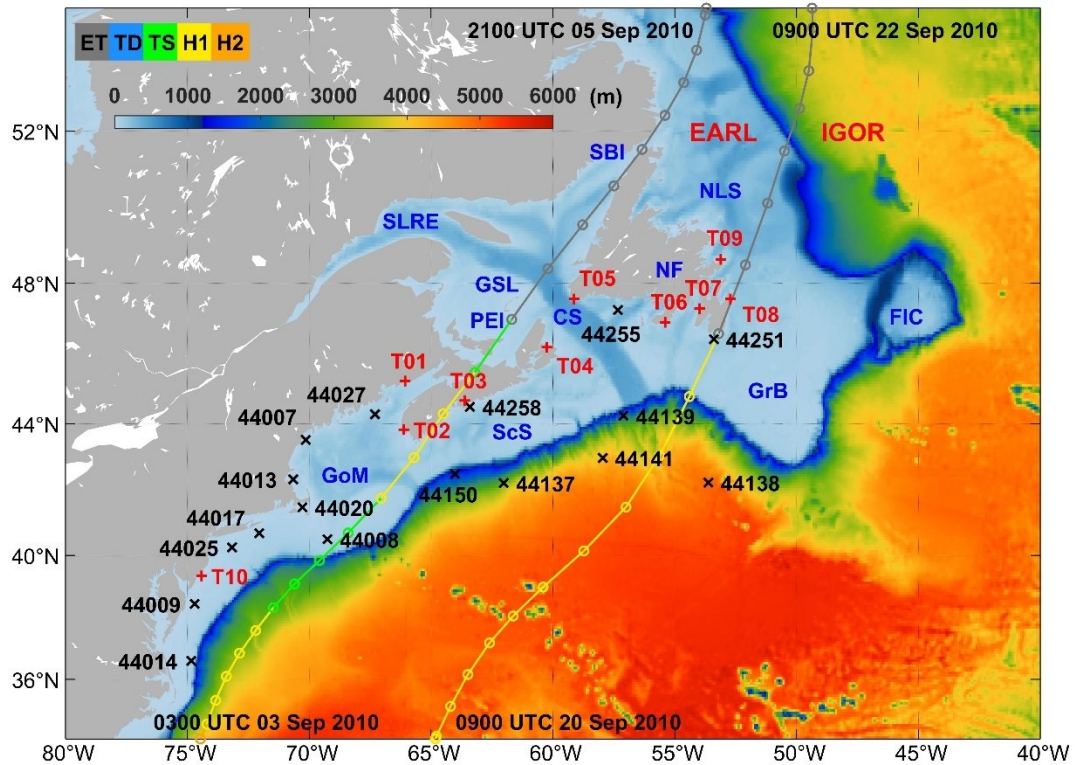
Figure 6.1: Domains and major topographic features of the NWA for the coupled wave-circulation model. Black marks denote wave buoy observations. Red marks denote tide gauge observations. See Table 6.4 for names of tide gauges. Abbreviations are used for the Newfoundland and Labrador Shelves (NLS), St. Lawrence River Estuary (SLRE), Strait of Belle Isle (SBI), Gulf of St. Lawrence (GSL), Cabot Strait (CS), Prince Edward Island (PEI), Newfoundland (NF), Grand Banks (GrB), Flemish Cap (FlC), Scotian Shelf (ScS), and Gulf of Maine (GoM). The storm tracks are shown by the solid circle lines in 3-hour intervals, together with hurricane strength indicated by the colors, including the extratropical (ET), tropical storm (TS), and hurricane (H1 or H2).

6.3 Observational Data

The observational data used in this study include in-situ observations and remote sensing measurements. These observational data are used here to assess the accuracy of numerical model results. The in-situ observations for ocean waves and sea surface temperature (SST) at 17 buoy stations in the study region (Fig. 6.1) were obtained from the National Data Buoy Center (NDBC, www.ndbc.noaa.gov) and ECCC (www.meds-sdmm.dfo-mpo.gc.ca). The SWHs and peak wave periods (PWPs) were measured at all buoys. The in-situ observations also include the hourly sea surface elevations observed at 10 tidal stations along the coastal regions of the eastern US and Canada. These sea level data were obtained

from the Canadian Tides and Water Levels Data Archive (tides.gc.ca/eng/data) and University of Hawaii Sea Level Center (*Caldwell et al.,* 2015; uhslc.soest.hawaii.edu).

The Optimally Interpolated (OI) SST daily product with a resolution of 9 km from the Remote Sensing Systems (RSS, www.remss.com) is used in this study. The OI SST product combines the through-cloud capabilities of the microwave data with the high spatial resolution and near-coastal capability of the infrared SST data. The weekly sea surface salinity product from the European Space Agency (ESA) Sea Surface Salinity (SSS) Climate Change Initiative (CCI) consortium is also used in this study (*Boutin et al.,* 2020). This weekly data set includes improved calibrated global SSS fields over a 10-year period (2010-2019) from all available satellite L-band radiometer measurements at a spatial resolution of 50 km. The reader is referred to *Reul et al.* (2020) for the validation and uncertainties of this dataset.

6.4 Hurricanes Earl and Igor

Hurricanes Earl and Igor were two major hurricanes that affected the NWA in September 2010. Earl was a Category-4 hurricane at its peak and had maximum winds of ~64.0 m/s over the western Atlantic on 2 September. The storm accelerated northeastward along the shelf break off the US coast and slowly weakened to a tropical storm after passing Cape Hatteras on 3 September. The storm reattained hurricane strength as it made landfall near Liverpool, Nova Scotia. The storm then became extratropical and translated through the GSL until it merged with another system over the Labrador Sea on 6 September (*Cangialosi,* 2011; Fig. 6.1). Hurricane Igor was the strongest cyclone of the season and the most destructive cyclone on record to strike Newfoundland (*Pasch and Kimberlain,* 2011). Igor reached Category-4 status, with peak winds of ~69.0 m/s on 15 September at low latitude of ~19°N. The storm weakened to a Category-1 hurricane on 20 September and started moving northeast toward Canada. Igor became an extratropical cyclone when it made landfall in Newfoundland on 21 September and was absorbed by another extratropical cyclone two days later (Fig. 6.1). These two hurricanes produced large wind waves and swells in the NWA. The intense WCIs during these two hurricanes will be investigated in Sections 6.5 and 6.6.

6.5 Effects of Currents on Waves

In this section, numerical model results are compared with the observational data introduced in Section 6.3 to assess the model performance and to examine the effects of WCIs on surface waves during Hurricanes Earl and Igor. The effects of currents on waves are investigated in terms of SWHs, PWPs, wave spectra and maximum SWHs.

6.5.1   Significant Wave Height

Figure 6.2 presents time series of the observed SWHs (H_s) and simulated SWHs in the fully-coupled (FC) and wave-only (WO) model runs at six buoy stations in September 2010. The positions of these six buoy stations are shown in Fig. 6.1. Buoy 44008 is on the LHS of, and close to, the storm track of Hurricane Earl. Buoys 44137, 44141, 44139 and 44138 are on the RHS of the storm track with increasing distances from the storm track. Buoy 44020 is located in the very shallow waters of Nantucket Sound. The observed maximum SWH (H_s^{max}) during Hurricane Earl in early September was ~8.1 m at buoy 44008 and ~10.2 m at buoy 44137. These large wind waves gradually dissipated as they spread out over the shelf break region. The observed H_s^{max} was ~6.0 m at buoy 44141 and ~4.8 m at buoy 44138. Figure 6.2 demonstrates that the FC run well reproduces the observed variations of SWHs at these buoys with simulated H_s^{max} of ~10.2 m at buoy 44137, ~6.4 m at buoy 44141, and ~4.6 m at buoy 44138. In comparison, the WO run produces similar H_s^{max} at buoy 44008 but overestimates H_s^{max} at the buoy stations on the RHS of the storm track. In other words, H_s^{max} is reduced due to the inclusion of WCIs with the largest reduction occurs at buoy 44141 (~0.81 m and ~13.2%; Fig. 2c).

After the peak winds, the observed SWHs at buoy 44008 exhibited an oscillating pattern in time with a period of ~18 hours, which is due to WCIs associated with strong near-inertial currents in the wake of Hurricane Earl. This near-inertial variability in SWHs is reproduced in the FC run but not in the WO run. The effect of near-inertial currents on the SWHs in the wake of hurricanes was also found in previous studies (e.g., *Gemmrich and Garrett,* 2012; *Wang and Sheng,* 2016). Based on long-term buoy observations, *Gemmrich and Garrett* (2012) estimated that the mean modulation of SWHs in the near-inertial band accounts for ~3.0% of the total SWHs. However, the modulation by near-inertial currents

of individual SWHs can be significant. Here, the difference of SWHs can be up to ~13.0% at buoy 44008 due to near-inertial currents in the wake of Hurricane Earl (Fig. 6.2a).
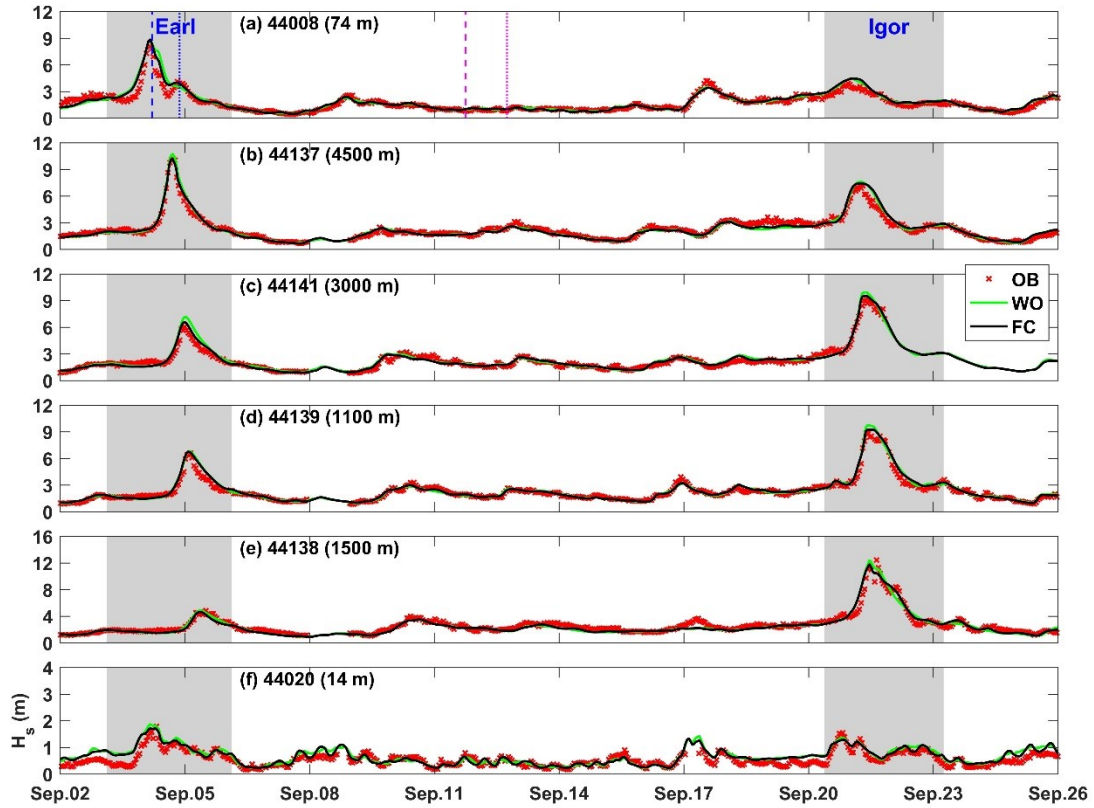
Figure 6.2: Time series of simulated SWHs in the wave-only (WO) and fully-coupled (FC) model runs against the observed values at six buoy stations in September 2010. The name and water depth of each buoy station are shown in each panel. The blue (magenta) lines represent the time for the analysis of wave spectra in Figs. 6.4 and 6.5.

During Hurricane Igor in late September, the FC run reproduces well the variations of SWHs at buoys 44137, 44141, 44139 and 44138 in terms of H_s^{max} and the oscillation of SWHs due to the near-inertial currents. In comparison, the WO run has larger values of H_s^{max} and overestimates the SWHs on both sides of the hurricane track (Figs. 6.2b-6.2e). This is due to the fact that ocean currents are generally in the following direction of surface waves on both sides of the hurricane track in response to the large size of Hurricane Igor. During Hurricane Igor, H_s^{max} is reduced by including WCIs with the maximum difference of ~0.94 m and ~9.0% at buoy 44138 (Fig. 6.2e).

In the GoM and adjacent waters, in additional to the effects of hurricane-driven currents on waves, strong tidal currents can modulate the mean wave variables at the semidiurnal

frequency. The GoM has strong semidiurnal M2 tidal currents with a tidal range of more than 10.0 m in the upper reaches of the Bay of Fundy (BoF) and around 1.0 m over the mouth of the GoM (*Chen et al.,* 2011). The temporal fluctuations of observed SWHs at buoys 44008 and 44020 during calm weather conditions are reproduced well in the FC run but not in the WO run. However, even in the FC run the errors are relatively large at buoy 44020. This is most likely due to the relatively coarse resolution (1/12°) of the coupled model, which is not able to simulate accurately wave evolution in Nantucket Sound. The effects of near-inertial currents and tides on waves will be further investigated in a future study.

Table 6.2: Summary of five error metrics for the SWHs predicted in the fully-coupled (FC) and wave-only (WO) model runs in September 2010. The error metrics include the scatter index (SI), relative bias (RB), root mean square error (RMSE), correlation coefficient (R) and relative variance (γ^2).

Buoy	Depth (m)	SI (%)		RB (%)		RMSE (cm)		R (%)		γ^2	
		FC	WO	FC	WO	FC	WO	FC	WO	FC	WO
44007	27	29.5	29.8	16.9	18.5	24.0	24.3	87.1	87.5	0.40	0.37
44008	75	18.6	21.5	5.4	5.3	32.3	37.4	95.7	94.2	0.12	0.16
44009	43	18.9	19.3	-4.0	-4.3	24.1	24.5	91.8	91.8	0.17	0.18
44013	64	19.6	19.0	0.0	-2.1	13.8	13.4	85.8	86.3	0.29	0.27
44014	45	27.9	26.6	11.7	8.5	39.1	37.3	94.2	93.9	0.20	0.20
44017	48	17.6	18.2	0.0	0.1	26.1	26.9	93.1	92.7	0.12	0.13
44020	14	28.5	30.5	14.7	16.8	15.8	16.9	84.5	84.9	0.31	0.34
44025	36	18.3	17.7	-3.9	-3.8	26.0	25.2	90.6	91.1	0.20	0.19
44027	185	26.5	27.4	14.2	15.2	29.3	30.2	91.5	92.0	0.22	0.23
44137	4500	12.3	12.9	-0.3	-0.7	28.8	30.1	97.5	97.4	0.06	0.06
44138	1500	14.0	15.5	-4.2	-4.4	36.9	40.8	96.9	96.4	0.06	0.08
44139	1100	10.8	11.9	3.1	2.8	24.9	27.5	98.3	97.9	0.04	0.05
44141	3000	11.1	14.1	1.7	3.8	25.7	32.5	98.3	97.7	0.04	0.06
44150	1300	13.6	14.1	2.8	2.7	28.7	29.6	97.4	97.5	0.05	0.06
44251	71	11.9	13.1	-2.0	-2.1	26.7	29.4	97.4	96.8	0.07	0.08
44255	179	15.4	17.1	0.1	0.2	28.0	31.2	95.1	94.6	0.11	0.14
44258	60	26.4	27.3	-1.4	-1.0	38.2	39.5	84.3	84.0	0.33	0.35
Average		18.9	19.8	3.2	3.3	27.6	29.2	93.0	92.8	0.16	0.17

Five error metrics are used in this study to quantity the model performance, which include the scatter index (SI), relative bias (RB), root mean square error (RMSE), correlation coefficient (R), and relative variance (γ^2) (see definitions in Appendix A). The error

metrics for SWHs in the FC and WO runs at 17 buoy stations are presented in Table 6.2. The errors in the FC run are smaller than those in the WO run at most buoy stations, since the variations of SWHs are generally better reproduced in the FC run (Fig. 6.2). For example, the simulated SWHs in the FC run have a RMSE of ~0.26 m and a SI of ~11.1% at buoy 44141 in comparison with ~0.33 m and ~14.1% in the WO run. Overall, the WO run generally overestimates H_s^{max} during two hurricanes and cannot reproduce the effects of near-inertial and tidal currents, with an average SI of ~19.8%. In comparison, the FC model better reproduces the peak values and temporal variations of the SWHs with an average SI of ~18.9%.

6.5.2   Peak Wave Period

Figure 6.3 presents time series of the observed PWPs and simulated values in the FC and WO runs at six buoy stations in September 2010. As Hurricanes Earl and Igor approached, the observed PWPs generally increased to ~10-18 s at these buoys. The observed PWPs dropped below 10 s as the storms left and the local winds weakened. Meanwhile, the observed PWPs occasionally shifted to higher or lower values. In comparison with the WO run, the FC run generally has slightly lower values of PWPs during the peak winds of the two hurricanes. The shift of PWPs are better reproduced in the FC run, such as at buoy 44008 during 11-13 September, at buoy 44141 on 9 September, and at buoy 44255 on 21 September (magenta marks in Fig. 6.3). These shifts indicate changes in wave spectra under the influence of currents, which will be discussed in Section 6.5.3.

The error metrics for the PWPs in the FC and WO runs at 17 buoy stations are presented in Table 6.3. Statistically, the FC run has smaller errors for the PWPs than the WO run at most buoy stations. For example, the overestimation of PWPs at buoy 44008 in WO run is reduced in the FC run, with the corresponding RB values decreasing from ~9.3% to ~6.6%. Overall, the WO run overestimates the PWPs with an average SI of ~27.5% and an average RB of ~5.4%. In comparison, the FC run better reproduces the variations of the PWPs with an average SI of ~26.4% and an average RB of ~4.1%.
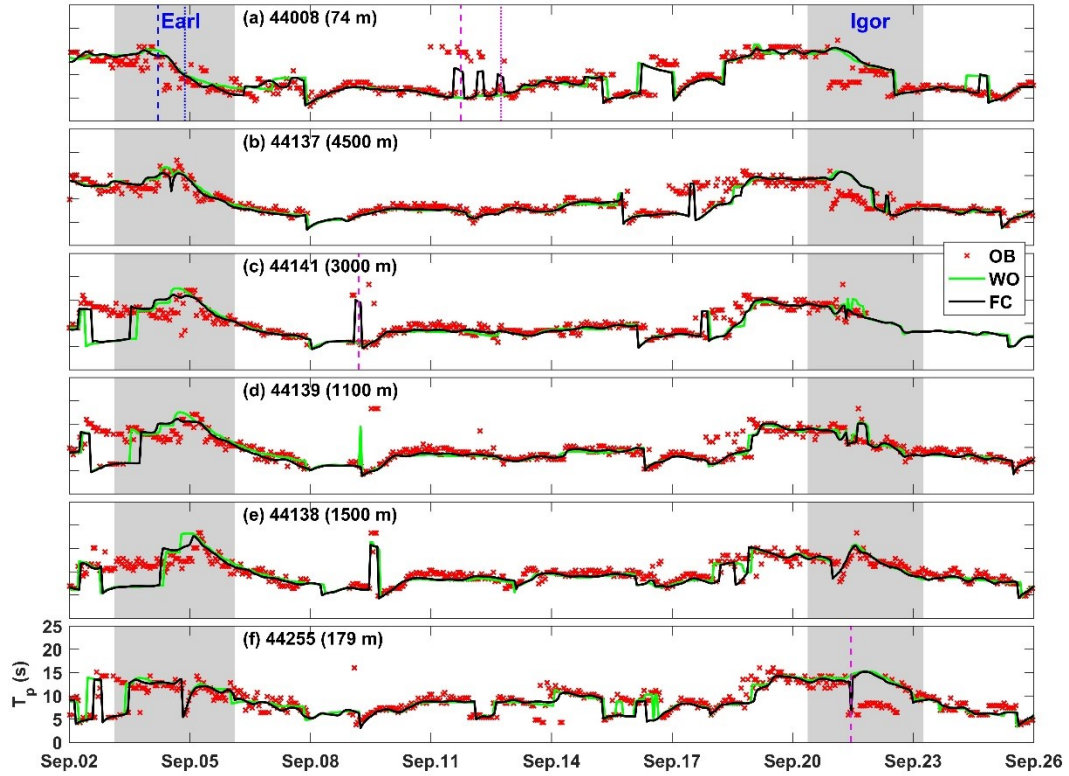
Figure 6.3: As in Figure 6.2, but for the PWPs.

Table 6.3: As in Table 6.2, but for the peak wave periods

Buoy	Depth (m)	SI (%)		RB (%)		RMSE (s)		R (%)		γ^2	
		FC	WO	FC	WO	FC	WO	FC	WO	FC	WO
44007	27	24.1	26.2	6.6	9.3	2.2	2.4	75.1	71.5	0.40	0.44
44008	75	22.5	24.1	0.8	1.1	2.0	2.2	75.2	71.1	0.47	0.53
44009	43	26.6	26.7	7.3	8.6	2.3	2.3	78.0	78.1	0.38	0.37
44013	64	36.9	42.9	12.6	17.0	2.9	3.4	70.7	61.1	0.49	0.64
44014	45	20.5	22.2	2.1	0.6	2.0	2.2	80.6	77.3	0.32	0.38
44017	48	19.9	22.5	1.4	4.1	1.8	2.0	86.3	82.6	0.23	0.29
44020	14	99.1	98.8	56.4	57.0	4.7	4.7	48.2	49.2	1.64	1.61
44025	36	24.3	26.0	3.8	5.8	2.2	2.3	81.3	78.8	0.31	0.35
44027	185	24.3	25.7	5.7	9.6	2.0	2.1	79.9	78.8	0.36	0.36
44137	4500	16.1	16.0	-2.2	-1.6	1.5	1.5	82.1	82.6	0.37	0.37
44138	1500	15.8	16.8	-4.6	-4.0	1.6	1.7	75.6	73.0	0.51	0.59
44139	1100	19.7	18.9	-5.4	-4.1	2.0	1.9	68.2	70.6	0.58	0.55
44141	3000	20.5	22.2	-4.6	-6.0	2.1	2.3	63.9	60.2	0.70	0.80
44150	1300	20.9	21.0	-1.6	-1.8	2.0	2.0	71.7	71.4	0.57	0.57
44251	71	20.0	19.6	-7.2	-6.6	2.0	1.9	58.5	61.5	0.72	0.70
44255	179	22.6	23.5	-1.6	1.1	2.1	2.1	61.9	59.8	0.72	0.78
44258	60	15.2	15.0	1.1	2.0	1.5	1.5	80.6	82.1	0.37	0.35
Average		26.4	27.5	4.1	5.4	2.2	2.3	72.8	71.2	0.54	0.58

6.5.3 Wave Spectra

We next examine the effect of WCIs on the wave frequency spectra, as shown in Fig. 6.4. At the time of peak winds during Hurricane Earl, the WO run slightly overestimates the spectral peak with a shift toward lower frequency at buoy 44008 on the LHS of the storm track (Fig. 6.4a). This corresponds to the overestimations of the SWH and PWP in the WO run at this time (blue dashed lines in Figs. 6.2a and 6.3a). At buoys 44137 and 44139, which are on the RHS of the storm track (Figs. 6.4b and 6.4c), the WO run overestimates the spectral peaks by up to ~35%, corresponding to the overestimations of H_s^{max} at these buoys (Figs. 6.2a and 6.2d). By comparison, the simulated wave spectra in the FC run agree better with the observations at these buoys. The differences in the spectral peaks between the two model runs are relatively small at buoy 44008 but significant at buoys 44137 and 44139, indicating that the overall influences of ocean currents on wave spectra are relatively weak on the LHS of the storm but significant on the RHS.

During Hurricane Igor, the WO run significantly overestimates the spectral peaks on both sides of the storm track (Figs. 6.4d and 6.4e) by up to ~27% at buoy 44138. By comparison, the FC run produces smaller spectral peaks and agree better with the observations. Therefore, the maximum SWHs are overestimated in the WO run but reproduced reasonably well in the FC run during Hurricanes Earl and Igor (Fig. 6.2). It should be noted that the effects of currents on wave spectra are strong on both sides of the storm track during Hurricane Igor, which is different from that during Hurricane Earl due mainly to the differences in the wind structures between the two hurricanes (Section 6.4).

The effects of currents on waves depend on the conditions of winds, waves and currents. During Hurricanes Earl and Igor, the ocean surface currents and winds are generally in the following directions on both side of the storm tracks. In the presence of following currents, the effective wind speeds acting on the ocean surface are reduced (*Ardhuin et al.,* 2012). This leads to the reduction of wave spectral peaks in the FC run in comparison with those in the WO run (Figs. 6.4a-6.4e). The reduction of wave spectral peaks is also attributed to the spatial advection of wave energy induced by currents (Eq. 6.2). Wave energy can be advected away from regions with strong currents toward surrounding regions with weak

currents, leading to wave energy divergence (convergence) over regions with strong (weak) currents in the FC run (Figs. 6.4a-6.4e).

The other important effects of currents on waves are the current-induced wavenumber shift due to the gradients of currents along the wave propagation directions (Eq. 6.3) and the current-induced wave refraction due to the gradients of currents along the wave crest directions (Eq. 6.4). The former decreases (increases) wave energy when waves propagate into (against) accelerating currents or against (into) deaccelerating currents. The latter changes wave propagations in space that mimics bathymetric effects (*Wang and Sheng, 2018*). The wave spectral peaks thus can be increased in the presence of currents, such as at buoy 44008 at 2100 UTC 04 September under the effect of near-inertial currents (Fig. 6.4f).
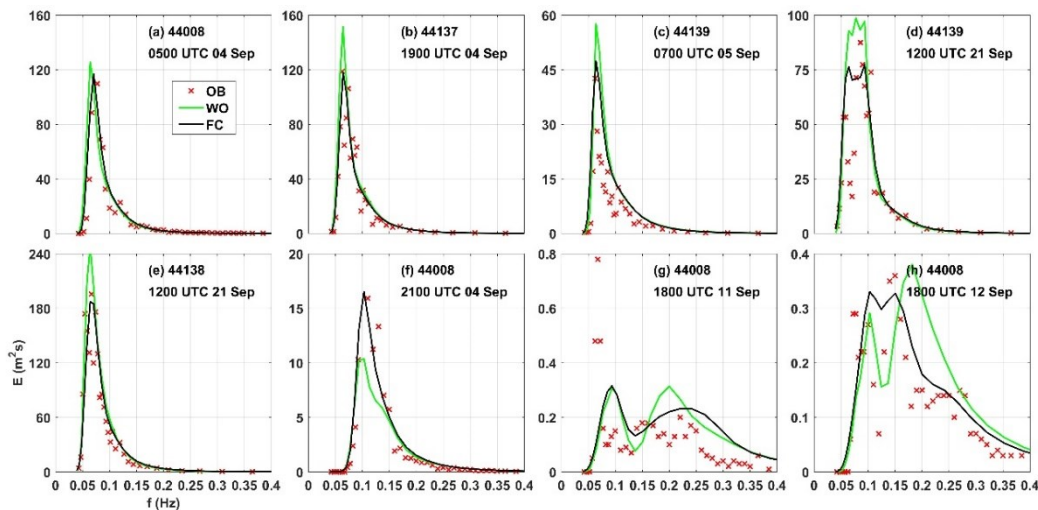
Figure 6.4: Observed (OB) and simulated wave frequency spectra in the fully-coupled (FC) and wave-only (WO) runs at different buoy stations in September 2010.

Figures 6.4g and 6.4h show the corresponding wave spectra when the PWPs shifted to higher values at buoy 44008 (magenta marks in Fig. 6.3a). At 1800 UTC 11 September, the observed wave spectrum at buoy 44008 had a bimodal structure. The observed increase in the PWP at this time was due to the relatively strong energy at the swell peak. In comparison with the WO run, the FC run produces a lower wind peak at buoy 44008 at this time and thus agrees better with the observations in terms of the wave spectrum (Fig. 6.4g) and PWP (Fig. 6.3a). The bimodal structure of wind and swell peaks are common during

storms, which contributes greatly to the highly variable feature of PWPs (*Collins et al.,* 2018). The other reason for the shift of PWPs is the shift of wave spectra induced by currents due to the Doppler effect. By including the effect of currents in the FC run, the wave spectrum is shifted toward lower frequencies at 1800 UTC 12 September (Fig. 6.4h).
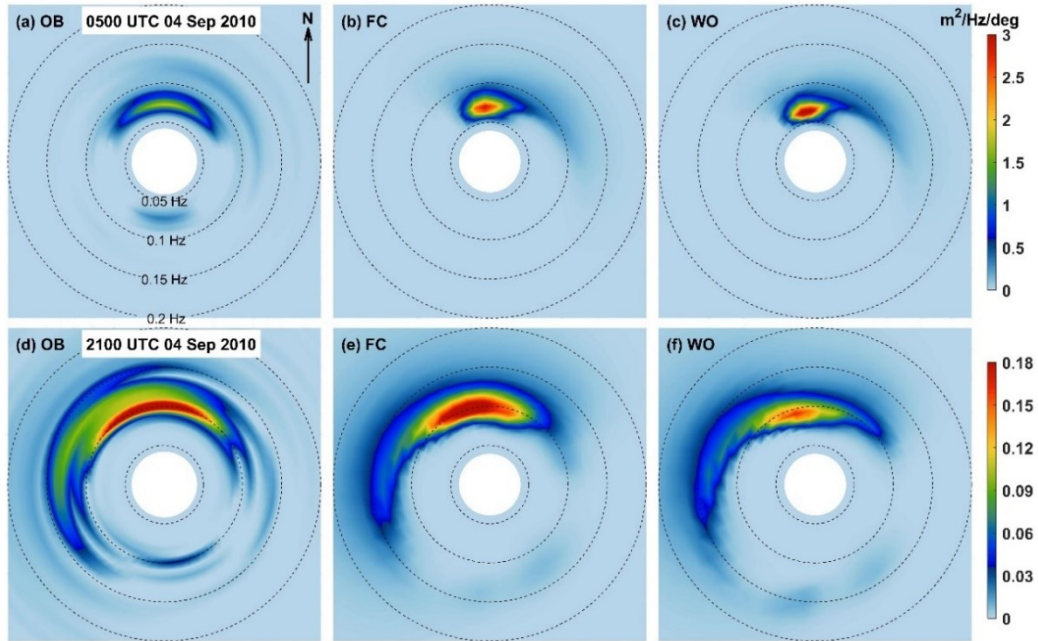
Figure 6.5: Observed (OB, a and d) and simulated 2D wave spectra in the fully-coupled (FC, b and e) and wave-only (WO, a and f) runs at buoy 44008 at 0500 UTC 4 September (a-c) and 2100 UTC 4 September (d-f) in 2010.

Ocean currents can affect the directional spread of wave energy. Figure 6.5 shows the observed and simulated directional wave spectra at buoy 44008 at 0500 UTC 4 September and 2100 UTC 04 September. The corresponding wave frequency spectra are shown in Figs. 6.4a and 6.4f. At 0500 UTC 4 September, the peak winds of Hurricane Earl at buoy 44008 generated strong wave energy that propagated northward with frequencies of 0.06-0.10 Hz (Fig. 6.5a). As the storm moved northward, the observed wave energy became weaker and broader spreading over the northwest and northeast with frequencies of 0.08-0.15 Hz (Fig. 6.5d). In comparison with the observed spectra, the simulated wave spectra are relatively narrow. Nevertheless, the FC run reproduces reasonably well the distributions of wave energy in both direction and frequency domains due to the inclusion of the effects of currents. In comparison with the FC run, wave energy in the WO run spreads in lower frequencies and in narrower directional bands. Moreover, the peak wave energy in the WO

run is significantly overestimated at 0500 UTC 4 September and underestimated at 2100 UTC 04 September, which are consistent with the comparisons of wave frequency spectra in Figs. 6.4a and 6.4f.

6.5.4 Maximum Significant Wave Height

The effects of currents on waves are further examined in terms of the swath map for the maximum SWHs (H_s^{max}) during Hurricanes Earl and Igor, as shown in Fig. 6.6. A swath map represents the distribution of the most energetic wave states during a storm event. During Hurricane Earl, the simulated swath in the FC run is biased to the RHS of the storm track with H_s^{max} of 10 m extending ~250 km (Fig. 6.6a). Hurricane Igor generates a wider swath due to the larger size of hurricane winds with H_s^{max} of 10 m extending ~450 km on the RHS of the storm track (Fig. 6.6d). In the WO run, the swaths are also biased to the RHS of the storm tracks but with larger magnitudes (Figs. 6.6b and 6.6e). By including the effects of currents, H_s^{max} can be reduced by up to ~10% close to the RHS of storm tracks (Figs. 6.6c and 6.6f). These findings are consistent with previous studies for other storms (e.g., *Wang and Oey*, 2008; *Wang and Sheng*, 2016; *Sun et al.*, 2018). During Hurricane Igor, the reduction of H_s^{max} however is not limited to the RHS of the storm track but also appears, to a smaller degree, on the LHS of the storm track (Fig. 6.6f).
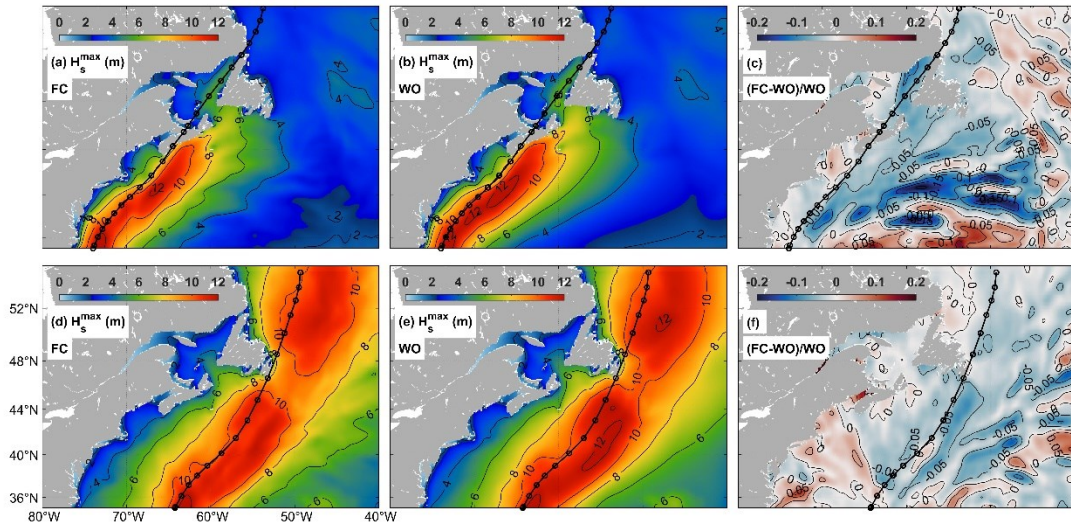

Figure 6.6: Swath maps of maximum SWHs in the (a and d) FC and (b and e) WO runs, and the (c and f) relative differences during Hurricanes (a-c) Earl and (d-f) Igor. The solid circle lines represent the hurricane tracks.

It should be noted that H_s^{max} can be reduced by more than ~20% over eddies associated with the Gulf Stream, although the absolute values of H_s^{max} are relatively small over these regions (Fig. 6.6c). Over these regions, H_s^{max} can also be increased by currents depending on the conditions of waves and eddies. The other important feature is the increase of H_s^{max} in the GoM, which can be more than ~15% in the BoF and ~5% near the mouth of the GoM during Hurricane Igor (Fig. 6.6f). The increase of H_s^{max} is due to not only the strong tidal currents but also the large surface elevations in the GoM. The WCIs can increase H_s^{max} and high surface elevations due to tides and surges modify the total water depth and allows the propagations of large waves.

6.6 Effects of waves on Circulations

In this section, results of different model runs are compared with observational data introduced in Section 6.3 to evaluate the model performance and to examine the effects of WCIs on circulation model results during Hurricanes Earl and Igor. The important physical mechanisms in the WCIs are investigated for the wave effects on the sea level, current, salinity, and temperature.

6.6.1 Sea Level

Figure 6.7 shows time series of the observed total sea level (η) and simulated values in the fully-coupled (FC) and circulation-only (CO) runs at six tide gauge stations in September 2010. The positions of the six tide gauge stations are shown in Fig. 6.1. There were large fluctuations of η due to tides at Saint John (Fig. 6.7a) and Yarmouth (Fig. 6.7b). In comparison with the model results in the CO run, the amplitudes of fluctuations in surface elevations at these two stations are reduced in the FC run. Surface elevations in the FC run thus have better agreement with the observed values with the RMSE of 0.40 m (0.24 m) at Saint John (Yarmouth) in comparison with 0.48 m (0.31 m) in the CO run. As Hurricane Earl moved northeastward, the storm created a weak surge of ~0.20 m at Halifax (Fig. 6.7c) and a peak surge of ~0.50 m at Port aux Basques (Fig. 6.7d). During Hurricane Igor, the storm surge was larger with a peak surge of ~1.04 m at Argentia (Fig. 6.7e). The FC run reasonably reproduces the storm surges during hurricanes with a peak surge of ~0.86 m at

Argentia during Hurricane Igor in comparison with that of ~0.72 m in the CO run. In other words, the peak storm surge can be increased by ~19.4% taking account of the wave effects.

The improved model performance due to the inclusion of the wave effects on surface elevations in the FC run is not limited to these tide gauge stations. Table 6.4 shows the error metrics for the total sea level in the FC and CO runs at 10 tide gauge stations. Both the CO and FC runs can reasonably reproduce surface elevations in September 2010 with the relative variance (γ^2) less than 0.15 for all stations. Overall, the FC run has smaller errors at all these stations with an average γ^2 of ~0.078 in comparison with ~0.085 in the CO run.

The above analyses demonstrate the important role of ocean surface waves in modulating surface elevations. Many previous studies also showed the effects of waves on the storm surge (e.g., *Kim et al.,* 2010; *Sheng et al.,* 2010; *Zou and Xie,* 2016; *Liu and Huang,* 2020). *Kim et al.* (2010) found that wave forcing can have a maximum contribution of ~40% to the simulated peak surge within a wide bay in Japan during Typhoon Anita (1970). *Sheng et al.* (2010) showed that wave effects account for ~20% of the peak surge at Duck Pier and 5%-10% inside Chesapeake Bay in the Mid-Atlantic region during Hurricane Isabel (2003). *Zou and Xie* (2016) showed that the wave setup accounts for 20% of the total surge in the GoM during an extratropical storm. *Liu and Huang* (2020) showed that the wave setup contributes between 6% and 35% to the total storm surge near the coast of Taiwan. However, the underlying mechanisms contributing to wave effects on surface elevations are not well quantified and require further investigations.

As mentioned in Section 2.2, effects of waves on circulations include the wave-dependent wind stress, wave-induced bottom stress, wave-enhanced vertical mixing and wave forces on currents. Figure 8 shows time series of differences between model runs at four stations, indicating the effects of waves on surface elevations from each physical mechanism. The differences between the FC and CO runs (FC-CO) shown in Fig. 6.8 (green lines) represent the overall effects of waves on surface elevations. At Saint John (Fig. 8a), surface waves reduce surface elevations by up to ~0.88 m (0.95 m) during Hurricane Earl (Igor). The reduction of surface elevations at Yarmouth (Fig. 6.8b) can be up to ~0.55 m (0.53 m)

during Hurricane Earl (Igor). Effects of waves on surface elevations are mostly attributed to the process of wave-induced bottom stress (blue lines). The enhanced bottom stress induced by waves acts as an extra energy sink and thus reduces the amplitudes of surface elevations. The additional wave forces (black lines) and wave-dependent wind stress (red lines) also show some effects but are of secondary importance. It should be noted that these two processes can have additional momentum fluxes acting on the surface and increase the amplitude of surface elevations. Therefore, the reduction of surface elevations due to the wave-induced bottom stress can be more than 100% and up to ~107% at Yarmouth during Hurricane Earl. The reduction, however, is compensated by the effects of wave forces and wave-dependent wind stress, which increase the surface elevations and account for ~4% and ~3% of the total wave effects, respectively (Fig. 6.8b). This is reasonable as the strong tidal amplitudes at these two stations are sensitive to the bottom stress.
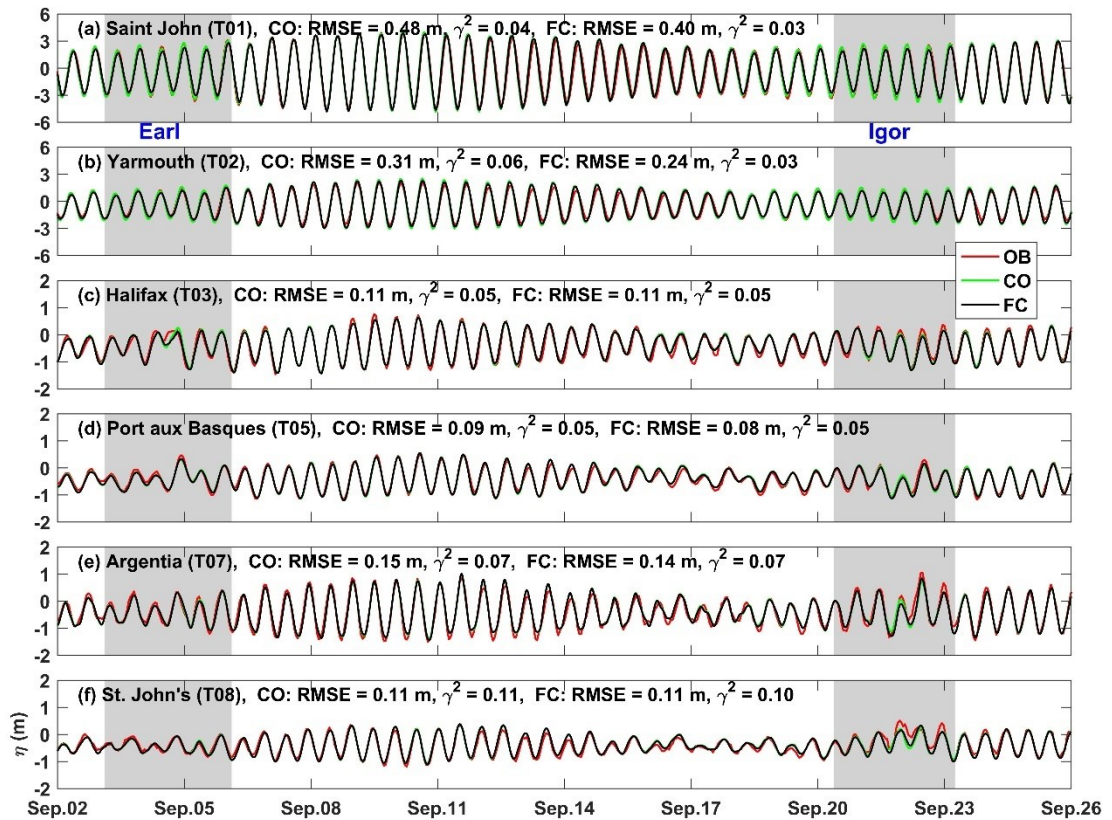

Figure 6.7: Time series of simulated sea level in the circulation-only (CO) and fully-coupled (FC) model runs against the observed values (OB) at six tide gauge stations in September 2010. The name of each station, the root mean square error (RMSE), and relative variance (γ^2) for the CO and FC model runs are shown in each panel.

178

Table 6.4: Summary of three error metrics for the sea level predicted in the fully-coupled (FC) and circulation-only (CO) model runs in September 2010. The error metrics include the root mean square error (RMSE), correlation coefficients (R) and relative variance (γ^2).

| Station	RMSE (cm)		R (%)		γ^2	
	FC	CO	FC	CO	FC	CO
Saint John (T01)	39.7	47.6	98.6	97.9	0.029	0.042
Yarmouth (T02)	23.7	31.0	98.6	98.5	0.035	0.059
Halifax (T03)	11.4	11.4	97.3	97.3	0.053	0.054
North Sydney (T04)	10.2	10.7	95.0	94.5	0.104	0.113
Port aux Basques (T05)	8.3	8.6	97.5	97.3	0.050	0.053
St. Lawrence (T06)	13.6	13.7	96.7	96.6	0.067	0.068
Argentia (T07)	14.4	14.5	96.8	96.8	0.065	0.066
St. John's (T08)	10.6	11.0	94.8	94.3	0.102	0.110
Bonavista (T09)	11.2	11.6	93.2	92.6	0.132	0.142
Duck Pier (10)	14.8	15.0	92.9	92.8	0.139	0.140
Average	15.8	17.5	96.1	95.9	0.078	0.085
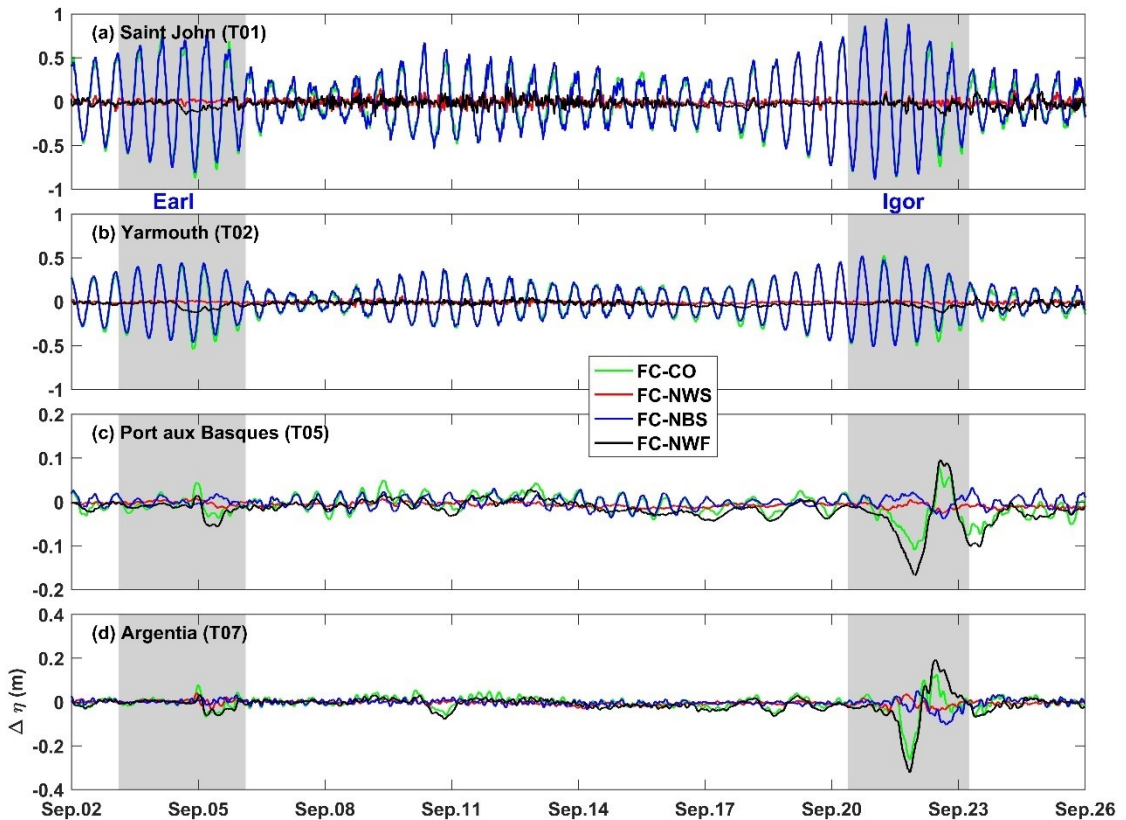
Figure 6.8: Time series of the differences between the fully-coupled (FC) run and the circulation-only (CO), no wave-dependent wind stress (NWS), no wave-enhanced bottom stress (NBS), and no wave force runs (NWF) at four tide gauge stations in September 2010.

The additional wave forces (black lines) and wave-dependent wind stress (red lines) become the dominant processes contributing to the overall effects of waves on surface elevations at Port aux Basques (Fig. 6.8c) and Argentia (Fig. 6.8d) during hurricanes, as tidal amplitudes are low at these two stations. At Port aux Basques (Fig. 6.8c), the overall effects of waves increase the storm surge by up to ~0.05 m (0.08 m) during Hurricane Earl (Igor). The increase of surface elevations at Argentia (Fig. 6.8d) can be up to ~0.08 m (0.14 m) during Hurricane Earl (Igor). The additional wave forces have a maximum contribution of ~152% for the peak surge at Argentia during Hurricane Igor. However, the effect of wave forces is compensated by the wave-induced bottom stress, which reduces the peak surge by ~41%. The wave-dependent wind stress plays a minor role at this time during Hurricane Igor but can be relatively important during Hurricane Earl. At Argentia (Fig. 6.8d) during Hurricane Earl, the wave-dependent wind stress makes the largest contribution (~53%) to the increase of the peak surge, followed by the wave forces (~42%).

It should be noted that remarkable wave-induced set-down occurs at these two stations before the approach of the peak storm surge during Hurricane Igor. In summary, effects of waves on the storm surge are mostly attributed to the wave-induced setup and set-down due mainly to additional wave forces. The wave-induced bottom stress dominates the effects of waves on surface elevations in the regions with strong tidal amplitudes but also in other coastal regions during relatively calm weather conditions. Among these three processes, the effect of wave-dependent wind stress is less apparent. The wave-dependent wind stress is estimated using different dependences of nondimensional roughness on the wave age under different sea states (*Lin and Sheng,* 2020). Otherwise, the formula suggested by *Charnock* (1955) is used, which depends on the wind speed. For both cases, the drag coefficients are limited within 2.4×10^{-3} at high winds (Section 6.2.2). Therefore, the wind stresses estimated using *Lin and Sheng* (2020) and *Charnock* (1955) are similar at high winds. The effects of wave-enhanced vertical mixing on surface elevations are relatively weak in all cases and thus are not shown in Fig. 6.8.

To quantify the effects of waves on tidal elevations, harmonic analysis including 11 main tidal constituents is performed at Saint John and Yarmouth using the UTide program (*Codiga,* 2011). The amplitudes and phases of the main semidiurnal constituent (M2) of

the observed and simulated sea levels in September 2010 are shown in Table 6.5. At Saint John and Yarmouth, the M2 tidal amplitudes are overestimated by up to ~18.1% in the CO run. By comparison, the M2 tidal amplitudes in the FC run have lower values and thus better agreement with the observed tidal amplitudes. The effects of waves on the sea level are not limited to the reduction of the tidal amplitude but also include a change in the tidal phase. Surface waves reduce the M2 tidal amplitude by up to ~8.6% and cause a phase lag of up to ~11.3 minutes at Saint John and Yarmouth. The changes of the amplitude and phase indicate the tidal energy dissipation and tidal deformation induced by waves mainly due to the enhanced bottom friction. Table 6.5 also shows the tidal amplitudes and phases for the simulated sea levels in the NBS run, which are nearly identical to those in the CO run. This further demonstrates that the wave-induced bottom stress is the most relevant process with regard to the effects of waves on surface elevations near the GoM.

Table 6.5: Observed and simulated tidal amplitudes and phases in the fully-coupled (FC) , circulation-only (CO) and no wave-induced bottom stress (NBS) runs for the M2 tide in September 2010. The wave-induced relative amplitude difference (RAD) is defined as the tidal amplitude difference between the FC and CO runs normalized by the value in the CO run. The wave-induced phase lag between the FC and CO runs is shown in minutes.

Station	Amplitude (m)				Phase (°)				RAD (%)	Phase lag (min)
	OB	FC	CO	NBS	OB	FC	CO	NBS		
Saint John (T01)	3.03	2.96	3.16	3.15	98.9	94.2	88.7	88.5	-6.1	11.3
Yarmouth (T02)	1.66	1.79	1.96	1.96	63.8	61.8	56.8	56.7	-8.6	10.4

6.6.2 Sea Surface Current

We now examine the effects of waves on surface currents. Figure 6.9 shows distributions of surface currents in the FC run and the differences between model runs at 1800 UTC 21 September during Hurricane Igor. In the FC run, the large-size hurricane generates strong surface currents in its rear quadrants with current speeds larger than 1.2 m/s flowing southeastward from the coastal regions of southern Newfoundland towards deep waters. In the front left quadrant, surface currents are southward, superposed on the inshore branch of Labrador Current with a magnitude of ~0.7 m/s. Surface currents are northeastward with a speed of up to ~1.0 m/s in the front right quadrant (Fig. 6.9a). The effects of waves on surface currents are significant, with modulation of current directions and reduction of

current speeds. Hurricane-driven surface currents are modulated by waves toward the anticyclone direction (Fig. 6.9b). Surface current speeds are reduced due to waves by up to ~1.0 m/s in the rear quadrants of the storm and up to ~0.5 m/s in the front quadrants. The significant reduction of current speeds is indicative of the effects of waves on the Labrador Current, which can be more than 60% during hurricanes. Surface waves can also affect the other large-scale circulation: the Gulf Stream (Fig. 6.9b). The main flow of the Gulf Stream separating from Cape Hatteras is strengthened and the locations of eddies are shifted due to the effects of waves. The strong tidal currents near the GoM are also modulated by surface waves. In the FC run, the maximum ebb tidal current at this time can be up to ~2.0 m/s in the inner GoM near the BoF and ~1.2 m/s at the mouth of the GoM near Georges Bank (GeB). Over these regions, tidal currents are reduced by including the wave effects, which corresponds to the reduced tidal amplitudes shown in Fig. 6.8. The maximum reduction of tidal currents due to waves occurs over GeB, which can be up to ~0.57 m/s and ~40.1%.

To identify the contributions to the effects of waves on surface currents from each process, the differences between the FC run and the NVM, NWF, NBS and NWS runs are shown in Figs. 6.9c-6.9f, respectively. The most important process for the reduction of surface currents under hurricanes is the wave-enhanced vertical mixing. The reduction of surface currents due to the wave-enhanced vertical mixing can even exceed the overall wave effects with a reduction of up to ~1.24 m/s over the coastal regions of southern Newfoundland (Fig. 6.9c). Surface waves mix the surface water with colder and saltier water in the subsurface and thus reduce the buoyancy forcing for currents. This indicates a significant role for the wave-induced baroclinic effects on circulations. However, the effect of wave-enhanced vertical mixing is compensated by the effect of wave forces. Wave forces on currents considerably strengthen surface currents, particularly over the Grand Banks (GrB) with an increase of up to ~0.70 m/s. Wave forces on currents are the main contribution for the strengthening of the Gulf Stream and weakening of the southward flow along the shelf break (Fig. 6.9d). For the reduction of tidal currents near the GoM, wave-induced bottom stress is the most important process (Fig. 6.9e), which is consistent with the analyses of the effects of waves on surface elevations (Section 6.6.1). The wave-dependent wind stress plays a role on changing surface currents but is of the least importance (Fig. 6.9f), as the

differences between the estimated drag coefficients (or wind stresses) in the FC and NWS runs are not significant.
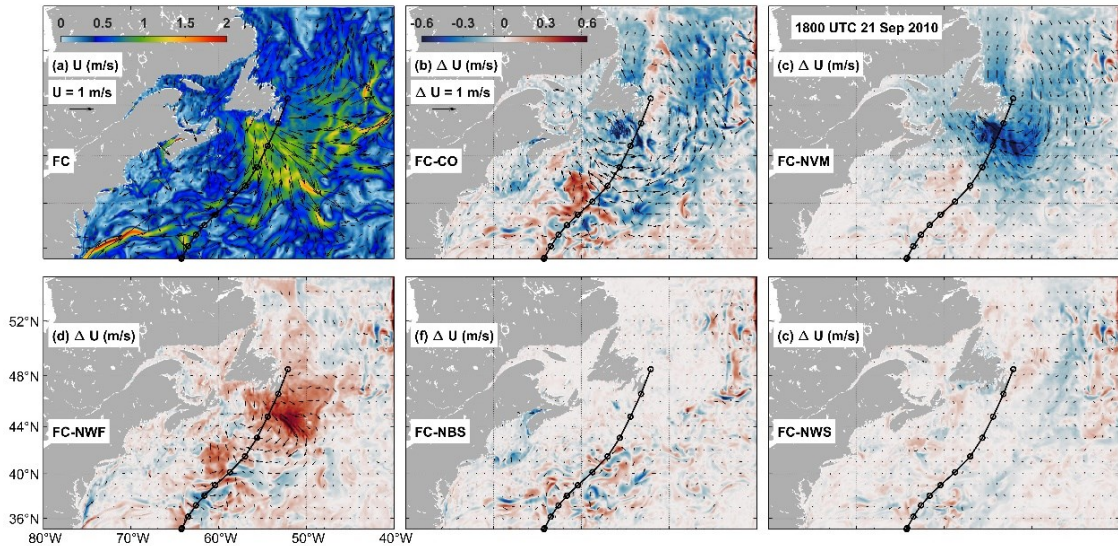

Figure 6.9: Distributions of surface currents in the (a) FC run and the differences between the FC run and (b) the CO, (c) NVM, (d) NWF, (e) NBS, and (f) NWS runs at 1800 UTC 21 September 2010 during Hurricane Igor. The arrows in (a) represent the surface current vectors in the FC run. The arrows in (b-f) represent the corresponding differences in the surface current vectors.

6.6.3   Sea Surface Salinity

Figure 6.10 shows the observed weekly-average sea surface salinity (SSS) from the ESA and the simulated values during Hurricanes Earl and Igor. During Hurricanes Earl and Igor, the FC run reproduces well several important features of SSS observed in the satellite measurements, including (i) the low-salinity plume from the St. Lawrence River Estuary (SLRE) that spreads over the western GSL and affects the SSS over the ScS after existing the GSL through the Cabot Strait (CS), (ii) the relatively fresh water over the Newfoundland and Labrador Shelves (NLS) transported by the Labrador Current, (iii) the relatively fresh water along the shelf break between the Gulf Stream and the east coast of the US, and (iv) the front of relatively salty water associated with the Gulf Stream near the shelf break.

To examine the effects waves on the SSS, the differences between the simulated weekly-average SST in the FC and CO runs during Hurricanes Earl and Igor are shown in Figs.

6.10c and 6.10f, respectively. During Hurricanes Earl and Igor, the most significant change of SSS induced by surface waves is the increase of SSS in GSL extending from the SLRE to the CS and ScS. The increase of SSS near the SLRE can be more than ~5.0 when the effects of waves are included. Surface waves also slightly increase the SSS over the NLS and the GoM. The SSS over shelf regions near the east coast of the US can be increased due to the reduced strength of the currents carrying the relatively fresh shelf water (Fig. 6.9). Over these regions, the SSS can also be reduced as the different front structures of saltier water associated with the Gulf Stream. Large differences appear in deep waters, which is mostly attributed to the different locations of eddies in the two model runs.
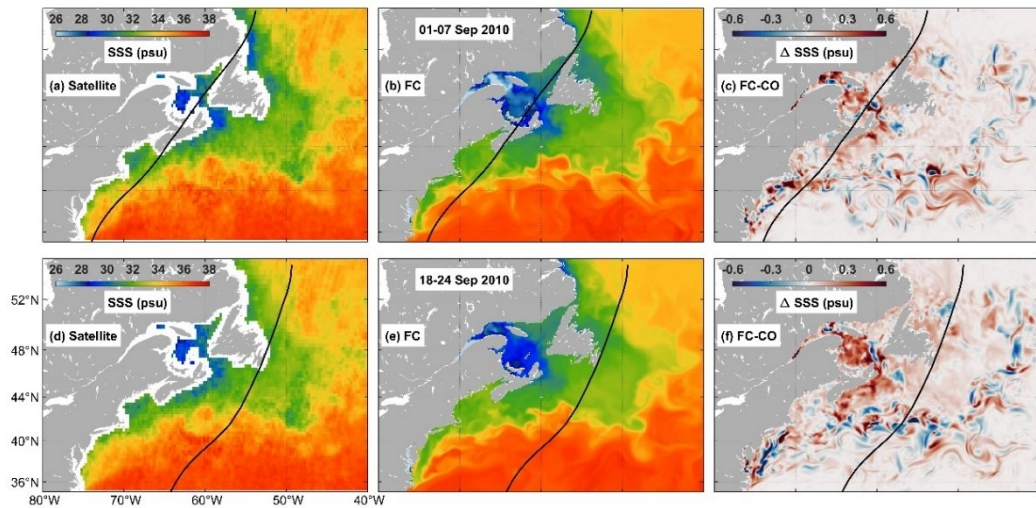

Figure 6.10: Weekly-average sea surface salinity from the (a and d) satellite measurements, (b and e) the FC run, and (c and f) the corresponding differences between the FC and CO runs during Hurricanes (a-c) Earl and (d-f) Igor in September 2010. The black lines show the hurricane tracks.

The physical processes contributing to the effects of waves on the SSS are then examined in Fig. 6.11. Figure 6.11 shows distributions of the SSS in the FC run and the differences between the FC run and other runs (CO, NVM, NWF, NBS and NWS) at 1800 UTC 21 September 2010 during Hurricane Igor. At this time, surface waves significantly increased the SSS over the NLS and western GSL by up to ~3.8 (Fig. 6.11b). The former is mostly attributed to the wave-enhanced vertical mixing (Fig. 6.11c) and the latter is mostly due to the additional wave forces (Fig. 6.11d). The additional wave forces also increase the SSS over the ScS and near the east coast of the US. The wave-dependent wind stress contributes

to the increase of SSS over the NLS, western GSL, and ScS, but is of the third order (Fig. 6.11f). The wave-indued bottom stress affects the locations of eddies and thus the SSS in deep waters. Otherwise, its effect on the SSS is surprisingly limited over shelf regions except for the regions with river input over very shallow waters, such as the inner SLRE (Fig. 6.11e).
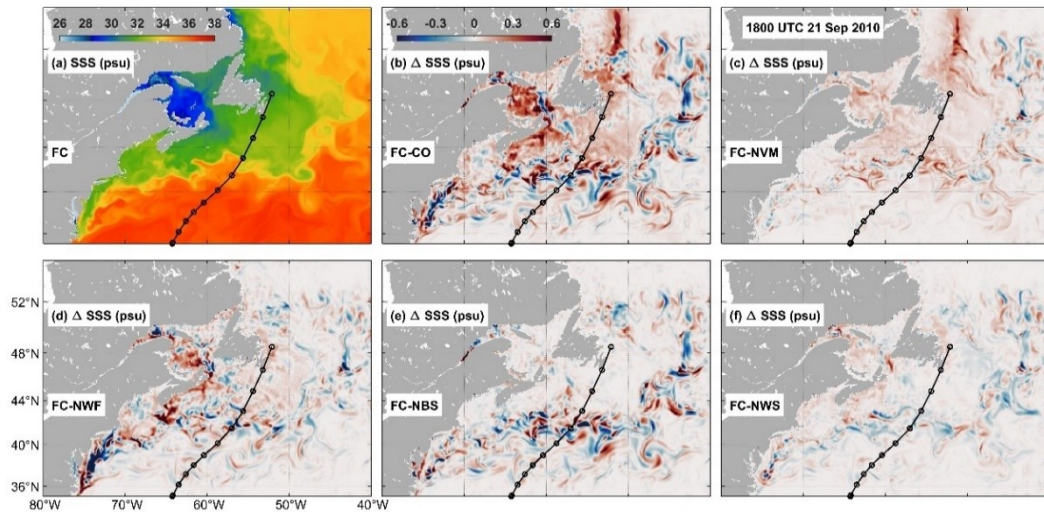

Figure 6.11: Distributions of sea surface salinity in the (a) FC run and the differences between the FC run and (b) the CO, (c) NVM, (d) NWF, (e) NBS, (f) NWS runs at 1800 UTC 21 September 2010 during Hurricane Igor.

6.6.4   Sea Surface Temperature

We now examine the effects of waves on sea surface temperature (SST). Figure 6.12 shows time series of the observed SST and simulated SST in the FC and CO runs at six buoy stations in September 2010. The positions of these six buoy stations are shown in Fig. 6.1. The observed SST at buoy 44007 fluctuated around ~18.0°C under the effect of strong tidal currents in the GoM before Hurricane Earl and then decreased from ~18.0°C to ~14.0°C with the passage of the storm (Fig. 6.12a). Similar surface cooling during Earl was also found at buoys 44150 and 44255 (Figs. 6.12b-6.12c). In particular, the observed SST at buoy 44150 dropped from ~20.0°C to ~14.0°C over ~10 hours during Earl as it was close to the storm track. Hurricane Igor caused strong surface cooling at buoys 44139 and 44251 (Figs. 6.12d-6.12e). The observed SST at buoy 44251 near Newfoundland underwent a sharp drop of ~6.5°C, from ~14.5°C to ~8.0°C, during Igor. At buoy 44009, the observed

SST was higher than those at the above-mentioned five buoy stations with the SST above 22.0°C due to its location at a relatively low latitude and the effect of the Gulf Stream (Fig. 6.12f). The model results in the CO run generally overestimate the SST at these stations in September 2010. In particular, the hurricane-induced surface cooling is not intense enough in the CO run with some overestimations of SST after hurricanes. By comparison, the FC run generally has lower values of SST and better reproduces the observed variations of SST for both the tidal modulation of SST and cooling induced by hurricanes at different buoy stations.
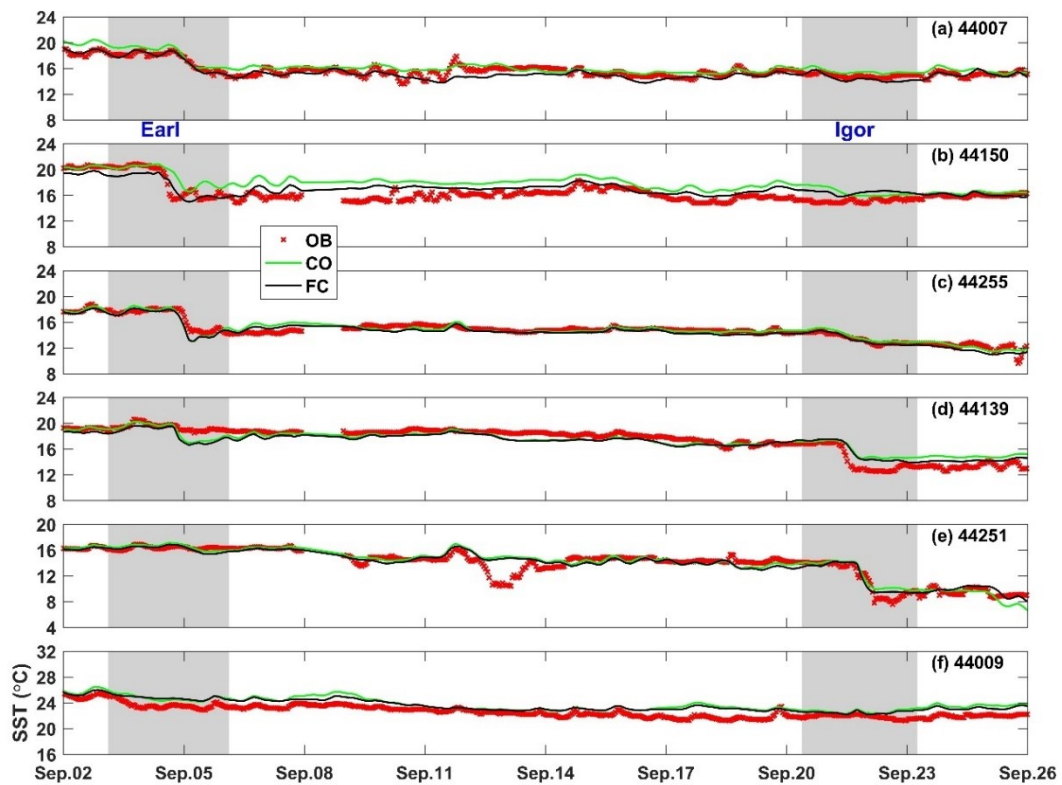
Figure 6.12: Time series of simulated sea surface temperature in the circulation-only (CO) and fully-coupled (FC) runs against the observed values (OB) at six buoy stations in September 2010.

The performances of FC and CO runs at the other buoy stations are similar with those discussed above. To quantify their performances in reproducing the observed SST, the error metrics for the SST in the FC and CO runs at 14 available buoy stations are presented in Table 6.6. During the study period, the CO run generally overestimates the SST at these stations with positive RB values except for buoys 44139 and 44258. The positive RB values

in the CO run can be up to ~9.0% with a RMSE of ~1.8°C at buoy 44150. By comparison, the FC run has lower values of SST and thus better agreement with the observed values at most buoy stations. Overall, the FC run has an average SI of ~5.3% and an average γ^2 of ~0.29 compared to ~6.3% and ~0.36 in the CO run. Overall, ocean surface waves generally strengthen the hurricane-induced surface colling and cause lower SST.

Table 6.6: Summary of five error metrics for the sea surface temperature predicted in the fully-coupled (FC) and circulation-only (CO) runs at 14 buoy stations in September 2010.

Buoy	Depth (m)	SI (%)		RB (%)		RMSE (°C)		R (%)		γ^2	
		FC	CO	FC	CO	FC	CO	FC	CO	FC	CO
44007	27	4.1	5.1	-2.2	3.7	0.6	0.8	90.3	90.9	0.22	0.22
44008	75	7.2	8.2	4.0	4.6	1.3	1.5	71.1	64.6	0.51	0.62
44009	43	4.6	5.4	4.2	4.9	1.0	1.2	89.9	86.3	0.20	0.28
44013	64	2.9	3.7	0.7	1.9	0.5	0.7	93.7	92.8	0.12	0.16
44014	45	4.8	4.6	4.0	3.8	1.1	1.1	84.2	85.0	0.29	0.28
44017	48	3.5	3.7	2.5	2.7	0.7	0.8	91.9	91.2	0.19	0.20
44025	36	2.2	2.6	1.9	2.2	0.5	0.6	96.6	96.1	0.08	0.11
44027	185	9.3	11.8	6.8	8.6	1.2	1.6	66.0	61.9	0.87	1.39
44137	4500	7.0	7.3	4.8	4.9	1.4	1.4	77.0	73.2	0.41	0.46
44139	1100	5.4	5.6	-1.7	-0.1	0.9	1.0	94.8	93.6	0.17	0.20
44150	1300	6.8	10.8	3.8	9.0	1.1	1.8	82.8	78.8	0.34	0.38
44251	71	6.8	7.3	0.5	1.6	0.9	1.0	92.5	92.0	0.15	0.16
44255	179	3.8	3.7	-1.9	0.2	0.6	0.5	95.5	94.0	0.10	0.12
44258	60	8.3	8.9	-3.9	-4.3	1.3	1.2	76.1	75.8	0.43	0.42
Average		5.5	6.3	1.7	3.1	1.0	1.1	85.9	84.0	0.29	0.36

The SST are further examined by comparing the simulated daily-average SST with the satellite observations from the RSS during Hurricanes Earl and Igor (Fig. 6.13). On 5 September, the FC run reproduces well several important features observed in the satellite measurements, including: (i) the surface cooling induced by Earl, particularly near Halifax where Earl made landfall, (ii) the separation of the Gulf Stream from Cape Hatteras and meanders of the Gulf Stream, (iii) the cold Labrador Current from the north boundary of the model extending southward through the Flemish Pass, and (iv) the cold surface water in the inner GoM due to the strong tidal mixing (Figs. 6.13a-6.13b). The features of surface cooling, two large-scale circulations and tidal mixing also appeared on 22 September (Figs. 6.13d-6.13e). Hurricane Igor, traveling over the NLS, caused strong surface cooling over

the GrB and NLS. The strong wind intensified the southward Labrador Current with cold water of ~5°C spreading over the NLS and flowing through the Flemish Pass. The effect of this cold water extended further south with the relatively cold shelf water penetrating between the warm Gulf Stream water and the east coast of the US. The meander of the Gulf Stream and eddies, however, are not well represented in the FC run, as the coupled model is purely prognostic without any data assimilation. The simulated values of SST in the FC run over the regions of the Gulf Stream are slightly higher than the observed values, which is also shown in Fig. 6.12f. Nevertheless, the FC run reproduces well the above-mentioned important features of the SST variations.
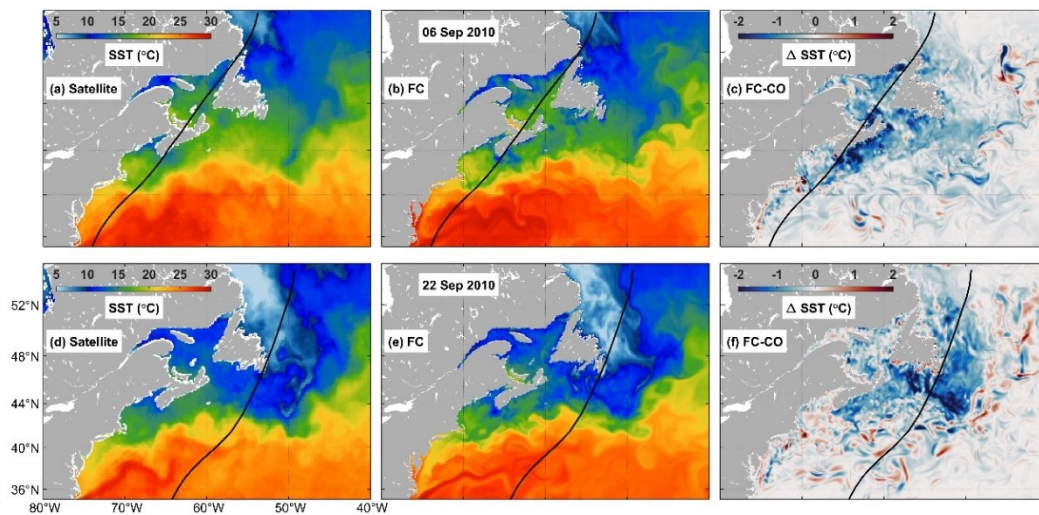

Figure 6.13: Daily-average sea surface temperature from the (a and d) satellite measurements, (b and e) the FC run, and (c and f) the corresponding differences between the FC and CO runs during Hurricanes (a-c) Earl and (d-f) Igor in September 2010. The black lines show the hurricane tracks.

To examine the effects of waves on the SST, differences between the simulated daily-average SST in the FC and CO runs during Hurricanes Earl and Igor are shown in Figs. 6.13c and 6.13f, respectively. During Hurricane Earl, surface waves reduce the SST along the hurricane track with a drop of more than ~3.0°C near the southern ScS, Prince Edward Island (PEI) and the Strait of Belle Isle (SBI). The reductions of SST induced by waves generally cover the entail GSL and shelf regions. During Hurricane Igor, reductions in SST of up to ~4.2°C are found over the south coast of Newfoundland with the. Overall, ocean surface waves largely strengthen the surface cooling induced by hurricanes near the storm

tracks. The effects of waves on SST can spread widely over the shelf regions where intense wave energy dissipation occurs.

The physical processes contributing to the effects of waves on the SST are then examined in Fig. 6.14. Figure 6.14 shows distributions of the SST in the FC run and differences between the FC run and other runs (CO, NVM, NWF, NBS, and NWS) at 1800 UTC 21 September 2010. At this time, Hurricane Igor was continuing its northward move toward the Labrador Sea after its landfall in Newfoundland. Ocean surface waves greatly reduce the SST over the GrB and the nearby coastal regions of Newfoundland with a reduction in SST of up to ~4.3°C. This is similar with differences in the daily-average SST (Fig. 6.13f) but with more intense reductions of SST over a wider region induced by waves.

The wave-induced reduction of SST is mostly attributed to the wave-enhanced vertical mixing (Fig. 6.14c) and the additional wave forces on currents (Fig. 6.14d), followed by the wave-induced bottom stress (Fig. 6.14e). The effect of wave-enhanced vertical mixing is mostly concentrated on the NLS and extend toward the ScS. This process reduces the strength of southward currents carrying cold water but also mixes the surface water with subsurface cold water, leading to lower SST (Fig. 6.14c). The effect of additional wave forces reduces the SST over the GrB and ScS. This is due to the fact that additional wave forces strengthen the surface currents over the GrB and thus increase the southward transport of the cold water from the Labrador Current (Fig. 6.9d). The cold water then affects the nearby regions extending from the GrB to the ScS. On the other hand, additional wave forces increase the SST over the shelf break near the east coast of the US and the mean path of the Gulf Stream. As shown in Fig. 6.9d, additional wave forces also reduce the strength of the southward flow of cold water along the shelf break and enhance the mean flow of the Gulf Stream, which result in the increase of SST over these regions (Fig. 6.14d). The wave-induced bottom stress reduces the tidal mixing near the GoM by weakening tidal amplitudes and currents (Fig. 6.14e). The wave-dependent wind stress compensates the reductions of SST over the GrB due to the wave-enhanced vertical mixing and additional wave forces, as this process weakens surface currents over this region. However, the effect of this process on the SST is of the last order (Fig. 6.14f).

As mentioned above, hurricanes generate significant temperature changes in the upper ocean in the vicinity of storm tracks. The strong surface cooling during Hurricane Earl is analyzed as an example. Figure 6.15 presents differences in the SST between 5 September and 3 September in 2010 during Hurricane Earl based on the RSS satellite measurements and the simulated SST in the FC and CO runs. Satellite measurements showed systematic SST cooling on the RHS of the storm track over the regions ranging from the deep water to the ScS and GSL. In particular, strong surface cooling occurred near the ScS where the storm made landfall, with a reduction in SST of up to ~6.5°C.

The FC run reasonably reproduces the right-biased SST cooling pattern relative to the hurricane track with a maximum reduction in SST of ~6.8°C. By comparison, the surface cooling in the CO run is weaker, with a maximum reduction in SST of ~5.8°C. The discrepancy between satellite observations and model results over areas south of ~42°N can be attributed to the influence of the warm Gulf Stream. As shown in Fig. 6.13, the movement of Gulf Stream meanders is not precisely simulated in the model, which could be due to inadequate model resolutions and imperfect model physics.
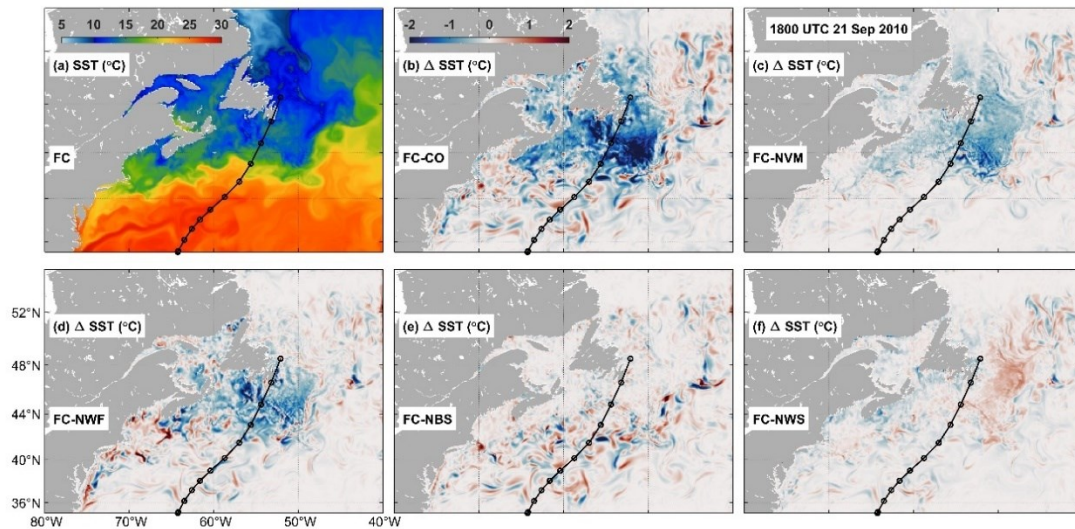

Figure 6.14: Distributions of sea surface temperature in the (a) FC run and the differences between the FC run and (b) the CO, (c) NVM, (d) NWF, (e) NBS, and (f) NWS runs at 1800 UTC 21 September 2010 during Hurricane Igor.
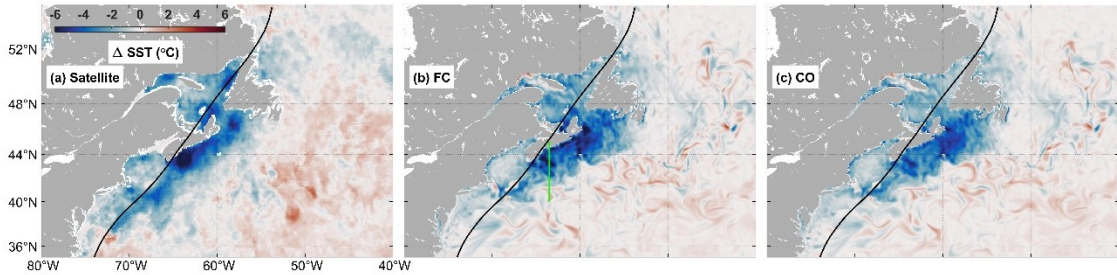
Figure 6.15: Comparison of SST cooling from the (a) RSS satellite data and model results in the (b) FC and (c) CO runs during Hurricane Earl. The black line in each panel represents the storm track. The green line in panel (b) marks a cross-shore transect for which model results are shown in Fig. 6.16.

6.6.5   Vertical Structure of Temperature

To show the vertical structure of temperature, a cross-shore transect along 63.5ºW over the ScS is selected (green line in Fig. 6.15), where the most intense temperature changes occur. Figure 6.16 shows the vertical structure of the daily-average temperature in the cross-shore transect before and after Hurricane Earl and the corresponding differences based on model results in the FC run. The ocean upper layer is highly stratified with a mixed layer depth (MLD) of ~15 m before the hurricane. Hurricane Earl reduces the vertical stratification, resulting in a deeper MLD of ~25 m after its passage. In the top ~25 m of the water column, the water temperature is decreased significantly from ~20°Cto ~15°C. The effect of the hurricane on the temperature structure shows some differences along the transect. Near the shelf break (43ºN), the water temperature is decreased in the top ~15 m and increased below it down to a depth of ~100 m. Near 44ºN, the largest temperature reduction is concentrated in the top ~25 m of the water column but the decrease in temperature can penetrate to a depth of ~100 m. In relatively shallow waters near the coast, the temperature reduction appears mostly in the top ~40 m.

Figure 6.17 shows temperature differences in the cross-section between different model runs after Hurricane Earl. The analyses in Section 6.6.4 demonstrate the important role of waves in the temperature changes induced by hurricanes. The temperature changes are not limited to the ocean surface but also appear in the subsurface. The differences between the FC and CO runs (Fig. 6.17a) show that waves can reduce the temperature at depths of more than ~100 m, with significant temperature changes occurring in the top ~25 m.
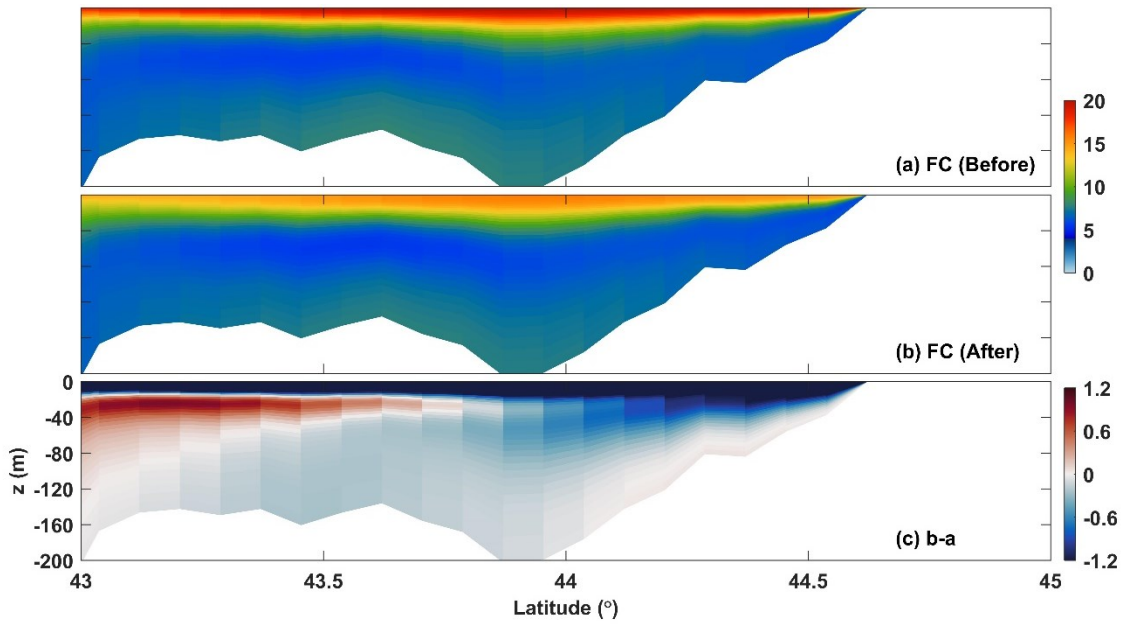
Figure 6.16: Distributions of the daily-average temperature in the cross-shore transect shown in Fig. 6.15 (a) before and (b) after Hurricane Earl and the (c) corresponding differences based on results in the FC run.
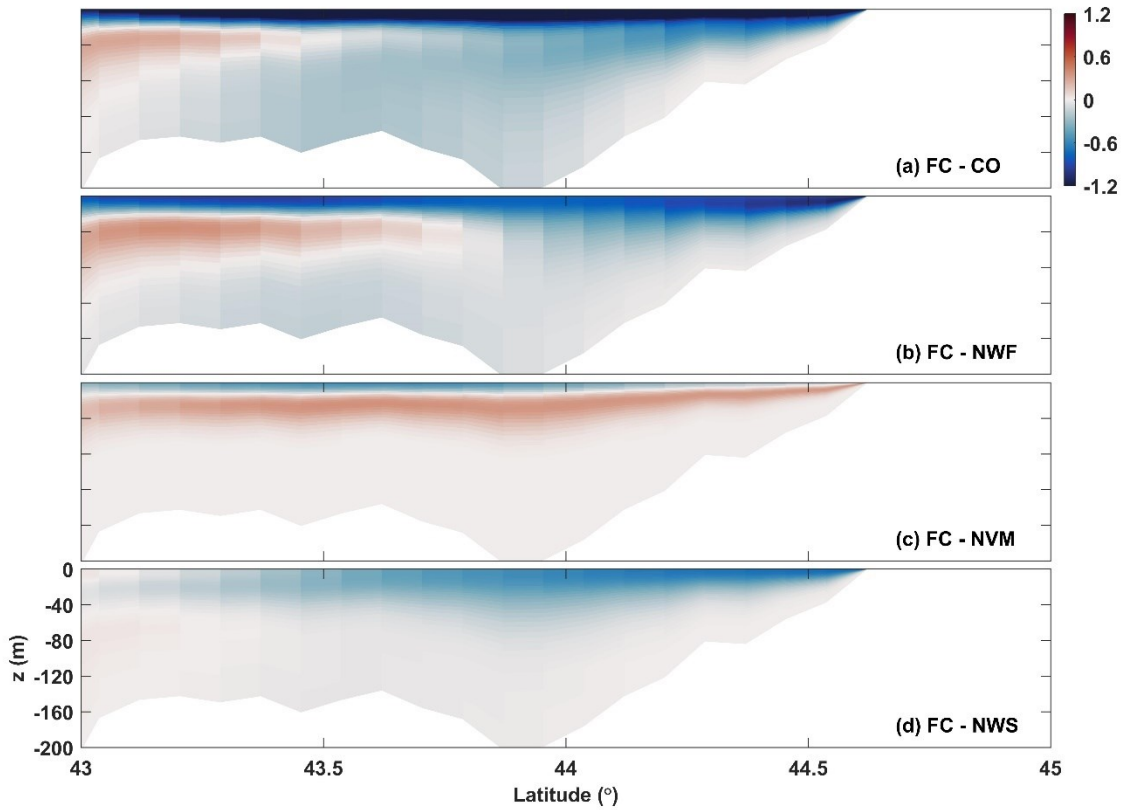

Figure 6.17: Temperature differences in the cross-section shown in Fig. 6.15 between the FC run and the (a) CO, (b) NVM, (c) NWF, and (d) NWS runs after Hurricane Earl.

The effect of waves on the vertical structure of temperature is mostly attributed to additional wave forces, which drive Stokes drift and extra currents that enhance the vertical mixing (Fig. 6.17b). The temperature reduction due to additional wave forces can be more than ~1.2°C near the coast. By comparison, the effect of using the wave-enhanced vertical mixing in the GLS scheme is limited to the top ~15 m with a decrease in temperature of ~0.3°C and an increase in temperature of ~0.3°C below (Fig. 6.17c). In addition, the wave-dependent wind stress also plays a role in the temperature changes with a decrease in temperature of ~0.5°C in the top ~40 m. This is due to the fact that the modulation of sea surface roughness can affect the heat fluxes and currents.

6.7 Summary and Conclusions

In this study, a fully-coupled 3D wave-circulation modelling system known as COAWST was applied and validated for the NWA to investigate the WCIs during Hurricanes Earl and Igor in September 2010. The circulation component ROMS was initialized with a realistic ocean state and driven by external forces including atmospheric fields, river runoff, tides, and lateral open boundary conditions. The wave component SWAN was driven by winds and 2D wave spectra at lateral open boundaries from global wave hindcasts provided by IFREMER. SWAN also received the current velocity components and sea surface elevations from ROMS. SWAN, in turn, provided necessary wave parameters to ROMS for the calculations of the effects of waves on circulations. To improve the representation of hurricane winds, the analysis data for Hurricanes Earl and Igor from the HWIND data set were blended into the large-scale winds from the ERA5 data set and the blended winds were used in the coupled model.

The observational data used in this study included buoy observations of SST, SWHs, PWPs, 1D and 2D wave spectra, tide gauge observations of sea levels, and satellite measurements of SST and SSS. A series of numerical experiments was performed to identify the effects of various processes in WCIs, including the fully-coupled run, wave-only run , circulation-only run, and four other model runs for different wave effects on circulations. The fully-coupled model was shown to capture important physics of WCIs under very different scales and environmental conditions with good performances in representing the SWHs, PWPs,

wave spectra, sea levels, SST and SSS. Our results demonstrated the important roles of WCIs in affecting physical environments over the NWA during Hurricanes Earl and Igor. The main findings can be summarized as follows:

(i) In the presence of ocean currents, the maximum SWHs generated by hurricanes are reduced by more than 10% along the storm track and more than 20% over the eddies associated with the Gulf Stream. In addition to the effects of the hurricane-driven strong currents, ocean surface waves experience an oscillating pattern after the peak winds due to the near-inertial currents in the wake of hurricanes and strong tidal modulations near the GoM. Comparisons of wave spectra show that wave energy can be redistributed in different frequencies and broader directional bands by currents.

(ii) The mechanisms for the effects of waves on the sea level variations can be different over different regions. Waves reduce the semidiurnal tidal amplitudes in the GoM by up to 8.6% and cause a phase lag of up to 11.3 minutes due mainly to the wave-induced bottom stress. The effects of waves on the storm surges are mostly attributed to the wave-induced setup and set-down due to wave forces on currents but compensated by the effect of wave-induced bottom stress. Overall, the peak storm surge can be increased by ~19.4% taking account of the wave effects.

(iii) Intense WCIs during hurricanes can affect hurricane-driven currents, tidal currents and the large-scale circulations. During Hurricane Igor, hurricane-driven surface currents are modulated toward the anticyclone direction by waves. The strength of the Labrador Current at the surface is reduced by waves with a decrease in current speeds of more than ~60.0% in the NLS. The decrease in current speeds is mostly attributed to the wave-induced baroclinic effects due to the wave-enhanced vertical mixing, but is compensated by the effect of additional wave forces. By including the wave effects, tidal currents are reduced by up to ~40.1% over the GeB during the maximum ebb tides due mainly to the wave-induced bottom stress.

(iv) During Hurricane Igor, surface waves significantly increase the SSS over the SLRE and ScS by up to ~3.8 and change the SSS near the east coast of the US due mostly to the additional wave forces, followed by the wave-enhanced vertical mixing. The wave-

dependent wind stress also contributes to the increase of SSS over these regions, but to a smaller degree. The SSS over the NLS is also increased by waves, which is mostly attributed to the wave-enhanced vertical mixing.

(v) Hurricanes Earl and Igor generated a highly right-biased SST cooling relative to the storm tracks with significant reductions in SST of more than ~6.5°C, as seen in both buoy and satellite observations. Ocean surface waves strongly strengthen the surface cooling induced by hurricanes near the hurricane track, with a reduction in SST of up to ~4.3°C over the GrB during Hurricane Igor. The effects of waves on SST can spread widely over the shelf regions where intense wave energy dissipation occurs. The wave-induced reduction of SST is mostly attributed to the wave-enhanced vertical mixing and the additional wave forces on currents, followed by the wave-induced bottom stress.

(vi) Hurricanes can change the vertical structure of water temperature. Hurricane Earl reduces the vertical stratification of the waver column and generates a deeper MLD after its passage. The effects of waves on the water temperature is not limited to the surface. During Hurricane Earl, the decrease of water temperature induced by waves appears in the depth of more than ~100 m, although the largest temperature decrease appears in the top ~25 m. The effects of waves on the vertical structure of water temperature are mostly attributed to the additional wave forces, followed by the wave-dependent wind stress and wave-enhanced vertical mixing. The wave-enhanced vertical mixing only decreases the water temperature in the top ~15 m and increases the temperature below.

CHAPTER 7

CONCLUSIONS

My doctoral research was motivated by the highly variable oceanographic conditions over the northwest Atlantic (NWA) under the effects wave-current-ice interactions (WCIIs). With strong tides, large-scale circulations, extreme storms and seasonal sea ice over the NWA, WCIIs are important physical processes affecting the physical environments in this region. However, numerical modelling of the WCIIs is of great challenge and has large uncertainties due to our limited understandings on the WCIIs. The main objective of my thesis was to advance our quantitative and predictive understandings of different mechanisms in the WCIIs and examine their effects on the ocean surface gravity waves, and 3D circulations from deep waters to coastal regions in the NWA. Among those physical processes within WCIIs, my doctoral research focused on following five specific aspects: (i) wind input to waves and wave dissipation in the presence of currents and sea ice, (ii) wave propagations in ice, (iii) effects of waves on the wind stress, (iv) depth-induced wave breaking at coastal waters, and (v) wave-current interactions (WCIs) during hurricanes.

The approaches used in my research included analyses of comprehensive observational data and the use of numerical models with different levels of complexity for simulating surface waves and 3D circulations. New parameterizations for the wave-dependent drag coefficient and depth-induced wave breaking were proposed based on analyses of observational data (Chapters 4 and 5). Different numerical models were developed for the NWA in my doctoral research, including a one-way coupled wave-circulation-ice model and a two-way coupled wave-circulation model. The numerical model results were validated using available in-situ and satellite observations for winds, waves, sea level, temperature and salinity. The one-way coupled wave-circulation-ice model was developed

for the NWA based on WAVEWATCH III (WW3) by specifying ocean currents and sea ice in order to investigate the processes for wind input to waves and wave dissipation in the presence of currents and sea ice (Chapter 2). This one-way coupled model was also used to investigate wave propagations in the ice-covered regions over the NWA during a winter storm (Chapter 3) and to assess the performances of different parameterizations for the drag coefficient, including the newly-developed wave-dependent parameterization in my doctoral research (Chapter 4). The two-way coupled wave-circulation model consisted of a third-generation wave model based on the Simulating WAves Nearshore (SWAN) and a 3D circulation model based on the Regional Ocean Modeling System (ROMS). The ROMS and SWAN were two-way coupled using the Model Coupling Toolkit (MCT) at a user-specific coupling interval. New parameterizations for the wave-dependent drag coefficient and depth-induced wave breaking were used in the two-way coupled model. WCIs during Hurricanes Earl and Igor from deep waters to coastal regions over the NWA were investigated based on model results of the two-way coupled model and available observations (Chapter 6). The mechanisms of WCIs considered in the wave model included the relative wind effect, current-induced spatial advection, wavenumber shift and wave refraction. The mechanisms of WCIs considered in the circulation model included the wave-dependent wind stress, wave-induced bottom stress, wave-enhanced vertical mixing, and 3D wave forces. A series of numerical experiments were conducted to quantify the effects of different mechanisms.

7.1 Main Results and Their Significance

In Chapter 2, the one-way coupled wave-circulation-ice model was used to evaluate four different source term packages (known as ST2/3/4/6) for the wind input and wave dissipation. The performances of ST2/3/4/6 were assessed using the available measurements from buoy stations and satellite altimeters. The model results of significant wave heights (SWHs), mean wave periods (MWPs), wave spectra, wind input and wave dissipation were examined during two periods: (i) winter storms in February and (ii) Hurricane Ophelia in September/October 2011. The model results demonstrated that ST6 has the best performance for SWHs and MWPs in the presence of strong currents and sea ice. These four packages perform differently under different sea states. Package ST6

generally overestimates SWHs under the wind-sea-dominated sea states due to strong wind input and fast wave growth but underestimates SWHs under the swell-dominated sea states due to low drag coefficient and strong swell dissipation. The effects of ocean surface currents and sea ice on the wave model performances were also investigated. The linear kinematic effects of surface currents on waves can cause nonlinear dynamic effects, which can be different among four different packages. Wave scattering in sea ice increases the wave directional spread and may cause an increase in SWHs. In the presence of sea ice, wind input is reduced and shifted to higher frequencies and wave dissipation is further suppressed.

In Chapter 3, the one-way coupled wave-circulation-ice modelling system was used to investigate wave propagations in the ice-covered regions of the NWA during a winter storm in March 2014. The applicability of two viscoelastic models (known as IC3/5) for wave dissipation in ice was investigated. Two essential ice rheological parameters (kinetic viscosity and elasticity) in these two viscoelastic models were determined by comparing the SWHs with observations from altimeters and buoys. Both viscoelastic models reproduce reasonably well the wave propagations in ice with the average scatter index less than 12.5% for the SWHs. In the inner ice pack, however, IC3 is superior to IC5, since IC5 produces unrealistic large waves. The two viscoelastic models perform differently in the inner ice pack, due largely to the nonlinear effect of different wave dissipation rates on the wind input for surface waves. In comparison with IC5, IC3 has a stronger dependence of the wave dissipation rate on the wave frequency and thus generates more rapidly wave energy decay in ice. Wave scattering leads to large decreases of SWHs and increases of mean wave periods in the inner ice pack due to the nonlinear effect on the wind input associated with broadening of the wave directional spread.

In Chapter 4, a new parameterization was proposed for the dependences of sea surface roughness on the wind speed and sea state based on field observations. The new parameterization features that the sea surface roughness has different dependences on the wave age under wind-sea-dominated, mixed and swell-dominated sea states. Younger waves have larger values of the drag coefficient under wind-sea-dominated and mixed sea states but older waves have larger values under swell-dominated sea states. The drag

coefficient predicted by the new parameterization is enhanced at low winds and levels off at high winds. The applicability of the new parameterization was investigated using the one-way coupled wave-circulation-ice model for the NWA. The wave model results during a winter storm in March 2014 were compared with the available measurements from buoys and satellite altimeters over the study region. Model results demonstrated that the new parameterization reduces deficiencies of three existing parameterizations of underestimating significant wave heights (SWHs) at low winds (or old waves) and overestimating SWHs at moderate and high winds (or young waves). This study revealed the role of ocean surface waves in the air-sea momentum exchange and improved the estimations of the wind stress by developing a new parameterization. This new parameterization was then also used in the two-way coupled wave-circulation model.

In Chapter 5, the performances of six commonly-used parameterizations for depth-induced wave breaking were assessed under different topography and wave conditions based on laboratory and field observations. These six parameterizations were shown to have reasonable performances in representing SWHs in shallow waters, but with their own limitations and drawbacks. The main differences between these six parameterizations were representations of the breaker index and the fraction of breaking waves. The widely-used parameterization suggested by *Battjes and Janssen* (1978, BJ78) using a constant breaker index underestimates SWHs in the locally-generated wave conditions and overestimates in the remotely-generated wave conditions over flat bottoms. The drawback of BJ78 was addressed by a parameterization suggested by *Salmon et al.* (2015, SA15). But SA15 has relatively larger errors in SWHs over sloping bottoms than BJ78. A new parameterization was proposed with a nonlinear dependence of the breaker index on the local bottom slope in shallow waters rather than the linear dependence used in SA15. This new parameterization was shown to have the best performance with an average scatter index of ~8.2% in representing SWHs at shallow waters.

In Chapter 6, the two-way coupled wave-circulation modelling system was used to investigate WCIs during Hurricanes Earl and Igor in the NWA. The coupled model was shown to capture important physics of WCIs under very different scales and environmental conditions with good performances in representing the SWHs, PWPs, wave spectra, sea

levels, sea surface salinity (SSS) and sea surface temperature (SST). The model results demonstrated the important roles of WCIs in affecting physical environments over the NWA during Hurricanes Earl and Igor. The maximum SWHs generated by hurricanes are reduced by more than 10% along the storm tracks and more than 20% over the eddies associated with the Gulf Stream in the presence of ocean currents. In addition to the effects of the hurricane-driven strong currents, ocean surface waves experience an oscillating pattern after the peak winds due to the near-inertial currents in the wake of hurricanes and strong tidal modulations near the Gulf of Maine (GoM). Surface waves, in turn, reduce the semidiurnal tidal amplitudes in the GoM by up to ~8.6% and cause the phase lag mainly due to the wave-induced bottom stress. Surface waves increase the peak storm surge by up to ~19.4% mainly due to additional wave forces on currents. Surface waves reduce the strength of Labrador Current at the surface under Hurricane Igor by more than ~60.0% due to the wave-enhanced vertical mixing but the reduction is compensated by the effect of additional wave forces. By including the wave effects, tidal currents are reduced by up to ~40.1% over the Georges Bank during the maximum ebb tides mainly due to the wave-induced bottom stress. Surface waves increase the SSS over the St. Lawrence River Estuary (SLRE) and Scotian Shelf (ScS) by up to ~3.8 during Hurricane Igor, which is mainly due to the additional wave forces, followed by the wave-enhanced vertical mixing. Surface waves strengthen the surface cooling induced by hurricanes near the hurricane track with a reduction in SST of up to ~4.3°C over the Grand Banks during Hurricane Igor. The wave-induced reduction in SST is mostly attributed to the wave-enhanced vertical mixing and the additional wave forces on currents, followed by the wave-induced bottom stress. Surface waves also strongly affect the vertical structure of water temperature with the decrease of water temperature at depths of more than ~100 m. The effects of waves on the vertical structure of water temperature are mostly attributed to the additional wave forces, followed by the wave-dependent wind stress and wave-enhanced vertical mixing.

The most important findings of my doctoral research include:

(i) In the spectral wave models, the source term packages for the wind input and wave dissipation have different performances under different sea sates. Package ST6 generally overestimates SWHs under the wind-wave-dominated sea states due to fast wave growth

but underestimates SWHs under the swell-dominated sea states due to low drag coefficient and strong swell dissipation.

(ii) Wave scattering can significantly modifies wave propagations in ice over the ECS during a winter storm in March 2014. Wave scattering leads to large decreases of SWHs and increases of mean wave periods in the inner ice pack due to the nonlinear effect on the wind input associated with broadening of wave directional spreads.

(iii) Ocean surface waves are important in determining the air-sea momentum flux. The sea surface roughness has different dependences on the wave age under different sea states.

(iv) The depth-induced wave breaking process relies on the wave conditions, water depth and bottom slope. The breaker index has a nonlinear dependence on the bottom slope in shallow waters rather than to be a constant.

(v) The inclusion of various WCI mechanisms in the coupled wave-circulation model significantly improves the model performance from deep waters to coastal regions in the NWA. Wave propagations are modulated by tides, hurricane-driven currents, and large-scale circulations. Surface waves, in turn, can affect the sea level, tides, circulation patterns, water temperature and salinity due to different mechanisms.

7.2 Future Work

Although significant achievements were made in my doctoral research on investigating some of the important physical processes for the WCIIs and their effects on ocean surface waves and 3D circulations over the NWA, there are some other applications can be conducted or some other scientific questions can be addressed in the future. For example, although the proposed new parameterizations for the drag coefficient and depth-induced wave breaking were shown to have improved performances in my research. Their applicability can be further examined in the applications under different conditions or for other geostrophic locations.

The effect of surface waves on the wind stresses was quantitatively estimated in the new parameterization proposed in the study with different dependences of sea surface roughness

on the wave age under different sea sates (Chapter 4). However, the wind stress may not be simply represented by the wind speed, wave age and significant wave height as used in the new parameterization. There are still large uncertainties for the estimation of wind stresses at low and high winds. Particularly, sea states are energetic with large waves and strong currents but field observations are relatively limited at high winds (*Potter et al.,* 2015). The wind stresses under tropical cyclones can be very different at different quadrants due to their different wave conditions (*Holthuijsen et al.,* 2012). With more advanced observations at high winds, one of the future research directions can be the quantitative estimations of the wind stresses under cyclones considering more physical effects, such as the wave directionality and sea spray.

From a broader perspective, my doctoral research improves our understandings on the important role of ocean surface waves in the coupled air-sea system by quantifying the effects of surface waves on the air-sea momentum exchange (Chapter 4). The imparts of ocean surface waves are not limited to the air-sea momentum exchange but also include the heat and gas exchanges between the atmosphere and ocean (*Cavaleri et al.,* 2012). Further researches should be done to quantify the effects of surface waves on the air-sea heat and gas exchanges and to investigate the impacts of surface waves to climate changes.

The two-way coupled wave-circulation model developed in my research can be used to further investigate the ocean responses to hurricanes in this dynamically complex region. It was shown in Chapter 6 that hurricanes can generate strong currents in the upper layer and affect the Gulf Stream, Labrador Current and strong tides in the Gulf of Maine and vice versa. The interactions of hurricanes with large-scale circulations and tides deserve further investigations in terms of the changes of the circulation pattern, mixing, heat budget and water transport. On the other hand, the WCIs in the NWA can be further investigated in different temporal or spatial scales. The study in Chapter 6 focuses on the WCIs during extreme events in a synoptic time scale. Further studies can be conducted by investigating the seasonal variation of WCIs in the upper layer in response to the seasonal forces. The effect of WCIs at some socially and economically important coastal waters can be further investigated with the development of a high resolution nested-grid coupled modelling system.

APPENDIX A

STATISTICS FOR MODEL COMPARISONS

The significant wave height (H_s) and mean wave periods $(T_{m01}$ and $T_{m02})$ can be calculated using the 2-D wave spectra $E(f,\theta)$ or the 1-D wave spectra $E(f)$:

$$H_s = 4(\iint E(f,\theta)\, df d\theta)^{1/2} \tag{A1}$$

$$T_{m01} = \iint E(f,\theta)\, df d\theta / \iint f E(f,\theta)\, df d\theta \tag{A2}$$

$$T_{m02} = (\iint E(f,\theta)\, df d\theta / \iint f^2 E(f,\theta)\, df d\theta)^{1/2} \tag{A3}$$

The five metrics suggested in previous studies (e.g., *Salmon et al.,* 2015; *Guo and Sheng,* 2015; *Mentaschi et al.,* 2013; *Lin and Sheng,* 2017) are used, which include the relative bias (RB), root mean square error (RMSE), scatter index (SI), correlation coefficient (R) and variance ratio (γ^2):

$$RB = \frac{1}{n}\sum_{i=1}^{n}(M_i - O_i)/\bar{O} \tag{A4}$$

$$RMSE = [\frac{1}{n}\sum_{i=1}^{n}(M_i - O_i)^2]^{1/2} \tag{A5}$$

$$SI = RMSE/\bar{O} \tag{A6}$$

$$R = \frac{\sum_{i=1}^{n}(M_i - \bar{M})(O_i - \bar{O})}{[\sum_{i=1}^{n}(M_i - \bar{M})^2 \sum_{i=1}^{n}(O_i - \bar{O})^2]^{1/2}} \tag{A7}$$

$$\gamma^2 = \frac{Var(M-O)}{Var(O)} \tag{A8}$$

where n is the total number of observations in each case, M and O denote respectively the modeled and observed values, the overbar indicates the mean value and Var stands for the variance.

The RB quantifies the degree of the overall overprediction (for a positive RB) or underprediction (for a negative RB) of observations by the model. The RMSE represents the standard deviation of model errors, and is widely used to quantify performances of

different model results for the same observed variable. Since the RMSE has the same units as the simulated (or observed) variable, it could not be used for a quantitative comparison of model errors for different variables with different units. Furthermore, since the wave conditions may differ significantly, the RMSE may also not be a good metric for comparisons of model errors between different cases. For example, when comparing model results with small-scale laboratory data, the RMSE of SWHs could be much smaller than the values for the model-field data comparisons.

The SI represents the mean of the absolute model errors normalized by the mean of observations. The SI is very useful for quantitative comparisons between different variables with different scales. Based on their definitions, the SI is always positive, and the RB is either positive or negative. Furthermore, the SI is equal or larger than the magnitude of the RB value. The correlation coefficient (R), which is defined as the square root of the covariance of the simulated and observed values divided by the product of their standard deviations, can be used to quantify a degree of the linear relation between simulated and observed values. A correlation of 1.0 (0.0) suggests a perfect (no) linear dependence between simulated and observed values. The variance ratio (γ^2) is defined as the variance of model errors normalized by the observed variance. A smaller value of γ^2 represents a better agreement between the simulated and observed values. Values of γ^2 less than unity indicate that the observed variance is reduced by the subtraction of the hindcasts from the observations. Values of γ^2 greater than or equal to unity can occur if the model is deficient in some important way or the observations are dominated by measurement noises. In this study, $\gamma^2 = 1$ is used as a threshold to assess the model performance.

APPENDIX B

A PARAMETRIC HURRICANE WIND MODEL

To well represent the wind fields associated with Hurricane Ophelia, a parametric hurricane wind model suggested by *Hu et al.* (2012) is inserted into the original CFSv2 wind fields. This parametric vortex was modified from the Holland-type vortex model (*Holland,* 1980) given as:

$$p(r) = p_c + (p_n - p_c)e^{-(R_m/r)^{B_1}} \tag{B1}$$

$$V_g(r) = \sqrt{\frac{B_1}{\rho_a}\left(\frac{R_m}{r}\right)^{B_1}(p_n - p_c)e^{-(R_m/r)^{B_1}} + \left(\frac{rf_c}{2}\right)^2} - \frac{rf_c}{2} \tag{B2}$$

where $p(r)$ and $V_g(r)$ are, respectively, the pressure and the gradient wind at radius r, p_n is the ambient pressure, p_c is the central pressure, R_m is the radius of maximum wind, B_1 is the hurricane shape parameter, ρ_a is the air density, and f_c is the Coriolis parameter. The Coriolis effect, translational velocity of the hurricane, and all available wind parameters from the National Hurricane Center (NHC) are used in constructing the wind fields associated with Hurricane Ophelia. The modified CFSv2 winds are made by first interpolating the original CFSv2 winds into the inner wave model grid (1/12°) and then inserting the parametric hurricane winds into the interpolated CFSv2 winds at each model time step. Similar vortex insertion methods were used in previous studies (e.g., *Wang and Sheng,* 2016).

As mentioned in Section 2.2.2, the scatter plots (Figs. 2.3g-2.3i) convincingly show the improvement in the modified CFSv2 compared with available measurements from buoys and satellites. The advantage by adding the parametric vortex model is more evidently shown in Figure B1. Figure B1 compares U_{10} from the original (blue line) and modified (black line) CFSv2 with observed values at four buoy stations along the hurricane track.

The locations of these four buoys are shown in Fig. 2.1. The modified CFSv2 winds reduce the underestimations of U_{10} at buoy 41041 and the overestimations at buoy 44141 for the peak values. In comparisons with the original CFSv2 winds, the modified winds also have better agreement with the observed values at buoys 41043 and 41044.
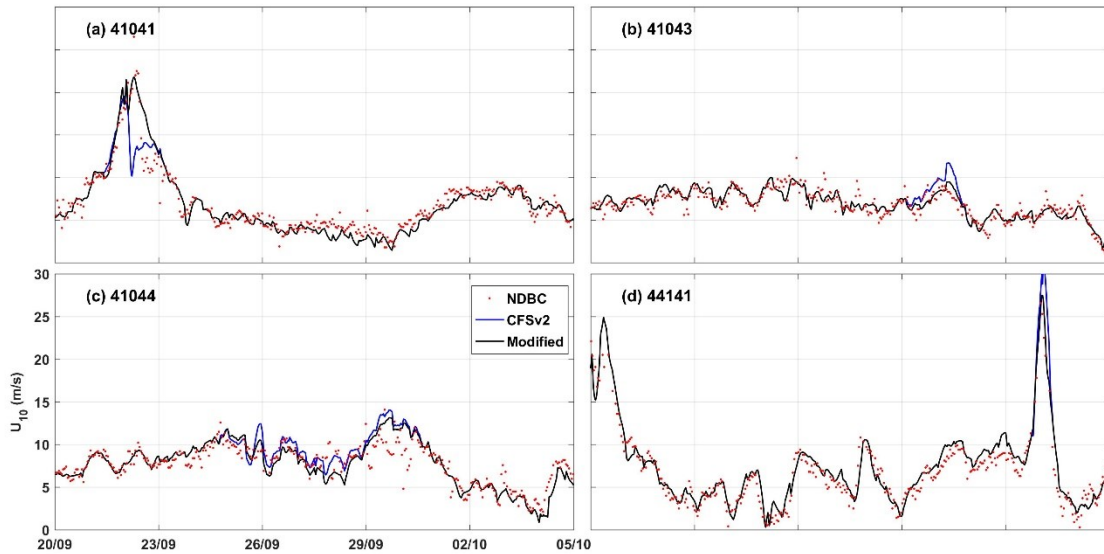

Figure B1: Time series of the wind fields (U_{10}) from the original (blue line) and modified (black line) CFSv2 against the observed values at four buoy stations (red dots) during the hurricane period (Hurricane Ophelia, 25 September-5 October) in 2011.

APPENDIX C

DEPENDENCES OF WAVE DISSIPATION ON ICE AND WAVE PROPERTIES

To investigate dependences of wave dissipation on ice and wave properties, a one-dimensional idealized case for wave propagations through an ice layer is set up based on WW3. The one-dimensional model domain is 154 km (in the x direction) with a spatial resolution of 1 km with the ice layer spreading the entire domain (Fig. C1). A JONSWAP wave spectrum (*Hasselmann et al.,* 1973) is specified at the model boundary ($x = 0$ km), which persistently propagates into ice. A series of numerical experiments are carried out using different values of the ice kinematic viscosity ($10^{-3} \leq v \leq 10^4 \, m^2 \, s^{-1}$), ice elasticity ($10^0 \leq G \leq 10^{12} \, Pa$), ice concentration ($0.05 \leq c_i \leq 1$), ice thickness ($0.1 \leq h_i \leq 8 \, m$), and SWH ($0.5 \leq H_s \leq 16 \, m$) and peak wave frequency ($0.05 \leq f_p \leq 0.6 \, Hz$) for the incident waves. The wave model runs for 24 hours and the model results reach a steady state by the end of model runs. To exclude the effects from other physical processes, only the physical process for wave dissipation in ice is used here. Similar model tests were carried out by *Collins and Rogers* (2017) to examine the empirical functions for wave dissipation in ice.

Waves propagating in ice from location A to B experience exponential decay (e.g., *Wadhams et al.,* 1988; *Meylan et al.,* 2014; *Meylan et al.,* 2018) given as:

$$E_B(f) = E_A(f)exp(-\alpha_1 x) \qquad \text{(C1)}$$

where x is the distances from location A to B in the wave propagation direction, α_1 is the apparent attenuation rate, E_A and E_B are the wave spectra at two locations. The apparent attenuation rate can be calculated using the wave spectra or SWHs given as:

$$\alpha_1 = -\ln{(E_B/E_A)}/x = -2\ln{(H_{sB}/H_{sA})}/x \tag{C2}$$

where $H_{sA} = 4\sqrt{E_A}$ and $H_{sB} = 4\sqrt{E_B}$ are the SWHs at two locations. As other source terms are not used in this idealized experiment, wave attenuation is entirely due to the non-conservative wave dissipation in ice. The apparent attenuation rate is thus identical to the wave dissipation rate in this case, which represents the mean wave dissipation rate across the wave spectrum. Figure C1 shows variations of the SWHs and MWPs with increasing distances into the ice in the one-dimensional idealized case. The incident wave has a JONSWAP spectrum with the SWH of 4.0 m and peak frequency of 0.1 Hz. The ice layer has a concentration of 0.5 and a thickness of 0.5 m. At low elasticity and viscosity regimes (e.g., $v = 0.05\ m^2s^{-1}$ and $G = 10^2 Pa$), waves predicted by IC3 show exponential decay with the SWH of ~3.2 m and MWP of ~9.2 s at $x = 150$ km. In comparison, IC5 has much lower wave dissipation rates for the same ice rheological parameters so that the incident wave is only slightly dissipated with the SWH of ~3.9 m at $x = 150$ km (Fig. C1a). The wave dissipation rates predicted by IC3/5 have large values for relatively higher viscosity regimes (e.g., $v = 5.0\ m^2s^{-1}$). For example, the SWH predicted by IC3 is reduced to 0.8 m at $x = 150$ km and the MWP is increased to 12.5 s (Figs. C1c-C1d).

The increasing MWP along the wave propagation direction is due to the relatively higher wave dissipation rate for wave energy at higher frequencies. Figure C2 shows the variations of wave spectra along the wave propagation direction. Wave energy is decayed slightly at low frequencies but decayed rapidly at high frequencies with the increasing distances into ice (Figs. C2a-C2b). Wave energy at high frequencies predicted by IC3 is more rapidly decayed than that by IC5 using the same ice rheological parameters (v and G). For example, wave energy predicted by IC3 at $f = 0.2$ Hz and $x = 150$ km is around four orders of magnitude larger than that by IC5 at low viscosity and elasticity regimes (black lines in Fig. C2c). These differences become larger at relatively higher viscosity regimes (black lines in Fig. C2d). Our results are consistent with the findings in *Mosig et al.* (2015). Wave spectra predicted by IC3/5 are similar at high elasticity regimes (red lines in Figs. C2c-C2d), indicating similar values of wave dissipation rate.
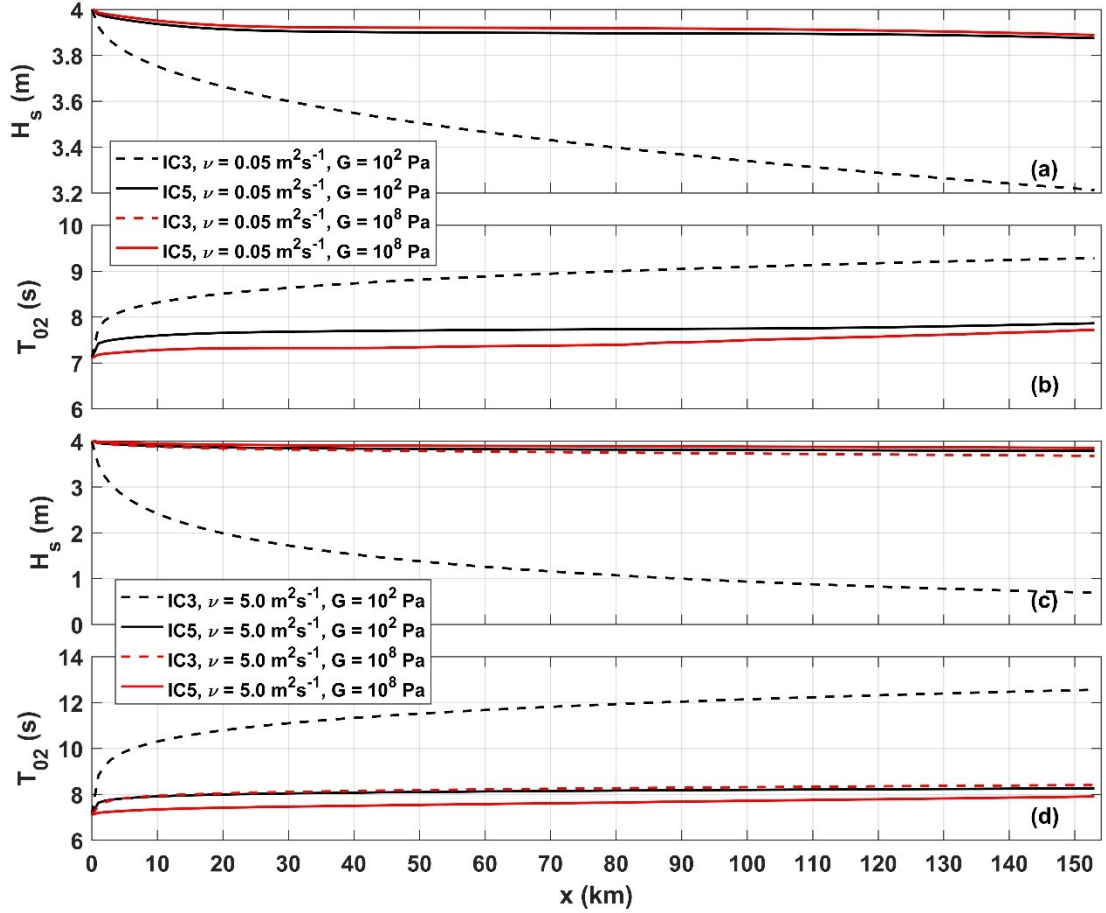
Figure C1: Variations of the simulated SWHs (H_s) and MWPs (T_{m02}) with the increasing distances into ice predicted by the wave model using two different viscoelastic models (IC3/5) with different values of ice viscosity (v) and elasticity (G). The red dashed line in panel (a) is overlaid by the red solid line.

In addition to the two ice rheological parameters (v and G) discussed above, the wave dissipation rate may also depend on other ice and wave properties. We next investigate the dependences of the wave dissipation rate on the kinematic viscosity (v), elasticity (G), ice concentration (c_i), ice thickness (h_i), significant wave height (SWH or H_s) and peak wave frequency (f_p) of the incident wave. Figure C3 shows the variations of the apparent wave attenuation rate (α_1) at $x = 150$ km in terms of G, v, h_i and f_p. Our results demonstrate that the values of α_1 predicted by IC3/5 do not change for different incident SWHs, which is expected since different incident SWHs do not affect the wave dispersion relations for these two viscoelastic models (*Mosig et al.,* 2015). The values of α_1 monotonously increase with the increasing ice concentration, as a result of the scaling of wave dissipation term (S_{ice}). In the following analyses of different model runs, the incident

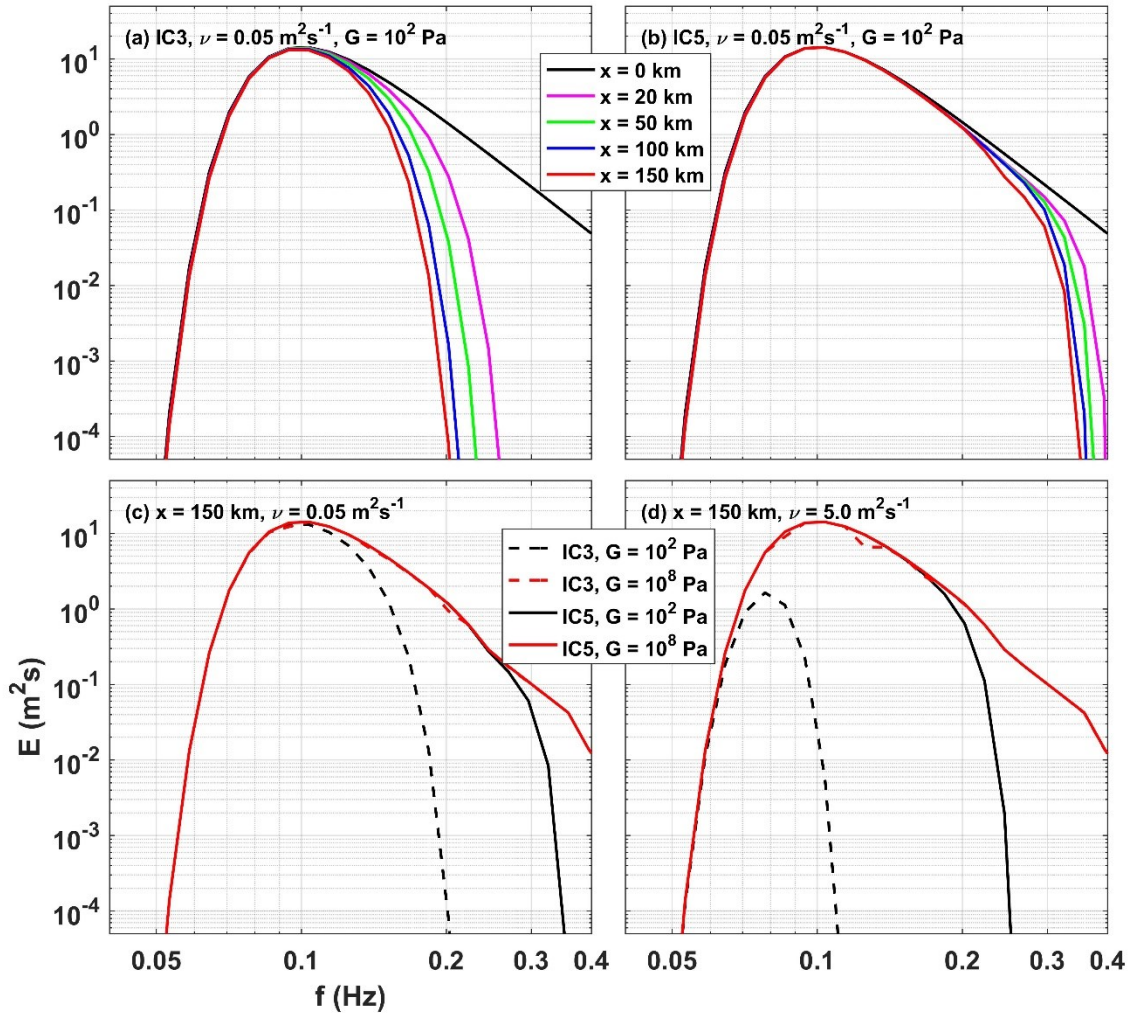waves have the same SWH of 4.0 m and the sea ice concentrations have the same value of 0.5.

Figure C2: Variations of the wave spectra at different locations in ice produced by the wave model using (a) IC3 and (b) IC5 with $v = 0.05\ m^2 s^{-1}$ and $G = 10^2\ Pa$. Panels (c-d) show the wave spectra at $x = 150$ km produced by the wave model using IC3 (dashed lines) and IC5 (solid lines) with (c) $v = 0.05\ m^2 s^{-1}$ and (d) $v = 0.05\ m^2 s^{-1}$.

Figure C3 shows the variations of α_1 in terms of v, G, h_i and f_p for $H_s = 4.0$ m and $c_i = 0.5$. Physically, the increase of ice viscosity leads to more wave energy dissipation. As shown in Fig. C3a, this is predicted by IC3/5 with similar values of α_1 at high elasticity regimes (red lines). At lower elasticity regimes, the ice floes are more flexible and thus produce stronger wave dissipation (black lines). In comparison with IC5, IC3 is more sensitive to the changing of elasticity with much larger values of α_1 at low elasticity

regimes. It should be noted that α_1 predicted by IC3 first increases at low viscosity regimes and then decreases at moderate viscosity regimes until it keeps growing again at high viscosity regimes (black lines). This is due to the changing of different wave modes for the solutions of wave dispersion (*Mosig et al.,* 2015).

The ice floes with lower elasticity are generally more flexible and thus can dissipate more wave energy (*Cheng et al.,* 2017). This is generally predicted by IC3/5 with different variations, as shown in Fig. C3b. With the increase of G, α_1 predicted by IC3 initially remains similar values with a slight increase at around $G = 10^4\,Pa$ and then gradually decreases to low values at high elasticity regimes (dashed lines). By companion, α_1 predicted by IC5 has similar variations but with some differences in magnitude (solid lines). The values of α_1 predicted by IC3 are about one order of magnitude lager than those by IC5 at low elasticity regimes (e.g., $G \leq 10^4\,Pa$). At high elasticity regimes, the values of α_1 predicted by IC3/5 become identical.

The effect of ice thickness on α_1 is readily understood based on the fact that waves encountered thicker ice floes are more easily attenuated. The apparent dissipation rate, however, does not increase continuously but saturates at a maximum value with the increasing ice thickness (Fig. C3c). The increasing peak frequency of the incident wave causes more wave energy dissipation (Fig. C3d), as more wave energy is spread at high frequencies. Wave energy at high frequencies can easily dissipated in ice and swells at low frequencies can penetrate great distances in ice as observed in previous field experiments (e.g., *Meylan et al.,* 2014; *Collins et al.,* 2015). Thus, the values of α_1 vary over several orders of magnitude across the rang of frequency considered. For a comparison of two models (IC3/5) in Figs. C3c-C3d, α_1 predicted by IC3 has much larger values that the counterparts by IC5.

The above-mentioned features are similar with the wave dissipation rate shown in *Mosig et al.* (2015). The main difference is that α_1 shown in Fig. C3b does not continuously decrease with the increasing elasticity but levels off at a low value at high elasticity regimes. Although the wave dissipation rate is low at high elasticity regimes, wave energy at high frequencies is still easily dissipated. This leads to a slightly reduction of the SWH at $x =$

150 km (Fig. C1a). The apparent wave dissipation rate α_1 thus has a low limit. This is also the reason that α_1 has a minimum value at low viscosity regimes (Fig. C3a).
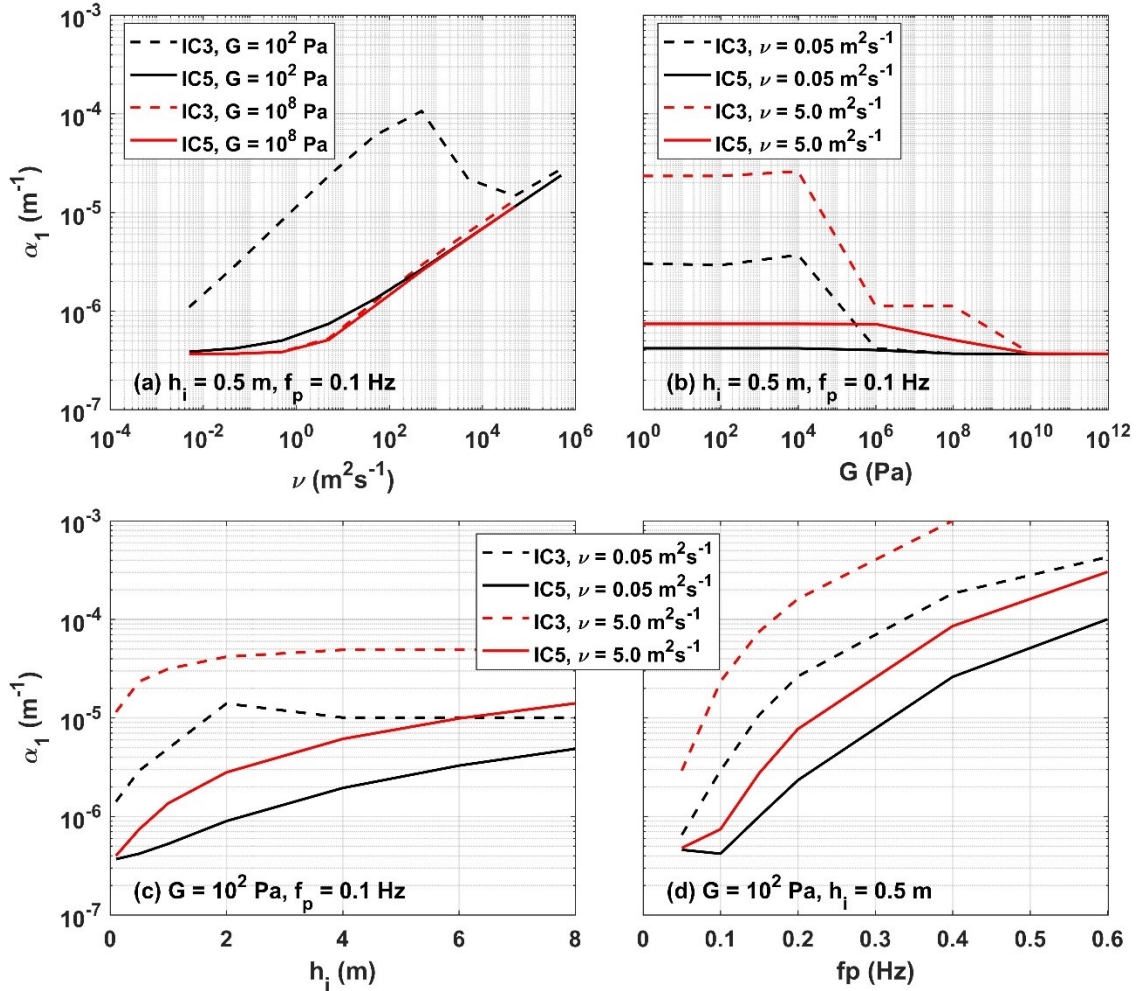

Figure C3: Variations of the apparent wave attenuation rate (α_1) predicted by IC3/5 in terms of the (a) ice viscosity (ν), (b) ice elasticity (G), (c) ice thickness (h_i) and (d) peak frequency (f_p) of the incident wave. The incident SWH is 4.0 m and the ice concentration is 0.5 for all cases.

APPENDIX D

THE DELILAH NEARSHORE EXPERIMENT

This section provides an additional analysis on the performances of six existing parameterizations in the data set of the DELILAH nearshore experiment. To distinguish the performances under different wave conditions, the model results and field observations of these cases are separated into different subsets in terms of incident wave directions (Fig. D1), normalized water depths ($k_p d$, Fig. D2) and wave ages (c_p/U_{10}, Fig. D3) at deep waters. Here c_p is the peak phase speed of waves and U_{10} is the wind speed at 10 m above the sea surface. The wave age c_p/U_{10} can be used to classify the sea state (e.g. *Wu et al.,* 2016), namely the swell-dominated wave condition ($c_p/U_{10} > 1.2$) and wind wave condition ($c_p/U_{10} < 1.2$).

It is shown in Fig. D1 that the cases with smaller values of the incident wave angle tend to have less errors, since the incident wave energy are better represented in 1D wave simulations for small incident wave angles. While there are no remarkable differences between two counterparts as shown in Figs. D2-D3, indicating that the performances of different parameterizations is not very sensitive to the normalized water depth and wave age. As discussed in Section 5.4.1, the effects of ambient currents and wind energy input may contribute to the significant dispersion of SI-RB data points. It should be noted that the field experiment was conducted in an energetic current region with the observed longshore currents up to 1.72 m/s and observed across-shore currents up to 0.72 m/s. A further study should be made by conducting 2D wave simulations to examine the effects of currents, wind energy inputs and wave refractions.
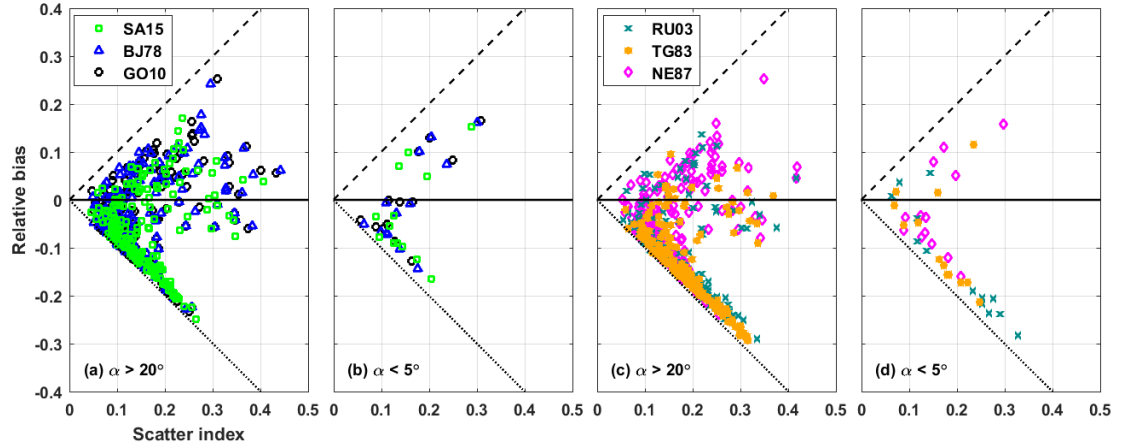
Figure D1: Scatter plots of the relative bias versus the scatter index calculated from observed and simulated SWHs in the data set of the DELILAH project for large (a and c) and small (b and d) values of incident wave angles. The simulated SWHs in Figs. D1-D3 are generated by SWAN using (a-b) SA15, BJ78 and GO10 and (c-d) TG83, NE87 and RU03 for depth-induced wave breaking.
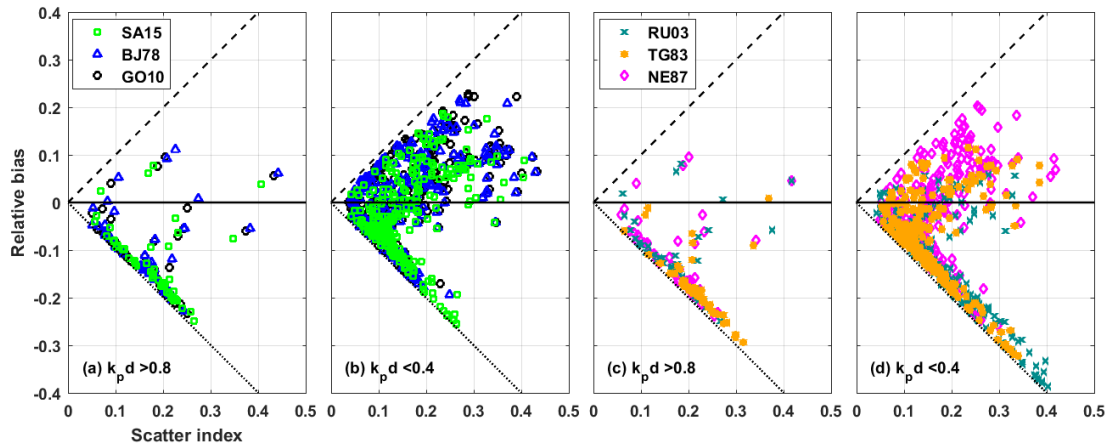

Figure D2: Scatter plots of the relative bias versus the scatter index calculated from observed and simulated SWHs in the data set of the DELILAH project for large (a and c, $k_p d > 0.8$) and small (b and d, $k_p d < 0.4$) values of deep-water normalized water depths.
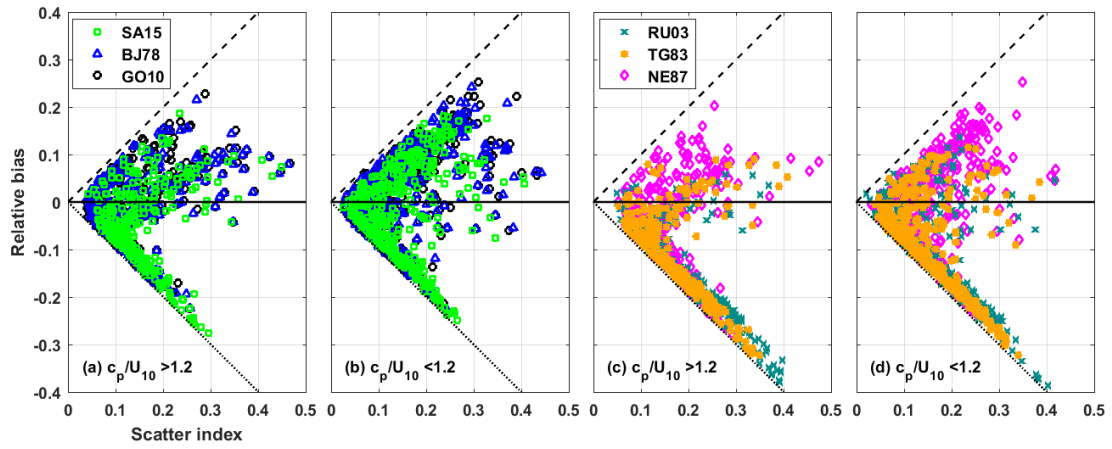
214

Figure D3: Scatter plots of the relative bias versus the scatter index calculated from observed and simulated SWHs in the data set of the DELILAH project for swell-dominated conditions (a and c, wave age $c_p/U_{10} > 1.2$) and wind wave conditions (a and c, wave age $c_p/U_{10} < 1.2$).

APPENDIX E

COPYRIGHT PERMISSION

Revisiting dependences of the drag coefficient at the sea surface on wind speed and sea state

Author: Shangfei Lin,Jinyu Sheng

Publication: Continental Shelf Research

Publisher: Elsevier

Date: 16 December 2020

Journal Author Rights

BACK   CLOSE WINDOW

Assessing the performance of wave breaking parameterizations in shallow waters in spectral wave models

Author: Shangfei Lin,Jinyu Sheng

Publication: Ocean Modelling

Publisher: Elsevier

Date: December 2017

Journal Author Rights

BACK   CLOSE WINDOW

BIBLIOGRAPHY

Agnew, T., and Howell, S. (2003). The use of operational ice charts for evaluating passive microwave ice concentration data. *Atmos.-Ocean*, 41(4), 317-331. doi:10.3137/ao.410405

Alekseeva, T., Tikhonov, V., Frolov, S., Repina, I., Raev, M., Sokolova, J., Sharkov, E., Afanasieva, E., and Serovetnikov, S. (2019). Comparison of Arctic Sea Ice concentrations from the NASA team, ASI, and VASIA2 algorithms with summer and winter ship data. *Remote Sens.*, 11(21), 2481. doi:10.3390/rs11212481

Allsop, N.W.H., Durand, N., and Hurdle, D.P. (1998). Influence of steep seabed slopes on breaking waves for structure design. *Proc. 26th Int. Conf. Coast. Eng.,* 906-919. doi:10.1061/9780784404119.067

Altiparmak, F., Gen, M., Lin, L., and Paksoy, T. (2006). A genetic algorithm approach for multi-objective optimization of supply chain networks. *Comput. Ind. Eng.,* 51(1), 196-215. doi:10.1016/j.cie.2006.07.011

Anctil, F., and Donelan, M.A. (1996). Air-water momentum flux observations over shoaling waves. *J. Phys. Oceanogr.*, 26(7), 1344-1353. doi:10.1175/1520-0485(1996)026 <1344:AMFOOS>2.0.CO;2

Apotsos, A., Raubenheimer, B., Elgar, S., and Guza, R.T. (2008). Testing and calibrating parametric wave transformation models on natural beaches. *Coast. Eng.,* 55(3), 224-235. doi:10.1016/j.coastaleng.2007.10.002

Arcilla, A.S., Roelvink, J.A., O'Connor, B.A., Reniers, A., and Jimenez, J.A. (1994). The Delta flume '93 experiment. *Coastal Dynamics 1994,* 488-502.

Ardhuin, F., Boutin, G., Stopa, J., Girard-Ardhuin, F., Melsheimer, C., Thomson, J., Kohout, A., Doble, M., and Wadhams, P. (2018). Wave attenuation through an Arctic

marginal ice zone on 12 October 2015: 2. Numerical modeling of waves and associated ice breakup. *J. Geophys. Res.,* 123(8), 5652-5668. doi:10.1002/2018JC013784

Ardhuin, F., Chapron, B., and Collard, F. (2009). Observation of swell dissipation across oceans. *Geophys. Res. Lett.,* 36(6), L06607. doi:10.1029/2008GL037030

Ardhuin, F., Gille, S.T., Menemenlis, D., Rocha, C.B., Rascle, N., Chapron, B., Gula, J., and Molemaker, J. (2017). Small-scale open ocean currents have large effects on wind wave heights. *J. Geophys. Res.,* 122(6), 4500-4517. doi:10.1002/2016JC012413

Ardhuin, F., Herbers, T.H.C., Watts, K.P., van Vledder, G.P., Jensen, R., and Graber, H.C. (2007). Swell and slanting-fetch effects on wind wave growth. *J. Phys. Oceanogr.,* 37(4), 908-931. doi:10.1175/JPO3039.1

Ardhuin, F., Rascle, N., and Belibassakis, K. A. (2008). Explicit wave-averaged primitive equations using a generalized Lagrangian mean. *Ocean Modell.,* 20(1), 35-60. doi: 10.1016/j.ocemod.2007.07.001

Ardhuin, F., Rogers, E., Babanin, A. V., Filipot, J. F., Magne, R., Roland, A., Van der Westhuysen, A., Queffeulou, P., Lefever, J.M., Aouf, L., and Collard, F. (2010). Semiempirical dissipation source functions for ocean waves. Part I: Definition, calibration, and validation. *J. Phys. Oceanogr.,* 40(9), 1917-1941. doi:10.1175 /2010JPO4324.1

Ardhuin, F., Roland, A., Dumas, F., Bennis, A. C., Sentchev, A., Forget, P., Wolf, J., Girard, F., Osuna, P., and Benoit, M. (2012). Numerical wave modelling in conditions with strong currents: Dissipation, refraction, and relative wind. *J. Phys. Oceanogr.,* 42(12), 2101-2120. doi:10.1175/JPO-D-11-0220.1

Ardhuin, F., Sutherland, P., Doble, M., and Wadhams, P. (2016). Ocean waves across the Arctic: Attenuation due to dissipation dominates over scattering for periods longer than 19 s. *Geophys. Res. Lett.,* 43(11), 5775-5783. doi:10.1002/2016GL068204

Babanin, A. V. (2011). Breaking and dissipation of ocean surface waves. Cambridge Univ. Press, Cambridge, U. K.

Babanin, A. V., and Makin, V. K. (2008). Effects of wind trend and gustiness on the sea drag: Lake George study. *J. Geophys. Res.,* 113, C02015. doi:10.1029/2007JC004233

Babanin, A. V., van der Weshuijsen, A., Chalikov, D., and Rogers, W. E. (2017). Advanced wave modeling, including wave-current interaction. *J. Mar. Res.,* 75(3), 239-262. doi: 10.1357/002224017821836798

Babanin, A. V., Young, I. R., and Banner, M. L. (2001). Breaking probabilities for dominant surface waves on water of finite constant depth. *J. Geophys. Res.,* 106(C6), 11659-11676. doi:10.1029/2000JC000215

Baldock, T.E., Holmes, P., Bunker, S., and van Weert, P. (1998). Cross-shore hydrodynamics within an unsaturated surf zone. *Coast. Eng.,* 34(3-4), 173-196. doi:10.1016/S0378-3839(98)00017-9

Baldock, T. E., and Huntley, D. A. (2002). Long-wave forcing by the breaking of random gravity waves on a beach. *Proceedings of the Royal Society A: Math., Phys. Eng. Sci.,* 458(2025), 2177-2201. doi:10.1098/rspa.2002.0962

Battjes, J.A., and Janssen, J.P.F.M. (1978). Energy loss and set-up due to breaking of random waves. *Proc. 16th Int. Conf. Coast. Eng.,* 569-587. doi:10.1061/9780872621909.034

Battjes, J.A., and Beji, S. (1992). Breaking waves propagating over a shoal. *Proc. 23rd Int. Conf. Coast. Eng.,* 41-50. doi:10.1061/9780872629332.003

Battjes, J. A., and Stive, M. J. F. (1985). Calibration and verification of a dissipation model for random breaking waves. *J. Geophys. Res.,* 90(C5), 9159-9167. doi: 10.1029/JC090iC05p09159

Benetazzo, A., Carniel, S., Sclavo, M., and Bergamasco, A. (2013). Wave-current interaction: Effect on the wave field in a semi-enclosed basin. *Ocean Modell.,* 70, 152-165. doi:10.1016/j.ocemod.2012.12.009

Bennetts, L. G., and Squire, V. A. (2012). On the calculation of an attenuation coefficient for transects of ice-covered ocean. *Proceedings of the Royal Society A: Math., Phys. Eng. Sci.,* 468(2137), 136-162. doi:10.1098/rspa.2011.0155

Bennis, A. C., Ardhuin, F., and Dumas, F. (2011). On the coupling of wave and three-dimensional circulation models: Choice of theoretical framework, practical implementation and adiabatic tests. *Ocean Modell.,* 40(3-4), 260-272. doi:10.1016/j.ocemod.2011.09.003

Bi, X., Gao, Z., Liu, Y., Liu, F., Song, Q., Huang, J., Huang, H., Mao, W., and Liu, C. (2015). Observed drag coefficients in high winds in the near offshore of the South China Sea. *J. Geophys. Res.,* 120(13), 6444-6459. doi:10.1002/2015JD023172

Bidlot, J.R., Janssen, P., and Abdalla, S. (2007). A revised formulation of ocean wave dissipation and its model impact. Tech. Rep., 509, ECMWF, Reading, U. K.

Birkemeier, W.A., Donoghue, C., Long, C.E., Hathaway, K.K., and Baron, C.F. (1997). 1990 DELILAH nearshore experiment: Summary report. Tech. Rep. No. AEWES-TR-CHL-97-24, U.S. Army Corps of Eng., Vicksburg, Miss.

Black, P.G., D'Asaro, E.A., Drennan, W.M., French, J.R., Niiler, P.P., Sanford, T.B., Terrill, E.J., Walsh, E.J., and Zhang, J.A. (2007). Air-sea exchange in hurricanes: synthesis of observations from the coupled boundary layer air-sea transfer experiment. *Bull. Am. Meteor. Soc.,* 88(3), 357-374. doi:10.1175/BAMS-88-3-357

Boers, M. (1997). Simulation of a surf zone with a barred beach; Part 1: wave heights and wave breaking. *Oceanographic Literature Review*, 4(44), 292.

Booij, N., Ris, R.C., and Holthuijsen, L.H. (1999). A third-generation wave model for coastal regions: 1. Model description and validation. *J. Geophys. Res.,*104(C4), 7649-7666. doi:10.1029/98JC02622

Bottema, M., and van Vledder, G.P. (2009). A ten-year data set for fetch-and depth-limited wave growth. *Coast. Eng.,* 56(7), 703-725. doi:10.1016/j.coastaleng.2009.01.012

Boutin, G., Ardhuin, F., Dumont, D., Sévigny, C., Girard-Ardhuin, F., and Accensi, M. (2018). Floe size effect on wave-ice interactions: Possible effects, implementation in wave model, and evaluation. *J. Geophys. Res.,* 123(7), 4779-4805. doi:10.1029/2017JC013622

Boutin, J., Vergely, J.-L., Reul, N., Catany, R., Koehler, J., Martin, A., Rouffi, F., Arias, M., Chakroun, M., Corato, G., Estella-Perez, V., Guimbard, S., Hasson, A., Josey, S., Khvorostyanov, D., Kolodziejczyk, N., Mignot, J., Olivier, L., Reverdin, G., Stammer, D., Supply, A., Thouvenin-Masson, C., Turiel, A., Vialard, J., Cipollini, P., and Donlon, C. (2020). ESA Sea Surface Salinity Climate Change Initiative: Weekly sea surface salinity product, v2.31, for 2010 to 2019. Centre for Environmental Data Analysis.

Bourgault, D., and Koutitonsky, V. G. (1999). Real-time monitoring of the freshwater discharge at the head of the St. Lawrence Estuary. *Atmos.-Ocean*, 37(2), 203-220.

doi:10.1080 /07055900.1999.9649626

Bradley E., Coppin, P., and Godfrey, J. (1991). Measurements of sensible and latent heat flux in the western equatorial Pacific Ocean. *J. Geophys. Res.,* 96(S01), 3375-3389. doi:10.1029/90JC01933

Caldwell, P. C., Merrifield, M. A., and Thompson, P. R. (2015). Sea level measured by tide gauges from global oceans-the Joint Archive for Sea Level holdings (NCEI Accession 0019568), Version 5.5, NOAA National Centers for Environmental Information, Dataset. doi:10.7289/V5V40S7W

Camenen, B., and Larson, M. (2007). Predictive formulas for breaker depth index and breaker type. *J. Coast. Res.,* 23(4 (234)), 1028-1041. doi: 10.2112/05-0566.1

Canadian Ice Service (CIS) (2005). Manual of standard procedures for observing and reporting ice conditions (MANICE), Environment Canada, Ottawa.

Cangialosi, J. P. (2011). Tropical cyclone report: Hurricane Earl (AL072010), 25 August-4 September 2010. Miami, FL: National Hurricane Center.

Cavaleri, L. (2009). Wave modeling-missing the peaks. *J. Phys. Oceanogr.,* 39(11), 2757-2778. doi:10.1175/2009JPO4067.1

Cavaleri, L., Alves, J. H., Ardhuin, F., Babanin, A., Banner, M., Belibassakis, K., Benoit, M., Donelan, M., Groeneweg, J., Herbers, T.H.C., and Hwang, P.A.E.M. (2007). Wave modelling-the state of the art. *Prog. Oceanogr.,* 75(4), 603-674. doi:10.1016/j.pocean.2007.05.005

Cavaleri, L., Fox-Kemper, B., and Hemer, M. (2012). Wind waves in the coupled climate system. *Bull. Am. Meteor. Soc.,* 93(11), 1651-1661. doi:10.1175/BAMS-D-11-00170.1

Chalikov, D. (1995). The parameterization of the wave boundary layer. *J. Phys. Oceanogr.,* 25(6), 1333-1349. doi:10.1175/1520-0485(1995)025<1333:TPOTWB>2.0.CO;2

Chalikov, D. V., and Belevich, M. Y. (1993). One-dimensional theory of the wave boundary layer. *Bound.-Layer Meteor.,* 63(1), 65-96. doi:10.1007/BF00705377

Charnock, H. (1955). Wind stress on a water surface. *Q. J. R. Meteorol. Soc.,* 81(350), 639-640. doi:10.1002/qj.49708135027

Chen, C., Huang, H., Beardsley, R. C., Xu, Q., Limeburner, R., Cowles, G. W., Sun, Y., Qi, J., and Lin, H. (2011). Tidal dynamics in the Gulf of Maine and New England Shelf: An application of FVCOM. *J. Geophys. Res.,* 116, C12010. doi:10.1029/2011JC007054

Chen, G., and Belcher, S.E. (2000). Effects of long waves on wind-generated waves. *J. Phys. Oceanogr.,* 30(9), 2246-2256. doi:10.1175/1520-0485(2000)030<2246:EOLWOW >2.0.CO;2

Chen, X., Hara, T., and Ginis, I. (2020). Impact of Shoaling Ocean Surface Waves on Wind Stress and Drag Coefficient in Coastal Waters: 1. Uniform Wind. *J. Geophys. Res.,* 125(7), e2020JC016222. doi:10.1029/2020JC016222

Chen, W., Banner, M. L., Walsh, E. J., Jensen, J. B., and Lee, S. (2001). The Southern Ocean Waves Experiment. Part II: Sea surface response to wind speed and wind stress variations. *J. Phys. Oceanogr.,* 31(1), 174-198. doi:10.1175/1520-0485(2001)031<0174:TSOWEP>2.0.CO;2

Chen, Y., Chen, L., Zhang, H., and Gong, W. (2019). Effects of wave-current interaction on the Pearl River Estuary during Typhoon Hato. *Estuar. Coast. Shelf Sci.,* 228, 106364. doi:10.1016/j.ecss.2019.106364

Cheng, S., Rogers, W.E., Thomson, J., Smith, M., Doble, M.J., Wadhams, P., Kohout, A.L., Lund, B., Persson, O.P., Collins III, C.O. and Ackley, S.F. (2017). Calibrating a viscoelastic sea ice model for wave propagation in the Arctic fall marginal ice zone. *J. Geophys. Res.,* 122(11), 8770-8793. doi:10.1002/2017JC013275

Cheng, S., Stopa, J., Ardhuin, F., and Shen, H. H. (2020). Spectral attenuation of ocean waves in pack ice and its application in calibrating viscoelastic wave-in-ice models. *The Cryosphere,* 14(6), 2053-2069. doi:10.5194/tc-14-2053-2020

Chi, L., Wolfe, C. L., and Hameed, S. (2018). Intercomparison of the Gulf Stream in ocean reanalyses: 1993-2010. *Ocean Modell.,* 125, 1-21. doi:10.1016/j.ocemod.2018.02.008

Codiga, D.L. (2011). Unified Tidal Analysis and Prediction Using the UTide Matlab Functions. Technical Report 2011-01. Graduate School of Oceanography, University of Rhode Island, Narragansett, RI. 59.

Collins, C. O., and Rogers, W. E. (2017). A Source Term for Wave Attenuation by Sea Ice in WAVEWATCH III: IC4. NRL Report NRL/MR/7320-17-9726, Naval Research Laboratory, Stennis Space Center, MS, 25.

Collins, C. O., Potter, H., Lund, B., Tamura, H., and Graber, H. C. (2018). Directional wave spectra observed during intense tropical cyclones. *J. Geophys. Res.,* 123(2), 773-793. doi:10.1002/2017JC012943

Collins, C. O., Rogers, W. E., and Lund, B. (2017). An investigation into the dispersion of ocean surface waves in sea ice. *Ocean Dyn.,* 67(2), 263-280. doi:10.1007/s10236-016-1021-4

Collins, C. O., Rogers, W. E., Marchenko, A., and Babanin, A. V. (2015). In situ measurements of an energetic wave event in the Arctic marginal ice zone. *Geophy. Res. Lett.,* 42(6), 1863-1870. doi:10.1002/2015GL063063.

Copernicus Climate Change Service (C3S) (2017): ERA5: Fifth generation of ECMWF atmospheric reanalyses of the global climate. Copernicus Climate Change Service Climate Data Store (CDS).

Cummings, J. A., and Smedstad, O. M. (2013). Variational data assimilation for the global ocean. In Data Assimilation for Atmospheric, Oceanic and Hydrologic Applications (Vol. II). Springer, Berlin, Heidelberg.

Dalyander, P. S., Butman, B., Sherwood, C. R., Signell, R. P., and Wilkin, J. L. (2013). Characterizing wave-and current-induced bottom shear stress: US middle Atlantic continental shelf. *Cont. Shelf Res.,* 52, 73-86. doi:10.1016/j.csr.2012.10.012

Davis, C., Wang, W., Chen, S. S., Chen, Y., Corbosiero, K., DeMaria, M., Dudhia, J., Holland, G., Klemp, J., Michalakes, J., Reeves, H., Rotunno, R., Snyder, C., and Xiao, Q. (2008). Prediction of landfalling hurricanes with the advanced hurricane WRF model. *Mon. Wea. Rev.,* 136(6), 1990-2005. doi:10.1175/2007MWR2085.1

Dietrich, J. C., Zijlema, M., Westerink, J. J., Holthuijsen, L. H., Dawson, C., Luettich Jr, R. A., Jensen, R.E., Smith, J.M., Stelling, G.S. and Stone, G. W. (2011). Modeling hurricane waves and storm surge using integrally-coupled, scalable computations. *Coast. Eng.*, 58(1), 45-65. doi: 10.1016/j.coastaleng.2010.08.001

Doble, M. J., De Carolis, G., Meylan, M. H., Bidlot, J. R., and Wadhams, P. (2015). Relating wave attenuation to pancake ice thickness, using field measurements and model results. *Geophy. Res. Lett.,* 42(11), 4473-4481. doi:10.1002/2015GL063628

Dobson, F. W., Smith, S. D., and Anderson, R. J. (1994). Measuring the relationship between wind stress and sea state in the open ocean in the presence of swell. *Atmos.-Ocean,* 32(1), 237-256. doi:10.1080/07055900.1994.9649497

Donelan M. A. (1990). Air-sea interaction. The Sea, B. LeMehaute and D. M. Hanes, Eds. *Ocean Engineering Science*, John Wiley and Sons, 9, 239-292.

Donelan, M. A., Curcic, M., Chen, 1. S., and Magnusson, A. K. (2012). Modeling waves and wind stress. *J. Geophys. Res.,* 117(C11). doi: 10.1029/2011JC007787

Donelan, M. A., Drennan, W. M., and Katsaros, K. B. (1997). The air-sea momentum flux in conditions of wind sea and swell. *J. Phys. Oceanogr.,* 27(10), 2087-2099. doi:10.1175 /1520-0485(1997)027<2087:TASMFI>2.0.CO;2

Donelan, M. A., Haus, B. K., Reul, N., Plant, W. J., Stiassnie, M., Graber, H. C., Brown, O.B., and Saltzman, E. S. (2004). On the limiting aerodynamic roughness of the ocean in very strong winds. *Geophys. Res. Lett.,* 31, L18306. doi:10.1029/2004GL019460

Drennan, W. M. (2006). On parameterisations of air-sea fluxes. *Atmosphere-Ocean Interactions,* 2, 1-34.

Drennan, W. M., Graber, H. C., Hauser, D., and Quentin, C. (2003). On the wave age dependence of wind stress over pure wind seas. *J. Geophys. Res.,* 108(C3), 8062. doi:10.1029/2000JC000715

Drennan, W. M., Kahma, K. K., and Donelan, M. A. (1999). On momentum flux and velocity spectra over waves. *Bound.-Layer Meteor.,*92, 489-515. doi:10.1023/A: 1002054820455

Drennan, W. M., Taylor, P. K., and Yelland, M. J. (2005). Parameterizing the sea surface roughness. *J. Phys. Oceanogr.,* 35(5), 835-848. doi:10.1175/JPO2704.1

Dumont, D., Kohout, A., and Bertino, L. (2011). A wave-based model for the marginal ice zone including a floe breaking parameterization. *J. Geophys. Res.,* 116 (C4), C04001. doi:10.1029/2010JC006682

Edson, J. B., Jampana, V., Weller, R.A., Bigorre, S. P., Plueddemann, A. J., Fairall, C.W., Miller, S.D., Mahrt, L., Vickers, D., and Hersbach, H. (2013). On the exchange of momentum over the open ocean. *J. Phys. Oceanogr.,* 43(8), 1589-1610. doi: 10.1175/JPO-D-12-0173.1

Edson, J., Crawford, T., Crescenti, J., Farrar, T., Frew, N., Gerbi, G., Helmis, C., Hristov, T., Khelif, D., Jessup, A., and Jonsson, H. (2007). The coupled boundary layers and air-sea transfer experiment in low winds. *Bull. Amer. Meteor. Soc.,* 88(3), 341-356. doi: 10.1175/BAMS-88-3-341

Egbert, G. D., and S. Y. Erofeeva (2002). Efficient inverse modelling of barotropic ocean tides. *J. Atmos. Oceanic Technol.*, 19(2), 183-204. doi:10.1175/1520-0426(2002)019<0183:EIMOBO>2.0.CO;2

Eldeberky, Y. (1996). Nonlinear transformation of wave spectra in the nearshore zone (Ph.D. thesis). Delft University of Technology, Department of Civil Engineering, The Netherlands.

Emerson, S., and Bushinsky, S. (2016). The role of bubbles during air-sea gas exchange. *J. Geophys. Res.,* 121(6), 4360-4376. doi:10.1002/2016JC011744

Fairall, C. W., Bradley, E. F., Hare, J. E., Grachev, A. A., and Edson, J. B. (2003). Bulk parameterization of air-sea fluxes: Updates and verification for the COARE algorithm. *J. Clim.*, 16(4), 571-591. doi:10.1175/1520-0442(2003)016<0571:BPOASF>2.0.CO;2

Fan, Y., Ginis, I., Hara, T., Wright, C. W., and Walsh, E. J. (2009). Numerical simulations and observations of surface wave fields under an extreme tropical cyclone. *J. Phys. Oceanogr.*, 39(9), 2097-2116. doi:10.1175/2009JPO4224.1

Feddersen, F., and Trowbridge, J. H. (2005). The effect of wave breaking on surf-zone turbulence and alongshore currents: A modeling study. *J. Phys. Oceanogr.,* 35(11), 2187-2203. doi:10.1175/JPO2800.1

Fernandez, E., and Lellouche, J. M. (2018). Product User Manual for the Global Ocean Physical Reanalysis product GLOBAL_REANALYSIS_PHY_001_030. Report CMEMS-GLO-PUM, (001-030), 15.

Fox, C., and Squire, V. A. (1994). On the oblique reflexion and transmission of ocean waves at shore fast sea ice. *Phil. Trans. Roy. Soc. London. Series A: Phys. Eng. Sci.,*347 (1682), 185-218. doi:10.1098/rsta.1994.0044

French, J. R., Drennan, W. M., Zhang, J. A., and Black, P. G. (2007). Turbulent fluxes in the hurricane boundary layer. Part I: Momentum flux. *J. Atmos. Sci.,* 64(4), 1089-1102. doi:10.1175/JAS3887.1

Galley, R.J., Babb, D., Ogi, M., Else, B.G.T., Geilfus, N.X., Crabeck, O., Barber, D.G. and Rysgaard, S. (2016). Replacement of multiyear sea ice and changes in the open water season duration in the Beaufort Sea since 2004. *J. Geophys. Res.,* 121(3), 1806-1823. doi:10.1002/2015JC011583

Gao, Z., Wang, Q., and Wang, S. (2006). An alternative approach to sea surface aerodynamic roughness. *J. Geophys. Res.,* 111, D22108. doi:10.1029/2006JD007323

García-Nava, H., Ocampo-Torres, F. J., Osuna, P., and Donelan, M. A. (2009). Wind stress in the presence of swell under moderate to strong wind conditions. *J. Geophys. Res.,* 114, C12008. doi:10.1029/2009JC005389

Garratt, J. R. (1977), Review of drag coefficients over oceans and continents. *Mon. Wea. Rev.,* 105(7), 915-929. doi:10.1175/1520-0493(1977)105<0915:RODCOO>2.0.CO;2

Gavrikov, A. V., Krinitsky, M. A., and Grigorieva, V. G. (2016). Modification of Globwave satellite altimetry database for sea wave field diagnostics. *Oceanology,* 56 (2), 301-306. doi:10.1134/S0001437016020065

Geernaert, G. L., Davidson, K. L., Larsen, S. E., and Mikkelsen, T. (1988). Wind stress measurements during the tower ocean wave and radar dependence experiment. *J. Geophys. Res.,* 93(C11), 13913-13923. doi:10.1029/JC093iC11p13913

Geernaert, G. L., Larsen, S. E., and Hansen, F. (1987). Measurements of the wind stress, heat flux, and turbulence intensity during storm conditions over the North Sea. *J. Geophys. Res.,* 92(C12), 13127-13139. doi:10.1029/JC092iC12p13127

Gemmrich, J., and Garrett, C. (2012). The signature of inertial and tidal currents in offshore wave records. *J. Phys. Oceanogr.,* 42(6), 1051-1056. https://doi.org/ 10.1175/JPO-D-12-043.1

GlobWave/DD/PUG (2013). GlobWave Product User Guide. SatOC, Ifremer, NOC, CLS, Report No.: 21891/08/I-EC.

Goda, Y. (2010). Reanalysis of regular and random breaking wave statistics. *Coast. Eng. J.,* 52(1), 71-106. doi:10.1142/S0578563410002129

Gong, W., Lin, Z., Chen, Y., Chen, Z., Shen, J., and Zhang, H. (2018). Effect of waves on the dispersal of the Pearl River plume in winter. *J. Mar. Syst.,* 186, 47-67. doi:10.1016 /j.jmarsys.2018.05.003

Guérin, T., Bertin, X., Coulombier, T., and de Bakker, A. (2018). Impacts of wave-induced circulation in the surf zone on wave setup. *Ocean Modell.,* 123, 86-97. doi:10.1016/j.ocemod.2018.01.006

Guo, L., and Sheng, J. (2015). Statistical estimation of extreme ocean waves over the eastern Canadian shelf from 30-year numerical wave simulation. *Ocean Dyn.,* 65(11), 1489-1507. doi:10.1007/s10236-015-0878-y

Guo, L., and Sheng, J. (2017). Impacts of climate changes on ocean surface gravity waves over the eastern Canadian shelf. *Ocean Dyn.,* 67(5), 621-637. doi:10.1007/s10236-017-1046-3

Haidvogel, D. B., Arango, H. G., Hedstrom, K., Beckmann, A., Malanotte-Rizzoli, P., & Shchepetkin, A. F. (2000). Model evaluation experiments in the North Atlantic Basin: simulations in nonlinear terrain-following coordinates. *Dynamics of atmospheres and oceans,* 32(3-4), 239-281. doi:10.1016/S0377-0265(00)00049-X

Hasselmann, K., Barnett, T.P., Bouws, E., Carlson, H., Cartwright, D.E., Enke, K., Ewing, J.A., Gienapp, H., Hasselmann, D.E., Kruseman, P. and Meerburg, A. (1973). Measurements of wind-wave growth and swell decay during the Joint North Sea Wave Project (JONSWAP). Deutches Hydrographisches Institut, A8, 1-95.

Hasselmann, S., Hasselmann, K., Allender, J. H., and Barnett, T. P. (1985). Computations and parameterizations of the non-linear energy transfer in a gravity-wave spectrum. Part II: Parameterizations of the non-linear energy transfer for application in wave models. *J. Phys. Oceanogr.*, 15(11), 1378-1391. doi:10.1175/1520-0485(1985)015<1369:CAPOTN>2.0.CO;2

Hauser, D., Branger, H., Bouffies-Cloché, S., Despiau, S., Drennan, W. M., Dupuis, H., Durand, P., Durrieu de Madron, X., Estournel, C., Eymard, L., and Flamant, C. (2003). The FETCH experiment: An overview. *J. Geophys. Res.,* 108(C3), 8053. doi:10.1029/2001JC001202

Hebert, D.A., Allard, R.A., Metzger, E.J., Posey, P.G., Preller, R.H., Wallcraft, A.J., Phelps, M.W. and Smedstad, O.M. (2015). Short-term sea ice forecasting: An assessment of ice concentration and ice drift forecasts using the US Navy's Arctic Cap Nowcast/Forecast System. *J. Geophys. Res.*, 120(12), 8327-8345. doi:10.1002/2015JC011283

Hegermiller, C. A., Warner, J. C., Olabarrieta, M., and Sherwood, C. R. (2019). Wave-

Current Interaction between Hurricane Matthew Wave Fields and the Gulf Stream. *J. Phys. Oceanogr.*, 49(11), 2883-2900. doi:10.1175/JPO-D-19-0124.1

Högström, U., Sahlée, E., Smedman, A. S., Rutgersson, A., Nilsson, E., Kahma, K. K., and Drennan, W. M. (2015). Surface stress over the ocean in swell-dominated conditions during moderate winds. *J. Atmos. Sci.,* 72(12), 4777-4795. doi:10.1175/JAS-D-15-0139.1

Holland, G. J. (1980). An analytic model of the wind and pressure profiles in hurricanes. *Mon. Wea. Rev.,* 108(8), 1212-1218. doi:10.1175/1520-0493(1980)108<1212:AAMOTW>2.0.CO;2

Holthuijsen, L. H. (2010). Waves in oceanic and coastal waters. Cambridge university press.

Holthuijsen, L. H., and Tolman, H. L. (1991). Effects of the Gulf Stream on ocean waves. *J. Geophys. Res.,* 96(C7), 12755-12771. doi:10.1029/91JC00901

Holthuijsen, L. H., M. D. Powell, and J. D. Pietrzak (2012). Wind and waves in extreme hurricanes. *J. Geophys. Res.,* 117, C09003. doi:10.1029/2012JC007983

Hsu, S. A. (1974). A dynamic roughness equation and its application to wind stress determination at the air-sea interface. *J. Phys. Oceanogr.*, 4(1), 116-120. doi:10.1175/1520-0485(1974)004<0116:ADREAI>2.0.CO;2

Hu, K., Chen, Q., and Kimball, S. K. (2012). Consistency in hurricane surface wind forecasting: an improved parametric model. *Nat. Hazards,* 61(3), 1029-1050. doi:10.1007/s11069-011-9960-z

Huang, Y., Weisberg, R. H., and Zheng, L. (2010). Coupling of surge and waves for an Ivan-like hurricane impacting the Tampa Bay, Florida region. *J. Geophys. Res.*, 115, C12009. doi:10.1029/2009JC006090.

Hwang, P. A. (2011). A note on the ocean surface roughness spectrum. *J. Atmos. Ocean. Tech.,* 28(3), 436-443. doi:10.1175/2010JTECHO812.1

Jafari, A., Cartwright, N. (2012). Evaluation of a parametric-type wave transformation model against field and laboratory data. *Proc. 33rd Int. Conf. Coast. Eng.,* 569-587. doi:10.9753/icce.v33.waves.51

Janssen, J. A. M. (1997). Does wind stress depend on sea-state or not? - A statistical error analysis of HEXMAX data. *Bound.-Layer Meteor.,* 83(3), 479-503. doi: 10.1023/A: 1000336814021

Janssen, P.A. (1989). Wave-induced stress and the drag of air flow over sea waves. *J. Phys. Oceanogr.*, 19(6), 745-754. doi: 10.1175/1520-0485(1989)019<0745:WISATD>2.0. CO;2

Janssen, P.A. (1991). Quasi-linear theory of wind-wave generation applied to wave forecasting. *J. Phys. Oceanogr.,* 21(11), 1631-1642. doi:10.1175/1520-0485(1991)021 <1631:QLTOWW>2.0.CO;2

Janssen, P.A. (2004). The interaction of ocean waves and wind. Cambridge University Press.

Jarosz, E., Mitchell, D. A., Wang, D. W., and Teague, W. J. (2007). Bottom-up determination of air-sea momentum exchange under a major tropical cyclone. *Science,* 315(5819), 1707-1709. doi:10.1126/science.1136466

Jensen, M.S. (2004). Breaking of waves over a steep bottom slope (Ph.D. thesis). Hydraulics and Coastal Engineering Laboratory, Department of Civil Engineering, Aalborg University, Denmark.

Jiang, Q., Sullivan, P., Wang, S., Doyle, J., and Vincent, L. (2016). Impact of swell on air-sea momentum flux and marine boundary layer under low-wind conditions. *J. Atmos. Sci.,* 73(7), 2683-2697. doi:10.1175/JAS-D-15-0200.1

Johnson, H. K., Højstrup, J., Vested, H. J., and Larsen, S. E. (1998). On the dependence of sea surface roughness on wind waves. *J. Phys. Oceanogr.,* 28(9), 1702-1716. doi: 10.1175/1520-0485(1998)028<1702:OTDOSS>2.0.CO;2

Kalantzi, G. D., Gommenginger, C., and Srokosz, M. (2009). Assessing the performance of the dissipation parameterizations in WAVEWATCH III using collocated altimetry data. *J. Phys. Oceanogr.,* 39(11), 2800-2819. doi:10.1175/2009JPO4182.1

Katsardi, V. (2007). Surface water waves in intermediate and shallow water depths (Ph.D. thesis). Imperial College, London.

Keller, J. B. (1998). Gravity waves on ice-covered water. *J. Geophys. Res.,* 103(C4), 7663-7669. doi:10.1029/97JC02966

Kim, S. Y., Yasuda, T., and Mase, H. (2010). Wave set-up in the storm surge along open coasts during Typhoon Anita. *Coast. Eng.,* 57(7), 631-642. doi:j.coastaleng.2010.02.004

Kirby, J. T., and Chen, T. M. (1989). Surface waves on vertically sheared flows: approximate dispersion relations. *J. Geophys. Res.*, 94(C1), 1013-1027. doi:10.1029/JC094iC01p01013.

Kohout, A. L., Williams, M. J. M., Dean, S. M., and Meylan, M. H. (2014). Storm-induced sea-ice breakup and the implications for ice extent. *Nat.,* 509(7502), 604-607. doi:10.1038/nature13262

Kohout, A. L., Williams, M. J. M., Toyota, T., Lieser, J., and Hutchings, J. (2016). In situ observations of wave-induced sea ice breakup. *Deep Sea Res. Part II: Topical Stud. Oceanogr.,* 131, 22-27. doi:10.1016/j.dsr2.2015.06.010

Komen, G. J., Cavaleri, L., Donelan, M., Hasselmann, K., Hasselmann, S., and Janssen, P. A. E. M. (1996). Dynamics and modelling of ocean waves. Cambridge university press.

Komen, G. J., Hasselmann, K., Hasselmann, K. (1984). On the existence of a fully developed wind-sea spectrum. *J. Phys. Oceanogr.,* 14(8), 1271-1285. doi:10.1175/1520-0485(1984)014<1271:OTEOAF>2.0.CO;2

Kudryavtseva, N. A., and Soomere, T. (2016). Validation of the multi-mission altimeter wave height data for the Baltic Sea region. *Estonian J. Earth Sci.,* 65(3), 161-175. doi:10.3176/earth.2016.13

Kumar, N., Voulgaris, G., and Warner, J. C. (2011). Implementation and modification of a three-dimensional radiation stress formulation for surf zone and rip-current applications. *Coast. Eng.,* 58(12), 1097-1117. doi:10.1016/j.coastaleng.2011.06.009

Kumar, N., Voulgaris, G., Warner, J. C., and Olabarrieta, M. (2012). Implementation of the vortex force formalism in the coupled ocean-atmosphere-wave-sediment transport (COAWST) modeling system for inner shelf and surf zone applications. *Ocean Modell.,* 47, 65-95. doi:10.1016/j.ocemod.2012.01.003

Large, W. G., and Pond, S. (1981). Open ocean momentum flux measurements in moderate to strong winds. *J. Phys. Oceanogr.,* 11(3), 324-336. doi:10.1175/1520-0485(1981)011<0324:OOMFMI>2.0.CO;2

Le Roux, J. P. (2007). A simple method to determine breaker height and depth for different deepwater wave height/length ratios and sea floor slopes. *Coast. Eng.,* 54(3), 271-277. doi:10.1016/j.coastaleng.2006.10.001

Li, J., Kohout, A. L., and Shen, H. H. (2015). Comparison of wave propagation through ice covers in calm and storm conditions. *Geophys. Res. Lett.,* 42(14), 5935-5941. doi:10.1002/2015GL064715

Li, J., Kohout, A. L., Doble, M. J., Wadhams, P., Guan, C., and Shen, H. H. (2017). Rollover of apparent wave attenuation in ice covered seas. *J. Geophys. Res.,* 122(11), 8557-8566. doi: 10.1002/2017JC012978

Li, J., Ma, Y., Liu, Q., Zhang, W., and Guan, C. (2019). Growth of wave height with retreating ice cover in the Arctic. *Cold Reg. Sci. Tech.,* 164, 102790. doi:10.1016 /j.coldregions.2019.102790

Li, Q. L., Cheng, X. L., and Zeng, Q. C. (2016). Gustiness and coherent structure under weak wind period in atmospheric boundary layer. *Atmospheric and Oceanic Science Letters,* 9(1), 52-59. doi:10.1080/16742834.2015.1086176

Lin, S., and Sheng, J. (2017). Assessing the performance of wave breaking parameterizations in shallow waters in spectral wave models. *Ocean Modell.,* 120, 41-59. doi:10.1016/j.ocemod.2017.10.009

Lin, S., and Sheng, J. (2020). Revisiting dependences of the drag coefficient at the sea surface on wind speed and sea state. *Cont. Shelf Res.,* 207, 104188. doi:10.1016/j.csr. 2020.104188

Lin, S., Sheng, J., and Xing, J. (2020). Performance evaluation of parameterizations for wind input and wave dissipation in the spectral wave model for the northwest Atlantic ocean. *Atmos.-Ocean,* 58 (4), 258-286. doi:10.1080/07055900.2020.1790336

Liu, A. K., and Mollo-Christensen, E. (1988). Wave propagation in a solid ice pack. *J. Phys. Oceanogr.,* 18(11), 1702-1712. doi:10.1175/1520-0485(1988)018<1702:WPIASI >2.0.CO;2

Liu, D., Tsarau, A., Guan, C., and Shen, H. H. (2020a). Comparison of ice and wind-wave modules in WAVEWATCH III in the Barents Sea. *Cold Reg. Sci. Techn.,* 172, 103008. doi:10.1016/j.coldregions.2020.103008

Liu, Q., Babanin, A. V., Zieger, S., Young, I. R., and Guan, C. (2016). Wind and wave climate in the Arctic Ocean as observed by altimeters. *J. Climate,* 29(22), 7957-7975. doi:10.1175/JCLI-D-16-0219.1

Liu, Q., Babanin, A., Fan, Y., Zieger, S., Guan, C., and Moon, I. J. (2017). Numerical simulations of ocean surface waves under hurricane conditions: Assessment of existing model performance. *Ocean Modell.,* 118, 73-93. doi: 10.1016/j.ocemod.2017.08.005

Liu, Q., Rogers, W. E., Babanin, A., Li, J., and Guan, C. (2020b). Spectral Modeling of Ice-Induced Wave Decay. *J. Phys. Oceanogr.,* 50(6), 1583-1604. doi:10.1175/JPO-D-19-0187.1

Liu, W. C., and Huang, W. C. (2020). Investigating typhoon-induced storm surge and waves in the coast of Taiwan using an integrally-coupled tide-surge-wave model. *Ocean Eng.,* 212, 107571. doi:10.1016/j.oceaneng.2020.107571

Longuet-Higgins, M. S., and Stewart, R. W. (1962). Radiation stress and mass transport in gravity waves, with application to 'surf beats'. *J. Fluid Mech.,* 13(4), 481-504.

Maat, N., Kraan, C., and Oost, W. A. (1991). The roughness of wind waves. *Bound.-Layer Meteor.,* 54(1), 89-103. doi:10.1007/BF00119414

Madsen, O. S. (1994). Spectral wave-current bottom boundary layer flows. *Proc. 24th Int. Conf. Coast. Eng.,* 384-398. doi:10.1061/9780784400890.030

Madsen, O.S., Poon, Y.K., Graber, H.C. (1988). Spectral wave attenuation by bottom friction: theory. *Proc. 21th Int. Conf. Coast. Eng.,* 492-504. doi:10.1061/9780872626874. 035

Mai, S., Ohle, N., Zimmermann, C. (1999). Applicability of wave models in shallow coastal waters. In Proc. of the 5th Int. Conf. on Coastal and Port Engineering in Developing Countries (COPEDEC), Cape Town, South Africa.

Mao, M., and Xia, M. (2018). Wave-current dynamics and interactions near the two inlets of a shallow lagoon-inlet-coastal ocean system under hurricane conditions. *Ocean Modell.,* 129, 124-144. doi:10.1016/j.ocemod.2018.08.002

Marchesiello, P., McWilliams, J. C., and Shchepetkin, A. (2001). Open boundary conditions for long-term integration of regional oceanic models. *Ocean Modell.,* 3(1-2), 1-20. doi:10.1016/S1463-5003(00)00013-5

Mason, E., Molemaker, J., Shchepetkin, A. F., Colas, F., McWilliams, J. C., and Sangrà, P. (2010). Procedures for offline grid nesting in regional ocean models. *Ocean Modell.,* 35(1-2), 1-15. doi:10.1016/j.ocemod.2010.05.007

McWilliams, J., J. Restrepo, and E. Lane (2004). An asymptotic theory for the interaction of waves and currents in coastal waters. *J. Fluid Mech.,* 511, 135-178. doi:10.1017/S0022112004009358

Meier, W. N., Fetterer, F., Stewart, J. S., and Helfrich, S. (2015). How do sea-ice concentrations from operational data compare with passive microwave estimates? Implications for improved model evaluations and forecasting. *Annals of Glaciology,* 56(69), 332-340. doi:10.3189/2015AoG69A694

Meier, W. N., Peng, G., Scott, D. J., and Savoie, M. H. (2014). Verification of a new NOAA/NSIDC passive microwave sea-ice concentration climate record. *Polar Res.,* 33(1), 21004. doi:10.3402/polar.v33.21004

Mellor, G. (2003). The three-dimensional current and surface wave equations. *J. Phys. Oceanogr.,* 33:1978-1989. doi:10.1175/1520-0485(2003)033<1978:TTCASW>2.0.CO;2

Mellor, G. (2008). The depth-dependent current and wave interaction equations: A Revision. *J. Phys. Oceanogr.*, 38(11), 2587-2596. doi:10.1175/2008JPO3971.1

Mellor, G. (2015). A combined derivation of the integrated and vertically resolved, coupled wave-current equations. *J. Phys. Oceanogr.*, 45(6), 1453-1463. doi:10.1175/JPO-D-14-0112.1

Mentaschi, L., Besio, G., Cassola, F. and Mazzino, A. (2013). Problems in RMSE-based wave model validations. *Ocean Modell.,* 72, 53-58. doi:10.1016/j.ocemod.2013.08.003

Metzger, E. J., Helber, R., Hogan, P. J., Posey, P. G., Thoppil, P. G., Townsend, T. L., Wallcraft, A.J., Smedstad, O.M., Franklin, D.S., Zamudo-Lopez, L., and Phelps, M. W. (2017). Global ocean forecast system 3.1 validation testing. Tech. rep (Report NRL/MR/7320-17-9722).

Meylan, M. H., and Masson, D. (2006). A linear Boltzmann equation to model wave scattering in the marginal ice zone. *Ocean Modell.,* 11(3-4), 417-427. doi:10.1016/j.ocemod.2004.12.008

Meylan, M. H., Bennetts, L. G., and Kohout, A. L. (2014). In situ measurements and analysis of ocean waves in the Antarctic marginal ice zone. *Geophys. Res. Lett.,* 41(14), 5046-5051. doi:10.1002/2014GL060809

Meylan, M. H., Bennetts, L. G., Mosig, J. E. M., Rogers, W. E., Doble, M. J., and Peter, M. A. (2018). Dispersion relations, power laws, and energy loss for waves in the marginal ice zone. *J. Geophys. Res.,* 123(5), 3322-3335. doi:10.1002/2018JC013776

Miles, J. W. (1957). On the generation of surface waves by shear flows. *J. Fluid Mech.,* 3(2), 185-204.

Mitsuta Y., and Tsukamoto O. (1978). Drag coefficients in light wind. *Bulletin of the Disaster Prevention Research Institute,* 28(2), 25-32.

Moghimi, S., Klingbeil, K., Gräwe, U., and Burchard, H. (2013). A direct comparison of a depth-dependent radiation stress formulation and a vortex force formulation within a three-dimensional coastal ocean model. *Ocean Modell.,* 70, 132-144. doi:10.1016/j.ocemod.2012.10.002

Monbaliu, J. (1994). On the use of the Donelan wave spectral parameter as a measure for the roughness of wind waves. *Bound.-Layer Meteor.,* 67(3), 277-291. doi: 10.1007/BF00713145

Monin, A. S., and Obukhov, A. M. F. (1954). Basic laws of turbulent mixing in the surface layer of the atmosphere. *Tr. Akad. Nauk SSSR Geophiz. Inst.,* 24(151), 163-187.

Moon, I. J., Ginis, I., and Hara, T. (2004). Effect of surface waves on air-sea momentum exchange. Part II: Behavior of drag coefficient under tropical cyclones. *J. Atmos. Sci.,* 61(19), 2334-2348. doi:10.1175/1520-0469(2004)061<2334:EOSWOA>2.0.CO;2

Mosig, J. E., Montiel, F., and Squire, V. A. (2015). Comparison of viscoelastic-type models for ocean wave attenuation in ice-covered seas. *J. Geophys. Res.,* 120(9), 6072-6090. doi:10.1002/2015JC010881

Nelson, R.C. (1987). Design wave heights on very mild slopes - an experimental study. *Transactions of the Institution of Engineers, Australia. Civil Eng.,* 29(3), 157-161.

Newyear, K., and Martin, S. (1997). A comparison of theory and laboratory measurements of wave propagation and attenuation in grease ice. *J. Geophys. Res.,* 102(C11), 25091-25099. doi:10.1029/97JC02091

Niu, Q., and Xia, M. (2017). The role of wave-current interaction in Lake Erie's seasonal and episodic dynamics. *J. Geophys. Res.,* 122(9), 7291-7311. doi:10.1002/2017JC012934

Ohashi, K., and Sheng, J. (2013). Influence of St. Lawrence River discharge on the circulation and hydrography in Canadian Atlantic waters. *Cont. Shelf Res.,* 58, 32-49. doi:10.1016/j.csr.2013.03.005

Olabarrieta, M., Warner, J. C., and Kumar, N. (2011). Wave-current interaction in Willapa Bay. *J. Geophys. Res.,* 116, C12014. doi:10.1029/2011JC007387

Olabarrieta, M., Warner, J. C., Armstrong, B., Zambon, J. B., and He, R. (2012). Ocean-atmosphere dynamics during Hurricane Ida and Nor'Ida: An application of the coupled ocean-atmosphere-wave-sediment transport (COAWST) modeling system. *Ocean Modell.,* 43, 112-137. doi:10.1016/j.ocemod.2011.12.008

Oost, W. A., Komen, G. J., Jacobs, C. M. J., and Van Oort, C. (2002). New evidence for a relation between wind stress and wave age from measurements during ASGAMAGE. *Bound.-Layer Meteor.,*103, 409-438. doi:10.1023/A:1014913624535

Pan, Y., Sha, W., Zhu, S., and Ge, S. (2008). A new parameterization scheme for sea surface aerodynamic roughness. *Prog. Nat. Sci.,* 18(11), 1365-1373. doi:10.1016/j.pnsc.2008.05.006

Parekh, A., Gnanaseelan, C., and Jayakumar, A. (2011). Impact of improved momentum transfer coefficients on the dynamics and thermodynamics of the north Indian Ocean. *J. Geophys. Res.,* 116, C01004. doi:10.1029/2010JC006346

Pasch, R. J., and Kimberlain, T. B. (2011). Tropical cyclone report: Hurricane Igor (AL112010), 8-21 September 2010. Miami, FL: National Hurricane Center.

Perrie, W., and Hu, Y. (1996). Air-ice-ocean momentum exchange. Part 1: Energy transfer between waves and ice floes. *J. Phys. Oceanogr.,* 26(9), 1705-1720. doi:10.1175/1520-0485(1996)026<1705:AMEPTB>2.0.CO;2

Perrie, W., Tang, C. L., Hu, Y., and DeTracy, B. M. (2003). The impact of waves on surface currents. *J. Phys. Oceanogr.,* 33(10), 2126-2140. doi:10.1175/1520-0485(2003)033<2126:TIOWOS>2.0.CO;2

Perrie, W., Toulany, B., Resio, D. T., Roland, A., and Auclair, J. P. (2013). A two-scale approximation for wave-wave interactions in an operational wave model. *Ocean Modell.,* 70, 38-51. doi:10.1016/j.ocemod.2013.06.008

Perrie, W., Toulany, B., Roland, A., Dutour-Sikiric, M., Chen, C., Beardsley, R.C., Qi, J., Hu, Y., Casey, M.P., and Shen, H. (2018). Modelling North Atlantic Nor'easters with modern wave forecast models. *J. Geophys. Res.,* 123(1), 533-557. doi:10.1002/2017JC012868

Phillips, O. M. (1984). On the response of short ocean wave components at a fixed wavenumber to ocean current variations. *J. Phys. Oceanogr.,* 14(9), 1425-1433. doi:10.1175/1520-0485(1984)014<1425:OTROSO>2.0.CO;2

Phillips, O. M. (1985). Spectral and statistical properties of the equilibrium range in wind-generated gravity waves. *J. Fluid Mech.,* 156, 505-531.

Pizzo, N. E., Deike, L., and Melville, W. K. (2016). Current generation by deep-water breaking waves. *J. Flu. Mech.,* 803, 275-291. doi:10.1017/jfm.2016.469

Polnikov, V. G., and Lavrenov, I. V. (2007). Calculation of the nonlinear energy transfer through the wave spectrum at the sea surface covered with broken ice. *Oceanology,* 47(3), 334-343. doi:10.1134/S0001437007030058

Potter, H. (2015), Swell and the drag coefficient. *Ocean Dyn.,* 65(3), 375-384. doi:10.1007/s10236-015-0811-4

Potter, H., Graber, H. C., Williams, N. J., Collins III, C. O., Ramos, R. J., and Drennan, W. M. (2015). In situ measurements of momentum fluxes in typhoons. *J. Atmos. Sci.,* 72(1), 104-118. doi:10.1175/JAS-D-14-0025.1

Powell, M. D., Houston, S. H., Amat, L. R., and Morisseau-Leroy, N. (1998). The HRD real-time hurricane wind analysis system. *J. Wind Eng. Ind. Aerod.,* 77, 53-64. doi:10.1016/S0167-6105(98)00131-7

Powell, M. D., Vickery, P. J., and Reinhold, T. A. (2003). Reduced drag coefficient for high wind speeds in tropical cyclones. *Nat.,* 422, 279-283. doi:10.1038/nature01481

Prakash, K. R., and Pant, V. (2020). On the wave-current interaction during the passage of a tropical cyclone in the Bay of Bengal. *Deep Sea Research Part II: Topical Studies in Oceanography,* 172, 104658. doi:10.1016/j.dsr2.2019.104658

Rapizo, H., Waseda, T., Babanin, A. V., and Toffoli, A. (2016). Laboratory experiments on the effects of a variable current field on the spectral geometry of water waves. *J. Phys. Oceanogr.,* 46, 2695-2717. doi:10.1175/JPO-D-16-0011.1

Rascle, N., and Ardhuin, F. (2013). A global wave parameter database for geophysical applications. Part 2: Model validation with improved source term parameterization. *Ocean Modell.,* 70, 174-188. doi:10.1016/j.ocemod.2012.12.001

Rattanapitikon, W. (2007). Calibration and modification of energy dissipation models for irregular wave breaking. *Ocean Eng.,* 34(11-12), 1592-1601. doi:10.1016/j.oceaneng. 2006.11.005

Rattanapitikon, W., Shibayama, T. (2000). Verification and modification of breaker height formulas. *Coast. Eng. J.,* 42(04), 389-406. doi: 10.1142/S0578563400000195

Reichl, B. G., Hara, T., and Ginis, I. (2014). Sea state dependence of the wind stress over the ocean under hurricane winds. *J. Geophys. Res.,* 119(1), 30-51. doi:10.1002/2013JC 009289

Reul, N., Grodsky, S.A., Arias, M., Boutin, J., Catany, R., Chapron, B., d'Amico, F., Dinnat, E., Donlon, C., Fore, A. and Fournier, S. (2020). Sea surface salinity estimates from spaceborne L-band radiometers: An overview of the first decade of observation (2010-2019). *Remote Sens. Environ.,* 242, 111769. doi:10.1016/j.rse.2020.111769

Rogers, W. E., Babanin, A. V., and Wang, D. W. (2012). Observation-consistent input and whitecapping dissipation in a model for wind-generated surface waves: Description and simple calculations. *J. Atmos. Ocean. Tech.,* 29, 1329-1346. doi:10.1175/JTECH-D-11-00092.1

Rogers, W. E., Hwang, P. A., and Wang, D. W. (2003). Investigation of wave growth and decay in the SWAN model: three regional-scale applications. *J. Phys. Oceanogr.,* 33(2), 366-389. doi:10.1175/1520-0485(2003)033<0366:IOWGAD>2.0.CO;2

Rogers, W. E., P. Posey, L. Li, and R. A. Allard (2018). Forecasting and hindcasting waves in and near the marginal ice zone: Wave modeling and the ONR "Sea State" field experiment. NRL Memorandum Report NRL/MR/7320-18-9786, Naval Research Laboratory, Stennis Space Center, MS, 179.

Rogers, W. E., Thomson, J., Shen, H. H., Doble, M. J., Wadhams, P., and Cheng, S. (2016). Dissipation of wind waves by pancake and frazil ice in the autumn Beaufort Sea. *J. Geophys. Res.,* 121(11), 7991-8007. doi:10.1002/2016JC012251

Romero, L., and Melville, W. K. (2010). Airborne observations of fetch-limited waves in the Gulf of Tehuantepec. *J. Phys. Oceanogr.,* 40(3), 441-465. doi:10.1175/2009JPO 4127.1

Ruessink, B.G., Michallet, H., Bonneton, P., Mouazé, D., Lara, J., Silva, P.A., Wellens, P. (2013). Globex: wave dynamics on a gently sloping laboraty beach. *Proceedings Coastal Dynamics 2013,* 1351-1362.

Ruessink, B. G., Walstra, D. J. R., and Southgate, H. N. (2003). Calibration and verification of a parametric wave model on barred beaches. *Coast. Eng.,* 48(3), 139-149. doi:10.1016/S0378-3839(03)00023-1

Ruest, B., Neumeier, U., Dumont, D., Bismuth, E., Senneville, S., and Caveen, J. (2016). Recent wave climate and expected future changes in the seasonally ice-infested waters of the Gulf of St. Lawrence, Canada. *Climate Dyn.,* 46(1-2), 449-466. doi:10.1007/s00382-015-2592-3

Saha, S., Moorthi, S., Wu, X., Wang, J., Nadiga, S., Tripp, P., Behringer, D., Hou, Y.T., Chuang, H.Y., Iredell, M., and Ek, M. (2014). The NCEP climate forecast system version 2. *J. Climate,* 27(6), 2185-2208. doi:10.1175/JCLI-D-12-00823.1

Salmon, J. E., Holthuijsen, L. H., Zijlema, M., van Vledder, G. P., and Pietrzak, J. D. (2015). Scaling depth-induced wave-breaking in two-dimensional spectral wave models. *Ocean Modell.,* 87, 30-47. doi:10.1016/j.ocemod.2014.12.011

Seemanth, M., Bhowmick, S. A., Kumar, R., and Sharma, R. (2016). Sensitivity analysis of dissipation parameterizations in a third-generation spectral wave model, WAVEWATCH III for Indian Ocean. *Ocean Eng.,* 124, 252-273. doi:10.1016/j.oceaneng.2016.07.023

Shanas, P. R., Aboobacker, V. M., Albarakati, A. M., and Zubier, K. M. (2017). Climate driven variability of wind-waves in the Red Sea. *Ocean Modell.,* 119, 105-117. doi:10.1016/j.ocemod.2017.10.001

Shen, H., Perrie, W., Hu, Y., and He, Y. (2018). Remote sensing of waves propagating in the marginal ice zone by SAR. *J. Geophys. Res.,* 123(1), 189-200. doi:10.1002/

2017JC013148

Sheng, Y. P., Alymov, V., and Paramygin, V. A. (2010). Simulation of storm surge, wave, currents, and inundation in the Outer Banks and Chesapeake Bay during Hurricane Isabel in 2003: The importance of waves. *J. Geophys. Res.,* 115, C04008. doi:10.1029/ 2009JC005402

Shi, Q., and Bourassa, M. A. (2019). Coupling ocean currents and waves with wind stress over the Gulf Stream. *Remote Sens.,* 11(12), 1476. doi:10.3390/rs11121476

Smedman, A. S., Guo Larsén, X., Högström, U., Kahma, K. K., and Pettersson, H. (2003). Effect of sea state on the momentum exchange over the sea during neutral conditions. *J. Geophys. Res.*, 108(C11), 3367. doi:10.1029/2002JC001526

Smith, S. D., and Banke, E. G. (1975). Variation of the sea surface drag coefficient with wind speed. *Q. J. R. Meteorol. Soc.,* 101(429), 665-673. doi:10.1002/qj.49710142920

Smith, S. D. (1980). Wind stress and heat flux over the ocean in gale force winds. *J. Phys. Oceanogr.,* 10(5), 709-726. doi:10.1175/1520-0485(1980)010<0709:WSAHFO>2.0. CO;2

Smith, S. D. (1988). Coefficients for sea surface wind stress, heat flux, and wind profiles as a function of wind speed and temperature. *J. Geophys. Res.*, 93(C12), 15467-15472. doi:10.1029/JC093iC12p15467

Smith, S. D., Anderson, R. J., Oost, W. A., Kraan, C., Maat, N., De Cosmo, J., ... and Chadwick, H. M. (1992). Sea surface wind stress and drag coefficients: The HEXOS results. *Bound.-Layer Meteor.,* 60(1), 109-142. doi: 10.1007/BF00122064

Soloviev, A. V., Lukas, R., Donelan, M. A., Haus, B. K., and Ginis, I. (2014). The air-sea interface and surface stress under tropical cyclones. *Scientific Reports,* 4(1), 1-6. doi:10.1038/srep05306

Squire, V. A. (2020). Ocean wave interactions with sea ice: a reappraisal. *Ann. Rev. Fluid Mech.,* 52, 37-60. doi:10.1146/annurev-fluid-010719-060301

Stacey, M.W. (1999). Simulations of the wind-forced near-surface circulation in knight inlet: a parameterization of the roughness length. *J. Phys. Oceanogr.,* 29(6),1363-1367. doi:10.1175/1520-0485(1999)029<1363:SOTWFN>2.0.CO;2

Stive, M. J. F. (1985). A scale comparison of waves breaking on a beach. *Coast. Eng.,* 9(2), 151-158. doi:10.1016/0378-3839(85)90003-1

Stoker, J.J. (1957). Water Waves: The Mathematical Theory with Applications. Interscience Publishers Inc., New York, 567.

Stopa, J. E., Ardhuin, F., and Girard-Ardhuin, F. (2016a). Wave climate in the Arctic 1992-2014: seasonality and trends. *Cryosphere,* 10(4), 1605-1629. doi:10.5194/tc-10-1605-2016

Stopa, J. E., Ardhuin, F., Babanin, A., and Zieger, S. (2016b). Comparison and validation of physical wave parameterizations in spectral wave models. *Ocean Modell.,* 103, 2-17. doi:10.1016/j.ocemod.2015.09.003

Stopa, J. E., Ardhuin, F., Stutzmann, E., and Lecocq, T. (2019). Sea state trends and variability: Consistency between models, altimeters, buoys, and seismic data (1979-2016). *J. Geophys. Res.,* 124(6), 3923-3940. doi:10.1029/2018JC014607

Stroeve, J., Hamilton, L. C., Bitz, C. M., and Blanchard-Wrigglesworth, E. (2014). Predicting September sea ice: Ensemble skill of the SEARCH sea ice outlook 2008-2013. *Geophys. Res. Lett.,* 41(7), 2411-2418. doi:10.1002/2014GL059388

Sun, Y., Chen, C., Beardsley, R. C., Xu, Q., Qi, J., and Lin, H. (2013). Impact of current-wave interaction on storm surge simulation: A case study for Hurricane Bob. *J. Geophys. Res.*, 118(5), 2685-2701. doi:10.1002/jgrc.20207

Sun, Y., Perrie, W., and Toulany, B. (2018). Simulation of Wave-Current Interactions Under Hurricane Conditions Using an Unstructured-Grid Model: Impacts on Ocean Waves. *J. Geophys. Res.*, 123(5), 3739-3760. doi:10.1029/2017JC012939

SWAN Team (2013). http://swanmodel.sourceforge.net/.

Takagaki, N., S. Komori, N. Suzuki, K. Iwano, and R. Kurose (2016). Mechanism of drag coefficient saturation at strong wind speeds, *Geophys. Res. Lett.,* 43(18), 9829-9835. doi:10.1002/2016GL070666

Takagaki, N., S. Komori, N. Suzuki, K. Iwano, T. Kuramoto, S. Shimada, R. Kurose, and K. Takahashi (2012). Strong correlation between the drag coefficient and the shape of the wind sea spectrum over a broad range of wind speeds. *Geophys. Res. Lett.,* 39, L23604. doi: 10.1029/2012GL053988

Taylor, P. K., and Yelland, M. J. (2001). The dependence of sea surface roughness on the height and steepness of the waves. *J. Phys. Oceanogr.,* 31(2), 572-590. doi:10.1175/1520-0485(2001)031<0572:TDOSSR>2.0.CO;2

Terray, E. A., Donelan, M. A., Agrawal, Y. C., Drennan, W. M., Kahma, K. K., Williams, A. J., Hwang, P.A., and Kitaigorodskii, S. A. (1996). Estimates of kinetic energy dissipation under breaking waves. *J. Phys. Oceanogr.,* 26(5), 792-807. doi:10.1175/1520-0485(1996)026<0792:EOKEDU>2.0.CO;2

Thomson, J., Ackley, S., Girard-Ardhuin, F., Ardhuin, F., Babanin, A., Boutin, G., Brozena, J., Cheng, S., Collins, C., Doble, M., and Fairall, C. (2018). Overview of the arctic sea state and boundary layer physics program. *J. Geophys. Res.,* 123(12), 8674-8687. doi:10.1002/2018JC013766

Thomson, J., and Rogers, W. E. (2014). Swell and sea in the emerging Arctic Ocean. *Geophys. Res. Lett.,* 41(9), 3136-3140. doi:10.1002/2014GL059983

Thomson, J., D'Asaro, E. A., Cronin, M. F., Rogers, W. E., Harcourt, R. R., and Shcherbina, A. (2013). Waves and the equilibrium range at Ocean Weather Station P. *J. Geophys. Res.,* 118(11), 5951-5962. doi:10.1002/2013JC008837

Thornton, E. B., and Guza, R. T. (1983). Transformation of wave height distribution. *J. Geophys. Res.,* 88(C10), 5925-5938. doi:10.1029/JC088iC10p05925

Ting, C. H., Babanin, A. V., Chalikov, D., and Hsu, T. W. (2012). Dependence of drag coefficient on the directional spreading of ocean waves. *J. Geophys. Res.,* 117, C00J14. doi:10.1029/2012JC007920

Tivy, A., Howell, S.E., Alt, B., McCourt, S., Chagnon, R., Crocker, G., Carrieres, T., and Yackel, J.J., (2011). Trends and variability in summer sea ice cover in the Canadian Arctic based on the Canadian Ice Service Digital Archive, 1960-2008 and 1968-2008. *J. Geophys. Res.,* 116, C03007. doi:10.1029/2009JC005855

Toledo, Y., Agnon, Y. (2012). Stochastic evolution equations with localized nonlinear shoaling coefficients. *European Journal of Mechanics-B/Fluids,* 34, 13-18. doi:10.1016/j.euromechflu.2012.01.007

Tolman, H. L., and Chalikov, D. (1996). Source terms in a third-generation wind wave model. *J. Phys. Oceanogr.*, 26(11), 2497-2518. doi:10.1175/1520-0485(1996)026<2497:STIATG>2.0.CO;2

Tuomi, L., Kanarik, H., Björkqvist, J.V., Marjamaa, R., Vainio, J., Hordoir, R., Höglund, A., and Kahma, K. K. (2019). Impact of ice data quality and treatment on wave hindcast statistics in seasonally ice-covered seas. *Frontiers in Earth Science,* 7, 166. doi:10.3389 /feart.2019.00166

Uchiyama, Y., McWilliams, J.C., Shchepetkin, A.F. (2010). Wave-current interaction in an oceanic circulation model with a vortex-force formalism: application to the surf zone. *Ocean Modell.*, 34(1-2), 16-35. doi:10.1016/j.ocemod.2010.04.002

Umlauf, L., and Burchard, H. (2003). A generic length-scale equation for geophysical turbulence models. *J. Mar. Res.*, 61(2), 235-265. doi:10.1357/002224003322005087

Urrego-Blanco, J., and Sheng, J. (2012). Interannual variability of the circulation over the eastern Canadian shelf. *Atmos.-Ocean,* 50(3), 277-300. doi:10.1080/07055900.2012. 680430

van der Westhuysen, A. J. (2009). Modelling of depth-induced wave breaking over sloping and horizontal beds. In Proc. 11th International Workshop on Wave Hindcasting and Forecasting, Halifax.

van der Westhuysen, A.J. (2010). Modeling of depth-induced wave breaking under finite depth wave growth conditions. *J. Geophys. Res.,* 115, C01008. doi:10.1029/2009JC00 5433

Vickers, D., and Mahrt, L. (1997). Fetch limited drag coefficients. *Bound.-Layer Meteor.,* 85(1), 53-79. doi:10.1023/A:1000472623187

Vickery, P. J., Wadhera, D., Powell, M. D., and Chen, Y. (2009). A hurricane boundary layer and wind field model for use in engineering applications. *J. Appl. Meteor. Climatol.,* 48(2), 381-405. doi:10.1175/2008JAMC1841.1

Villas Bôas, A.B., Ardhuin, F., Ayet, A., Bourassa, M.A., Brandt, P., Chapron, B., Cornuelle, B.D., Farrar, J.T., Fewings, M.R., Fox-Kemper, B. and Gille, S.T. (2019). Integrated observations of global surface winds, currents, and waves: requirements and challenges for the next decade. *Frontiers in Marine Science,* 6, 425. doi:10.3389/fmars. 2019.00425

Wadhams, P. (1973). Attenuation of swell by sea ice. *J. Geophys. Res.,* 78(18), 3552-3563. doi:10.1029/JC078i018p03552

Wadhams, P., Squire, V. A., Goodman, D. J., Cowan, A. M., and Moore, S. C. (1988). The attenuation rates of ocean waves in the marginal ice zone. *J. Geophys. Res.,* 93(C6), 6799-6818. doi:10.1029/JC093iC06p06799

Wang, D. P., and Oey, L. Y. (2008). Hindcast of waves and currents in Hurricane Katrina. *Bull. Amer. Meteor. Soc.,* 89(4), 487-496. doi:10.1175/BAMS-89-4-487

Wang, L., Perrie, W., Long, Z., Blokhina, M., Zhang, G., Toulany, B., and Zhang, M. (2018). The impact of climate change on the wave climate in the Gulf of St. Lawrence. *Ocean Modell.,* 128, 87-101. doi:10.1016/j.ocemod.2018.06.003

Wang, P., and Sheng, J. (2016). A comparative study of wave-current interactions over the eastern Canadian shelf under severe weather conditions using a coupled wave-circulation model. *J. Geophys. Res.,* 121(7), 5252-5281. doi:10.1002/2016JC011758

Wang, P., and Sheng, J., (2018). Tidal modulation of surface gravity waves in the Gulf of Maine. *J. Phys. Oceanogr.,* 48(10), 2305-2323. doi:10.1175/JPO-D-17-0250.1

Wang, P., Sheng, J., and Hannah, C. (2017). Assessing the performance of formulations for nonlinear feedback of surface gravity waves on ocean currents over coastal waters. *Cont. Shelf Res.,* 146, 102-117. doi:10.1016/j.csr.2017.08.014

Wang, Q., Lu, P., Zu, Y., Li, Z., Leppäranta, M., and Zhang, G. (2019). Comparison of passive microwave data with shipborne photographic observations of summer sea ice concentration along an Arctic cruise path. *Remote Sens.,* 11(17), 2009. doi:10.3390/rs11172009

Wang, R., and Shen, H. H. (2010). Gravity waves propagating into an ice-covered ocean: A viscoelastic model. *J. Geophys. Res.,* 115, C06024. doi:10.1029/2009JC005591

Wang, Y., Holt, B., Erick Rogers, W., Thomson, J., and Shen, H. H. (2016). Wind and wave influences on sea ice floe size and leads in the Beaufort and Chukchi Seas during the summer-fall transition 2014. *J. Geophys. Res.,* 121(2), 1502-1525. doi:10.1002/2015JC011349

Warner, J. C., Armstrong, B., He, R., and Zambon, J. B. (2010). Development of a coupled ocean-atmosphere-wave-sediment transport (COAWST) modeling system. *Ocean Modell.,* 35(3), 230-244. doi:10.1016/j.ocemod.2010.07.010

Warner, J. C., Sherwood, C. R., Arango, H. G., and Signell, R. P. (2005). Performance of four turbulence closure models implemented using a generic length scale method.

Ocean Modell., 8(1-2), 81-113. doi:10.1016/j.ocemod.2003.12.003

Warner, J. C., Sherwood, C. R., Signell, R. P., Harris, C. K., and Arango, H. G. (2008). Development of a three-dimensional, regional, coupled wave, current, and sediment-transport model. *Computers & Geosciences,* 34(10), 1284-1306. doi:10.1016/j.cageo. 2008.02.012

WAVEWATCH III Development Group (WW3DG) (2016). User manual and system documentation of WAVEWATCH III version 5.16. Tech. Note 329, NOAA/NWS/NCEP/MMAB, College Park, MD, USA, 326.

WAVEWATCH III Development Group (WW3DG) (2019). User manual and system documentation of WAVEWATCH III version 6.07. Tech. Note 333, NOAA/NWS/NCEP/ MMAB, College Park, MD, USA, 465.

Weber, J. E. (1987). Wave attenuation and wave drift in the marginal ice zone. *J. Phys. Oceanogr.,* 17(12), 2351-2361. doi:10.1175/1520-0485(1987)017<2351:WAAWDI> 2.0.CO;2

Wei, Z., Miyano, A., and Sugita, M. (2016). Drag and bulk transfer coefficients over water surfaces in light winds. *Bound.-Layer Meteor.,* 160(2), 319-346. doi:10.1007/s10546-016-0147-8

Weitz, M., and Keller, J. B. (1950). Reflection of water waves from floating ice in water of finite depth. *Comm. Pure Appl. Math.,* 3, 305-318. doi:10.1002/cpa.3160030306

Wolf, J., and Prandle, D. (1999). Some observations of wave-current interaction. *Coast. Eng.*, 37(3-4), 471-485. doi:10.1016/S0378-3839(99)00039-3

Wu, J. (1980). Wind-stress coefficients over sea surface near neutral conditions-A revisit. *J. Phys. Oceanogr.,* 10(5), 727-740. doi:10.1175/1520-0485(1980)010<0727:WSCOSS >2.0.CO;2

Wu, J. (1982). Wind-stress coefficients over sea surface from breeze to hurricane. *J. Geophys. Res.,* 87(C12), 9704-9706. doi:10.1029/JC087iC12p09704

Wu, L., Rutgersson, A., and Sahlée, E. (2015). Upper-ocean mixing due to surface gravity waves. *J. Geophys. Res.*, 120(12), 8210-8228. doi:10.1002/2015JC011329

Wu, L., Rutgersson, A., Sahlée, E., and Guo Larsén, X. (2016). Swell impact on wind stress and atmospheric mixing in a regional coupled atmosphere-wave model. *J. Geophys. Res.*, 121(7), 4633-4648. doi:10.1002/2015JC011576

Wu, Y., Tang, C., and Hannah, C. (2012). The circulation of eastern Canadian seas. *Prog. Oceanogr.,*106, 28-48. doi:10.1016/j.pocean.2012.06.005

Xia, M., Mao, M., and Niu, Q. (2020). Implementation and comparison of the recent three-dimensional radiation stress theory and vortex-force formalism in an unstructured-grid coastal circulation model. *Estuar. Coast. Shelf Sci.,* 240, 106771. doi:10.1016/j.ecss.2020.106771

Xiao, W., Liu, S., Wang, W., Yang, D., Xu, J., Cao, C., Li, H., and Lee, X. (2013), Transfer coefficients of momentum, heat and water vapour in the atmospheric surface layer of a large freshwater lake. *Bound.-Layer Meteor.,* 148(3), 479-494. doi:10.1007/s10546-013-9827-9

Xie, L., Wu, K., Pietrafesa, L., and Zhang, C. (2001). A numerical study of wave-current interaction through surface and bottom stresses: Wind-driven circulation in the South Atlantic Bight under uniform winds. *J. Geophys. Res.*, 106(C8), 16841-16855. doi:10.1029/2000JC000292

Xu, Y., He, H., Song, J., Hou, Y., and Li, F. (2017). Observations and modeling of typhoon waves in the South China Sea. *J. Phys. Oceanogr.,* 47(6), 1307-1324. doi:10.1175/JPO-D-16-0174.1

Yelland, M., and Taylor, P. K. (1996). Wind stress measurements from the open ocean. *J. Phys. Oceanogr.,* 26(4), 541-558. doi:10.1175/1520-0485(1996)026<0541:WSMFTO>2.0.CO;2

Young, I. R., and Babanin, A. V. (2006). Spectral distribution of energy dissipation of wind-generated waves due to dominant wave breaking. *J. Phys. Oceanogr.,* 36(3), 376-394. doi:10.1175/JPO2859.1

Young, I. R., and Ribal, A. (2019). Multiplatform evaluation of global trends in wind speed and wave height. *Sci.,* 364(6440), 548-552. doi:10.1126/science.aav9527

Young, I. R., Sanina, E., and Babanin, A. V. (2017). Calibration and cross validation of a global wind and wave database of altimeter, radiometer, and scatterometer

measurements. *J. Atmos. Oceanic Tech.,* 34(6), 1285-1306. doi:10.1175/JTECH-D-16-0145.1

Yu, L. (2019). Global air-sea fluxes of heat, fresh water, and momentum: energy budget closure and unanswered questions. *Annu. Rev. Mar. Sci.,* 11, 227-248. doi:10.1146/annurev-marine-010816-060704

Zachry, B. C., Schroeder, J. L., Kennedy, A. B., Westerink, J. J., Letchford, C. W., and Hope, M. E. (2013). A case study of nearshore drag coefficient behavior during Hurricane Ike (2008). *J. Appl. Meteor. Climatol.,* 52(9), 2139-2146. doi:10.1175/JAMC-D-12-0321.1

Zamora-Sillero, E., Hafner, M., Ibig, A., Stelling, J., and Wagner, A. (2011). Efficient characterization of high-dimensional parameter spaces for systems biology. *BMC Systems Biology,* 5(1), 1-22.doi: 10.1186/1752-0509-5-142

Zhao, D., and Li, M. (2019). Dependence of wind stress across an air-sea interface on wave states. *J. Oceanogr.,*75(3), 207-223. doi:10.1007/s10872-018-0494-9

Zhao, X., Shen, H. H., and Cheng, S. (2015). Modeling ocean wave propagation under sea ice covers. *Acta Mechanica Sinica,* 31(1), 1-15. doi:10.1007/s10409-015-0017-5

Zheng, J., Mase, H., Demirbilek, Z., Lin, L. (2008). Implementation and evaluation of alternative wave breaking formulas in a coastal spectral wave model. *Ocean Eng.,* 35(11-12), 1090-1101. doi:10.1016/j.oceaneng.2008.05.001

Zieger, S., Babanin, A. V., Rogers, W. E., and Young, I. R. (2015). Observation-based source terms in the third-generation wave model WAVEWATCH. *Ocean Modell.,* 96, 2-25. doi:10.1016/j.ocemod.2015.07.014

Zieger, S., Vinoth, J., and Young, I. R. (2009). Joint calibration of multiplatform altimeter measurements of wind speed and wave height over the past 20 years. *J. Atmos. Ocean. Tech.,* 26(12), 2549-2564. doi:10.1175/2009JTECHA1303.1

Zijlema, M., Van Vledder, G.P., Holthuijsen, L.H. (2012). Bottom friction and wind drag for wave models. *Coast. Eng.,* 65, 19-26. doi:10.1016/j.coastaleng.2012.03.002

Zou, Q., and Xie, D. (2016). Tide-surge and wave interaction in the Gulf of Maine during an extratropical storm. *Ocean Dyn.,* 66(12), 1715-1732. doi:10.1007/s10236-016-1002-7